THÈSE

En vue de l'obtention du

DOCTORAT DE L'UNIVERSITÉ DE TOULOUSE

Délivré par :

Université Toulouse 3 Paul Sabatier (UT3 Paul Sabatier)

Présentée et soutenue par :

Oluwakemi DARE-IDOWU

le 17 décembre 2021

Titre :

Impact of climate and anthropogenic effects on the energy, water, and carbon budgets of monitored agrosystems: multi-site analysis combining modelling and experimentation.

École doctorale et discipline ou spécialité :

ED SDU2E : Surfaces et interfaces continentales, Hydrologie

Unité de recherche :

CESBIO – Centre d'Etudes Spatiales de la Biosphère

Directeur/trice(s) de Thèse :

Aurore BRUT et Lionel JARLAN

Jury :

M. Christian Brümmer, Rapporteur
M. Bernard Longdoz, Rapporteur
M. Benjamin Loubet, Examinateur
M. Joan Cuxart, Examinateur
Mme. Fabienne Lohou, Examinatrice
Mme. Valérie le Dantec, Examinatrice

THÈSE

En vue de l'obtention du
DOCTORAT DE L'UNIVERSITÉ DE TOULOUSE
Délivré par l'Université Toulouse 3 – Paul Sabatier

Présentée et soutenue par
Oluwakemi DARE-IDOWU

Impact of climate and anthropogenic effects on the energy, water, and carbon budgets of monitored agrosystems: multi-site analysis combining modelling and experimentation.

Ecole doctorale : **SDU2E - Science de l'Univers, de l'Environnement de l'Espace**
Spécialité : **Surfaces et l'interfaces continentales, Hydrologie**
Unité de recherche : **CESBIO – Centre d'Etudes Spatiales de la Biosphère**

Thèse dirigée par
Aurore BRUT et Lionel JARLAN

Jury
M. Christian Brümmer, Rapporteur

M. Bernard Longdoz, Rapporteur

M. Benjamin Loubet, Examinateur

M. Joan Cuxart, Examinateur

Mme. Fabienne Lohou, Examinatrice

Mme. Valérie le Dantec, Examinatrice

Mme. Aurore Brut, Directrice de thèse

M. Lionel Jarlan, Co-directeur de thèse

Remerciements

'My name might be on this dissertation, but you all birthed it'

First, I thank The Light, to whom I owe all.

My sincere gratitude goes to my supervisors Aurore Brut and Lionel Jarlan for their invaluable supervision. I am deeply indebted to you Mme. Aurore, I really am. To Joan Cuxart, thank you for being an incredible teacher particularly during my secondment in Mallorca.

Aaron Boone, you are a light, and you showed me the way with SURFEX. To the members of the jury and thesis committee; Fabienne Lohou, Gilles Boulet, thank you for accepting this role, and for providing a road map all through. Also, I appreciate Christian Brümmer and Bernard Longdoz for agreeing to review and read this very long manuscript.

I am grateful to the directors of the CESBIO laboratory, Laurent Polidori, and Zribi Mhrez. Lawrence, thank you for your hearty laughter, it pacifies! A special 'thank you' to Vincent Rivalland, Valerie Le-Dantec, and Tiphaine Tallec for your guidance and constructive suggestions, to Michel Le Page and Sylvian for the talks and 'comment vas tu(s)'.

My gratitude to Maria-José Escorihuela for the opportunity to be a part of the ACCWA team as an early-stage researcher, and for granting access to isardSAT. A special mention goes to the UIB-Physics team for a memorable stay at the Universitat de les Illes Balears.

I acknowledge the Petroleum Technology Development Fund for funding this program, and a special shout-out to my specials (Julie, Jessica, Sam M., Ola, Nike, Tobi, …) for the beautiful moments here and there. To the *Fenouilladians*, thank you for those special wood-walks and meaningful conversations, and to Skoop, unsere Gespräche haben mich über Wasser gehalten.

Prof. Babatunde Rabiu, you have been HIS wonder in my life. Finally, to my mummy, daddy, Sam S., and my tKtKtK zGzBmBms- you all rock!

“*The pollution of the planet is only an outward reflection of an inner psychic pollution*”

Eckhart Tolle

So, keep the hearth of your thoughts pure.

Table of content

List of figures

List of tables

List of abbreviations and symbols

BS	Bare Soil	–
BR	Bowen Ratio	–
C	Carbon	–
$\boldsymbol{CO_2}$	Carbon dioxide	–
$\boldsymbol{c_s}$	Specific heat capacity of the soil	J kg^{-1} K^{-1}
$\boldsymbol{c_{sap}}$	Specific heat capacity of the sap	J kg^{-1} K^{-1}
EBC	Energy Balance Closure	–
EBR	Energy Balance Ratio	–
EC	Eddy Covariance	–
$\boldsymbol{Es}$	Soil evaporation	mm
$\boldsymbol{Ei}$	Intercepted water	mm
$\boldsymbol{ET}$	Evapotranspiration	mm
$\boldsymbol{G}$	Ground Heat Flux	W m^{-2}
$\boldsymbol{GAI}$	Green Area Index	m^{2} m^{-2}
$\boldsymbol{G_{st}}$	Ground heat storage	W m^{-2}
$\boldsymbol{H}$	Sensible heat flux	W m^{-2}
$\boldsymbol{H_{st}}$	Sensible heat storage	W m^{-2}
HFP	Heat Flux Plate	–
IRGA	InfraRed Gas Analyzer	–
ISBA	Interactions Between the Soil-Biosphere-Atmosphere	–
ISBA-MEB	ISBA- Multi Energy Balance	–
$\boldsymbol{LAI}$	Leaf Area Index	m^{2} m^{-2}
$\boldsymbol{LE}$	Latent Heat Flux	W m^{-2}
LSM	Land Surface Model	–
LST	Land Surface Temperature	^{0}C
$\boldsymbol{L_{st}}$	Latent heat storage	W m^{-2}
$\boldsymbol{LWin}$	Incoming longwave radiation	W m^{-2}
$\boldsymbol{LWout}$	Outgoing longwave radiation	W m^{-2}
$\boldsymbol{NEE}$	Net Ecosystem Exchange	$\mu mol\ m^{-2} s^{-1}$
$\boldsymbol{NEP}$	Net Ecosystem Production	$gC\ m^{-2} yr^{-1}$
$\boldsymbol{P}$	Rainfall	mm
$\boldsymbol{PAR}$	Photosynthetic active radiation	$\mu mol\ m^{-2} s^{-1}$

$\boldsymbol{R_A}$	Autotrophic Respiration	$\mu mol\ m^{-2} s^{-1}$
$\boldsymbol{RECO}$	Ecosystem Respiration	$\mu mol\ m^{-2} s^{-1}$
$\boldsymbol{R_H}$	Heterotrophic Respiration	$\mu mol\ m^{-2} s^{-1}$
$\boldsymbol{Rn}$	Net Radiation	W m^{-2}
$\boldsymbol{S_P}$	Photosynthesis storage	W m^{-2}
$\boldsymbol{SR}$	Soil Respiration	gC m^{-2} d^{-1}
$\boldsymbol{swc}$	Soil Water Content	%
$\boldsymbol{SWin}$	Incoming shortwave radiation	W m^{-2}
$\boldsymbol{SWout}$	Outgoing shortwave radiation	W m^{-2}
$\boldsymbol{TA}$	Air Temperature	ºC
$\boldsymbol{Tr}$	Transpiration	mm
$\boldsymbol{TS}$	Surface Temperature	ºC
$\boldsymbol{T_S}$	Soil Temperature	ºC
$\boldsymbol{WS}$	Wind Speed	$m\ s^{-1}$
$\boldsymbol{WD}$	Wind Direction	º
$\boldsymbol{z_{EC}}$	Measuring height of eddy covariance system	m
$\boldsymbol{\lambda_s}$	Thermal conductivity of the soil	W m^{-1} K^{-1}
$\boldsymbol{\lambda_v}$	Latent heat of vaporization of water	J kg^{-1}
$\boldsymbol{\rho_s}$	Soil density	kg m^{-3}
$\boldsymbol{\rho_a}$	Air density	kg m^{-3}

Abstract

Croplands have been proven to be key components in the global climate system, and in response to the growing populace, they are under expansion. The cost of this expansion includes a depletion of the soil-carbon stocks due to intensive farming, higher irrigation water demand in the face of water scarcity, and the alteration of both the local climate and the surface energy pattern through ecosystem processes. Hence, an in-depth understanding of the functioning of croplands is required, alongside the processes governing the land-surface exchanges of energy, water, and carbon fluxes. Within this context, the aim of my thesis is to contribute to the knowledge-base of the functioning of croplands, and to understand the transport processes within the soil-vegetation-atmosphere continuum through the assessment of the surface energy balance, and the analysis of water and carbon budget.

The first part of this work was a surface energy balance study over two experimental croplands in southwestern France (Lamasquère (FR-Lam), and Auradé (FR-Aur)) using measurements obtained from the eddy covariance (EC) system under different scenarios from 2005 to 2015. One of such scenarios involved the selection of contrasting crop years using rainfall amount as a proxy, another analyzed the energy balance closure (EBC) under different phenological stages for different crop types while also considering the influence of soil-works and atmospheric conditions. Overall, our results showed that the site-specific characteristics exerts a stronger impact on the EBC because EBC was generally higher in FR-Aur (82%) than in FR-Lam (67%) under all scenarios- even for the same crop type. Similarly, phenologies and rainfall have crucial control on the surface fluxes, while their impact on the EBC remains unclear. During the wet seasons, over 42% of total net radiation (Rn) was accounted for by the latent heat flux (LE), which was 9% higher than the LE in the dry year. Similarly, the ground heat flux (G) is strongly modulated by vegetation; G accounts for 30% of Rn for low vegetation, and at the peak of growth, it falls below 16% due to canopy shading. Finally, analysis of the sensible heat advection revealed that it is a significant component of the surface energy budget.

The second part of this study questions the representation of the energy balance of maize and wheat in Soil–Vegetation–Atmosphere-Transfer (SVAT) models using 10 years of EC measurements from 2006 to 2019 considering the high representativeness of these crops in southwestern France. To this objective, a comparison between the single-source and the Multi-source Energy Balance version (ISBA-MEB) of the Interactions between the Soil–Biosphere Atmosphere (ISBA) model were evaluated. The models were evaluated with the photosynthetic option activated using only *in-situ* forcings. The result showed that the convective fluxes were properly reproduced by both models with R^2 ranging between 0.41 and 0.80 (RMSE < 59 W m^{-2}) for the sensible heat flux and between 0.63

and 0.89 (RMSE < 59 W m^{-2}) for LE. Statistics also showed that in 80% of the cases, ISBA-MEB was in better agreement with the *in-situ* data with an R^2 value that is 1-11% higher, and a RMSE that is 2–31% lower than ISBA. Furthermore, the evapotranspiration (ET) partitioning of both models into plant transpiration compared very well with the sap flow measurements obtained over maize-2015 in FR-Lam- although, statistics in ISBA-MEB were slightly better (R^2 of 0.91 and RMSE of 0.07 mm h^{-1}). This proved the need to distinguish the energy budget of the soil from the vegetation particularly when the field is a mix of bare soils and vegetation. Finally, the analysis of the inter-annual variability of the water components provided insights into *how much* water is being used by plants, and *how much* is lost through soil evaporation and deep drainage.

The third part of this study is twofolds; the first is a comparative study of soil efflux from an automated chamber (AC) and an EC system: Results show that both systems have comparable measurements: 0.03 gC m^{-2} to 9.4 gC m^{-2} for the EC, and 0.1 gC m^{-2} to 10.7 gC m^{-2} for AC, but they are weakly correlated (R^2 is 0.51 and RMSE is 1.51 gC m^{-2} d^{-1}). This discrepancy is perhaps due to the difference in operating principle, difficulty in reconciling the footprints of both systems, and errors resulting from the limitations of both systems.

The second part is the performance assessment of ISBA-MEB in the estimation of some carbon components over 4 wheat and 7 maize years. Vegetation indices drawn from MODIS were used to represent the weeds and regrowths, and this presented slight improvements in the estimates- R^2 ranged between 0.72 and 0.96 for the gross primary production (GPP), 0.53 and 0.90 for the ecosystem respiration ($RECO$), and 0.60 and 0.81 for the net ecosystem exchange (NEE). Also, the RMSEs are within acceptable ranges of 1.1 gC m^{-2} d^{-1} to 2.1 gC m^{-2} d^{-1} for GPP, 0.7 gC m^{-2} d^{-1} to 2.0 gC m^{-2} d^{-1} for $RECO$, and 1.1 gC m^{-2} d^{-1} to 2.0 gC m^{-2} d^{-1} for NEE. Although these are preliminary findings, the performance of ISBA-MEB is largely satisfactory despite minimal calibration.

Keywords: Surface Energy Balance, SVAT, evapotranspiration, Eddy Covariance, Net Ecosystem Exchange

Résumé

Il a été prouvé que les terres cultivées sont des éléments clés du système climatique mondial et, en réponse à la croissance démographique, elles sont en expansion. Le coût de cette expansion comprend un appauvrissement des stocks de carbone du sol dû à l'agriculture intensive, une augmentation de la demande en eau d'irrigation face à la pénurie d'eau, et la modification du climat local et du schéma énergétique de surface par les processus écosystémiques. Il est donc nécessaire de comprendre en profondeur le fonctionnement des terres cultivées, ainsi que les processus qui régissent les échanges d'énergie, d'eau et de flux de carbone entre la terre et la surface. Dans ce contexte, l'objectif de ma thèse est de contribuer à la base de connaissances sur le fonctionnement des terres cultivées, et de comprendre les processus de transport dans le continuum sol-végétation-atmosphère par l'évaluation du bilan énergétique de surface, et l'analyse du bilan d'eau et de carbone.

La première partie de ce travail était une étude du bilan énergétique de surface sur deux terres cultivées expérimentales dans le sud-ouest de la France (Lamasquère (FR-Lam), et Auradé (FR-Aur)) en utilisant des mesures obtenues à partir du système de Covariance Eddy (EC) sous différents scénarios de 2005 à 2015. L'un de ces scénarios impliquait la sélection d'années culturales contrastées en utilisant la quantité de pluie comme proxy, un autre analysait la fermeture du bilan énergétique (EBC) sous différents stades phénologiques pour différents types de cultures tout en considérant également l'influence des travaux du sol et des conditions atmosphériques. Dans l'ensemble, nos résultats ont montré que les caractéristiques spécifiques du site exercent un impact plus fort sur l'EBC car l'EBC était généralement plus élevé en FR-Aur (82%) qu'en FR-Lam (67%) dans tous les scénarios - même pour le même type de culture. De même, les phénologies et les précipitations ont un contrôle crucial sur les flux de surface, alors que leur impact sur l'EBC reste flou. Pendant les saisons humides, plus de 42% du rayonnement net total (Rn) était représenté par le flux de chaleur latente (LE), qui était de 9% supérieur au LE de l'année sèche. De même, le flux de chaleur du sol (G) est fortement modulé par la végétation; G représente 30% de Rn pour une végétation basse, et au pic de croissance, il tombe en dessous de 16% en raison de l'ombrage de la canopée. Enfin, l'analyse de l'advection de la chaleur sensible a révélé qu'elle est une composante importante du bilan énergétique de surface.

La deuxième partie de cette étude questionne la représentation du bilan énergétique du maïs et du blé dans les modèles Sol-Végétation-Atmosphère-Transfert (SVAT) en utilisant 10 années de mesures EC de 2006 à 2019 en considérant la forte représentativité de ces cultures dans le sud-ouest de la France. Dans cet objectif, une comparaison entre la version monosource et la version multi-source du bilan énergétique (ISBA-MEB) du modèle Interactions entre le sol, la biosphère et l'atmosphère (ISBA) a été évaluée. Les modèles ont été évalués avec l'option photosynthétique activée en utilisant uniquement des forçages in-situ. Les résultats montrent que les flux convectifs ont été correctement reproduits par les deux modèles avec un R^2 compris entre 0,41 et 0,80 (RMSE < 59 W m^{-2}) pour le flux de chaleur sensible et entre 0,63 et 0,89 (RMSE < 59 W m^{-2}) pour LE. Les statistiques ont également montré que dans 80% des cas, ISBA-MEB était en meilleur accord avec les données in-situ avec une valeur R^2 supérieure de 1-11% et une RMSE inférieure de 2-31% à ISBA. En outre, le partitionnement de l'évapotranspiration (ET) des deux modèles en transpiration de la plante s'est très bien comparé aux mesures de flux de sève obtenues sur le maïs-2015 dans FR-Lam- bien que les statistiques d'ISBA-MEB aient été légèrement meilleures (R^2 de 0,91 et RMSE de 0,07 mm h^{-1}). Cela a prouvé la nécessité de distinguer le budget énergétique du sol de celui de la végétation, en particulier lorsque le champ est un mélange de sols nus et de végétation. Enfin, l'analyse de la variabilité interannuelle des composantes de l'eau a permis de comprendre quelle quantité d'eau est utilisée par les plantes, et quelle quantité est perdue par l'évaporation du sol et le drainage profond.

La troisième partie de cette étude est double: la première est une étude comparative de l'efflux du sol à partir d'une chambre automatisée (AC) et d'un système EC: Les résultats montrent que les deux systèmes ont des mesures comparables: 0,03 gC m^{-2} à 9,4 gC m^{-2} pour la EC, et 0,1 gC m^{-2} à 10,7 gC m^{-2} pour la AC, mais elles sont faiblement corrélées (R^2 est 0,51 et RMSE est 1,51 gC m^{-2} d^{-1}). Cette divergence est peut-être due à la différence de principe de fonctionnement, à la difficulté de concilier les empreintes des deux systèmes et aux erreurs résultant des limites des deux systèmes.

La deuxième partie est l'évaluation des performances d'ISBA-MEB dans l'estimation de certaines composantes du carbone sur 4 années de blé et 7 années de maïs. Des indices de végétation tirés de MODIS ont été utilisés pour représenter les mauvaises herbes et les repousses, ce qui a permis d'améliorer légèrement les estimations - R^2 se situe entre 0,72 et 0,96 pour la production primaire gross (GPP), 0,53 et 0,90 pour la respiration de l'écosystème ($RECO$), et 0,60 et 0,81 pour l'échange net de l'écosystème (NEE). De même, les RMSE se situent dans des fourchettes acceptables de 1,1 gC m^{-2} d^{-1} à 2,1 gC m^{-2} d^{-1} pour la GPP, de 0,7 gC m^{-2} d^{-1} à 2,0 gC m^{-2} d^{-1} pour le $RECO$, et de 1,1 gC m^{-2} d^{-1} à 2,0 gC m^{-2} d^{-1} pour le NEE. Bien qu'il s'agisse de résultats préliminaires, les performances de l'ISBA-MEB sont largement satisfaisantes malgré une calibration minimale.

Mots clés : Bilan énergétique de surface, SVAT, évapotranspiration, covariance de Foucault, échange net entre écosystèmes.

General Introduction

General context

Eighty-three years ago, Guy Stewart Callendar made a monumental discovery. Known as the Callendar effect, this discovery linked the increasing anthropogenic carbon dioxide concentration to global warming (Fleming, 1998). Global warming refers specifically to the effect of the greenhouse gases (GHGs) (e.g., carbon dioxide (CO_2), nitrous oxide (N_2O), methane (CH_4)) on the Earth's average surface temperature. The Earth becomes overwarmed when the radiations leaving its surface are re-absorbed by these GHGs, thanks to their heat-trapping capacity. The dilemma stems from the increasing atmospheric concentration of these gases which is invoking a long-term change in the weather pattern of our planet. Consequently, climate change, which was once considered an issue for a long-distant future has firmly moved into our present as seen from recent events.

Over the past couple of years, natural disasters begging for climate actions have become a regular feature of our weather, and more so, major sectors of the economy (e.g., healthcare (Semenza et al., 2014), energy (Cronin et al., 2018), agriculture (Arora, 2019) etc) have been reportedly hit. Bringing the focus to the agricultural sector, the United Nations (UN) has projected the human population to rise by 26% in 2100. In response to this population rise, the expansion of croplands and intensification of agricultural practices becomes inevitable. As such, more water is required for irrigation, and more land-use changes would be witnessed. The twists between our food security and this impending climate crisis are numerous and complex:

(i) These land disturbances for cultivation threaten the soil-carbon stock, and the research published in the Proceedings of the National Academy of Sciences estimated that approximately 133bn Tonnes of carbon has been lost from the top 2 meters of the world's soil since the dawn of agriculture (Sanderman et al., 2018). Furthermore, according to West et al. (2004), a 20-year period of continuous tilling releases about 30% of the stored carbon. In these scenarios, the vulnerability of agriculture lies in the fact that with this increasing atmospheric CO_2 levels, the greenhouse effect is enhanced, and this increases atmospheric temperature.

(ii) According to the projection of Zhao et al. (2017), each degree-Celsius increase in the average global temperature could reduce the global yield of major crops by 3-6% because of hydric stress.

(iii) Stemming from increasing atmospheric demand, although the projected estimates are quite uncertain, the expected demand for fresh water by the irrigation sector would exceed the available resource. As a consequence, this additional water stress could cause an exponential climb in the vapor pressure deficit with a cost of reduced photosynthesis and growth in plants (Grossiord et al., 2020).

From the above scenarios, it is clear that the implication of the climate crisis is severe, and it goes beyond economic stress. First, it is a threat multiplier for undernourished and hungry people particularly countries without stable food systems. Second, in many developing countries, two-thirds of the population engage in agriculture for sustenance (Roser, 2013), while in the developed economies, roughly 6% of the populace are employed by the sector. Hence, a fall in agricultural production translates into employment and financial insecurity; and according to a report in the International Labor Organization, by 2030, the agricultural sector could lose 60% of its working hours to heat stress. Amidst these reasons, the primary sustainable development goals (SDGs) of the UN seeks to end poverty and hunger, while the 4 per 1000 Soils for Food Security and Climate- an initiative launched by the French government at the United Nations Climate Change Conference in 2015 has as its objective to sequester 0.4% of the atmospheric CO_2 every year. Unfortunately, engagements in activities that counter these initiatives is still on the high. Some of these include:

(i) Tillage: this soil-alteration procedure increases the exposure of organic matter for quicker microbial decomposition- this increases microbial respiration, and provides pathways for carbon emission (Mangalassery et al., 2014).

(ii) Residue management: in eastern and southern Europe for instance, some farmers still engage in stubble burning prior to planting (Airuse, 2016). This strategy has been identified to convert 70% of the stubble's carbon to $\mathrm{CO_2}$ (Abdurrahman et al., 2020).

(iii) Irrigation: referred to as the birch effect, when low irrigation amount is applied after a long period of drought, it causes an expulsion of $\mathrm{CO_2}$ pulses resulting from rapid decomposition.

Hence, for a possible realization of '4 per 1000', the aforementioned SDG goal, and similar initiatives, new and sustainable agricultural practices are required, and some include:

(i) Exploitation of the sequestering potential of croplands: This potential is linked to a proper identification of mechanisms and practices that trigger the emission of $\mathrm{CO_2}$ flux- this would preserve, and possibly increase the soil carbon stock.

(ii) Understanding the functioning of croplands: This includes how energy is partitioned over land surfaces, factors that regulate this, and the interaction of these fluxes.

(iii) Understanding the hydrological functioning of a plot: This involves soil-water balance assessment through the precise estimation of crop-water need for optimal irrigation.

Scientific context and questions

The Earth is a highly complex system formed by mutually interconnected subsystems (land, atmosphere, ocean), interfaces (land-atmosphere, atmosphere-ocean, land-ocean), and processes operating at different scales (Suni et al., 2015). A proper understanding of the whole system is predicated on the understanding of each component plus its interaction with the other subsystems e.g., land-atmosphere interaction. Land-atmosphere interactions are characterized by continuous exchanges, and these exchanges are critical in the Earth's micro-climate because it drives the water, energy, and carbon cycles (Findell et al., 2009).

Over the past decades, the need to understand the functioning of croplands alongside their interaction with the atmosphere has been a rising subject. A good prediction of these surface-atmosphere exchanges is crucial for water and energy recycling processes (Eltahir, 1996), and for numerical weather and climate predictions (Rowntree, 1991) because these fluxes impact the thermo-hydric characteristics of the lower atmosphere. Similarly, these fluxes govern the partitioning of water in the hydrological cycle, and so, they are key incatchment scale hydrology. Furthermore, these fluxes are significant in agronomy and serve as indicators for the physiological state of plants (e.g., the hydric status)- a good understanding of these processes is required for effective irrigation scheduling (Evett et al., 2009; Le Page et al., 2012) and yield forecasting (Yang et al., 2018).

Evapotranspiration (ET) fluxes have been recognized as one of the most uncertain components of the hydro-climatic system (Jasechko et al., 2013) especially over agrosystems which present high heterogeneity in terms of the hydric status, phenology, plants health etc. Some factors that inhibit accurate estimation of ET over croplands are as follows:

(i) Diversity in agricultural practices: E.g., irrigation. Irrigation locally reduces land surface temperature through enhanced stomatal opening and evapotranspiration while contrasting soil moisture condition exists in the neighboring non-irrigated surfaces (Lawston et al., 2015). This situation impacts the partitioning of the available energy into sensible (H) and latent heat fluxes (LE), while enhancing horizontal sensible heat advection from the surrounding drier surface (Lei and Yang, 2010). The response of the water and energy budget is that the partitioning of the available energy is altered, and a false ET is estimated because the advection becomes a source of energy for ET (Tolk et al., 2006; Lei and Yang, 2010). Other agricultural components that limit the accurate estimation of ET include differences in sowing dates, and fertilization (Singh et al., 2013).

(ii) Heterogeneity of agrosystems: To characterize land-atmosphere exchanges over large scales, surface heterogeneity in the form of topography or uneven canopy stress especially in mixed cropping poses a challenge. Heterogeneity heavily modifies the energy and water balance because of uneven land-atmospheric exchanges which could result to substantial errors (Liu et al., 2012; Xu et al., 2014).

(iii) Wide range in cultivated crops: The popular classification of crops is based on photorespiration (e.g., maize and sorghum as C4 crops; wheat and sunflower as C3 crops etc). Nonetheless, accurate assessment of ET requires a unique consideration of each crops characteristics (e.g., resistance to transpiration, crop roughness, solar reflection, rooting system etc).

Nevertheless, the need to quantify these exchanges has necessitated the development of several micro-meteorological instruments among which, the eddy covariance (EC) method used by EC systems has become a reference in the scientific community. Aside spatial limitations, it is known that the energy balance is never experimentally closed with EC fluxes (Foken et al., 2010). In the literatures (see Chapter 1 for a review), possible factors responsible for this non-closure include mismatch of footprints, storage terms, advection, etc. While some of these factors can be corrected, others cannot (Wilson et al., 2002; Du et al., 2014).

Beside EC methods, there is scintillometry and lysimetery. Scintillometers were limited until recently to the optical domain. As such, an optical scintillometer measures the scintillation of light in the optical domain that can be related to H; LE is then computed as a residual of the energy balance considering that the conduction flux (G) and the net radiation (Rn) are known within the footprint of the instrument. One major limitation of this instrument is that it applies the Monin-Obukhov

Similarity Theory (MOST) to estimate H, and the applicability of MOST is limited over complex terrains. In addition, lysimeters offer a promising alternative to estimate LE but the spatial representation is very limited, and a residual approach is also adopted.

Over the past decades, LSMs of different complexities have been developed for the assessment of surface-atmosphere exchanges. For example, there are conceptual approaches e.g., the FAO-56 double coefficient approach (Allen et al., 1998) that solves a simple soil water budget, and estimates ET by adjusting the climatic evaporative demand by an empirical coefficient. The latter called "the cultural coefficient" encompasses all the processes related to crop growth that are not explicitly represented by the model. This approach has been extensively assessed by comparison with *in-situ* measurements (Duchemin et al., 2006; El-Raki et al., 2007). Besides this, there are empirical models based on simple relationships using thermal infrared data and climatic variables (Jackson et al., 1977), and there are also models of higher complexities that are based on residual energy balance methods e.g., Surface Energy Balance Systems (Su, 2002), Surface Energy Balance Algorithm for Land (Bastiaanssen et al., 1998), Mapping EvapoTranspiration at a high-Resolution with Internalized Calibration (Allen et al., 2007). Similarly, there are physically based Soil-Vegetation-Atmosphere Transfer (SVAT) models that characterize exchanges between the soil-vegetation-atmosphere continuum e.g., Soil Plant Atmosphere and Remote Sensing Evapotranspiration (Boulet et al., 2015), Interactions between Soil-Biosphere-Atmosphere (Noilhan and Planton, 1989). Although rich literatures dealing with the evaluation of SVAT models over natural ecosystems exists, more assessment studies are needed particularly for highly dynamic agrosystems, with highly transient moisture conditions associated with irrigation. Finally, regarding the importance of agrosystems within the global climate, a hot issue is the representation of agricultural practices (e.g., irrigation) within SVAT models (Druel et al., 2021).

PhD motivation, objectives, and organization of this manuscript

Within the context of the above issues, the focus of my thesis is to better understand the functioning of two crop sites (Lamasquère (FR-Lam) and Auradé (FR-Aur)) situated in southwestern France. This focus has been partitioned into three research objectives:

1. The first investigated the variability of the energy balance closure at both sites under different crop types, phenologies, and farm practices. Attention was given to the influence of atmospheric conditions and sensible heat advection on the surface energy budget. Given the

high applicability of EC fluxes especially in the validation of LSMs, this study aims to better understand the quality of the measured fluxes and provide clues to narrow the energy gap.

2. The second objective is a performance evaluation and comparison of a single-source model (Interactions between the Soil-Biosphere-Atmosphere: ISBA), and its double-source version (Multi Energy Balance: ISBA-MEB) in the simulation of energy and water fluxes over six seasons of irrigated maize and four seasons of non-irrigated wheat in FR-Lam. Evaluation was carried out using EC measurements, and a special attention was paid to the ET partitioning by these models. This comparative study could help users in deciding *what* model configuration to use, and at *what* level of surface heterogeneity.
3. Over the same crops in (2), the third objective evaluated the potential of ISBA-MEB to correctly simulate the carbon components as a possible gap-filling resource by testing against EC measurements. This analysis would provide insights into the carbon status of the plot and demonstrates the relevance of certain farm practices within the carbon budget.

This manuscript is composed of six chapters:

1. Chapter 1 reviews the general concept of the soil-vegetation-atmosphere exchanges with attention to the surface energy, water, and carbon balance.
2. Chapter 2 describes the two experimental sites, their set-up, measuring and data-processing protocols, and describes some remotely sensed data. The later section of this chapter describes the LSM used in this study.
3. The third chapter is dedicated to a surface energy balance study over FR-Lam and FR-Aur.
4. In chapter 4, the performance of ISBA and ISBA-MEB in simulating the components of the energy, and water budget is evaluated.
5. In chapter 5, we present and analyse the first results of the carbon components simulated with ISBA-MEB against EC measurements.
6. Chapter 6 sums up all these results and provided some perspectives.

Introduction générale

Le contexte général

Il y a quatre-vingt-trois ans, Guy Stewart Callendar a fait une découverte monumentale. Connue sous le nom d'effet Callendar, cette découverte établissait un lien entre l'augmentation de la concentration de dioxyde de carbone anthropique et le réchauffement climatique (Fleming, 1898). Le réchauffement climatique désigne spécifiquement l'effet des gaz à effet de serre (GES) (par exemple, le dioxyde de carbone (CO_2), l'oxyde nitreux (N_2O), le méthane (CH_4) etc.) sur la température moyenne de la surface de la Terre. La Terre se surchauffe lorsque les radiations qui quittent sa surface sont réabsorbées par ces GES, grâce à leur capacité de piégeage de la chaleur. Le dilemme provient de l'augmentation de la concentration atmosphérique de ces gaz qui invoque un changement à long terme du modèle météorologique de notre planète. Par conséquent, le changement climatique qui était autrefois considéré comme un problème pour un avenir lointain, s'est fermement installé dans notre présent comme le montrent les événements récents.

Au cours des deux dernières années, les catastrophes naturelles nécessitant des actions climatiques sont devenues une caractéristique régulière de notre temps, et plus encore, des secteurs majeurs de l'économie (par exemple, les soins de santé (Semenza et al., 2014), l'énergie (Cronin et al., 2018), l'agriculture (Arora, 2019) etc. En mettant l'accent sur le secteur agricole, l'Organisation des Nations Unies (ONU) a prévu que la population humaine augmenterait de 26 % en 2100. Cette augmentation de la population déclenchera inévitablement l'expansion des terres agricoles pour la production alimentaire. Ainsi, pour satisfaire la demande alimentaire, on assisterait à davantage de changements dans l'utilisation des terres et de pratiques agricoles intensives, et donc à une augmentation des besoins en eau pour l'irrigation. Les torsions entre notre sécurité alimentaire et cette crise climatique imminente sont nombreuses et complexes :

(i) Les perturbations des sols pour la culture menacent le stock mondial de carbone, et la recherche publiée dans les Actes de l'Académie Nationale des Sciences a estimé qu'environ 133bn Tonnes de carbone ont été perdues des 2 mètres supérieurs du sol mondial depuis l'aube de l'agriculture (Sanderman et al., 2018), et selon West et al. (2004), une période de 20 ans de labourage continu libère environ 30% du carbone stocké dans le sol. Dans ces scénarios, la vulnérabilité de la production agricole réside dans le fait qu'avec cette augmentation des niveaux de (CO_2) atmosphérique, certaines cultures alimentaires subiraient probablement des pertes de rendement et même de qualité nutritionnelle, par exemple le maïs (Reiny, 2007), le blé (Navarro et al., 2020), etc.

(ii) De même, selon la projection de Zhao et al. (2017), chaque degré Celsius d'augmentation de la température moyenne mondiale réduirait le rendement mondial des principales cultures de 3 à 6 %. Cela signifie qu'avec cette accélération des pénuries alimentaires, la demande alimentaire croissante de la population en augmentation ne serait pas satisfaite.

(iii) En outre, découlant de l'augmentation de la demande atmosphérique, bien que les estimations projetées soient assez incertaines, la demande d'eau douce prévue par le secteur de l'irrigation dépasserait les ressources en eau disponibles. Par conséquent, ce stress hydrique supplémentaire entraînerait une augmentation exponentielle du déficit de pression de vapeur avec un coût de réduction de la photosynthèse et de la croissance des plantes (Grossiord et al., 2020).

D'après les scénarios ci-dessus, l'implication de la crise climatique est grave et va au-delà du stress économique. Tout d'abord, elle constitue un multiplicateur de menaces pour les personnes sous-alimentées et affamées, notamment dans les pays dépourvus de systèmes alimentaires stables. Deuxièmement, dans de nombreux pays en développement, deux tiers de la population sont engagés dans l'agriculture pour leur subsistance (Roser, 2013), tandis que dans les économies développées, environ 6 % de la population est employée dans ce secteur, même si la plupart sont employés en aval de la chaîne agricole. Néanmoins, une baisse de la productivité agricole se traduit automatiquement par une baisse de l'emploi et de la sécurité financière; et selon un rapport de l'Organisation internationale du travail, d'ici 2030, environ 60% des heures de travail pourraient être perdues dans ce secteur en raison du stress thermique. Pour ces raisons, les principaux objectifs de développement durable (ODD) de l'ONU visent à mettre fin à la pauvreté et à la faim. En outre, les 4 pour 1000 Sols pour la sécurité alimentaire et le climat; une initiative lancée par le gouvernement français lors de la Conférence des Nations Unies sur le changement climatique en 2015 a pour objectif de séquestrer 0,4% du (CO_2) atmosphérique chaque année. Malheureusement, de nombreux agriculteurs pratiquent encore des activités qui découragent la séquestration du carbone, par ex :

(i) Travail du sol : cette procédure d'altération du sol augmente l'exposition de la matière organique à une décomposition microbienne rapide, ce qui favorise la perte de carbone organique du sol et augmente la respiration microbienne grâce à une porosité accrue (Mangalassery et al., 2014).

(ii) Gestion des résidus : dans la partie orientale et méridionale de l'Europe par exemple, les agriculteurs pratiquent encore le brûlage des chaumes avant la plantation (Airuse, 2016). Cette stratégie de gestion des résidus a été identifiée pour convertir environ 70% du carbone à l'intérieur du chaume en (CO_2) (Abdurrahman et al., 2020).

(iii) Irrigation des parcelles : appelé l'effet bouleau, lorsqu'une faible irrigation est appliquée après une longue période de sécheresse, elle provoque une expulsion des impulsions de (CO_2) en raison d'une activité accrue de décomposition.

Par conséquent, pour une réalisation possible des "4 pour 1000", des objectifs du SDG, et d'autres initiatives similaires, de nouveaux objectifs sont nécessaires dans la gestion agricole, et certains comprennent :

(i) L'exploitation du potentiel de séquestration des terres cultivées : Ce potentiel est lié à une bonne identification des mécanismes déclenchant l'augmentation des niveaux atmosphériques de (CO_2), et des pratiques favorisant la séquestration du carbone.

(ii) Comprendre le fonctionnement des terres cultivées : Cela inclut la façon dont l'énergie est répartie, et les facteurs qui régulent cela.

(iii) Comprendre le fonctionnement hydrologique d'une parcelle : Cela implique une bonne connaissance de l'eau disponible, et une estimation précise des besoins en eau des cultures pour guider et optimiser l'irrigation, autrement dit, l'évaluation du bilan eau-sol pour aborder l'utilisation durable de cette ressource.

Contexte et questions scientifiques

La Terre est un système très complexe formé de sous-systèmes mutuellement interconnectés (terre, atmosphère, océan), de ses interfaces (terre-atmosphère, atmosphère-océan, terre-océan) et de processus fonctionnant à différentes échelles temporelles et spatiales (Suni et al., 2015). Une bonne compréhension de l'ensemble du système repose sur notre compréhension du fonctionnement de chaque composant, en particulier de son interaction avec les autres sous-systèmes, par exemple l'interaction terre-atmosphère. Les interactions terre-atmosphère sont caractérisées par des échanges continus, et ces échanges jouent un rôle essentiel dans le microclimat de la Terre en pilotant les cycles de l'eau, de l'énergie et du carbone (Findell et al., 2009).

Au cours des dernières décennies, la nécessité de comprendre le fonctionnement des terres cultivées ainsi que son interaction avec l'atmosphère par le biais des échanges de flux d'eau, d'énergie et de carbone à l'interface sol-végétation-atmosphère a été un sujet de recherche important. Une bonne prédiction de ces flux est cruciale pour les processus de recyclage de l'eau et de l'énergie (Eltahir, 1996), ainsi que pour les prévisions météorologiques et climatiques numériques (Rowntree, 1991) car ces flux ont un impact sur les caractéristiques thermo-hydriques de la basse atmosphère. De même, les flux d'eau et d'énergie régissent le partage de l'eau dans le cycle hydrologique, et sont donc des variables clés pour l'hydrologie à l'échelle du bassin versant. En outre, les échanges d'eau sont de la plus haute importance en agronomie, servant d'indicateurs de l'état physiologique des plantes (par exemple, l'état hydrique), et une bonne connaissance de ces processus pourrait être efficace pour la programmation de l'irrigation (Evett et al., 2009; Le Page et al., 2012) et la prévision du rendement (Yang et al., 2018).

Cependant, les flux d'énergie associés à l'évapotranspiration ont été reconnus comme l'une des composantes les plus incertaines du système hydro-climatique (Jasechko et al., 2013), en particulier dans les agrosystèmes qui présentent parfois un niveau élevé d'hétérogénéité en termes d'état hydrique, de phénologie, de santé des plantes, etc. Certaines complexités empêchant l'estimation précise de l'ET sur les terres cultivées sont les suivantes :

(i) Diversité des pratiques agricoles : Par exemple, l'irrigation. L'irrigation diminue localement la température de la surface terrestre des agrosystèmes par une ouverture stomatique et une évapotranspiration accrue, alors que des conditions d'humidité du sol contrastées existent dans les surfaces voisines non irriguées (Lawston et al., 2015). Cette situation peut affecter radicalement la répartition de l'énergie disponible en flux de chaleur sensible et latente, tout en augmentant l'advection horizontale de chaleur sensible depuis la surface environnante plus sèche (Lei et Yang, 2010), ce qui modifie bien sûr le modèle du bilan énergétique local de la basse atmosphère. La réponse du bilan hydrique et énergétique est que la répartition de l'énergie disponible et de l'ET est altérée, et une fausse ET est estimée car l'advection de chaleur sensible devient une source d'énergie pour l'évapotranspiration dans une telle situation (Tolk et al., 2006; Lei et Yang, 2010). Une autre pratique agricole qui introduit des incertitudes dans les estimations de l'ET est la différence dans les dates de semis, et la fertilisation. La grande variabilité et le manque de précision de ces dates entraînent une forte hétérogénéité des stades phénologiques et du développement de la végétation (Singh et al., 2013).

(ii) Hétérogénéité des agrosystèmes : Pour la caractérisation des échanges terre-atmosphère à l'échelle du champ, l'hétérogénéité de surface sous forme d'hétérogénéité de la topographie ou d'inégalité de stress et de résistance du couvert végétal (par exemple, dans les cultures mixtes) pose un problème majeur. L'hétérogénéité modifie fortement le bilan énergétique et hydrique en raison des transferts terre-atmosphère inégaux de quantité de mouvement, d'eau, de chaleur et d'autres constituants, ce qui pourrait entraîner des erreurs substantielles dans l'évapotranspiration mesurée (Liu et al., 2012; Xu et al., 2014).

(iii) Large éventail de cultures cultivées : La classification populaire des cultures est basée sur la photorespiration (par exemple, le maïs et le sorgho pour les cultures C4; le blé et le tournesol pour les cultures C3, etc). Néanmoins, l'évaluation précise de l'ET exige la prise en compte unique des caractéristiques de chaque culture (par exemple, la résistance à la transpiration, la rugosité de la culture, la réflexion, le système d'enracinement, etc.) Cela introduit une complexité qui nécessite une connaissance précise du fonctionnement hydrologique de chaque culture.

Néanmoins, l'observation des échanges terre-atmosphère a motivé le développement de plusieurs instruments micro-météorologiques parmi lesquels, la méthode de eddy covariance (EC) utilisée par les systèmes de eddy covariance a été largement acceptée comme référence par la communauté scientifique. Outre les limitations spatiales, il est connu que le bilan énergétique n'est jamais fermé expérimentalement avec les flux de covariance de tourbillon (Foken et al., 2010). Dans la littérature (voir le chapitre 2 pour une revue), les facteurs responsables possibles de cette non-clôture ont été identifiés, par exemple, l'inadéquation des empreintes, les termes de stockage, l'advection, etc. Certains de ces facteurs peuvent être corrigés tandis que d'autres (Wilson et al., 2002; Du et al., 2014). En outre, à partir de nombreuses études expérimentales (par exemple Stoy et al., 2013; Panin et al., 1998), les pires fermetures ont été trouvées dans les terres cultivées avec environ 62-80%-, en particulier en raison de la grande hétérogénéité des terres cultivées comme souligné ci-dessus.

Outre les méthodes CE, d'autres approches ont été développées et largement testées, par exemple la scintillométrie et la lysimétrie. Jusqu'à récemment, les scintillomètres étaient limités au domaine optique. En tant que tel, un scintillomètre optique mesure la scintillation de la lumière dans le domaine optique qui peut être liée aux flux de chaleur sensible; LE, est ensuite calculé comme un résidu du bilan énergétique en considérant que les flux de conduction et le rayonnement net sont bien connus dans l'empreinte de l'instrument. La principale limite de cet instrument est qu'il applique la théorie de similitude de Monin-Obukhov (MOST) pour estimer H, et que l'applicabilité de MOST est limitée sur les surfaces complexes. Enfin, les lysimètres offrent une alternative prometteuse pour estimer LE mais la représentation spatiale est très limitée et une approche résiduelle est également adoptée.

Au cours des dernières décennies, plusieurs modèles de surface terrestre (LSM) de différentes complexités et précisions ont été développés pour l'évaluation des échanges d'eau et d'énergie. Par exemple, il existe des approches conceptuelles, comme l'approche à double coefficient de la FAO-56 (Allen et al., 1998) qui résout un bilan hydrique simple du sol et estime l'ET en ajustant la demande évaporative climatique par un coefficient empirique. Ce dernier appelé "coefficient cultural" englobe tous les processus liés à la croissance des cultures qui ne sont pas explicitement représentés par le modèle. Cette approche a été largement évaluée par comparaison avec des mesures in-situ (Duchemin et al., 2006; El-Raki et al., 2007). En outre, il existe des modèles empiriques basés sur des relations simples utilisant des données infrarouges thermiques et des variables climatiques (Jackson et al., 1977), ainsi que des modèles plus complexes basés sur des méthodes de bilan énergétique résiduel, par exemple, les systèmes de bilan énergétique de surface (Su, 2002), l'algorithme de bilan énergétique de surface pour la terre (Bastiaanssen et al., 1998), la cartographie de l'évapotranspiration à haute résolution avec étalonnage internalisé (Allen et al., 2007), etc. De même, il existe des modèles de transfert sol-végétation-atmosphère (SVAT) basés sur la physique qui caractérisent les échanges entre le continuum sol-végétation-atmosphère, par exemple, Soil Plant Atmosphere and Remote Sensing Evapotranspiration (Boulet et al., 2015), Interaction Soil Biosphere Atmosphere (Noilhan et Planton, 1989). Bien qu'il existe une riche littérature traitant de l'évaluation des modèles SVAT pour les écosystèmes naturels (Blyth et al., 2011; Boone et al., 2009), davantage d'études d'évaluation de ceux-ci sont nécessaires sur les agrosystèmes caractérisés par un changement rapide de l'état de surface, et des conditions d'humidité hautement transitoires associées aux pratiques d'irrigation. En outre, en ce qui concerne l'importance des agrosystèmes dans l'interaction surface-atmosphère, notamment comme levier potentiel pour l'adaptation à la crise climatique imminente, une question brûlante de la communauté de modélisation SVAT est la représentation des pratiques agricoles dans les modèles SVAT, y compris l'irrigation (Druel et al., 2021).

Motivation de la thèse, objectifs et organisation de ce manuscrit

Dans le contexte des questions ci-dessus, l'objectif de ma thèse de doctorat est de mieux comprendre le fonctionnement de deux sites de cultures (Lamasquère et Auradé) situés dans le sud-ouest de la France. Ce centre d'intérêt a été divisé en trois objectifs de recherche :

1. Le premier objectif a étudié la variabilité de la fermeture du bilan énergétique sous différents types de cultures, phénologies et pratiques de gestion agricole sur les deux sites de culture. Une attention particulière a été accordée à l'influence des conditions atmosphériques et de l'advection sur le bilan énergétique. Étant donné la grande applicabilité des flux d'énergie de surface, en particulier dans la validation des modèles de surface terrestre, cette étude vise à mieux comprendre la qualité des flux mesurés sur les sites FR-Lam et FR-Aur sous différents scénarios et à fournir des indices sur la façon de réduire l'écart d'énergie de surface.
2. Le deuxième objectif est une évaluation et une comparaison des performances d'un modèle à source unique (ISBA) et de sa version à double source (ISBA-MEB) dans la simulation des flux d'énergie et d'eau sur six saisons de maïs irrigué et quatre saisons de blé non irrigué à Lamasquère. La validation a été effectuée à l'aide de mesures provenant d'un système de covariance de tourbillon, et une attention particulière a été accordée à la capacité de partitionnement de ces modèles. Cette étude comparative pourrait aider les utilisateurs à décider de la configuration du modèle à utiliser en fonction du niveau d'hétérogénéité de la surface.
3. Sur les mêmes cultures que dans (2), le troisième objectif a évalué le potentiel du modèle ISBA-MEB à simuler correctement les composants du carbone comme une ressource possible pour combler les lacunes. Cette performance a été testée par rapport aux mesures du système de eddy covariance. Cette étude pourrait donner un aperçu de l'état du carbone de la parcelle et pourrait démontrer la pertinence de certaines pratiques de l'agriculteur pour le budget carbone.

Ce manuscrit est composé de six chapitres :

1. Le chapitre 1 passe en revue le concept général des échanges sol-végétation-atmosphère en accordant une attention particulière à l'évaluation du bilan énergétique, du bilan hydrique et du bilan carbone sur les terres cultivées.
2. Le chapitre 2 décrit les deux sites expérimentaux, leur mise en place, les protocoles d'acquisition des mesures, le prétraitement de ces jeux de données, ainsi que certaines données de télédétection utilisées dans cette étude. La dernière section du chapitre 2 fournit la description du modèle de surface terrestre (LSM) utilisé pour l'estimation des échanges surface terrestre-atmosphère d'intérêt.
3. Le troisième chapitre est consacré à une étude du bilan énergétique de surface sur Lamasquere et Aurade.
4. Dans le quatrième chapitre, les performances d'ISBA et d'ISBA-MEB dans la simulation des composantes du bilan énergétique et hydrique sont évaluées.

5. Dans le chapitre 5, nous présentons et analysons les premiers résultats des composantes du carbone simulées avec le modèle ISBA-MEB par rapport aux mesures du système eddy covariance.
6. Le chapitre 6 résume tous ces résultats et fournit quelques perspectives concernant ces sujets.

Chapter 1: Observation and modeling of the land-atmosphere exchanges over agrosystems: State of the art

1.1 Concepts description

Croplands play an important role in the climate system as they represent around 20% of the habitable land area (FAO, 2020)). In response to natural and anthropogenic processes, these agrosystems are in continuous interaction with the atmosphere. These flows are regulated by two basic conservation principles that are completely dependent on each other: the mass conservation and the energy balance. The terms of the three main cycles (energy, water, and carbon) governing the functioning of land surface and of agrosystems are summarized in Figure 1.1. A good understanding of the functioning of agrosystems requires precise quantification of these components, and identification of factors that regulate them. The general context of my thesis falls within this domain.

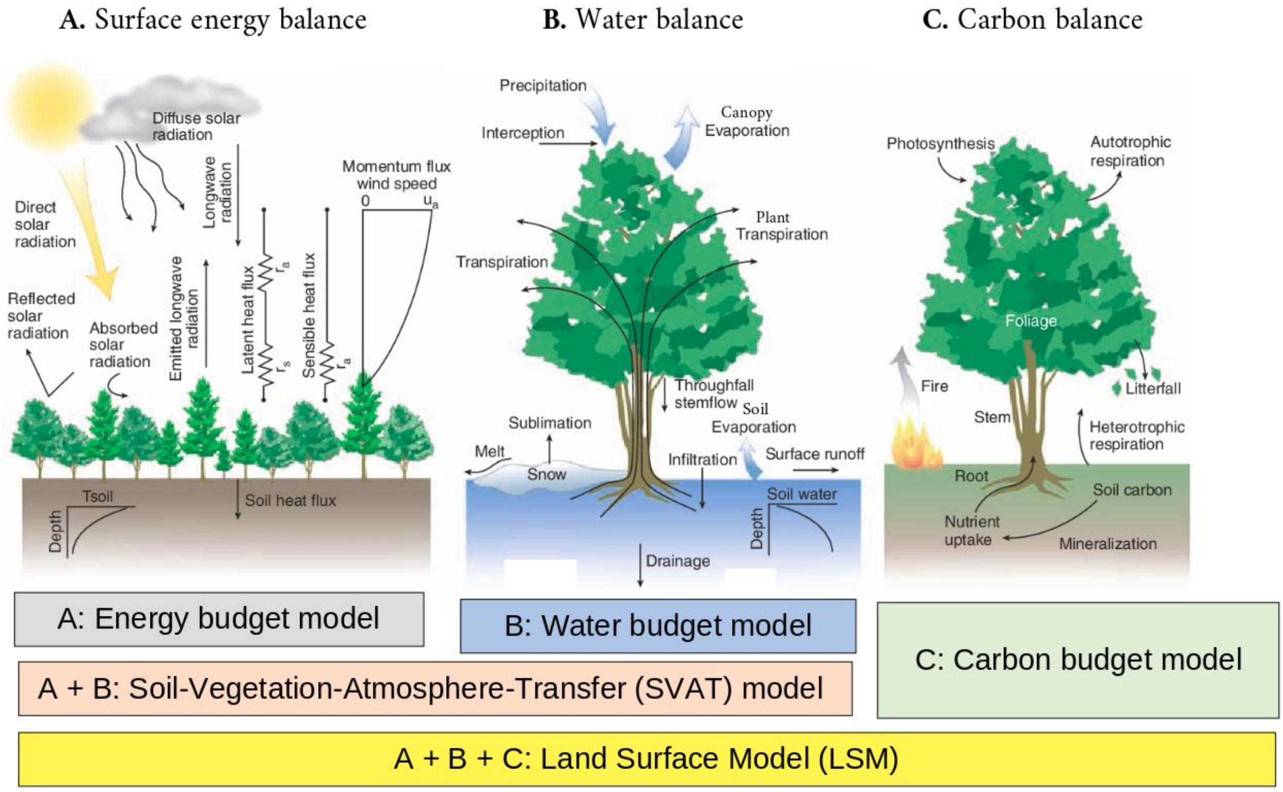

Figure 1.1: A schematic representation of the surface energy fluxes (A), water cycle (B), and carbon cycle (C); where the latent heat flux in A is presented as (plant transpiration + soil/canopy evaporation) in B, and it is closely linked to the photosynthetic and respiratory processes in C. Source: Bonan (2008).

1.1.1 The surface energy balance

The Earth's surface receives energy from the sun, absorbs some, while the canopy and the underlying ground re-emits some in the form of infrared radiation. The net radiation (Rn in W m^{-2}) at the surface is the sum of the absorbed fractions of the incoming solar radiation (R_G in W m^{-2}), and of the atmospheric infrared radiation (R_A in W m^{-2}), reduced by the emitted infrared radiation. Rn can be written as follows:

$$Rn = (1{-}\propto)\, R_G + \varepsilon(R_A - \sigma_{SB} TS^4) \tag{1.1}$$

Where $\propto$ is the surface albedo, ε is the surface emissivity, σ_{SB} (in W m^{-2} K^{-4}) is the Stefan-Boltzmann constant, and TS (in K) is the surface temperature. The surface energy balance (SEB) is the framework guiding any theoretical description of the Earth's climate system (Mauder et al., 2020). It is a balance equation for a surface, or a volume typically applied to the interface between the atmosphere and the elements of the surface. It accounts for inputs, outputs, and storages within the internal constituents. Traditionally, the SEB is taken for an infinitesimal volume comprising the interface for steady state conditions, with no storage or tendency (Cuxart et al., 2015). Then, the SEB can be expressed as in Equation 1.2, where all components are W m^{-2}.

$$Rn = LE + H + G \tag{1.2}$$

LE and H represent the latent and sensible heat flux respectively. They are the convection fluxes of a turbulent atmosphere due to humidity and temperature difference between the atmosphere and the land surface. G is the conduction heat flux in the ground. This equation is used in a number of applications, both in measurement and modeling, and readers are referred to Garratt (1992) for an extensive discussion of this classical equation.

1.1.2 The water budget

As far as agriculture, and water resource research is concerned, $ET(LE)$ holds the highest importance in the water-(surface energy) balance. More importantly, its value lies in its constituents; Tr: this is the water transpired by the plants, E_S: is the water lost by the soil via evaporation, and E_i: is the water evaporated from the canopy after interception (see Figure 1.2). In a simplified form, ET can be assessed as the residual of a water-balance equation in accordance with the mass conservation principle as expressed in Equation 1.3.

$$ET = P + Irrig + \Delta S - R - D_{Perc} \tag{1.3}$$

Where P, $Irrig$ and ΔS are the water inputs representing rainfall, irrigation, and the change in the soil moisture storage over a certain period, respectively. R is surface runoff, D_{Perc} is deep percolation, all expressed in mm. These components are important for agro-hydrological purposes such as irrigation planning (Calera et al., 2017), crop-water stress monitoring (Ihuoma and Madramootoo, 2017) etc.

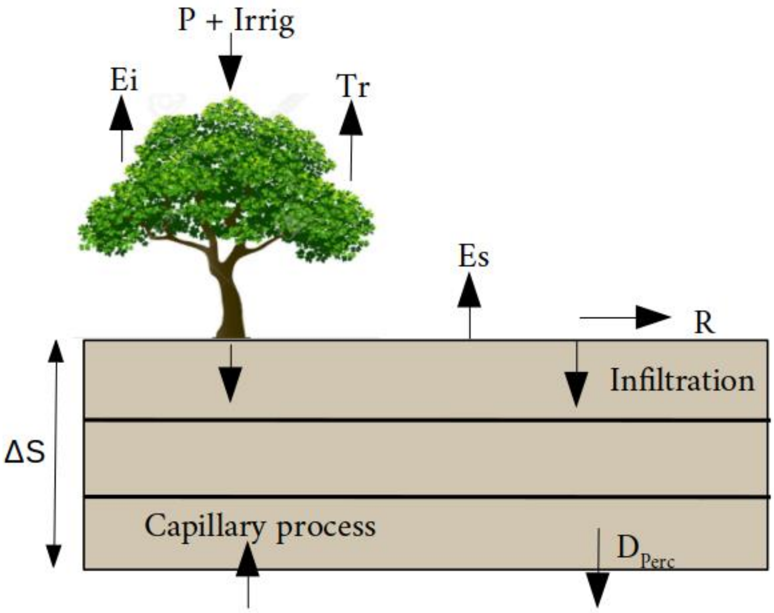

Figure 1.2: The different components of the soil-water balance; $ET = Tr + Ei + Es$

1.1.3 The carbon budget

As depicted in Figure 1.1, biogeochemical processes exert a huge control over the hydrological functioning of plants; consequently altering ecosystem processes such as carbon assimilation, respiration etc. Some of these processes are described below.

Photosynthesis

Based on nutrition mode, a living organism is either an autotroph i.e., it synthesizes inorganic matter into organic substances, or a heterotroph- i.e., it is unable to synthesize its own components, and therefore relies on exogenous sources of organic matter. Most plants practice autotrophism via photosynthesis. Photosynthesis ($\boldsymbol{GPP}$ for 'gross primary production' in $\mu mol\ m^{-2}\ s^{-1}$) is a light-energized oxidation-reduction process that drives the reduction and oxidation of carbon dioxide ($\mathrm{CO_2}$) and water ($\mathrm{H_20}$) respectively to release oxygen molecules ($\mathrm{0_2}$) and carbohydrates ($\mathrm{C_6H_{12}0_6}$) as expressed in Equation 1.4.

$$6CO_2 + 6H_2O = C_6H_{12}0_6 + \ 60_2 \tag{1.4}$$

Respiration

All living organisms respire. Over a cropland, this breathing ($\boldsymbol{RECO}$ for 'ecosystem respiration' in $\mu mol\ m^{-2}\ s^{-1}$) can be decomposed into the following:

(i) Above-ground autotrophic respiration (RAa): This is the flux of $\mathrm{CO_2}$ into the atmosphere via the stomates and lenticels of plants.

(ii) Below-ground autotrophic respiration (RAb): This respiration originates mainly from the root system.

(iii) Below-ground heterotrophic respiration (RHb): This refers to the flux of CO_2 (directed towards the atmosphere) linked to the activity of the soil biota within the soil.

The below ground respirations i.e., $RAb + RHb$ is termed soil respiration (SR).

Net ecosystem exchange

The net flux of $\mathrm{CO_2}$ ($\boldsymbol{NEE}$ for 'net ecosystem exchange' in $\mu mol\ m^{-2}\ s^{-1}$) is the balance between the $\mathrm{CO_2}$ exchanged at the biosphere-atmosphere interface (Equation 1.5). NEE is composed of the turbulent vertical $\mathrm{CO_2}$ flux (F_C) that is measured by the eddy covariance system, the $\mathrm{CO_2}$ storage (F_{CS}) which is the accumulation or depletion of $\mathrm{CO_2}$ below the measuring system, and the $\mathrm{CO_2}$ advection flux (A_{CO2}) (see Chapter 2).

$$NEE = RECO + \ GPP \tag{1.5}$$

Net ecosystem production

The net ecosystem production ($\boldsymbol{NEP}$ in gC m^{-2} yr^{-1}) expressed in Equation 1.6 is the integral of NEE over a specified period. This study integrates over a cultural year that runs from the 1st of October to the 30th of September of the following year.

$$NEP = \int_{1st\ Oct}^{30th\ Sep} NEE \qquad (1.6)$$

Following the meteorological sign convention, a negative sign is adopted for GPP (a flux towards the surface), and a positive for $RECO$ (a flux away from the surface). Also, when all the lateral carbon fluxes are considered, a negative and positive NEP means that the plot is a carbon sink and source, respectively.

1.2 Observation techniques of land surface exchanges

For several decades, a variety of *in-situ* methods have been devised to monitor and quantify land surface exchanges, and each method dictates its resolution and measurement interpretation. Among these, some micro-meteorological techniques used in agricultural research are presented below.

1.2.1 Eddy covariance method

Based on wide acceptability, the EC method has stood out from other methods. It simply estimates fluxes as the covariance between the turbulent fluctuation of the vertical wind velocity (w) and the mixing ratio (s) (Equation 1.7).

$$F = \bar{\rho}\overline{w's'} \qquad (1.7)$$

where ρ is the dry air density, $'$ is the fluctuation, the bar represents the mean, and the gas mixing ratio can be temperature for H, water vapor for LE, or CO_2 density. From the early experimental campaigns (of Elagina et al., 1973; Elagina et al., 1978) that compared EC measurements with Bowen-ratio measurements, it became apparent that the energy balance at the Earth's surface cannot be experimentally closed, and this is termed the 'non closure problem'- where the sum of the turbulent fluxes $(LE + H)$ is less than the available energy $(Rn - G)$. Later validation attempts of Equation 1.2 were made in Australia, 1981 (Leuning et al., 1982), in Germany, 1984 (Koitzsch et al., 1988), in

Canada, 198(2-4) (Desjardins, 1985), in Russia, 1988 (Tsvang et al., 1991), in Estonia, 1990 (Foken et al., 1993), in USA, 1989 (Kanemasu et al., 1992), in Austria, 1989 (Bernhofer, 1992), in South Africa, 2000-2014 (Majozi et al., 2017), in China (Li et al., 2005), in (Wilson et al., 2002), in Germany (Imukova et al., 2016) etc. From these SEB studies, it is evident that irrespective of a site's climate, location, instrumentation, vegetation type, phenology, etc), the surface energy can only be closed within a certain margin.

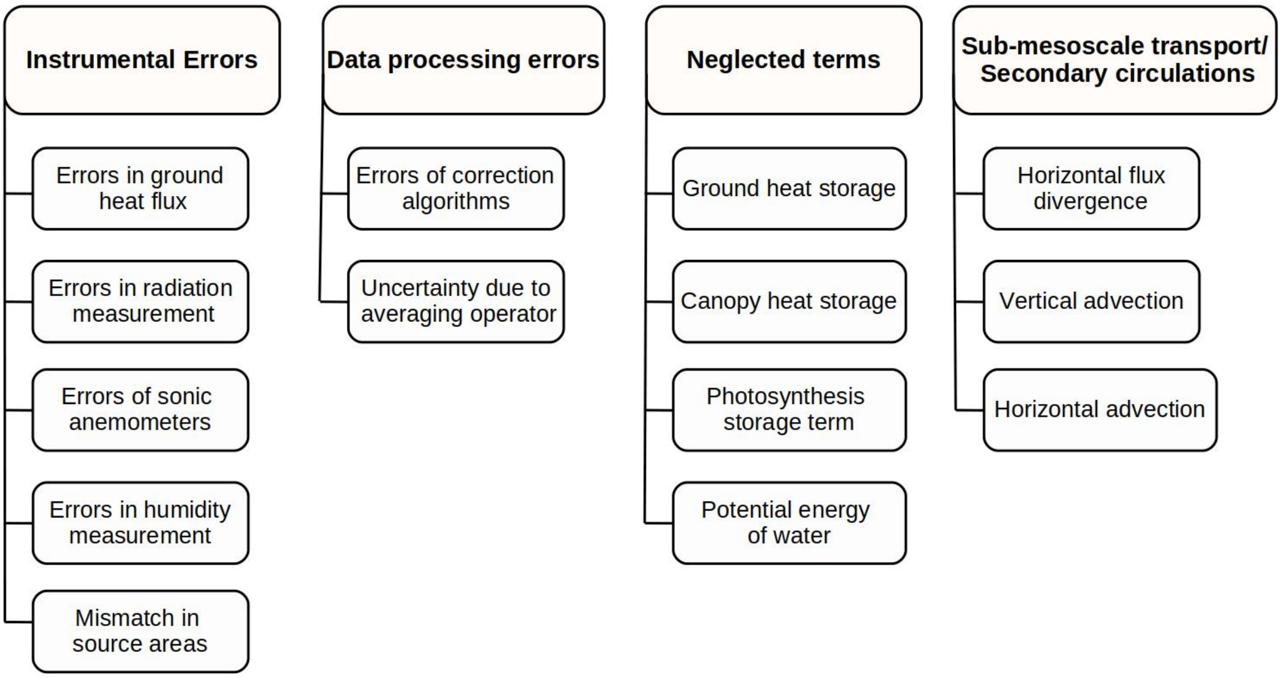

Figure 1.3: Classification of the possible reasons for the non-closure of the surface energy balance. (Source: Mauder et al., 2020, modified).

Several factors (see Figure 1.3) have been reported as being responsible for this non-closure (Stoy et al., 2013; Wilson et al., 2002; Mauder et al., 2020), of which a few are described below:

(i) Instrumental, and data processing errors: According to Foken and Wichura, (1996), large imbalances are due to the use of inappropriate instruments, plus poor data handling. These errors could result from poor installation, wrong calibration, inappropriate maintenance procedures etc. To improve data quality, common guides were proposed (see Foken and Wichura, 1996; Foken, 2012; Aubinet et al., 2012). Despite strict obedience to these recommendations, the surface energy balance is only closed within a certain margin.

(ii) Mismatch in source area: Schmid (1997) discussed practical questions pertaining to the scale and representativeness of each energy budget component, and subsequently proffered three different versions of representativeness criteria for this point-to-area fluxes (see Schmid, 1997). However, these representations present limited values if the scale of measurement of the ground heat flux (usually a single point of about 0.04 m^2) cannot be matched with the scale of the turbulent fluxes (~0.5 km^2 according to Stannard et al. 1994), and that of the net radiation. Combatting this limitation by on-site instruments remains currently far-fetched.

(iii) Storage terms and unknown sinks: This is a combination of two factors-

  (a) The placement of the measuring instruments: EC systems are mounted at a reference height (few meters) above the ground. Between this height and the ground, there exists an air storage term that remains uncaptured by the EC system especially when non-turbulent processes are predominant (e.g., in the nighttime (Xu et al., 2019). In addition, heat flux plates are often buried at 5-10 cm depths inside the soil-; the energy stored between the surface of the soil and the top of these plates are sometimes not considered.

  (b) Omitted components e.g., the energy linked to photosynthesis (Masseroni et al., 2012; Meyers and Hollinger, 2004), and biomass heat storage which is the physical heat energy storage owing to the changes in biomass temperature (Gu et al., 2007; Samson and Lemeur, 2001). In recent times, within the pan-European long-term research infrastructure ICOS (Integrated Carbon Observations System), the measurement of these storage terms had been mandated over flux sites for energy balance studies (Montagnani et al., 2018). Nonetheless, findings from many experimental studies have indicated that the inclusion of these terms Nonetheless, findings from many experimental studies have indicated that the inclusion of these terms improve the closure by only 5-7% in croplands (see Masseroni et al. (2014); Xu et al. (2017); Eshonkulov et al. (2018) for reviews).

(iv) Violation of theoretical assumptions: The EC method must fulfil several theoretical requirements. One is the steady state assumption (Taylor, 1938). This is the Taylor's hypothesis, and it requires that the eddies must not undergo any property change as they pass by the tower. Unfortunately, this requirement is often compromised when the background wind becomes negligible (De Roo et al., 2018), and when aggregation period is extended for large-scale eddies (Mauder et al., 2020). The solution here involves a simultaneous measurement of fluxes using multiple and spatially distributed EC systems (Mahrt, 2010), and this is expensive. All in all, a slight departure from the EC requirements renders measurements from the EC system questionable (Foken and Wichura, 1996).

Spatial heterogeneity: Another EC requirement is a uniformly flat, and horizontal terrain- even though surface heterogeneity is an undeniable reality of most land surfaces. This surface unevenness results in horizontal exchanges with non-zero fluctuation averages- this is an outright violation of EC requirements (Burba and Anderson, 2005). Over croplands for instance, the presence of advection is an indication of a non-equilibrium horizontal mean of temperature, specific humidity, and wind speed over the field, even under steady-state conditions (Philip, 1959). This often-neglected process has been mentioned in literatures as a significant contributor to the surface energy imbalance (see reviews of Oncley et al., 2007; Foken 2008; Cuxart et al., 2016). Unfortunately, direct advection measurement is difficult, and it requires a sophisticated set up. Nevertheless, some quantitative attempts have been made. Cuxart et al. (2016) estimated the sensible heat advection (A_H) and compared it with the residual energy obtained over some crop fields during the BLLAST campaign. Their analysis revealed that on a hectometer scale, low-frequency structures with motions longer than the averaging time of the turbulent fluxes could represent tens of W m^{-2} of extra energy. Similarly, on a dry summer day at the University of the Balearic Islands, Mauder et al. (2020) reported A_H reaching 50 W m^{-2} in the early afternoon.

(v) Inadequate averaging time: Given the existence of large eddy structures, the typical averaging periods (between 15-30 min), which permits the non-violation of the Taylor's frozen turbulent hypothesis earlier mentioned has been recognized by several experimental studies as insufficient (Finnigan et al., 2003; Charuchittipan et al., 2014; Xu et al., 2017). For proof, these studies compared the closure of the energy balance after extending the averaging time from 30-mins, few hours, even up to few days. Xu et al. (2017) observed that the closure increased with the averaging period- but they pointed out some uncertainties surrounding this '*good closure*' e.g., the non-stationarity of the fluxes, and advective processes. Similarly, Charuchittipan et al. (2014) observed a significant improvement in the closure when averaging time was increased for tall vegetation.

Unfortunately, an experimental closure of the SEB is a quality indicator of EC measurements. Besides, it is important to ascertain if the non-closure is linked to instrumentation, or physical limitations. The challenges this non-closure pose include: (i) a caution in the interpretation of EC measurements especially when making comparison with models (Liu et al., 1999; Culf et al., 2002), (ii) within the flux community, some studies have hinted the possibility that the errors responsible for this imbalance could have been projected onto the carbon fluxes that are measured by EC systems (Twine et al., 2000; Wilson et al., 2002).

Some experimental studies (e.g Stoy et al. 2013; Panin et al., 1998) have found worst closures over croplands, and better closures over forests. This brings forth questions pertaining to the relationship between the stability of ecosystems and their level of closure. Within this context, the first objective of my PhD is a surface energy balance study over Lamasquère and Auradé, and this analysis is presented in Chapter 3.

1.2.2 Scintillometry technique

Scintillometry is a ground-based technique that uses the intensity fluctuations of electromagnetic radiations propagating through a turbulent medium (de Bruin et al., 2017). This approach was birthed following the emergence of remote sensing techniques that required *in-situ* fluxes integrated over large areas e.g., over the average pixel size of satellite images for complementary information and evaluation purposes (Solignac et al., 2009) given the short footprint of EC systems. Scintillometers provide measurements of sensible heat fluxes over scales ranging from a few hundreds of meters up to 10 km (Hoedjes et al., 2007). Furthermore, based on the emission spectrum of the transmitter, scintillometers can be classified as either near infrared (common wavelengths between 850 nm, 880 nm and 940 nm), or microwave (common wavelengths of 1.86 mm, 3.19 mm and 11.11 mm) (Li and Xu, 2019). Scintillometers that operate at near infrared range include: (i) The small aperture scintillometer (SAS), (ii) The large aperture scintillometer (LAS): these operate at ~0.9 $\mu m,$ and can provide measurements over long-path lengths between 0.5 and 5 km (Wang et al., 1978), (iii) the extra-large aperture scintillometer (XLAS): this operates at the same wavelength as LAS, but it is required for path-length applications greater than 5km; also, it has an aperture almost twice that of LAS (de Bruin et al., 2017) (iv) the millimeter-wave scintillometer (MWS): these operate between 1000-11000 μm; they are sensitive to both humidity and temperature scintillations, and so can measure LE directly (de Bruin et al., 2017).

In spite of the spatial attractiveness of scintillometery, its major limitation is its reliance on the semi-empirical Monin-Obukhov similarity theory for the calculation of H- which is unlike the EC method that measures turbulent fluxes directly. Nevertheless, as a bonus, scintillometers provide reliable measurements over heterogeneous terrains, and so has high applicability over such landscapes (Gruber et al., 2014; Rotach et al., 2017; Chehbouni et al., 1999).

1.2.3 Lysimetry

The first lysimeter was designed in 1875 by Edward Lewis Sturtevant to estimate the percolation of water through the soil, and over at least, the past three centuries and a half, lysimeters have become one of the standard tools for ET estimation (Howell et al., 1991). In agricultural research, lysimeters are simply containers (cylindrical, or rectangular depending on crop type) filled with soil in which the reference plant is grown. The bottom of this device is inserted into the soil, while a few cms of the upper part is left visible above the ground. This device observes the precipitation received, and the actual ET (Allen et al., 2011; Babaee et al., 2019). Traditionally, a lysimeter's footprint ranges between 0.05 to 40 m^2, and recently, this has been enlarged. Lysimeters are of three categories: (i) non-weighing, constant water-table types: this is often implemented over plots with high water-table, and over plots where the water-table inside and outside the lysimeter is maintained at the same level, (ii) non-weighing, percolation types: these are for plots that experience high precipitation, where the soil-water changes are determined by sampling and neutron methods, (iii) weighing types: here, the changes in soil water are determined by either weighing the entire unit with a scale, or by supporting the lysimeter hydraulically (Allen et al., 2011). The limitation of a lysimeter is its sensitivity to discontinuous vegetation within and with-out the lysimeter, and soil heterogeneity (Makkink, 1959).

1.2.4 Sap flow method

Sap flow method holds the most advantages over other techniques for direct assessment of plant transpiration. It uses heat as a tracer for sap movement by obtaining the difference in temperature measured by the thermocouples placed above and below the heater. This temperature difference is proportional to the mass flow rate of the sap (Smith and Allen, 1996). Based on operating principles, there are two sap flow methods: (i) the stem heat balance (SHB): this is suitable for woody (Steinberg et al., 1989) and herbaceous stems (Baker and van Bavel, 1987) with diameters between 2-125 mm (ii) the trunk sector heat balance method: this is for trees with diameters larger than 120 mm. Its principle is similar to that of SHB, but the heat is applied internally to a segment of the trunk and not to the entire circumference like in SHB.

Sap flow methods can offer continuous transpiration monitoring, but they have limitations over heterogeneous terrains because it requires a scaling procedure (Granier, 1987; Becker, 1998).

1.3 Modeling of the land surface budgets and fluxes

Like all *in-situ* systems, the aforementioned systems are spatially limited, cumbersome, and expensive. Mathematical models are alternative tools, and over the past decades, the flux community has experienced a surge of state-of-the-art models of various complexities. The following section presents some models for the simulation of *ET* and other SEB components.

1.3.1 Surface energy balance models

These models are grounded in the theory of the energy balance which requires a combination of ground-based and land surface temperatures (*LST*) to estimate *ET* by partially or fully solving the energy balance as a residual of the available energy from short-wave and long-wave radiation (Equation 1.2). In a broad sense, based on the parameterization of energy sinks and sources at the land-surface interface, these models can be divided into: single-source, dual-source, and multiple-source models (not discussed) (see Figure 1.4). For a proper structural representation of the surface energy transfer, a choice between these three is required.

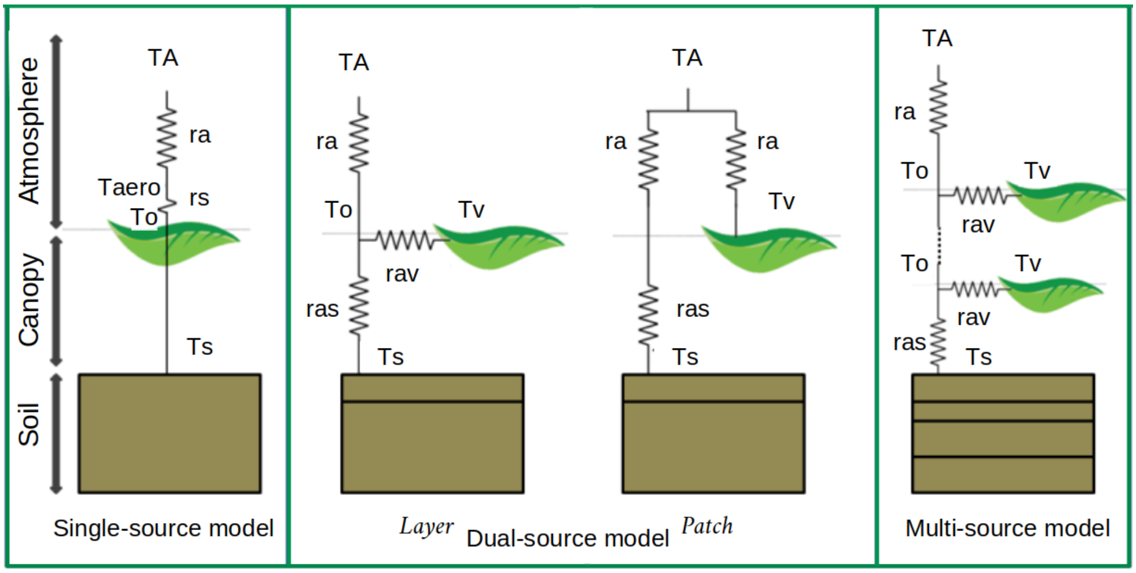

Figure 1.4: Schematic representation of the different resistance networks (surface and aerodynamic resistances to heat and water vapor) used in surface energy balance models. (Source: Saadi et al., 2018), modified)

Single-source models

In this approach, the land surface is treated as a big leaf with a uniform layer; i.e., the model maps the properties of the whole component into a single leaf without distinguishing the soil and canopy (e.g., Bonan, 1996; Sellers et al., 1996; Dickinson et al., 1998). These simple models were founded on the Penman-Monteith equation (Monteith, 1965) based on the influence of surface controls on total evapotranspiration, and they are well adapted for ET estimation over highly dense canopies (Monteith and Unsworth, 1990). A large number of one-dimensional single-source SEB approaches have been proposed, and they calculate LE as a residual by evaluating Rn, H, and G. The sensible heat flux is estimated using Equation 1.8 to be proportional to the air temperature (TA in K) and the aerodynamic surface temperature (T_{aero} in K):

$$H = \rho_a C_p \frac{T_{aero} - TA}{r_a} \tag{1.8}$$

Where r_a (in s m^{-1}) is the aerodynamic resistance of the transfer of sensible heat between the height of the canopy source, and the air at the reference height above the canopy. ρ_a is the air density (kg m^{-3}), and C_p is the specific heat capacity of the air at constant pressure (J kg^{-1} K^{-1}). T_{aero} is the extrapolation of the air temperature profile above the canopy downwards towards an effective roughness height above the zero plane displacement height (Tang et al., 2013). Quite a number of single-source SEB models have been developed; a few of these include the Simple Surface Energy Balance model (SSEB: Bartholic et al., 1972), Regional Evapotranspiration Model Using Crop Surface Temperature (RETMCST: Soer, 1980), Surface Energy Balance Index (SEBI; Menenti and Choudhury, 1993), Simplified Surface Energy Balance Index (S-SEBI; Roerink et al., 2000), Surface Energy Balance System (SEBS; Su, 2002), Surface Energy Balance Algorithm for Land (SEBAL; Bastiaanssen et al., 1998), Mapping Evapotranspiration at High Resolution with Internalized Calibration (METRIC; Allen et al., 2007) etc. These models depend on remote-sensing techniques and solve the energy balance on a pixel-by-pixel basis based on the contrast between dry and wet limits when combined with some *in-situ* variables (Li et al., 2009).

The first SEB model developed for the estimation of ET using remotely-sensed LST can be credited to SSEBS. An airplane-mounted thermal camera was used to obtain the radiative temperature over an agricultural area mixed with crops and soils, on the basis of which soil moisture and ET were estimated using a simple surface energy balance model. The limitation of this model is that it requires direct measurement of crop and soil temperature- this makes it difficult to implement on a large scale.

RETMCST estimates the actual ET using remotely-sensed crop surface temperature, thus specifically solving the spatial limitation encountered in SSEBS. Like in SSEBS, the crop surface temperature is an important indicator of the rate of evapotranspiration, and the soil-water status. This model introduced the concept of Businger-Dyer concept (Businger, 1996; Businger et al., 1971; Dyer 1967) which is based on the use of the Monin-Obukhov length as a proxy for atmospheric stability (Monin and Obukhov, 1954) in the calculation of surface heat fluxes. Also, an expression based on an additional resistance for heat transport was introduced; it assumes that the roughness length for heat is equal to the roughness of momentum because there was not enough profile data to estimate it.

The SEBI methodology was proposed by Menenti and Choudhury (1993) on the basis of Penman-Monteith equation (Monteith, 1973), and it involves the estimation of heat fluxes based on the calculation of two extreme limits (a dry condition of zero ET with all available energy converted to H, and a wet condition of potential ET with minimum H). The first evaluation of this model was performed over DAISEX99 experimental area (Jia et al., 2001). The limitation of the *fixed* temperature-boundary conditions in SEBI was fundamental to the derivation of S-SEBI model which allows varying surface temperature as a function of changing reflectance values (Roerink et al., 2000). This new model determines a reflectance dependant maximum temperature for an extremely dry condition, and a reflectance dependant minimum temperature for an extremely wet condition for a realistic partitioning of $Rn - G$ into H and LE (Roerink et al., 2000). Another theoretical advantage of S-SEBI is that it does not require any additional meteorological data (Roerink and Menenti, 1999).

SEBAL included several developments, and treated some common problems encountered in many remote sensing flux algorithms, and so in SEBAL, (i) the temperature gradient between the aerodynamic surface and the air at a reference height increases proportionally with the radiative surface temperature because the air temperature at the reference height, when it is much higher than the canopy, can be assumed to be weakly variable in space; (ii) a semi-empirical model has been developed to calculate the heat flux in the soil as a function of the radiative temperature and the reflectance of the short-wavelength radiation obtained from remote sensing as well as the fraction of vegetation estimated with NDVI; (iii) a semi-empirical method has been developed to estimate the flux of effective momentum based on radiative surface temperature and reflectance of short wavelengths, and the flux is then used to estimate the average roughness length for the momentum transfer (see Bastiaanssen et al., 1998 for review). METRIC is based on the same structure as SEBAL, but it uses a reference ET (Penman-Monteith) to describe the potential ET.

For better representation of large and heterogeneous terrains, the SEBS model estimates turbulent fluxes using the influence of evaporative fraction from satellite data and meteorological variables. The deficiency of SEBS is that it requires many input parameters. Although single-source models are simple, a major constraint lies in their inability to distinguish canopy from soil.

Dual-source model

The restriction of single-source models to homogeneous surfaces necessitated the development of dual-source models. This new approach explicitly differentiates the interaction of the atmosphere with the soil, from that of the vegetation especially over sparsely-vegetated terrains. Within a dual-source model, the surface radiometric temperature is decomposed into the soil and vegetation temperature; hence, ET is treated as the sum of the canopy's transpiration and soil evaporation (Norman et al., 1995; Kustas and Norman, 1999). For simplicity, and while adopting the proposal of Lhomme et al. (2012), and Boulet et al. (1991), the mechanism of a dual-source scheme can be parameterized in two manners:

(i) The layer or coupled approach: Here, energy and matter leave and enter the atmosphere only through the canopy, and so the soil is completely prohibited from a direct interaction with the atmosphere. In other words, the soil and heat sources are fully coupled through a resistance network organized in series (Boulet et al., 2015) (see Figure 1.4).

(ii) The patch or uncoupled approach: Here, the canopy and soil are located side by side, and interact independently with the overlying atmosphere, but remain thermally uncoupled from each other. The incoming energy is partitioned between the vegetation and the underlying soil using the factor f_c for the vegetation, and $(1 - f_c)$ for the bare soil (Lhomme and Chehbouni, 1999). This scheme is suitable for areas with distinct clumped vegetation surrounded by a large expanse of bare soils (Norman et al., 1995). SEB models based on this approach include the Two Source Energy Balance Model (TSEB: Norman et al., 1995), Atmosphere-Land Exchange Inverse (ALEXI: Anderson et al., 1997), Disaggregated ALEXI (DisALEXI: Norman et al., 2003), Two-source Trapezoid Model for Evapotranspiration (TTME: Long and Singh, 2012) etc.

Kustas et al. (1996) compared a single-source model (SSM) and a dual-source model over a semi-arid range ($f_c > 50\%$), and a tall-grass prairie ($f_c < 50\%$). From their results, the SSM had difficulty in estimating the sensible heat flux over the tall grass prairie site. The average difference between the observation and the SSM estimate was 55% compared to the 30% obtained by the dual source model.

1.3.2 SVAT models

Land surface models (LSMs) solve jointly the energy and the water balance of land surface, and for the most up-to-date, the carbon budget as well. LSMs were first developed by the atmospheric modeling community (Manabe, 1969) to provide physical boundary conditions at the land-atmosphere interface to solve numerical equations of atmospheric processes (Bonan, 2008). LSMs are usually embedded into coupled models (e.g., General Circulation Model, Regional Climate Model etc) that are aimed at the global prediction of the future state of the Earth under anthropogenic forcings (IPCC, 2007). Depending on the representation of evapotranspiration, and according to the simplification suggested in Pitman (2003), LSMs can be put under 3 classes.

(i) The first generation (1st gen) LSM: This can be traced back to meteorologist-climatologist Syukuro Manabe, the 2021 Nobel prize awardee in Physics. Using simple energy balance and hydrological equations, Manabe (1969) implemented the first LSM within a climate model to investigate the interaction between the hydrological cycle of the terrestrial space, and the atmosphere. In these early generation models, the parameterization of land surface processes was represented in very crude ways, e.g., they used simple aerodynamic bulk transfer equations including uniform prescriptions of surface parameters while ignoring the conduction of heat into the soil. Another conceptual limitation of the model is that it assumes a 15 cm water-holding capacity for the global soil, and according to Sato et al. (1989), the constant availability of soil moisture within the bucket model introduces significant errors in the estimation of ET in comparison with the Penman-Monteith equation (Monteith, 1981) which provides more realistic estimates. In short, the Manabe bucket model completely ignores critical processes of soil water movement (e.g., capillary, and gravitational processes) making these models indeed primitive for land surface processes (Yang, 2003; Pitman, 2003).

(ii) The second generation (2nd gen) LSM: A fundamental advancement was marked following Deardorff's Force restore soil model (see Deardorff, 1977). This analogous model presented an efficient representation of soil moisture and heat transfer between a single vegetation layer, and the soil layer. This representation permitted evaporation from the soil and the wet foliage of the canopy, as well as plant transpiration. Models that included this Deardorff (1977)-type model include Biosphere-Atmosphere Transfer Scheme (Yang and Dickinson, 1996), Simple Biosphere model (Sellers, 1986), Common Land Model (Dai et al., 2003), Interaction Surface Biosphere Atmosphere (Noilhan and Planton, 1989) in its initial version. Unlike in the 1st gen, background soil in the 2nd gen interact actively with the atmosphere-; this gave way to the integration of satellite data into LSMs (Sellers et al., 1994). One major drawback of 2nd gen is that the canopy conductance is modelled empirically, and it models only transpiration without addressing carbon uptake by plants.

(iii) The third generation (3rd gen) LSM: This brought the integration of photosynthetic and stomatal conductance models into LSMs (e.g., Collatz et al., 1991; Sellers et al., 1992; Calvet al., 1998). Based on the functioning of stomates, the canopy conductance is represented by semi-mechanistic models of leaf photosynthesis in place of empirical representations (e.g., Jarvis, 1976). LSMs have evolved with increasing capability to respond to changes that impact the climate and the dynamics of the Earth system- (e.g., soil moisture dynamics, stomatal functioning, soil hydrology, run off, soil temperature, plant, and soil carbon cycling etc.). See Figure 1 of Fisher and Koven (2020) for the evolution of LSMs starting from the 70's.

One strong point of SVAT is its fine time steps (typically 30-mins). However, their application is limiting because of the difficulty in acquiring *in-situ* data as forcings, for calibration, and for evaluation. Over our current site of study (FR-Lam), there has been numerous model evaluation efforts (both SVAT and SEB models) (Table 1.1).

Table 1.1: Review of some ET estimation studies over FR-Lam

Model	**Crop and Timeline considered**	**Reference**
SPARSE	Wheat (2007, 2009, 2011, 2013)	Delogu et al., 2018
ISBA	Wheat (2006 - 2010)	Etchanchu et al., 2017
TSEB and SetHyS	Wheat (2007), Maize (2006, 2008)	Bigeard et al., 2019
ORCHIDEE-CROP	Wheat (2006), Maize (2006)	Wu et al., 2016

In spite of the large number of models that have been evaluated over FR-Lam, assessment of generic models over longer crop succession is required. Hence, the second objective of this study evaluates a LSM over 11 years of continuous cropping. The result of this analysis is presented in Chapter 4.

1.4 Carbon balance

Asides from the hydrological processes, understanding and parameterization of biogeochemical processes of croplands has remained an important subject in the micro-meteorologist community. The pattern and availability of soil water exerts a significant control over the variability of plants' transpiration, and consequently, this alters ecosystem processes (Scott et al., 2006). The issue here lies in understanding how croplands, in the presence of different wet-dry cycles, and management practices control the uptake of CO_2, and the ecosystem respiratory efflux. The net ecosystem exchange (NEE) can be measured on a field scale, but it does not reveal the underlying assimilatory and respiratory processes. Although NEE is usually partitioned using models (Hollinger et al., 1994; Reichstein et al., 2005), uncertainties and errors introduced by this partitioning procedure can be significant when making an annual or multi-annual budget. Given this limitation and those discussed in section 1.2.1, a number of approaches have been developed. These can be categorized into four: (i) remote sensing-based methods (Potter et al., 2003; Goetz et al.; 2009), (ii) data-driven methods (Papale and Valentini, 2003), (iii) process-based methods (Huntzinger et al., 2013), and (iv) land surface models.

Over the past decades, many numerical models with different frameworks (carbon assimilation (Knorr and Heimann, 1995), light use efficiency (Monteith, 1972), biochemical processes (Fung et al., 1987; Heimann and Keeling, 1989)) have been developed. Furthermore, each of these approaches is characterized as either (i) a soil-vegetation-atmosphere transfer (SVAT) scheme: which considers the physiological properties of vegetation, and how it affects the energy and water balance, or (ii) an ecological model: which emphasizes the relationship between soil water content, soil properties, and vegetation (Arora, 2002). One of these approaches exploit the coupling of biogeochemical modules and SVAT schemes to provide estimates of water, energy, and carbon fluxes. In the following section, we present a brief review of some popular biogeochemical models used to simulate the carbon cycles in terrestrial ecosystems.

(i) Soil-Plant-Atmosphere continuum model (SPAC): This is a 10-layer process-based model that is a combination of simple models of plant and soil hydraulics, carbon assimilation, vegetation-environment interaction (Williams et al., 1996). The photosynthesis process of Farquhar and Von Caemmerer (1982) is used, and the canopy process is modeled using the distributed approach i.e., net radiation, atmospheric saturation deficit, and leaf conductance vary with depth within the canopy. Another uniqueness of this model is that the stomatal conductance for each canopy layer is calculated in order to maximize the daily carbon gain per unit leaf nitrogen within the limitations of canopy water storage and soil-to-canopy water transport (Williams et al., 1996). In general, SPAC treats the canopy with a high level of detail, and so, it requires a large number of inputs.

(ii) Ecosys: Ecosys is a process-based model that has been rigorously examined over different ecosystems including irrigated and rain-fed croplands (Grant, 2001; Grant et al., 2004; Grant et al., 2007). This model represents multiple canopy and soil layers with fully coupled carbon, water, energy, and nutrient cycles. The carbon uptake is primarily controlled by the plant water status which is estimated from some convergence solutions that equilibrate total root water uptake with transpiration (Grant et al., 2007). Similar to SPAC, canopy exchanges are estimated through a multi-layered soil-root-canopy system by creating non-uniformity in the horizontal distribution of leaves within each canopy layer.

(iii) ORCHIDEE: Organizing Carbon and Hydrology in Dynamic EcosystEms (Krinner et al., 2005) is birthed from the coupling of a SVAT model (SECHIBA: Ducoudre et al., 1993; de Rosnay and Polcher, 1998) to a photosynthesis model (STOMATE: Viovy, 1996), and dynamic global vegetation model (DGVM: Sitch et al., 2003). The stomatal conductance is formulated according to Ball et al. (1987), while the photosynthesis processes of C3 and C4 crops are represented using the approach of Farquhar et al. (1980), and Collatz et al. (1992). For the canopy processes, the distributed approach is adopted; here, the photosynthetic capacity is parameterized as an exponentially decreasing function of the canopy's depth (Krinner et al., 2005). For a proper representation of canopy/leaves distribution, this model was built on the concept of plant functional types (PFT) which groups species with similar functional characteristics (see Table 1 in Krinner et al. (2005) for the recommended parameter value used in ORCHIDEE for each PFT).

(iv) ORCHIDEE-STICS: ORCHIDEE-STICS (Gervois et al., 2004) is a derivative of ORCHIDEE after being coupled with a crop model (STICS: Brisson et al., 1998). This coupling is due to the inability of ORCHIDEE to properly represent the phenologies of cultivated crops while giving no consideration to activities like sowing, fertilization, irrigation etc. Also, due to the absence of an explicit nitrogen cycle in ORCHIDEE, with STICS, crop yields can be estimated. Some drawbacks of ORCHIDEE-STICS are: (i) soil depth is fixed at 2 m, which could create a false water stress situation, (ii) soil plowing is a popular practice among farmers which strongly influences CO_2 efflux; unfortunately, this activity is not represented in ORCHIDEE-STICS as a process, but rather, the model simplifies it by using a reduced turnover time for agricultural soil pools. This limits the model's ability to quantitatively reconstruct(estimate) past(current) carbon budgets of agrosystems (Gervois et al., 2007).

(v) ISBA-Ags: This is a coupling of a SVAT model (ISBA: Noilhan and Planton, 1989) with the photosynthesis model of Jacobs, (1994) and Jacobs et al. (1996). This is the model evaluated in this study, and readers are directed to Chapter 2 for its full description.

Many model-data comparisons have been conducted over FR-Lam. For instance, using measurements obtained during the CERES 2005 and 2007 field campaign, Noilhan et al. (2011) conducted an evaluation of the A-gs-12P configuration of ISBA. The objective was to see if there would be an improvement in the surface fluxes (wheat in 2007) following the coupling of the water and carbon cycle using the configuration of Calvet et al., 1998. A very good agreement was obtained with the *in-situ*, although, the study was limited only to a few days. In 2011, Wu et al., 2016 evaluated the ORCHIDEE-CROP model in FR-Lam over a longer time scale (a season of winter wheat and summer maize). The model was very sensitive to sudden bursts of CO_2 fluxes due to increased litter decomposition, and overall, if the uncertainties surrounding the *in-situ* measurement were considered, the model performed very well in capturing the dynamics of NEE. Similarly, Li et al., 2011 evaluated ORCHIDEE-STICS, and investigated the impact of different management strategies on carbon fluxes over several European sites including FR-Lam (-covering only one maize season in 2006). This model showed a fair performance in reproducing the seasonal NEE with an R^2 of 0.74, and RMSE of 0.51 gC m^{-2} d^{-1}. Furthermore, Pique et al. (2020) implemented a simple crop model (Simple Algorithm For Yield Estimates-CO_2) over FR-Lam, and its major drawback is its heavy reliance on remotely sensed information. This makes simulations at a finer scale difficult, and also makes this model unsuitable as a forecasting tool.

The third objective of my thesis performed a long-term evaluation of ISBA-A-gs (in its Multi Energy Balance option) over 4 wheat and 6 maize seasons in FR-Lam. Depending on its performance, this model may prove to be an effective tool for predicting agrosystems' response to water stress and heat waves. The preliminary analysis is presented in Chapter 5.

Some main ideas of this chapter

- Since the growing population has necessitated the expansion of croplands which are sources of anthropogenic CO_2 fluxes, a balance must be struck between increasing crop productivity and sequestering more carbon.

- Climate change exacerbates water stress. Quantification of the soil-water component is required for proper management of agricultural water.

- This chapter presented a state of art of the different methods of acquiring the surface-atmosphere exchanges.

Chapter 2: Site description, data, and model presentation

2.1 General introduction

This research relied on measurements taken over two experimental croplands: Lamasquère (FR-Lam) and Auradé (FR-Aur), which are about 40 km from Toulouse, in southwestern France. In this chapter, a full description of these study sites is given, alongside instrumentation description, measurements taken over them and the data processing protocols. In the second part of this chapter, a description of the ISBA model used in this study is presented, focusing on the main equations representing the surface energy budget, soil water/energy transport, and the photosynthesis processes together with the parameterizations relevant to this study. Also, the different relevant improvements of the standard ISBA model would be discussed.

2.2 Site description and data

2.2.1 Site description

FR-Lam (43°49’ N 1°23’ E) and FR-Aur (43° 54’ N 1° 10’ E) have been subject to intense cultivation over the past 30 years. Both agrosystems are part of the Regional Spatial Observatory (OSR), the Zone Atelier Pyrénées-Garonne (ZA PYGAR), the Integrated Carbon Observation System (ICOS), and the Critical Zone Observatories (OZCAR) projects (Gaillardet et al., 2018).

Lamasquère site

FR-Lam is an experimental farm under the management of the Purpan Engineering School. It is a flat 24 ha farmland situated in the Haute-Garonne region. Located at 180 m above sea level (a.s.l), this site borders the Touch river on its eastern side. The perimeter of this site is a thick forest especially in the western, eastern, and southern direction (see Figure 2.1). The culture rotation is a combination of summer maize and winter wheat, including cover crops like mustard, faba beans, and wheat regrowths preceding summer crops. The farmer usually plants wheat (*Triticum aestivum* L.) at the beginning of October, and harvests it the following summer within the first two weeks of July. Harvest residues of wheat are often left on site before deep tillage and plowing; these are seedbed preparatory practices for the sowing of maize (*Zea mays* L.) in the spring of the following cropping year. Maize is usually sown between April and mid-May, irrigated in phases over a 5-days period, and harvested green between mid-August and early September of the same year for livestock feeding. In addition, organic and mineral fertilizers are customarily applied over this plot.

Auradé site

Unlike the topographically homogeneous FR-Lam, FR-Aur is situated on a slope (3%) on an open hill. This slope creates a significant height difference (~15 m) at certain locations on this 23.5 ha farmland. Under the management of a private owner (Mr. Andreoni), this farmland experiences a more diversified cultivation (of wheat, barley, rapeseed, and sunflower), but no deep plowing. In addition, the farmer practices only mineral fertilization, and it is never irrigated probably due to the absence of a nearby water source, and because the farmer mainly cultivate winter crops. Like in FR-Lam, the winter crops (wheat and rapeseed) are sown in autumn and harvested in early July, and their harvest residues are also left on site for a while before being incorporated into the soil. Sunflower and barley were grown only once in 2007 and 2015, respectively; hence, no focus was given to these crops because they are not statistically representative. Also, Table 2.1 presents the climatic and general characteristics of these plots.

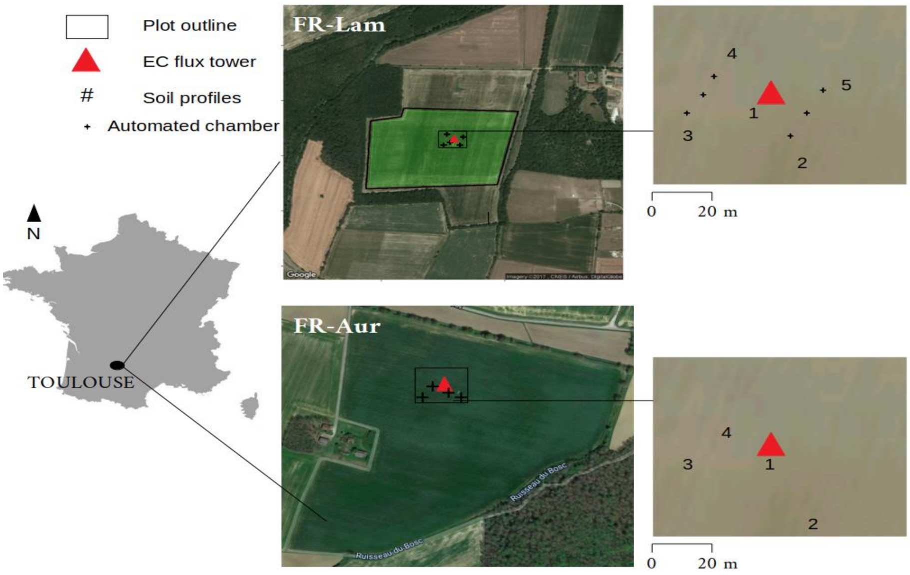

Figure 2.1: Geographical positioning of the study sites in southwestern France (left map), the experimental set-up (in the middle), and the spatial distribution of the devices (on the right) in Lamasquère and Auradé site. The numbers on the right image represent the pits' locations where the heat flux plates, temperature and moisture sensors are buried. The red triangle is the installation point of the EC tower, and the small black crosses are the locations of the automated chamber devices in FR-Lam.

Table 2.1: General site and climatic information. The average climatic variables were computed between the 1st of January, and the 31st of December. Similarly, the annual precipitation was calculated as the mean of the cumulative rain over the same period. At both sites, average meteorological values were computed between 2005 and 2015.

Climatic conditions	**Lamasquère**	**Auradé**
Dominant wind direction	W, NW, SE	W, SE, NW, E
Average incoming radiation	157 W m^{-2}	174 W m^{-2}
Average air temperature	12.8 ºC	13.0 ºC
Annual precipitation	735.7 mm	617 mm
Average humidity	76.8%	84.4%
Soil classification Clay; Loam; Sand	54%; 33.7%; 12%	32.3%; 47.1%; 20.6%
Wind speed	1.9 m s^{-1}	2.8 m s^{-1}
Wind distribution	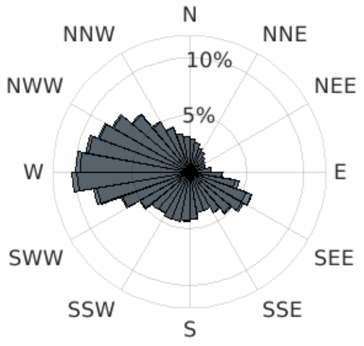	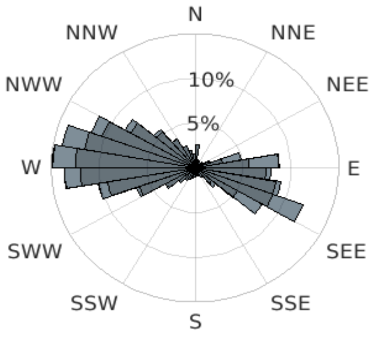

Figure 2.2 displays the crop rotation cycles and the evolution of the leaf area index (*LAI*) at both sites, while Table 2.2 and Table 2.3 highlights the succession and timeline of each crop, and agricultural practices at FR-Lam and FR-Aur, respectively.

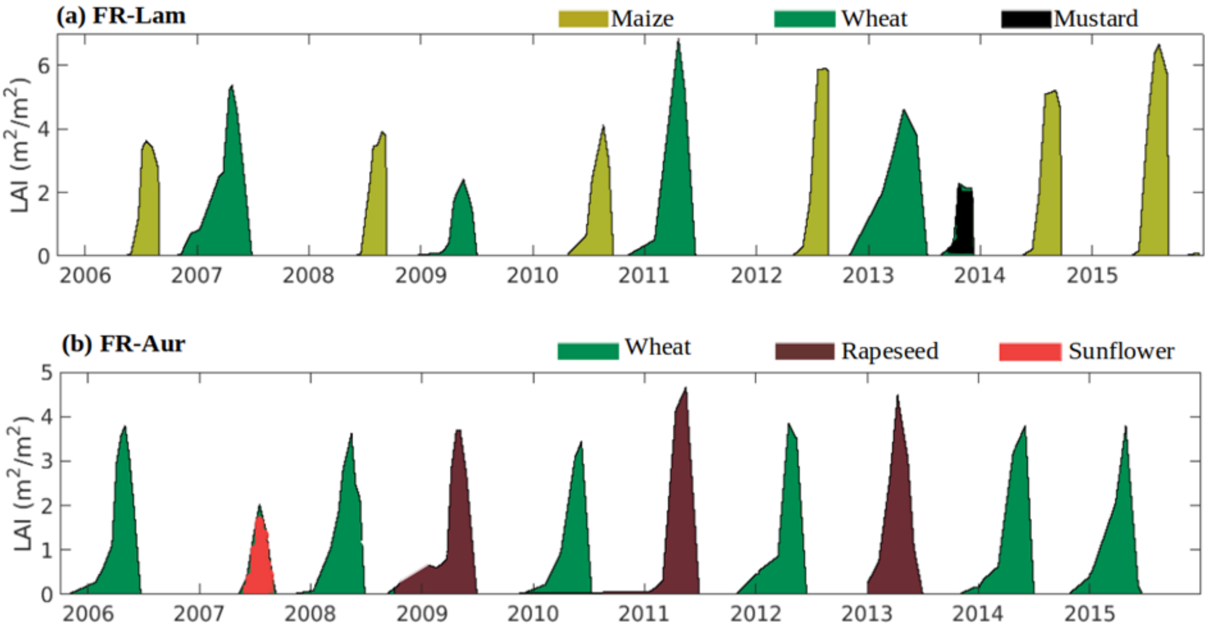

Figure 2.2: Timeline and crop rotation at FR-Lam and FR-Aur site from 2005 to 2016.

Table 2.2: Crop rotation, and operational dates (planting, harvest, and tillage) of the FR-Lam plot between 2005 and 2019.

Year	Crop rotation
2005	**WW** (HV: 11/07/2005)
2006	DT (05/01/2006); ST (30/03/2006); **SM** (PP: 01/05/2006 HV: 31/08/2006); ST (10/10/2006); **WW** (PP: 18/10/2006)
2007	**WW** (HV: 30/06/2007); DT (29/11/2007)
2008	**SM** (PP: 20/05/2008 HV: 11/09/2008); ST (14/11/2008); **WW** (PP: 19/11/2008)
2009	**WW** (HV: 13/07/2009 HV); ST (28/10/2009); DT (17/11/2009)
2010	**SM** (PP: 21/04/2010 HV: 17/10/2010); **WW** (PP: 03/11/2010)
2011	**WW** (HV: 30/06/2011); Re (01/09/2011); DT (25/11/2011)
2012	**SM** (PP: 27/04/2012 HV: 23/08/2012); ST (17/10/2012); **WW** (PP: 29/10/2012)
2013	**WW** (HV: 22/07/2013); ST (16/08/2013); MD (PP: 21/08/2013 HV: 04/12/2013); DT (10/12/2013)
2014	**SM** (PP: 14/05/2014 HV: 22/09/2014); DT (21/10/2014)
2015	**SM** (PP: 05/05/2015 HV: 08/09/2015; ST (14/10/2015); **WW** (PP: 04/11/2015)
2016	**WW** (HV: 20/07/2016); ST (10/08/2016); MD (PP: 17/08/2016 HV: 12/12/2016)
2017	ST (17/01/2017); **SM** (PP: 28/04 HV: 05/09/2017); ST (30/10/2017); **WW** (PP: 16/11/2017)
2018	**WW** (HV: 10/07/2018); Re (23/08/2018); ST (25/09/2018)
2019	ST (19/03/2019); **SM** (PP: 22/04/2019 HV: 11/09/2019); **WW** (PP: 28/10/2019)

WW is winter wheat, **SM** is summer maize, MD is mustard, Re is regrowth, ST is slight tillage, DT is deep tillage, PP and HV represent the sowing, and the harvest date respectively. The greyed years are out of scope in this current study.

Table 2.3: Crop rotation, and operational dates (planting, harvest, and tillage) of the FR-Aur plot between 2005 and 2015.

Year	Crop rotation
2005	**WW** (PP: 27/10/2005)
2006	**WW** (HV: 29/07/2006); ST (30/09/2006)
2007	SF (PP: 10/04/2007 HV: 20/09/2007); ST (25/09/2007); **WW** (PP: 26/10/2007)
2008	**WW** (HV: 10/07/2008); ST (24/07/2008); **RP** (PP: 04/09/2008)
2009	BY (HV: 30/06/2009); ST (15/11/2009); **WW** (PP: 19/11/2009)
2010	**WW** (HV: 15/07/2010); ST (01/09/2010); **RP** (PP: 20/09/2010)
2011	**RP** (HV: 30/06/2011); ST (22/09/2011); **WW** (PP: 27/10/2011)
2012	**WW** (HV: 12/06/2012); ST (01/09/2012); **RP** (PP: 16/09/2012)
2013	**RP** (HV: 05/07/2013); ST (26/09/2013); **WW** (PP: 26/10/2013)
2014	**WW** (HV: 10/07/2014); ST (08/08/2014); BY (PP: 22/10/2014)
2015	BY (HV: 27/06/2015); ST (20/07/2015)

WW is winter wheat, SF is sunflower, BY is barley, **RP** is rapeseed, ST is slight tillage, PP and HV represent the planting, and the harvest date respectively.

2.2.2 Experimental data sets

At the center of both sites (see Figure 2.1), a mast housing the eddy covariance (EC) system, and meteorological instruments is installed to optimize the fetch in the direction of the prevailing winds. Towering at 3.65 m (210° N) in FR-Lam (up until the year 2018), and at 2.8 m in FR-Aur, these EC systems were positioned in such a way that at least, a distance of 1 m is maintained between the canopy top and the EC systems. At both sites, meteorological measurements are taken and averaged at half-hourly resolution, and backup sensors are available for redundancy, and often used in gap-filling. Table 2.4 presents details about this instrumentation. Regarding information on the vegetation characteristics and site operations (irrigation, sowing, harvest, tillage), this information is gathered through regular surveys and continuous monitoring.

Table 2.4: Instrumentation and study-relevant measurements taken at FR-Lam and FR-Aur

Parameter	Unit	Model (Brand)
Air temperature	ºC	HMP35A (2005-2013); HMP155 (2013-2017) (VAISALA) and PT100 since 2017
Wind speed/direction	m s^{-1}/º	Windvane, Wind Sonic (Young Prop; Gill Ltd)
Rainfall	mm	ARG100 (Environmental measurement Ltd); TRWS-415 (MPS system Ltd.) since 2017
Incoming, outgoing, and diffuse Photosynthetically active radiation	µmol m^2 s^{-1}	2005-2013 : PAR/LE (Solems), 2013-2021 : PQS1 (Kipp & Zonen)
Incoming and diffuse solar radiation (SW_In, SW_Dif)	W m^{-2}	SPN1 (Delta T) (2013-2021)
Net radiation	W m^{-2}	CNR1 (2005-2012), CNR4 (2013-2021) (Kipp & Zonen)
Net radiation	W m^{-2}	NR-lite (2005-2013) (Kipp & Zonen)
Latent and Sensible heat flux	W m^{-2}	Li-7500 (Li-Cor) + CSAT (Campbell Sci. Ltd from 2005 to 2017) & Li-7200 (Li-Cor) + HS50 (Gill Ltd) from 2013 till date
Ground heat flux	W m^{-2}	HPS01SC (Hukseflux)
Soil temperature	ºC	T109 (Campbell Scientific Ltd)
Soil water content	%	CS616 TDR (Campbell Scientific Ltd), ML2X ThetaProbe (Delta-T Devices Ltd)
3-D wind speed & speed of sound	m s^{-1}	CSAT3 (Campbell Scientific Ltd) 2005-2017 & HS50 (Gill Ltd.) 2013-2021

2.2.2.1 Biophysical measurements

Over the studied years, we used two methods to measure the LAI, and the Green Area Index (GAI) which concerns the whole green matter. LAI is measured using the destructive method. During the growing season, LAI is monitored about five to six times. The sampling protocol involves collecting vegetation at 10 to 20 sampling points inside a footprint area representative of the crop plot. After vegetation collection, the leaves are separated from the stalks, then, these detached leaves are placed on the transparent bed of the Li-3100 planimeter (LiCor, Lincoln, NE, USA), and they are conveyed across the scanning bed that rapidly digitizes the area, length, and width of these leaves. Using these destructively-obtained LAI measurements, a continuous LAI dataset is constructed at a 30-mins time step using spline interpolation. Simultaneously, at these same sampling locations, measurements of the vegetation heights were obtained. Readers are referred to Béziat et al. (2009) for the detailed protocols for the different crops.

Since 2019, in accordance with the related ICOS protocol, a ceptometer (SS1 Sunscan Canopy Analysis System; Delta-T Devices), replaced this traditional method of LAI estimation. For comparison purposes, in addition to this indirect method, the ICOS protocol requires a simultaneous acquisition of a destructively-obtained leaf area index particularly towards each crop's vegetation peak. This is recommended because the Sunscan plant canopy analyzer system has the reputation to strongly underestimate the leaf area index due to its sensitivity to the photosynthetic active radiation under non-ideal light conditions (see Pokovai et al., 2019; Casa et al., 2019; Wilhem et al., 2000 for reviews).

Considering the fact that destructively-obtained LAI (LAI_{Destr} in this section) serve as a reference measurement used in the validation of measurements from indirect methods, LAI_{Destr} measurements taken between the 19th of June and 15th of July 2019 were used to correct the measurements from the Sunscan ($LAI_{Sunscan}$). A very simple approach was adopted; hence, its interpretation should be made with absolute care because only 8 LAI_{Destr} data points were available. Describing the relationship between LAI_{Destr} and $LAI_{Sunscan}$ by a linear equation, Figure 2.3a presents a scatterplot comparing both raw measurements, and Figure 2.3b displays the outcome of the correction exercise. These new values ($LAI_{Sunscan}Corr$) would be used in chapter 5 in the estimation of the carbon fluxes for the year 2019.

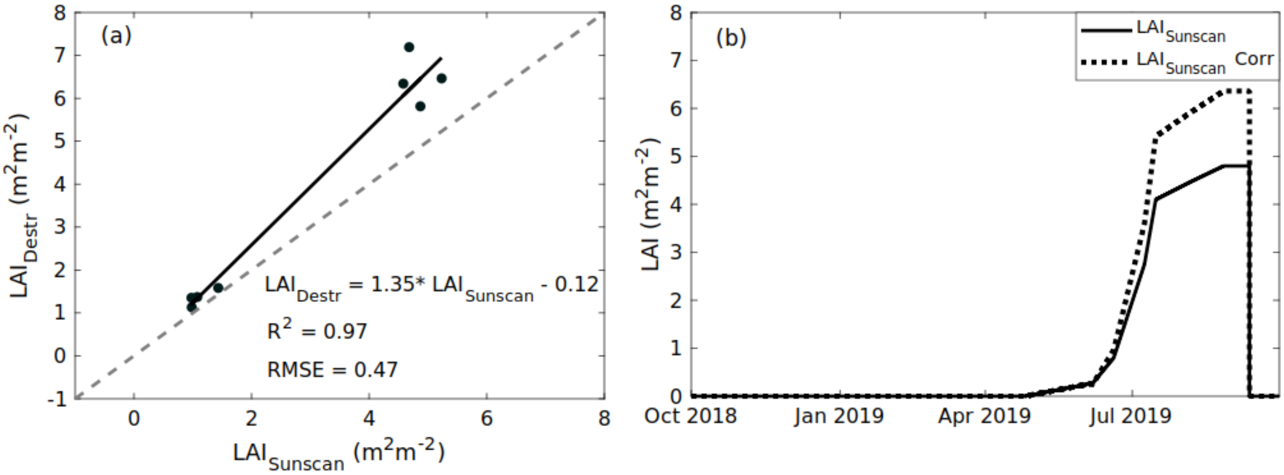

Figure 2.3: (a) Comparison of the LAI values obtained destructively (LAI_{Destr}), and from the Sunscan ($LAI_{Sunscan}$) between the 19th of June and 15th of July 2019 in FR-Lam over maize. (b) Time series of the raw $LAI_{Sunscan}$ values with its corrected values ($LAI_{Sunscan}Corr$).

2.2.2.2 Meteorological measurements

As shown in Table 2.4, net radiation was measured by various radiometers depending on periods. For instance, CNR1 (updated to CNR4 in 2012 with both models being used with an overlap of several months) is a 4-component radiometer mounted on a dedicated mast that measures up-welling and down-welling radiations at a rate of 1 sample per min integrated over 30 min. The total spectral range incorporates wavelengths from 0.3 to 50 µm. Shortwave radiation (0.3 to 3.5 µm) is measured by two CM3 pyranometers: one measures the incoming solar radiation ($SWin$), while the other measures the reflected shortwave radiation ($SWout$). NRLite sensors were also installed at both sites between 2008 and 2012, and redundant measurements of incoming solar radiation were performed with SPN1 sensor from 2013. Given that these instruments are frequently moved because of field operations, a data quality check was performed on the net radiation measurements, and the procedure is as follows:

(i) First, a visual inspection and comparison between the overlapping time series was done to eliminate erroneous data points.

(ii) Afterwards, a linear regression was carried out between the sensors (CNR1/NRLite or CNR1/CNR4), and the highest observed discrepancy was 26 W m^{-2} which is in good agreement with Kohsiek et al. (2007). Data points that presented strong dispersion around the regression line were eliminated.

(iii) Finally, the data from the best sensors (CNR1 and CNR4) were selected, and missing data were gap-filled with measurements from the other sensors.

For the HMP35A temperature and relative humidity probes, only a single level profile is set up at the height of the EC systems (at both sites). These Vaisala instruments were connected to a data logger, the output is measured every 15 seconds, and integrated into 30-min averages. Similarly, the measurements of other variables were carried out every minute, averaged over half an hour, and stored in the internal memory of the control units.

2.2.2.3 Soil Measurements

Soil water content and temperature

Between 2005 and mid-2012, the CS616 used the time-domain measurement method to measure the volumetric water content at the depths 0 cm, 5 cm, 10 cm, 30 cm, 50 cm, and 100 cm. At both sites, these sensors were replaced by ML2X theta-probes in 2012. Again, because these sensors age quickly on agricultural plots, in October 2018, they were replaced by Stevens hydra-probes (Ratiometric Coaxial Impedance Dielectric Reflectometer). The soil temperature profiles are similar to that of the soil water content, and the sensors for the soil moisture and soil temperature are collated in the same target pit. In accordance with ICOS instruction, and to obtain a valid spatial average of measurements, each site houses 5 target pits altogether, and pit 1, which is the permanent pit, is situated very close to the foot of the EC mast) (see Figure 2.1). See Béziat et al. (2009) for more information.

Ground heat flux and storage terms

One of the important and often-very-difficult components to measure is the ground heat flux (G), and it is the total amount of energy absorbed or emitted by the soil via conduction. With HFP01SC heat flux plates buried at 0.05 m depth, and at a 20 m distance from the EC system (see Figure 2.1), G, which is proportional to the voltage signal from the HFP sensors is obtained in W m^{-2}. The vertical temperature gradient between the surface and the deeper layers of the soil leads to a transfer of energy by diffusion described by the Fourier's law of heat conduction. For a layer of soil with uniform thermal conductivity, this law is expressed in Equation 2.1 as a projection on the vertical axis:

$$G = -\lambda_s \frac{dT_s}{dz} \qquad (2.1)$$

λ_s (W m^{-1} K^{-1}) stands for the thermal conductivity of the soil, and $\frac{dT_s}{dz}$ (K m^{-1}) is the vertical temperature gradient of the soil layer (Sauer and Horton, 2005). The energy stored in the layers above the HFPs (G_{st}) is accounted for using the continuity equation (Equation 2.2) taken from Campbell and Norman (1998).

$$G_{st} = \rho_s c_s \frac{\mathrm{d}T_s}{\mathrm{d}t} \tag{2.2}$$

Where dT_s (K) represents the average temperature change in the soil between the depth of 0.05 m and 0.01 m over a given time interval (dt (s)), ρ_s (kg m^{-3}) is the soil density, c_s (J kg^{-1} K^{-1}) is the specific heat capacity of the soil, and $\rho_s c_s$ is the volumetric heat capacity. See Campbell and Norman (1998) and Béziat et al. (2009) for details on the estimation of $\rho_s c_s$.

2.2.2.4 Eddy covariance measurements

An eddy covariance system uses the eddy covariance method to measure exchanges between the atmosphere, and the underlying land surface. This method was proposed by Montgomery (1948), Swinbank (1951), and Obukhov (1951). The EC system samples eddies for their vertical velocity, and the concentration of the scalar of interest (H_2O, CO_2, CH_4, N_2O etc). Figure 2.4 shows the flux towers installed at our study sites, and this offers the possibility of continuous flux measurement (see Table 1.1 in Foken et al. (2012) for the evolution of the EC system).

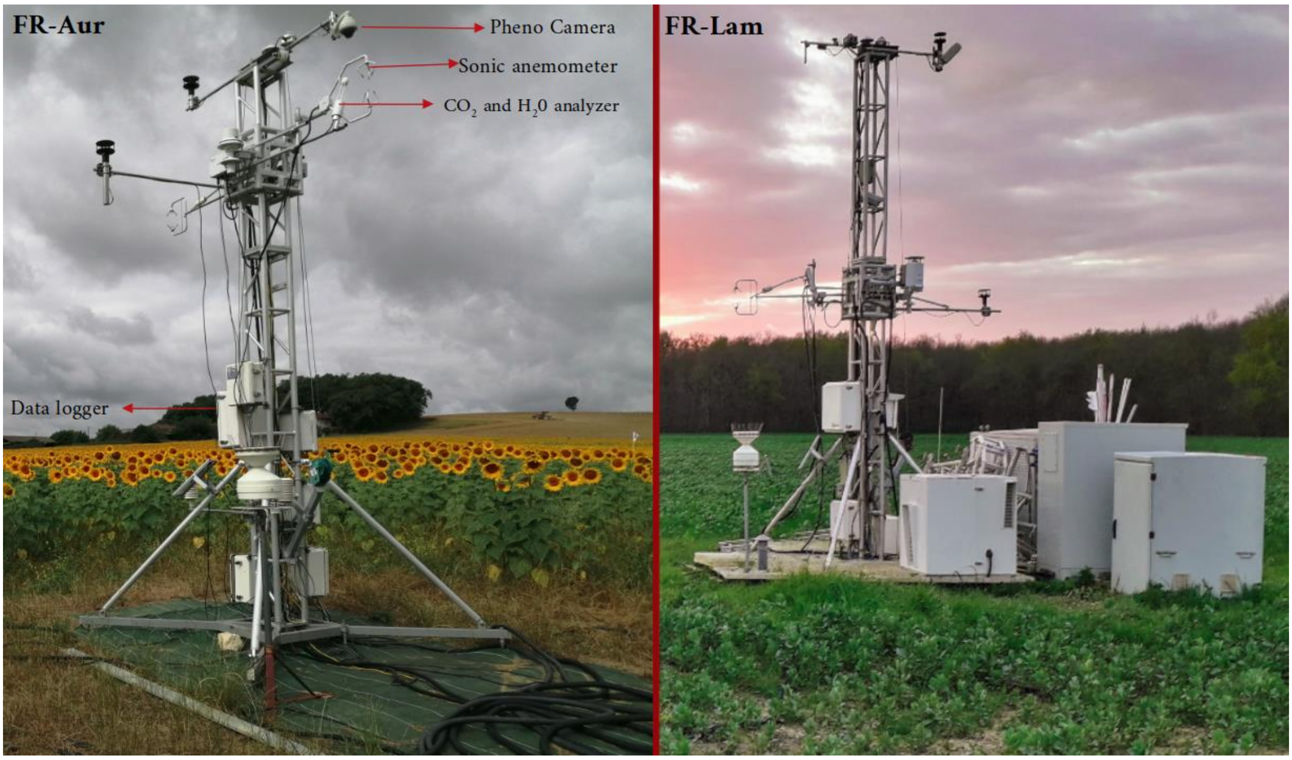

Figure 2.4: The eddy covariance flux tower installed at FR-Aur and FR-Lam with some components.

Turbulent exchanges at the surface (e.g., the sensible heat fluxes (H), the latent heat fluxes (LE), the vertical turbulent CO_2 flux (F_C) etc.) are measured by the EC system. An EC system consists of an

Infra-Red Gas Analyzer (IRGA), and a three-dimensional sonic anemometer (HS50, Gill Ltd or CSAT, Campbell). The sonic anemometer measures the 3-D high frequency wind speeds and sonic temperature, while the IRGA measures the fluctuations in the air temperature, water vapor density, CO_2 density etc.

There are two types of IRGAs: the closed-path (CP), and the open-path (OP). In the CP set up, the concentration of the sampling air is quantified by drawing the air around the sonic through a sampling tube to the IRGA; whereas in the OP design, the IRGA is situated a few centimeters away from the anemometer, and the sampling air must move freely between the two systems (see Haslwanter et al. (2009) and Burns et al. (2015) for the pros and cons of each design). At our experimental sites, measurements running from 2005 to 2018 were made with an OP system (Li7500). Although, between 2013 and 2017, both OP and CP were run in parallel at the two sites. In 2018 and afterwards (at FR-Lam), only the CP system (Li7200) was retained in compliance with ICOS's recommendation; and with this CP design, data loss due to precipitation is alleviated. In the former set-up, raw turbulent measurements were recorded at 20 Hz on a CR3000 data logger (Campbell Scientific Inc., Logan, UT, USA), and since 2018, they have been recorded at 10 Hz with a smart-flux data logger to ensure data synchronization between the sonic anemometer and the IRGA.

(i) Turbulent energy fluxes

The EC method is based on the direct measurement of high-frequency vertical winds (w) and a scalar concentration, such as water vapor (q) or air temperature (TA), giving LE and H through Equation 2.3 and Equation 2.4, respectively; with the assumption that the mean vertical velocity is negligible. These turbulent fluxes are estimated in W m^{-2} at a 30-min resolution as the mean covariance of the fluctuations of w and the scalar of interest.

$$LE = \lambda_v \rho_a \overline{w' q_a'} \tag{2.3}$$

$$H = \rho_a C_p \overline{w' TA'} \tag{2.4}$$

where q_a is the vapor density (kg kg^{-1}), TA is in °C, ρ_a is the moist air density (kg m^{-3}), C_p is the specific heat of dry air at constant pressure (J kg^{-1} K^{-1}), λ_v is the latent heat of water vaporization (J kg^{-1}), the over bar is the time average, and the prime represents the departure from the mean (e.g., $x' = x - \bar{x}$).

Storage terms

Asides from G_{st}, which has been underlined as a crucial fraction of G especially over agricultural sites (Moderow et al., 2009), there is also (i) S_{LE}, the latent heat storage change which is the portion of LE that is stored below the measuring height and so uncaptured by the EC system, (ii) S_H: As in S_{LE}, S_H is the sensible heat storage change in the canopy air, and (iii) S_P which is the biochemical energy flux fixed by photosynthetic activities. According to Meyers and Hollinger (2004), Moderow et al. (2009), and Aubinet et al. (2001), these terms are expressed as follows:

$$S_{LE} = \int_0^{z_{EC}} \lambda_v \rho_a \frac{\partial q_a}{\partial t} dz \tag{2.5}$$

$$S_H = \int_0^{z_{EC}} \rho_a C_p \frac{\partial \mathrm{TA}}{\partial t} dz \tag{2.6}$$

$$S_P = \propto_C GPP \tag{2.7}$$

Where z_{EC} (m) is the measuring height of the EC system, z represents the various measuring levels (0.5 m, 1.5 m, and 2 m in our sites), GPP is the gross primary productivity, and $\propto_C$ is the equivalent solar energy used in CO_2 fixation, and it is approximately 422 kJ per mole of CO_2 fixed by photosynthesis (Nobel, 1974). For a thorough representation of the energy budget, these terms were considered later on in this study to examine their respective importance in the surface energy balance closure.

(ii) Carbon fluxes

With the same assumptions of horizontal homogeneity and steady state conditions, turbulent vertical CO_2 fluxes are measured by the EC system. In compliance with the standards of the flux community, the net ecosystem exchange (NEE in μmol m^{-2} s^{-1}) is quantified as the sum of the flux measured directly by the EC system (F_C), and the rate of change of the CO_2 molar fraction (F_{CS}) in the air space below the measuring height of F_C that is not influenced by turbulence. At FR-Lam and FR-Aur, F_{CS} is calculated according to the description in Aubinet et al. (2001), but with only one measuring height for CO_2 concentration. See Equations 2.8 and 2.9 for the derivatives of F_C and F_{CS}, respectively.

$$F_C = \overline{\rho_d}\overline{w'X'_{CO_2}} \tag{2.8}$$

$$F_{Cs} = \frac{P_a}{R.TA} \cdot \frac{dc}{dt} \cdot z_{EC} \tag{2.9}$$

Where ρ_d (kg m^{-3}) is the dry air density, X'_{CO_2} is the mixing ratio (dry mole fraction of CO_2). Again, the over-bars and primes represent the averaging operator and fluctuations, respectively obtained according to Reynold's decomposition. Furthermore, P_a is the atmospheric pressure at z_{EC}, c is the CO_2 concentration at z_{EC}, and R (J K^{-1} mol^{-1}) is the molar gas constant. This methodology (Equation 2.9) is known to underestimate F_{cs} by about 20–25% (Saito et al., 2005). However, it is often used for ecosystems with short vegetation, such as croplands and grasslands, where F_{Cs} is assumed to be low (Moureaux et al., 2006; Verma et al., 2005). After the computation of the NEE, flux filtering and gap filling procedures were performed following the recommendations of CarboEurope-IP (www.carboeurope.org) in section 2.2.3.

2.2.2.5 Soil respiration measurements

Automated chamber measurements

CO_2 efflux of the soil surface were measured using six automated chambers (AC) that were installed within the EC's footprint, and at a distance 15-20 m from the EC tower (see Figure 2.1 for distance and Figure 2.5 for device view) in FR-Lam. These 0.23 m x 0.7 m x 0.227 m stainless steel chambers were thrust into the soil at 0.05-0.10 m depths to limit leakages and diffusion. The set-up measures CO_2 accumulation in each chamber alternately for 17.5 minute period every 6 hours- and so, four cycles of measurements are taken per day (at 00:00h, 06:00h, 12:00h, and 18:00h). The chambers are connected in series to a gas analyzer (LI820, LI-COR, Lincoln, NE, USA). A pump maintains a constant air circulation in and out of the chamber at a constant flow rate of 1 L min^{-1}, and a fan is in constant operation to provide an adequate amount of mixing (Bigaignon, 2020). Finally, all green vegetation present in the chamber are habitually clipped to the ground to ensure that only soil respiration was measured.

Figure 2.5: Automated chamber

This study considered measurements taken between the 1st of January 2013 and December 31st of December 2015. For each time stamp, the average carbon flux is computed only when at least measurements from three ACs were available (see Equation (2.10a) for flux calculation per chamber). In addition, flux uncertainties (AC_{uncer}) were estimated using the random error calculation in Equation (2.10b).

$$SR_{AC} = \frac{h \times M_m}{V_m} \left(\frac{dC}{dt}\right)_{t=\,t_0} \tag{2.10a}$$

$$AC_{uncer} = \frac{SD}{\sqrt{n}} \tag{2.10b}$$

Where h is the headspace height (cm), M_m is the molar weight of C in CO_2 (C = 12 g mol^{-1}), V_m is the molar volume in standard conditions (24.1 L mol^{-1} at 20 ^{o}C) and $\left(\frac{dC}{dt}\right)_{t=\,t_0}$ is the slope (in ppb) obtained from the regression of concentration vs. time at t_0 (i.e., 50 s after the chamber's closure). SR_{AC} values were filtered by means of a mixture of goodness-of-fit statistics and visual inspection. Also, SD is the standard deviation based on the measurements from the automated chambers, and n is the number of chambers in consideration. Out of the 4,380 measurements captured during this period, only about 10% was retained. The data sets were profiled as follows: (i) bare soil selection for appropriate comparison with eddy covariance measurements, (ii) retainment of data points corresponding to a net ecosystem exchange of flag 0 (i.e., EC fluxes that were not gap-filled), and (iii) removal of outliers and erroneous data points by means of a mixture of visual inspection and the setting of an error margin for measurements of the same cycle. Readers are referred to Tallec et al.

(2019) for the functioning of the ACs, and Peyrard et al. (2016) for technical information. The retained SR_{AC} measurements used in this study are presented in Table 2.5 alongside their respective timelines.

Table 2.5: Timeline, and the number of retained data points from the automated chambers.

Period	Timeline	Nos of Data Points
1	23/07/2013 - 14/09/2013	106
2	07/12/2013 - 23/03/2014	174
3	18/12/2014 - 19/05/2015	154

Canopy chamber measurements

During the growing season of wheat (15th February 2007 - 19th April 2007), and maize (5th June 2008 - 26th June 2008), the net carbon flux (NEE_{CC}) was measured. This measurement was carried out using a 50 cm x 50 cm canopy chamber in combination with an IRGA of the Ciras 3 portable photosynthesis type installed within the footprint of the EC system (see Figure 2.6 for the set-up of the system). The chamber is covered with a transparent film to limit the effect of the greenhouse, while allowing solar radiation. Then, the chamber is sunk a few centimeters into the ground for sealing. The floor area is 1963.5 cm^2, the volume is 98175.0 cm^3, and the system is equipped with pipes for air intake at the bottom, and for reinjection at the top to ensure a closed system.

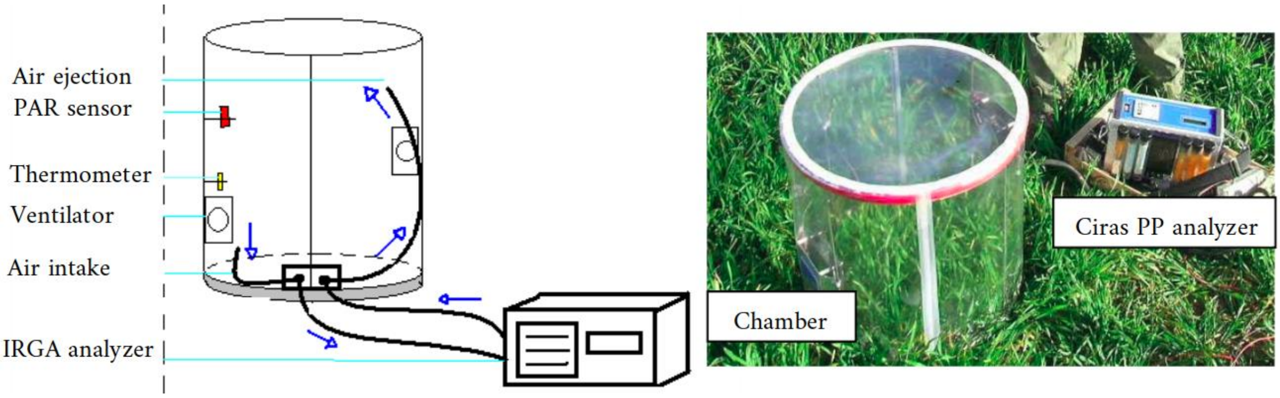

Figure 2.6: (a) a schematic representation of the canopy chamber; the blue arrows represent the chamber's atmospheric circuit, and the red marker is the PAR sensor. (b) the canopy chamber installed on the field in FR-Lam coupled with the analyzer.

This system is also equipped with a temperature sensor, a PAR sensor, and two fans placed at two different levels to stabilize the micro-climate within the chamber. The analyzer measures the rate of accumulation of CO_2 (if breathing dominates), or CO_2 decrease (if photosynthesis dominates) per unit time. Assuming a well-mixed and well-sealed system, the net carbon flux is estimated in gCO_2 m^{-2} h^{-1} using Equation 2.11.

$$NEE_{CC} = \left(\frac{dCO_2}{dt}\right)\left(\frac{V}{A}\right) \tag{2.11}$$

Where $\frac{dCO_2}{dt}$ is the change in the CO_2 concentration (in ppm) inside the chamber over time dt (90 secs in our case), V (in m^3) is the chamber volume, and A (in m^2) is the floor area covered by the chamber. When $dCO_2 \geq 50$ ppm, and $dt \geq 90$ secs, the condition within the chamber departs strongly from the external conditions. Hence, beyond these thresholds, the analyzer was programmed to stop measurement in order to ensure that the measurements within the chamber are constantly comparable to the external natural conditions. This is because within the chamber, an extremely high CO_2 concentration not only modifies the behavior of living organisms, but also the CO_2 diffusion gradient between the soil and the atmosphere (De-Xing et al., 1996). In order to capture the spatial variability of the fluxes, different measuring locations were established within the footprint of the EC system, and each sample point had different vegetation characteristics in terms of height and leaf area.

Simultaneously, ecosystem respiration ($RECO_{CC}$) measurements were obtained using the covered version of the above canopy chamber; whose opacity disallows carbon uptake, while enabling the partitioning of photosynthetic and respiratory fluxes from NEE_{CC}. For wheat, 67 measurements were taken over a 5-days period, while over maize, 71 measurements were obtained over a 7-days period (see Table 2.6 for the retained data set). Finally, after each measurement, the characteristics of the overhead vegetation at each sampling point is obtained, and readers are directed to the reports of Léopold (2007) and De Lanfranchi (2008) for more information on this campaign. In the remaining part of this study, measurements from the automated and canopy chambers are represented by subscripts 'AC' and 'CC' respectively.

Table 2.6: Days of measurement, and the number of retained data points.

Wheat season		Maize season	
Date	Nos	05/06/2008	Nos
15/02/2007	10	11/06/2008	12
01/03/2007	3	12/06//2008	8
12/03/2007	8	18/06/2008	12
19/04/2007	6	19/06/2008	12
		20/06/2008	9
		26/06/2008	12

2.2.2.6 Sap flow measurements

Twenty selected maize plants (all located within the footprint of the EC) were equipped with sap flow sensors (Dynamax Inc.'s SGB19 and SGB25) from the 2nd of July 2015 to 23rd of August 2015 when the plants were close to physiological maturity (minimum LAI = 4.0 m^2 m^{-2}, minimum crop height = 1.59 m, mean diameter = 22.4 ± 3.4 mm) in FR-Lam. These sensors were strategically placed within the maximum contribution of the EC's footprint, and the selected maize stands were taken as representatives of the field. The measurements were performed using the Heat Balance Method (HBM) that was developed by Sakuratani (1981) and Baker and Van Bavel (1987) based on the thermal flow meter approach proposed by Thomas (1911). The measuring sensors consist of a heating resistor, a thermopile, and two thermocouples on both sides of the resistor as shown in the Figure 1 of Smith and Allen (1996). The rate of mass flow (F) in kg s^{-1} is expressed in Equation 2.12 according to Smith and Allen (1996) as:

$$F = \frac{q_f}{c_{sap} . \Delta T_{th}} \tag{2.12}$$

where q_f (W) is the amount of heat lost through convection in the moving sap, c_{sap} is the specific heat capacity of the sap (J kg^{-1} K), and ΔT_{th} (K) represents the difference in sap temperature measured by the thermocouples placed below and above the heater. Due to instrumental problems, measurements from 3 sensors were discarded. For comparison purposes with eddy covariance measurements, the sap flow data were extrapolated over the entire plot by multiplying the averaged sap flow from the retained sensors by the plant density (8.6 ft m^{-2}). For illustration purposes, Figure 2.7 presents the time series of the sap flow data between the 2nd of July and 22nd of July 2015.

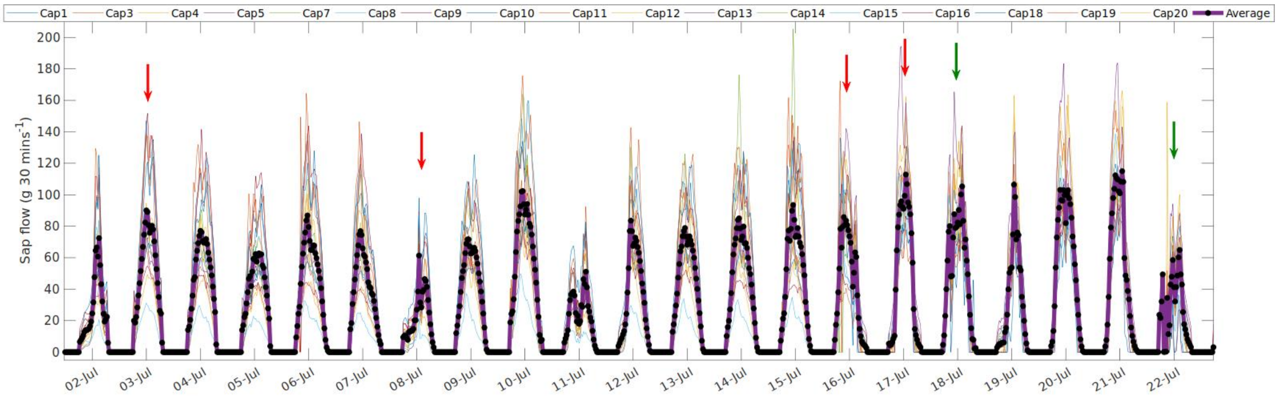

Figure 2.7: Diurnal course of sap flow rate between the 2nd of July and 22nd of July 2015. The solid purple line with black circles represents the average measurement of the 17 captors. The red and green arrows signify irrigation and rain events respectively.

2.2.2.7 LANDSAT Land Surface Temperature

Launched in 1999 (2013), Landsat 7 (8) satellites continuously provided multi-spectral imageries of the Earth with one and two thermal bands, respectively. From 2005 to 2015, Land Surface Temperature (*LST*) maps (138 for FR-Lam) and (134 for FR-Aur) were retrieved from Landsat 7 (ETM+) and Landsat 8 (OLI & TIRS) sensors at a high spatial resolution of 30 m at approximately 10h 30, which coincides with the passing time of the satellite over FR-Lam and FR-Aur (both experimental sites were captured on the same scene). The retrieved thermal data were processed by the LANDARTs tool, and the report of this processing technique has been well documented in Tardy et al. (2016). The acquired maps were filtered by discarding scenes taken under cloudy conditions, and also erroneous scenes with missing data due to the mechanical failure of the Scan Line Corrector (SLC) in Landsat 7 since 2003. From the 71 scenes retained for FR-Lam and the 52 for FR-Aur, *LST* data were retrieved as geo-located digital values and then corrected for atmospheric and surface emissivity effects using the LANDARTs tool. These retrieved temperature values were used in chapter 3 to estimate the spatial and temporal variability of the surface temperature over FR-Lam and FR-Aur by adopting the methodology developed in Cuxart et al. (2016).

2.2.2.8 MODIS leaf area index

Moderate Resolution Imaging Spectroradiometer (MODIS) is a payload imaging sensor that was launched in 1999 on board the Terra and in 2002 on board the Aqua satellite (Ozdogan and Gutman, 2008). This instrument provides continuous high-resolution coverage of the vegetation activity. The MODI3Q1 16-daily normalized difference vegetation index (NDVI) dataset at 250 m was sampled between 2005 and 2016. A simple interpolative exercise was performed for the 16-days NDVI values to daily values. Assuming the LAI-NDVI relationship described in Hadria et al. (2006) as provided in Equation 2.13a, the leaf area index was computed over the FR-Lam site.

$$LAI = -\frac{1}{k}\ln\left(\frac{NDVI_{max} - NDVI}{NDVI_{max} - NDVI_{soil}}\right) \tag{2.13a}$$

$$h_{veg} = \frac{(hveg_{max} - hveg_{\min})\,(NDVI_{max} - NDVI)}{(NDVI_{max} - NDVI_{\min})} \tag{2.13b}$$

Where k is the light extinction coefficient, which is a function of the crop type, $NDVI_{max}$ is the NDVI value for a highly dense canopy, and $NDVI_{soil}$ is the NDVI value over bare dry soils. These parameters were optimized to minimize the RMSE between the measured and the estimated LAI values (for the initially acquired 16-day data). According to the values reported in literatures over croplands, the following ranges were chosen for the calibration exercise (0.4-0.5 for k, 0.92-0.95 for $NDVI_{max}$, and 0.12-0.18 for $NDVI_{soil}$). The resulting optimal values are 0.44, 0.92, and 0.15 for $k, NDVI_{max}$ and $NDVI_{soil}$, respectively (see Figure 2.8 for *in-situ*-estimate comparison). Also, $hveg_{max}$ and $hveg_{min}$ were set to 40 and 5 cm as the maximum and minimum weed height, respectively, while $NDVI_{max}$ and $NDVI_{min}$ represent their respective NDVI values.

Similarly, 10-days averaged series of the vegetation height was also required as input for the model. These heights were estimated by assuming a simple empirical relationship (Equation (2.13b)) with the NDVI-; fixing a minimum ($hveg_{min}$) and maximum ($hveg_{max}$) height of 5 cm and 40 cm, respectively for these plants. These LAI and $hveg$ estimates were used in chapter 5 to fill in for the unavailable vegetation characteristics during the intercropping periods.

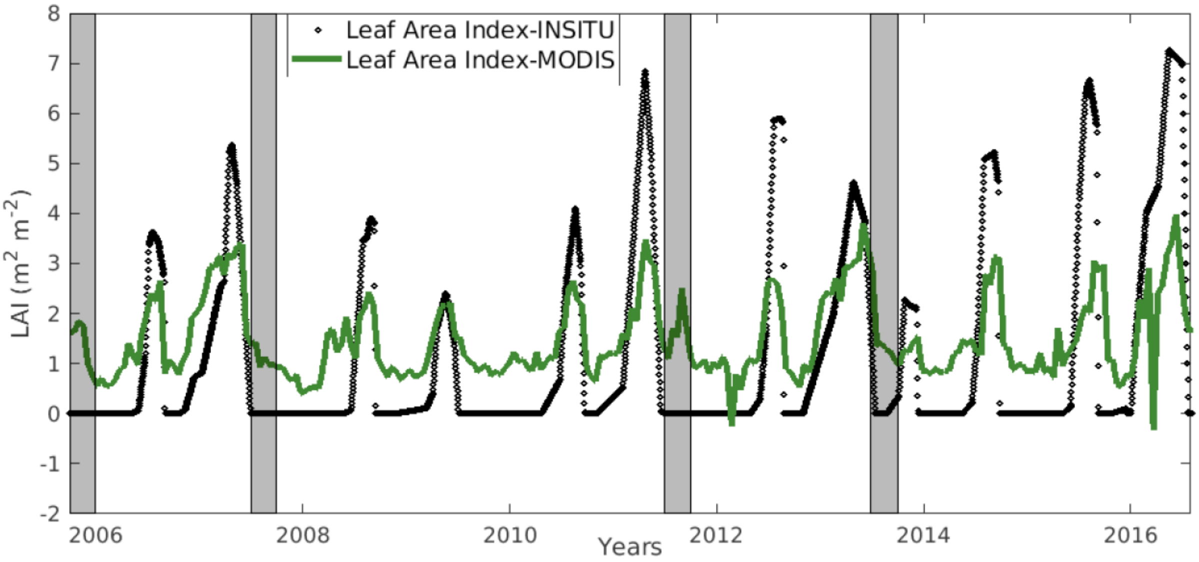

Figure 2.8: Time series comparing the *in-situ LAI* with *LAI* drawn from MODIS. The grey areas represent the periods of interest, i.e., the inter-cropping seasons.

2.2.3 Data processing

2.2.3.1 Eddy covariance data treatment

Time series, high-frequency EC data were post-processed with the EdiRe software package following the guidelines described in Lee et al. (2005), and Burba and Anderson (2010). Before the co-variances were calculated, outliers of six standard deviations from the population mean were removed from the time series. If four or more consecutive data points were detected with values larger than the standard deviation, then they were not considered as an extremity (Vickers and Mahrt, 1997). The time delay between the CSAT3 and Li-7500 was removed using a cross-correlation analysis. To ensure the CSAT3 is perfectly leveled, such that the vertical component (w) is perpendicular to the mean streamline plane, the coordinates were rotated using the double rotation method (Aubinet et al., 2000). According to Lee et al. (2005), this method is suitable for ideal sites with little slope and fair-weather conditions.

The effects of density fluctuations induced by heat fluxes on water vapor measurements when using the Li-7500 were corrected using the procedure outlined by Webb et al. (1980). The spectral loss in the high frequency band due to path-length averaging, sensor separation, and signal processing was also corrected using Moore (1986). For the calculation of the sensible heat flux, the sonic temperature was converted to actual air temperature following the method of Schotanus et al. (1983).

Furthermore, due to the high variability of the flux source area (which depends on the speed of the wind, wind direction, stability of the atmosphere, roughness surface, measuring height etc.), a footprint computation is performed using the parameterization proposed in Kljun et al. (2004). Eventually, a test on the footprint is performed, and data points were discarded if less than 90% of the flux came from within the plot (Kljun et al., 2004).

Finally, in compliance with the CarboEurope-IP standard, a series of tests (Foken et al., 2004; Foken and Wichura, 1996; Göckede et al., 2004) were carried out to check the quality of these fluxes. The goal of these tests was simply to assign a quality index (QI) between 0 to 2 (in order of decreasing quality) to each flux measurement. The first test entails verifying that before the application of the coordinate rotation, the vertical wind component is lower than the threshold value (0.35 m s^{-1}); and measurements that exceeded this threshold were tagged with a QI of 2. The second test was a stability test, to check if turbulence was sufficiently developed at the time of measurement in the surface boundary layer (see Béziat et al. (2009) for details). Finally, in obedience to Taylor's hypothesis of frozen turbulence (Taylor, 1938), a stationarity test is conducted in order to flag periods with non-stationary condition (see Béziat et al. (2009) for these calculations).

2.2.3.2 Partitioning of the net fluxes

The net ecosystem exchange is the combination of several components of the plant functioning. In simple terms, NEE is the net signal between two large fluxes; the flux associated with photosynthesis (GPP), and that which captures the total respiration processes ($RECO$). Although, NEE measurements are invaluable yardsticks for the amount of carbon being sequestered (or not), they do not reveal the underlying assimilatory and respiratory processes responsible for these fluxes (Reichstein et al., 2005). Multiple strategies (e.g., Hollinger et al., 1994; Papale and Valentini, 2003; Falge et al., 2001; Lasslop et al., 2010) have been devised for the partitioning of NEE into GPP and $RECO$. Nonetheless, this section presents only the Reichstein's partitioning approach that was implemented at our experimental sites, and the step-by-step processes are briefly explained as follows:

1. The starting point of this analysis are raw ungap-filled half-hourly NEE fluxes. Erroneous and day-time measurements ($SWin$ > 20 W m^{-2}) were discarded.

2. The resulting data set is divided into periods, each period is further divided into six temperature classes (according to quantiles), then each temperature class is categorized into 20 u^* (friction velocity) categories according to quantiles, and the average flux of each u^* category is computed.

3. The u^* threshold of each temperature class is defined as the mean of the lower u^* category when the average flux in this category reaches more than 95% of the average flux in the higher u^* category. Furthermore, this threshold is only acceptable if the correlation between the temperature and u^* values in the lower "u^* category" is weak ($|r| < 0.4$). Afterwards, the final u^* threshold for this period is defined as the median of the u^* thresholds of the six temperature classes (in point 2).

4. Steps 2-3 are repeated for the other periods of the whole data set (point 2), and the flux in each period is filtered according to the u^* threshold of its class; this is to account for the seasonal variability of the vegetative activities.

$$RECO = R_{ref} e^{E_o\left(\frac{1}{T_{ref}-T_o} - \frac{1}{T_s - T_o}\right)} \tag{2.14}$$

5. From Equation 2.14, the temperature sensitivity parameter (E_o) and the respiration (R_{ref}) at the reference temperature (T_{ref} set to 10 ºC) is computed for the whole data set. T_o is the temperature scale (-46.02 ºC) (Lloyd and Taylor, 1994), and T_s is the soil temperature at 5 cm. $RECO$ is the NEE taken during nighttime in the absence of carbon uptake.
6. E_o is computed for each period using a 15-days data with a 10-day overlapping rolling window (Beziat et al., 2009). To obtain the optimized values of E_o, a non-linear regression of Equation 2.14 is performed with E_o and R_{ref} initialized to 1. The acceptable $E_o$values are chosen to satisfy these two boundary conditions: (i) $0 < E_o < 450\ K$, (ii) RMSE of *in-situ* nighttime $RECO$ vs $RECO_{NN}$ must be lower than 0.5 gC m^{-2}.
7. With the optimized values obtained in (6), $RECO$ is recomputed.
8. Using the Lloyd and Taylor, 1994 model, seasonal R_{ref} values were computed with the E_o obtained in step 6 using a 4-days windows with no overlap (see Figure 2b in Reichstein et al., 2005).

To address the problem of missing data, the gap filling methodologies prescribed by Reichstein et al. (2005) was adapted for our experimental plots. Gap filling of EC data is inevitable because measurements that coincide with unfavorable weather conditions, instrumental failures etc. are often eliminated. In addition, according to Baldocchi et al. (2001), about 25%, 31%, 35% of the H, LE, and NEE fluxes might require data replacement. Hence, the gap-filling procedure adopted for NEE at our study site is as follows:

- For data gaps smaller than 1.5h, a linear interpolation was applied. For larger gaps, the marginal distribution sampling (MDS) and mean diurnal variation (MDV) methodology was employed (Papale et al., 2006; Moffat et al., 2007).
- For the MDS, the missing half-hour flow is replaced by the respective fluxes that was calculated some 'n' days before or after which have similar climatic conditions with the days

with missing data (where 'n' gradually increases in time window to avoid the influence of a rapid change in canopy cover).

- On the other hand, the MDV approach is applied in place of MDS when meteorological variables are missing. Hence, the missing half-hour flow is filled with an average of the flow taken on adjacent days at the same time.

9. Finally, from Equation 2.14, a time series of $RECO$ was computed. Nighttime periods were replaced with *in-situ* measurements, and from $NEE = -GPP + RECO$, GPP values were estimated.

For our study sites, Reichstein partitioning algorithm had been optimized by Béziat et al. (2009) for croplands, and it included the notion of crop functioning periods, depending on the surface state and phenology of the crop.

2.3 Model description and implementation

2.3.1 ISBA-A-gs

Interaction between Soil-Biosphere-Atmosphere-A-gs (ISBA-A-gs) (Calvet et al., 1998) was birthed from the coupling of the standard ISBA model with the semi-empirical photosynthesis model of Jacobs (1994). The standard ISBA model was originally formulated by Noilhan and Planton (1989) following the proposition of Deardorff, (1978) to parameterize water and energy exchanges with meteorological models over natural land surfaces. The modification of the ISBA model became necessary because it does not consider the functional relationship between the stomatal aperture and photosynthesis; that is, within ISBA, the stomatal resistance is estimated using the response of a simple empirical function to the external conditions of air temperature, incoming solar radiation, soil moisture, and humidity (Calvet et al., 1998). This Jacob’s model (or the A-gs model) proposed by Goudriaan et al. (1985) accounts for the effect of atmospheric CO_2 concentration on the stomatal aperture, and the leaf net assimilation of CO_2 is simulated using the physiological parameterization of the stomatal conductance. This approach presented in Jacobs (1994) was further modified in Jacobs et al. (1996) to account for the relationship between soil water stress and CO_2 assimilation, and it is this revision that was employed in ISBA-A-gs (Calvet et al., 1998).

The ISBA model (plus all its revisions) is integrated within SURFEX. SURFEX in French (SURFace EXternalisée) is a land and ocean surface platform (http://www.umr-cnrm.fr/surfex/) built by météo France in collaboration with the scientific community (Masson et al., 2013). In addition to ISBA, SURFEX contains other scientific models e.g., the Town Energy Budget (TEB) for the estimation of surface fluxes in urban areas, FLAKE for freshwater lakes etc. With consideration to the heterogeneities of land surfaces, the ISBA-A-gs model can be split into 19 tiles based on the plant functioning type, and the surface cover (see Table 1 in Boone et al. (2017)). Also, ISBA-A-gs is a single source model, and the energy and water balance are estimated using the same pixel. In the following section, full descriptions of the governing equations relevant to this study would be provided. In addition, due to the fact that the past decades has brought higher computational resources, Table 2.7 summarizes some improvements and additional parameterizations that the original ISBA model has benefited from, and a few of these would be discussed in the later sections.

Table 2.7: Improvements and additional parameterization witnessed by the standard ISBA.

Improved component	Parameterization	References	Related cost
Soil	2-L force restore	Noilhan and Planton, (1989) Mahfouf and Noilhan (1996)	Original
	3-L force restore	Boone et al. (1999)	Requires poorly known parameters
	Explicit multilayer scheme	Boone (2000) Decharme et al. (2011, 2016)	Requires many soil parameters at each layer
Vegetation and carbon	Evapotranspiration	Noilhan and Planton (1989)	Original
	Photosynthesis and C fluxes	Calvet et al. (1998)	Computing time increase by 45%
Energy scheme	Dual-source scheme	Boone et al. (2017)	Requires more parameters

2.3.1.1 The surface energy balance

As previously mentioned, ISBA-A-gs considers a single energy balance for the whole soil-vegetation system, and so, land-atmosphere transfers are related to the mean values of the surface temperature and soil moisture. The energy fluxes, Rn, H, and LE (all in W m^{-2}) are computed using Equations (2.15a-e); whereas the ground heat flux is estimated as the residual of the energy balance. With regards to LE, this term is estimated as the sum of the evapotranspiration from the canopy (Ev), and the evaporation from the soil surface (Es). Note that Ev is a combination of the plant's transpiration (Tr), and the water evaporated from the canopy covers after interception (Ei).

$$R_n = R_G(1-\propto) + \varepsilon(R_A - \sigma_{SB}\, TS^4) \tag{2.15a}$$

$$H = \rho_a c_p C_H WS\,(TS - TA) \tag{2.15b}$$

$$Ev = f_c \rho_a C_H WS h_v (q_{sat(TS)} - q_a) \tag{2.15c}$$

$$Es = [(1 - f_c)\rho_a C_H WS]\,[h_u q_{sat(TS)} - q_a] \tag{2.15d}$$

Where σ_{SB} is the Stefan-Boltzmann's constant (W m^{-2} K^{-4}), and R_A is the atmospheric infrared radiation in W m^{-2} reduced by the emitted infrared radiation. Also, $\propto$ is the surface albedo, and ε is the surface emissivity. In this study, the emissivities of the bare soil and vegetation were set to 0.90 and 0.97, respectively based on Jin and Liang (2006), while the total surface albedo, derived from the instantaneous ratio of up-welling radiation to down-welling radiation between 10h 30 and 15h in order to avoid low solar zenith angles (Kalma and Stanhill, 1969) was partitioned into $\propto_{soil}$ and $\propto_{veg}$ as a function of the vegetation coverage using $\propto = [f_c \propto_{veg} + (1 - f_c) \propto_{soil}]$ from Meng (2020).

Furthermore, C_H, and f_c stand for the drag coefficient, and the vegetation fraction cover, respectively. This study estimated f_c as a function of the leaf area index (Equation 2.15e), and no calibration was performed to adjust its coefficient (Liang, 2003).

$$f_c = 1 - e^{(-0.9LAI)} \quad \text{for maize and wheat} \tag{2.15e}$$

Also, q_a is the atmospheric specific humidity (kg kg^{-1}), and $q_{sat(TS)}$ is the specific humidity at saturation at TS. Finally, h_u, which is a function of the superficial soil moisture is the relative humidity at the ground surface; while h_v is the Halstead coefficient that is derived from Equation 2.15f using the concepts of aerodynamic resistance (R_a in s^{-1}) and surface resistance (R_s in s^{-1}) (Noilhan and Planton, 1989).

$$h_v = \frac{(1-\delta)R_a}{(R_a + R_s)} + \delta \tag{2.15f}$$

where δ is the fraction of the vegetation covered by intercepted water (see Jarvis, 1976). R_a is equal to $(C_H WS)^{-1}$, and R_s depends on the following four atmospheric factors whose values range between 0 and 1 (see Equations 2.15g – 2.15l):

(i) F_1: this measures the influence of PAR on the stomatal resistance of plants (Sellers et al., 1986; Dickinson, 1984).

(ii) F_2: this represents the effect of water stress on R_s (Thompson et al., 1981).

(iii) F_3: introduces the impact of atmospheric vapor pressure deficit on stomatal resistance (Jarvis, 1976; Sellers et al., 1986).

(iv) F_4**:** this factor represents the effect of air temperature on stomatal opening and surface resistance. These formulations as used in the ISBA-A-gs model are presented below:

$$R_s = \frac{R_{smin}}{(LAI\ F_1\ F_2\ F_3\ F_4)} \tag{2.15g}$$

$$F_1 = \frac{f + R_{smin}/R_{smax}}{(1+f)} \tag{2.15h}$$

$$F_2 = \frac{(w_2 - w_{wilt})}{w_{fc} - w_{wilt}} \quad if\ w_{wilt} \leq w_2 \leq w_{fc} \tag{2.15i}$$

$$F_3 = 1 - \gamma_{FE}(q_{sat(TS)} - q_a) \tag{2.15j}$$

$$F_4 = 1 - 1.6 \times 10^{-3}(298 - TA)^2 \tag{2.15k}$$

$$f = 0.55\ (\frac{R_G}{R_{GL}})(\frac{2}{LAI}) \tag{2.15l}$$

R_{smax} is arbitrarily fixed to 5000 s m^{-1} (Jacquemin and Noilhan, 1990); and w_2, w_{wilt}, and w_{fc} are the volumetric water content in the root zone, at wilt point, and at the field capacity, respectively. Also, γ_{FE} is an empirical parameter dependent on the vegetation type (Jacquemin and Noilhan, 1990), and f is a dimensionless term that represents the active incoming radiation on the canopy- this is constrained by a species-dependent R_G value that is set to 100 W m^{-2} for crops in the ISBA-A-gs model. In addition, the representation of the intercepted water was formulated in Deardorff (1978), and the revised version of Dickinson (1984) was adopted in the ISBA-A-gs model. This evaporated water is treated as in Equation 2.15m.

$$\frac{dW_r}{dt} = f_c P - (E_V - Tr) - veg_{runoff} \tag{2.15m}$$

$$Tr = f_c\ \frac{(1-\delta)}{(R_a + R_s)}\ (q_{sat(TS)} - q_a) \tag{2.15n}$$

where P is the rate of precipitation at the top of the canopy, the term $(E_V - Tr)$ represents the direct evaporation from the canopy, and veg_{runoff} is the amount of water that drips off the canopy after interception; veg_{runoff} is zero until W_r exceeds W_{rmax}. W_{rmax} is the maximum interception capacity which is proportional to the leaf area index of the plant as shown in Equation 2.15o (Noilhan and Planton, 1989).

$$W_{rmax} = 0.2LAI\ (mm) \tag{2.15o}$$

2.3.1.2 Vertical transfer of water and energy within the soil

In ISBA-A-gs, these transfers can be represented in two major ways:

(i) The force restore method (FR): This approach was originally formulated by (Bhumralkar, 1975), and it solves the vertical transportation of heat and moisture within the soil layers in two ways: (a) the 2-L option (Mahfouf and Noilhan, 1996), and (b) the 3-L option (Boone et al., 1999). The 2-L approach considers only two soil layers- a superficial thin layer (~0.01 m), and a single bulky layer just underneath the first layer; whereas, the 3-L version, which is an improved version, has a third layer that distinguishes the root zone from the sub-root zone (see Figure 2.9).

(ii) The multi-layer diffusion method (DIF): As a result of the limitations of the FR option (see Decharme et al. (2011) for review), DIF was introduced to solve the heat and mass transfer equations using the Richards equation (Decharme et al., 2011). DIF discretizes the total soil depth into N layers (14 at least) for the representation of either the homogeneous or heterogeneous vertical root distribution (see Figure 2.9), and uses the classical one-dimensional Fourier law to describe the heat transfer within the soil layers. In this study, these soil transfers were computed using 8 layers (0.01, 0.05, 0.10, 0.30, 0.50, 1.0, 1.5, and 2.0 m), and the first 6 depths were chosen in accordance with the availability of *in-situ* measurements. At each layer, DIF estimates the soil water content (swc in m^{3} m^{-3}), the soil matric potential ($\emptyset_i$ in m), the hydraulic conductivity (K in m s^{-1}) using the Brooks-Corey model (1966), and the governing equations for heat transfer at the surface are presented below.

$$\frac{dT_S}{dt} = C_T[G - \frac{\bar{\lambda}_l}{\Delta\tilde{z}_l}(TS - T_2)] \qquad (2.15p)$$

$$\frac{dT_i}{dt} = \frac{1}{c_{gi}}\frac{1}{\Delta z_i}[\frac{\bar{\lambda}_{i-1}}{\Delta\tilde{z}_{i-1}}(T_{i-1} - T_i) - \frac{\bar{\lambda}_l}{\Delta\widetilde{z'_l}}(T_i - T_{i+1}) \quad \text{if } i = 2, \ldots. N \qquad (2.15q)$$

Where C_T (K m^{-2} J^{-1}) is the surface composite thermal inertia coefficient parameterized as the harmonic mean between the soil and the vegetation thermal inertia coefficients weighted by the vegetation fraction (see Equation 8 in Noilhan and Planton, 1989). T_2 (K) is the mean temperature value over one day, Δz_i (m) represents the thickness of layer i, and $\Delta\widetilde{z'_l}$ (m) is the distance between two consecutive layers. Also, c_{gi} (J m^{-3} K^{-1}) and $\bar{\lambda}_l$ (W m^{-1} K^{-1}) represent the total heat capacity of the soil, and the inverse-weighted arithmetic mean of the thermal conductivity of the soil between two consecutive layers, respectively. Similarly, the soil water transfer process is computed using the following:

$$\frac{dw_i}{dt} = \frac{1}{\Delta z_i}\left[-\overline{k_\iota}\left(\frac{\emptyset_i - \emptyset_2}{\Delta\tilde{z}_\iota + 1}\right) - \overline{v_\iota}\left(\frac{\emptyset_i - \emptyset_2}{\Delta\tilde{z}_\iota}\right) + \frac{S1}{\rho_w}\right] \tag{2.15r}$$

$$\frac{dw_i}{dt} = \frac{1}{\Delta z_i}\left[F_{i-1} - F_i + \frac{S_i}{\rho_w}\right] \tag{2.15s}$$

$$F_i = \overline{k_\iota}\left(\frac{\emptyset_i - \emptyset_{i+1}}{\Delta\tilde{z}_i} + 1\right) + \overline{v_\iota}\left(\frac{\emptyset_i - \emptyset_i + 1}{\Delta\tilde{z}_i}\right)] \tag{2.15t}$$

where S_i (kg m^{-2} s^{-1}) is the soil water sink/source term, $\overline{k_\iota}$ (m s^{-1}) is the geometric mean over two consecutive nodes of the soil hydraulic conductivity, and v_i (m s^{-1}) is the isothermal vapor conductivity values (Decharme et al., 2011).

In this study, the soil moisture and soil temperature profiles were represented with the recent multi-layer soil diffusion scheme. We opted for this option because certain studies have shown it to outperform the FR method over croplands (Garrigues et al., 2017), and fallow fields (Decharme et al., 2011). Even many new generation LSMs are adopting it because of its suitability in the reproduction of long-term evolution of soil moisture and temperature. More importantly, sophisticated schemes like DIF allow better representation of processes e.g., the vertical distribution of the root profile (Braud et al., 2005), capillary processes (Anyah et al., 2008) etc. In addition, although the FR option provides us with a very simple framework, the availability of many discrete soil layers over the total soil column (in DIF) permits the consideration of the heterogeneity of a soil's vertical structure- this presents a more realistic representation. For further information, readers are directed to Decharme et al. (2011) and Boone et al. (1999) for the pros and cons of the DIF scheme respectively.

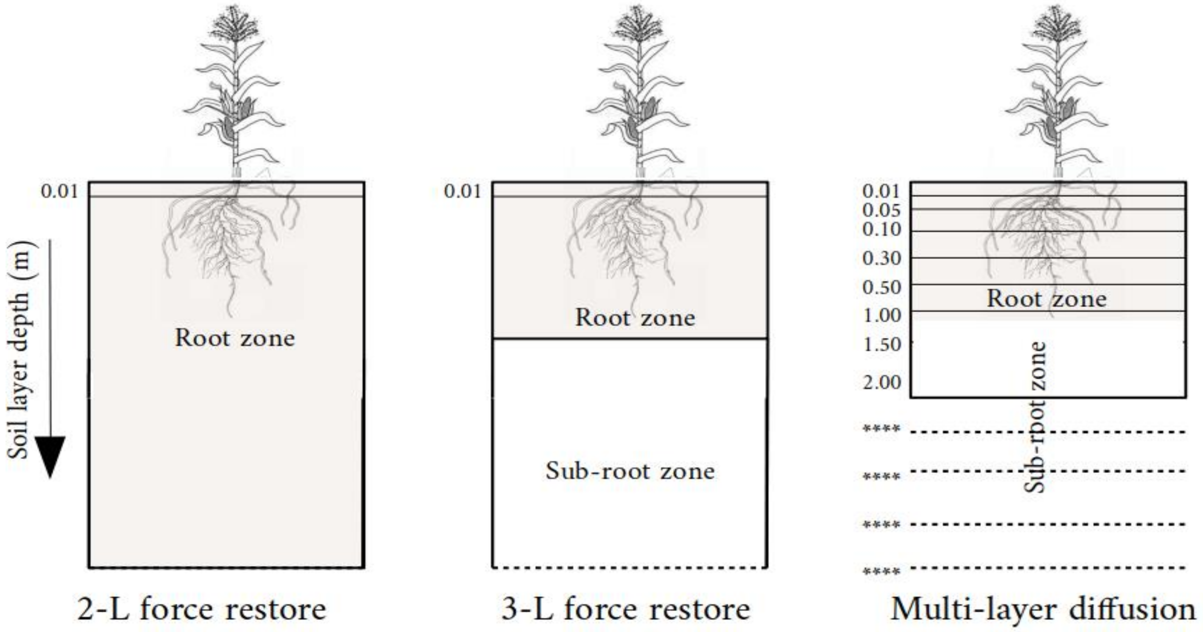

Figure 2.9: Schematic representation of the soil grid configurations available to ISBA-A-gs. (Source: Boone et al. (1999), modified).

2.3.1.3 Description of the carbon processes

Carbon assimilation by photosynthesis

(i) Within ISBA-A-gs, the purpose of the A-gs module is primarily to simulate the leaf stomatal conductance, and the net assimilation of CO_2 at a leaf level from the expression in Equation 2.16a (see section 3.2.3 of Jacobs, 1994 for the step by step formulation).

$$g_s = g_c + 1.6\,[A_n - A_{min}\left(\frac{D_s}{D_{max}}\,\frac{A_n+R_d}{A_m+R_d}\right) + R_d\left(1 - \frac{A_n+R_d}{A_m+R_d}\right)]/(C_s - C_i) \qquad (2.16a)$$

where g_c (m s^{-1}) is the cuticular conductance, A_n (mgCO_2 m^{-2} s^{-1}) is the leaf net assimilation, and A_{min} (mgCO_2 m^{-2} s^{-1}) is the residual photosynthetic rate. Also, g_s is highly sensitive to the specific humidity deficit (D_s in g kg^{-1}), the maximum air saturation deficit (D_{max} in kg kg^{-1}), the dark respiration (R_d in mgCO_2 m^{-2} s^{-1} which is 'A_m/9'), and the CO_2 concentration inside the leaf (C_i in ppm), and at the surface of the leaf (C_s in ppm). Also, A_n and A_{min} are represented as:

$$A_n = (A_{min} + R_d)\left[1 - e^{\left\{\frac{\varepsilon I_a}{((A_m + R_d))}\right\}}\right] - R_d \qquad (2.16b)$$

$$A_m = A_{m,max}\left[1 - e^{\left\{\frac{-g_m(C_i - \Gamma)}{((A_{m,max}))}\right\}}\right] \qquad (2.16c)$$

$$A_{min} = g_m \left[\frac{(g_s C_s + g_m \Gamma)}{(g_c + g_m)} - \Gamma\right] \tag{2.16d}$$

where A_m (mgCO_2 m^{-2} s^{-1}), ε (mg J^{-1}), I_a (nm), g_m (m s^{-1}), and Γ (ppm) represent the net assimilation, the quantum efficiency, the amount of PAR that gets to the leaf, the mesophyll conductance, and the CO_2 compensation concentration, respectively. Furthermore, ε is obtained from the product of ε_o and $(C_i - \Gamma)/(C_i + 2\Gamma)$, where ε_o is the maximum quantum use efficiency (see Table A1 of Gibelin et. al. (2006) for the standard values).

(ii) Afterwards, in order to couple this A-gs model with the vegetation model, the leaf stomatal conductance was scaled, and extrapolated over the whole canopy (Jacobs, 1994). Here, for simplicity, the working assumption is that the leaves are homogeneous and uniformly distributed vertically, i.e., TS, D_s, and C_s do not vary within the canopy, but PAR does. Hence, the photosynthetic rate of the entire canopy (A_{nl}) and the integrated canopy conductance (g_{sl}) can be calculated from the following equations.

$$A_{nl} = LAI \int_0^1 A_n \, d(\frac{z}{h}) \tag{2.16e}$$

$$g_{sl} = LAI \int_0^1 g_s \, d(\frac{z}{h}) \tag{2.16f}$$

where h (m) is the canopy height, and z (m) is the distance to the ground. For a detailed estimation of A_{nl} and g_{sl}, readers are directed to the Appendix B of Calvet et al. (1998). Some important parameters (and their standard values) in the A-gs photosynthesis model are also detailed in Table 2 of Calvet et al. (1998) for C3 and C4 crops.

Ecosystem respiration

The ecosystem respiration ($RECO$) is composed of RAa, RAb, and RHb (see Some general definitions).Where RAb and RHb are aggregated as the soil respiration (SR). For SR, this study adopts the parameterization of Norman et al. (1992). The empirical Equation 2.16g was fitted by Norman et al. (1992) to 900 observations of soil CO_2 fluxes; this was based on the chamber measurements taken during the 1989 FIFE experiment over three grassland sites in Kansas. As observed, this parameterization considers the influence of soil moisture and soil temperature; these are major factors that control the rate of CO_2 production in the soil (Singh et al., 1977).

$$SR = (0.135 + 0.054LAI) swc_{10} [e^{[0.069(T_{S10} - 25)]} \tag{2.16g}$$

From the above equation, the first free parameter '0.135' represents the minimum soil surface CO_2 flux, the second coefficient '0.054' highlights the dynamism of the leaf area index, and the factor '0.069' is the temperature coefficient also referred as Q10 = exp (10*0.069), then the reference soil temperature is 25 °C. In addition, swc_{10} (in %) and T_{s10} (in °C) are the soil water content and soil temperature at 10 cm depth (Norman et al., 1992).

According to the formulation of Gibelin et al. (2008), the second component of $RECO$, RAa, is estimated in the following sequence: (i) The dark respiration flux that was estimated in section 2.3.3.2 is integrated over the whole canopy to become Equation 2.16h. Afterwards, Rdc is averaged over 24h and converted into kg m^{-2} d^{-1} to obtain the respiration from the leaf biomass in Equation 2.16i.

$$R_{dc} = LAIR_d \tag{2.16h}$$

$$RAa = \sum_{24h} 10^{-6} \frac{M_C}{P_C M_{CO_2}} R_{dc} dt \tag{2.16i}$$

Where M_C and M_{CO_2} are the molecular weights of carbon and CO_2 (12 and 44 g mol^{-1}) respectively. Also, dt is the time step of the model in seconds, and P_C is the proportion of carbon in the dry plant biomass. In ISBA-A-gs, a constant P_C value of 40% is assumed (Calvet et al., 1998). The processes described above are formulated in the same manner for C3 and C4 crops, but some input parameters differ.

2.3.2 ISBA-A-gs-MEB

The composite soil-vegetation scheme (ISBA-Ag-s) was updated into the Multi-Energy Balance (ISBA-A-gs-MEB) by Boone et al. (2017). The rationale behind this update includes the necessity to explicitly distinguish the canopy from the soil (see Figure 2.10). Although single-source models like ISBA-Ag-s are simple, and founded on physically sound basis, certain experimental studies (see Kustas et al. (1999), and Li et al. (2009) for a review) have pointed out their unsuitability over sparse and heterogeneous surfaces. ISBA-A-gs-MEB, hereafter called ISBA-MEB, marks the transformation into an explicit multi-source scheme.

Initially, ISBA-MEB was designed to explicitly simulate a different energy budget for different components of a forested area by distinguishing the temperature of the snowpack covering the soil, from that of the soil, and of the overlying vegetation. Thereafter, the applicability of this model was extended to the under-story litter layer processes of forest regions (Napoly et al., 2017). For a schematic representation of the resistance network for the energy and water fluxes; (see Figure 1 in Boone et al., 2017). Also, readers are referred to Napoly et al. (2017) for the description and the governing equations of the litter scheme in ISBA-MEB; this layer was not activated in this study because the litter found at our study sites is negligible.

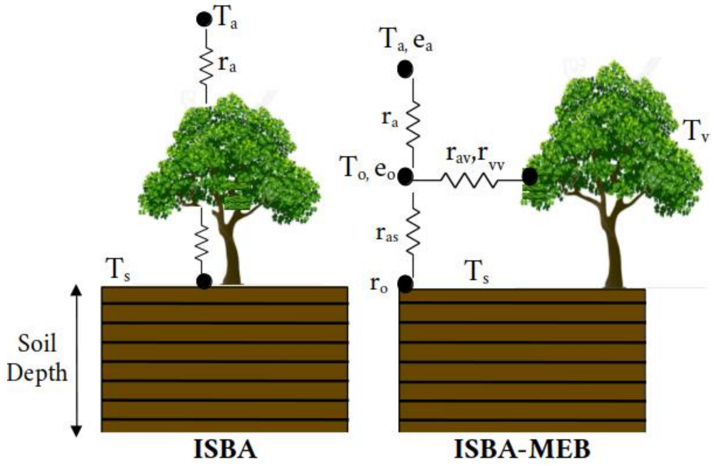

Figure 2.10: Comparative description of the single-source configuration (ISBA), and the dual-source configuration (ISBA-MEB).

2.3.2.1 The surface energy balance

Within ISBA-MEB, the energy budget components are aggregates of the canopy budget (subscript v), and that of the underlying ground (subscript g), while subscript 1 indicates the uppermost layer. The processes are described as follows:

$$R_n = R_{nv} + R_{ng} \tag{2.17a}$$

$$R_{nv} = C_v \frac{dT_v}{dt} + H_v + LE_v \tag{2.17b}$$

$$R_{ng} = C_{g,1} \frac{dT_{g,1}}{dt} + H_g + LE_g + G_{g,1} - L_f \emptyset_{g,1} \tag{2.17c}$$

Where C (J m^{-2} K^{-1}), T (K), L_f (J kg^{-1}), and $\emptyset$ (kg m^{-2} s^{-1}) represent the effective heat capacity, the temperature, the latent heat of fusion, and the phase change term, respectively. The sensible heat fluxes are defined as H_v: representing the heat flux between the vegetation and the canopy air space, H_g: the flux between the ground and the overlying canopy, H_c: the heat flux between the free atmosphere and the canopy space.

$$H_v = \rho_a \frac{(\mp_v - \mp_c)}{R_{av-c}} \tag{2.17d}$$

$$H_g = \rho_a \frac{(\mp_g - \mp_c)}{R_{ag-a}} \tag{2.17e}$$

$$H_c = \rho_a \frac{(\mp_c - \mp_a)}{R_{ac-a}} \tag{2.17f}$$

Here, R_{av-c}, R_{ag-a}, and R_{ac-a} represent the aerodynamic resistance between the vegetation and the canopy air space, between the ground and the canopy air space, and between the canopy air space and the atmosphere respectively (All *Rs* are in s^{-1}). For the formulation of these turbulent resistances, see Section 2.6 in Boone et al. 2017, and also Figure 1 in this reference for the schematic representation. $\mp$ (in J kg^{-1}) is a thermodynamic variable that is linearly related to the temperature of the sources as $\mp_x = B_x + A_x T_x$; where T_x corresponds to one of the surface temperatures of either the canopy, ground, or air. The coefficients A_x and B_x depend on the atmospheric variable in the turbulent diffusion scheme, and they are usually defined to cast $\mp$ in the form of dry static energy, or potential temperature, and are determined by the atmospheric model in coupled mode (see Appendix A of Boone et al. 2017). Similarly, the computation of the latent heat flux is consistent with the above, and it is represented as follows:

$$LE_v = \rho_a h_{sv} \frac{q_{satv} - q_c}{R_{av-c}} \tag{2.17g}$$

$$LE_g = \rho_a \frac{(q_g - q_c)}{R_{ag-c}} \tag{2.17h}$$

$$LE_c = \rho_a \frac{(q_c - q_a)}{R_{ac-a}} \tag{2.17i}$$

where q_{satv}, q_c, q_a and q_g (all in kg kg^{-1}) represent the vegetation specific humidity (SH) at saturation, SH of the canopy air, SH of the atmosphere, and the effective ground SH, respectively. On the other hand, G is modeled using the Fourier's law, and it is written as follows:

$$G_{g,1} = \frac{2(T_{g,1} - T_{g,2})}{[\left(\frac{\Delta z_{g,1}}{\lambda_{g,1}}\right) + (\left(\frac{\Delta z_{g,2}}{\lambda_{g,2}}\right))]} \tag{2.17j}$$

Where λ_g is the soil's thermal conductivity, which depends on the texture of the soil, its organic content, the soil-water status, and also on the thermal properties of the soil (Decharme et al., 2016; Napoly et al., 2016; Boone et al., 2017). For the soil-water-heat transfers, the three aforementioned schemes are available within ISBA-MEB. Similarly, the interception reservoir W_r and photosynthesis processes are represented the same way as in ISBA-A-gs (see Sections 2.3.1.1 and 2.3.1.3, respectively).

2.3.2.2 Additional parameterization

ISBA-MEB uses the absorption coefficient (τ_{LW}) to calculate the transmission of the longwave radiation through the vegetation (Napoly et al., 2020). This coefficient defines the canopy emission into the soil and back to the atmosphere, and it is expressed as follows:

$$\sigma_{LW} = 1 - e^{(-\tau_{LW} LAI)} \tag{2.17k}$$

The value of τ_{LW} varies between 0 and 1, and an increase in τ_{LW} signifies a decrease in the canopy transmission, and an increase in the emitted longwave radiation; while a τ_{LW} of 1 means that there is neither absorption, nor reflection by the canopy (Boone et al., 2017). This factor is required in the representation of the net longwave radiation of the ground, and of the vegetation canopy (see Equations (E2a-E2l), and Equations (E5a and E5c) in Boone et al. (2017).

Similarly, the leaf width parameter ($Leaf_w$) was included in the ISBA-MEB model for the parameterization of the aerodynamic conductance (R_{avg-c}) between the canopy and the surrounding air space; where:

$$R_{avg-c} = (g_{av} + g_{av}^{*})^{-1} \tag{2.17l}$$

The parameterization of the bulk canopy aerodynamic conductance (g_{av}) between the canopy and the canopy air is based on Choudhury and Monteith (1988), and it is defined as

$$g_{av} = \left(\frac{2LAI \propto_{av}}{\emptyset_v'}\right)\left(\frac{u_{hv}}{Leaf_w}\right)^{\frac{1}{2}}\left[1 - e^{\left(\frac{\emptyset_v'}{2}\right)}\right] \tag{2.17m}$$

Where u_{hv} in m s^{-1} is the wind speed at the top of the canopy, $\propto_{av}$ (in m s$^{-1/2}$) is the canopy conductance scale factor, and $\emptyset_v'$ is the attenuation coefficient for wind (Choudhury and Monteith, 1988). Finally, g_{av}^{*}, which is the conductance accounting for the free convection correction during unstable conditions from Sellers et al. (1986) is expressed as:

$$g_{av}^{*} = \left(\frac{LAI}{0.89\times10^{3}}\right)\left(\frac{T_v - T_c}{Leaf_w}\right)^{0.25} \qquad (T_v \geq T_c) \tag{2.17n}$$

Some recommended values of these parameters are defined in Table 3 of Boone et al. (2017). In the subsequent sections of this thesis, ISBA-A-gs would be referenced as ISBA for aesthetics.

2.4 Forcing information

Given the scarcity of field observations to force the surface state variables, LSMs are often used in "online mode" meaning that such models are coupled with atmospheric models. In the set-up of this current study, the "offline" version of ISBA was forced by *in-situ* atmospheric parameters. Four sets of information were required as inputs:

(i) The first set consists of biophysical information and others (e.g., vegetation and soil albedo, vegetation and soil emissivity, LAI, and vegetation height (h_{veg} in m)). These variables were prescribed on a 10-days average. In addition, the vegetation fraction cover (Equation 2.15e) and the roughness length of vegetation (Equation 2.18a) were computed as a function of the leaf area, and vegetation height, respectively.

$$z_o = 0.1h_{veg} \tag{2.18a}$$

Although, z_o does not characterize only vegetation, but every existing roughness element over the surface; it is quite an important parameter in flux simulation. Concerning Equations 2.15e and 2.18a, the coefficients were adopted from Liang, 2003 for f_c, and Wallace & Hobbs, 2006 for z_o for low cultural crops. No calibration was performed to adjust these values. This is consistent with the evaluation of the model's potential with minimal calibration. Table 2.8 provides some values and ranges of some vegetation characteristics used in this study.

Table 2.8: Values and ranges of the input variables for ISBA and ISBA-MEB.

Variable	Range	Reference
LAI	0 – 6.8	Measured
f_C	0 – 1.0	Estimated
h_{veg}	0 – 3	Measured
$\propto_{soil}$	0.12 – 0.16	Estimated
$\propto_{veg}$	0.17 – 0.28	Estimated

For each crop year, this study kept $\propto_{soil}$, $\propto_{veg}$, and the emissivities constant, that is independent of the soil moisture status, and vegetation development.

(ii) The second parameter set includes the meteorological variables at a reference height; air temperature (K), relative humidity (kg kg^{-1}), wind speed (m s^{-1}) and direction (°), air pressure (kPa), direct shortwave radiation (W m^{-2}), longwave radiation (W m^{-2}), and rainfall (kg m^{-2} s^{-1}). This reference height is the measurement height of the atmospheric forcings of the domain (in our case, 3.65 in FR-Lam).

(iii) The third parameter set consists of the site information; geographical coordinates, and the altitude of the domain. Concerning root distribution in maize, 87% of the root density was allocated to the depths between 0 cm and 50 cm, and the remaining percentage to the deeper layers (Jackson et al., 1996). For wheat, the root parameterization was set according to Garrigues et al. (2019), where for C3 crops, root_lin and root_ext are 0.05 and 0.961, respectively- these represent the extinction coefficient of the root, and the proportion of homogeneous root distribution in the root profile respectively. The total root depth of both crops was set to 1.5 m; this is expected to cover all the possible maximums found in the southwest of France (Battude et al., 2017). Then, this was constrained by extending the total soil column to 2 m. Finally, we explicitly represented the succession of crops and inter-crops by using the suitable patch for C3 (7), and C4 (8) crops.

2.5 Model implementation

Soil hydraulic parameters

Originally, SURFEX uses the Brooks and Corey (1966) model. However, as observed from the initial experimental runs, and even from the study of Garrigues et al. (2019), a significant underestimation of the *ET* term is obtained when the soil parameters estimated from the default pedotransfer function was used. In this study, to permit the vertical heterogeneous representation of the soil profile, these soil parameters were derived by prescribing known *in-situ* fractions of clay and sand for the first 6 layers under consideration using the Clapp and Hornberger (1978) pedotransfer function in the model. Table 2.9 presents a summary of the hydraulic properties used during the sap flow period. For the initial boundary condition, the simulations were initialized using *in-situ* soil water and temperature values across the considered soil depths.

Table 2.9: Soil texture, and soil hydraulic properties for the maize 2015 (only the sap flow period)

Layer (cm)	Clay (%)	Sand (%)	K (m s^{-1})	$\emptyset$ (m)	BCOEF	WP (m^3 m-3)	FC (m^3 m^{-3})	SAT (m^3 m^{-3})
0	51	12	0.0000001081	-0.5551	10.488	0.1052	0.2520	0.2913
5	52	11	0.0000001067	-0.5665	10.625	0.1062	0.2550	0.2924
10	53	10	0.0000001057	-0.5781	10.762	0.1152	0.2556	0.2933
30	50	11	0.0000001088	-0.5665	10.351	0.1045	0.2420	0.2933
50	48	11	0.0000001120	-0.5665	10.077	0.1033	0.2289	0.4222

$\emptyset$ is the soil matric potential, K is the hydraulic conductivity, and BCOEF is an empirical parameter that depends strongly on the soil texture (see Clapp and Hornberger, 1978).

Water table relaxation

By default, the multi-layer diffusion scheme provides a water table depth that the model uses as a low boundary condition for the soil moisture column; however, due to the proximity of FR-Lam to the Touch river, the depth computed by the model was too far below to account for the capillary processes. Consequently, as was observed from the preliminary runs, there was a strong underestimation of the volumetric water content, and of course evapotranspiration. The solution devised in Decharme et al. (2019) which uses a simple Newtonian relaxation approach to permit the upward movement of capillary fluxes was adapted by Aaron Boone to our study site, and this method is as follows:

(i) Add a source term to the water mass balance equation as follows:

$$\frac{dw}{dt} = \frac{dF}{dz} - S + C_{\tau}(w_{sat} - w) \tag{2.19a}$$

where w is the volumetric water content (m^3 m^{-3}), F is the vertical exchange flux computed using Darcy's law, S is a sink, that is the water lost through evaporation and root water extraction for transpiration, and z is the soil depth. The last term on the RHS of Equation 2.19a is the Newtonian relaxation term that nudges w towards w_{sat} when $C_{\tau} > 0$ (C_{τ} is in s^{-1}). For layer i, Equation 2.19a becomes

$$\frac{\Delta w_i}{\Delta t} = \frac{F_i - F_{i-1}}{\Delta z_i} - S_i + C_{\tau,i}(w_{sat,i} - w_i) \tag{2.19b}$$

where z_i is the depth of the bottom layer i, z_{i-1} represents the top of the layer i, and so, $\Delta z_i = z_i - z_{i-1}$ $(z_0 = 0)$. Then,

$$C_{\tau,i} = \frac{1}{\tau_{zi}} max\left\{0, \min[1, \frac{z_i - z_t}{z_i - z_{i-1}}]\right\} \tag{2.19c}$$

When $C_{\tau,i} > 0$, it means the water table is within or above the layer i (i.e., $z_t < z_i$). When $z_t > z_N$ (the water table depth is below the default level prescribed by the model, z_N), no water is added to the soil. To ensure a continuous transition to saturated conditions, Equation 2.19c uses a linear interpolation. The input variable provided locally to this water relaxation procedure is an ASCII file of the *in-situ* water table depth (in m), which must have values for all the time steps of the model (i.e., if xstep = 300s, time step per day becomes 288), where xstep is the surface time step.

2.6 Definition of statistical metrics

In this study, in comparison with field measurements, the performance of the ISBA and ISBA-MEB model were assessed using the Root-Mean-Square Error (RMSE), the coefficient of determination (R^2), and the Mean Absolute Error (MAE).

(i) RMSE: represents the root mean square deviation between the measured and simulated values.

(ii) R^2: expresses the proportion of variance in the simulated variable that is predicted from the observed.

(iii) MAE: the average magnitude of errors between the observation and simulated values.

$$RMSE = \frac{\sqrt{\sum_i^N (sim_i - obs_i)^2}}{N} \tag{2.20a}$$

$$R^2 = \frac{n\sum_{i=1}^N (sim_i obs_i) - \left(\sum_i^N sim_i\right)\left(\sum_i^N obs_i\right)}{\sqrt{\left[N\sum_{i=1}^N sim_i^2 - \left(\sum_{i=1}^N sim_i\right)^2\right]}\sqrt{\left[N\sum_{i=1}^N obs_i^2 - \left(\sum_{i=1}^N obs_i\right)^2\right]}} \tag{2.20b}$$

$$MAE = \frac{\sum_{i=1}^N |sim_i - obs_i|}{N} \tag{2.20c}$$

Where sim and obs are the simulated and observed values respectively, N is the size of the observation, and *i* represents the index of a given variable.

Some main ideas of this chapter

- ISBA-A-gs is birthed following the coupling of the standard ISBA model with the photosynthesis A-gs model.
- ISBA-A-gs is a single-source model that aggregates the properties of the vegetation and soil, and it was revised into the multi-source ISBA-A-gs-MEB that explicitly estimates the energy budget of the vegetation and soil separately.
- For ease, ISBA-A-gs and ISBA-A-gs-MEB would be referenced as ISBA and ISBA-MEB, respectively for aesthetics.
- In the representation of transfers within the soil, this study employed the multi-layer diffusion scheme (DIF); DIF solves the vertical transfer of water and energy within the soil by discretizing the soil into several layers.
- The DIF scheme is an improvement of the force restore approaches that represent the whole soil column by only 2-3 layers.

Some general definitions

This section provides a refresher of some major terms used in this study that would be recalled often.

1. Energy budget

(i) Net radiation (Rn): Is the balance between the incoming and outgoing solar radiation. It is the driver of the Earth's climate.

(ii) Latent heat flux (LE): This is the flux associated with evaporation, condensation, and transpiration of water from land surfaces (including vegetation).

(iii) Sensible heat flux (H): This the convective flux associated with the exchange of heat between the atmosphere and land surfaces.

(iv) Ground heat flux (G): This is the amount of heat transferred into or out of the soil substrate by conduction.

2. Water budget

(i) Evapotranspiration (ET): This is the total amount of water lost to the atmosphere by a land surface, and its constituents are:

   a. Transpiration (Tr): This is the water vapor released from plants as they transpire.
   b. Evaporation (Es): This is the water lost from the surface of a bare soil.
   c. Interception (Ei): This is the water evaporated from the surface of the canopy after interception.

(ii) Change in soil water storage (ΔS): This refers to the fluctuation in the water available at the different soil layers over a certain period.

(iii) Drainage (D): This is the water that is transported into the lower depths of the soil, often beyond plant's root.

3. Carbon budget

(i) Gross primary production (GPP): This is the amount of carbon fixed by the plant during photosynthesis.

(ii) Ecosystem respiration ($RECO$): This is a measure of the total respiration within the ecosystem, and this can be decomposed into:

   a. Above-ground autotrophic respiration (RAa): This is the plant's respiration through the leaves and stems via the stomates and lenticels.
   b. Below-ground autotrophic respiration (RAb): This refers to the respiration that occurs within the root systems.

c. Below-ground heterotrophic respiration (RHb): This is the respiration of the soil's biota.

Chapter 3: Surface energy balance and flux partitioning of annual crops in southwestern France

The results presented in this chapter are published in the following paper:

Dare-Idowu O., Brut A., Cuxart J., Tallec T., Rivalland V., Zawilski B., Ceschia E., Jarlan J.: **Surface energy balance and flux partitioning of annual crops in southwestern France**, Agricultural and Forest Meteorology, Volumes 308–309, 2021, 108529, ISSN 0168-1923, https://doi.org/10.1016/j.agrformet.2021.108529.

3.1 Introduction

The non-closure of the energy balance is the norm rather than an exception, especially over highly dynamic croplands. Given the critical role that croplands play in the climate system, and the need to understand the implications of the quality of eddy covariance measurements, the nature of this gap must be understood. Hence, qualitative, and quantitative analyses must be performed in order to understand the non-closure of the surface energy balance as a function of surface characteristics (e.g., crop type and state of plot), and atmospheric properties (e.g., climatic variables and turbulence statistics). This study analyzed a unique database of EC measurements spanning from 2005 to 2015.

3.2 Methodology

3.2.1 Surface state categorization

In the first part, the database is classified based on the surface state (SS) of the plot (see Figure 3.1 for the pictorial representation of these surface states). The description of the surface states are as follows: (i) Low crops run from 2 weeks after seed germination up until the crop height is less than or equal to $h/2$; where h is the maximum height attained by the crop, (ii) Developed crops are taken from $h/2$ until the initiation of senescence, (iii) Senescent crops run from the end of a developed crop phase up until harvest- maize is an exception because the farmer harvests it green for silage, (iv) Post harvest phase comprises of periods in the presence of harvest residues i.e., between the day of harvest, and the beginning of soil work, (v) Bare soil (or smooth soil) periods represent the seedbed preparation state for the next planting season, (vi) Large clods are bare, big clumped-soils resulting from deep tillage. Table 3.1 presents the relevant climatic parameters corresponding to each surface state.

Large Clods (LC) Smooth Soil (SBS) Low Wheat (LW) Developed wheat (DW) Senescence wheat (Senc) After wheat harvest (AWH)

Figure 3.1: Pictorial representation of the surface states.

Table 3.1: Surface state classification and label (in parenthesis), number of valid data points in 30-mins resolution (Nos), and the corresponding climatic conditions (total rainfall + irrigation (P in mm), and averaged air temperature (TA in °C)) obtained over each surface state.

FR-Lam			**FR-Aur**		
Surface State (SS)	**Nos**	***TA* (*P*)**	**Label (SS)**	**Nos**	***TA* (*P*)**
Large clods (LC)	11266	7.5 (822)	Large clods (LC)	18	22 (14)
Smooth bare soil (SBS)	12130	10 (986)	Smooth bare soil (SBS)	3637	11.7 (2307)
Low wheat (LW)	16596	7.5 (1287)	Low wheat (LW)	10074	7.6 (589)
Developed wheat (DW)	14566	16.2 (950)	Developed wheat (DW)	11481	17 (759)
After wheat harvest (AWH)	15616	15.3 (832)	After wheat harvest (AWH)	2959	20.7 (302)
Low maize (LM)	7326	18 (377)	Low rapeseed (LR)	5595	7.3 (670)
Developed maize (DM)	11159	20 (1073)	Developed rapeseed (DR)	10096	15.1 (820)
After maize harvest (AMH)	5342	15 (356)	After rapeseed harvest (ARH)	3906	21 (241)

3.2.2 Selection of contrasting years

In the second part, a comparative analysis was conducted. A dry crop-season (low rainfall) and wet crop-season (high rainfall) of the same crop type was selected. Overall, contrasting pairs of three different crop types (maize, wheat, and rapeseed) covering 8 growing seasons over FR-Lam and FR-Aur were determined. We selected the wettest and driest crop-seasons with the best data quality, and the retained dataset are presented in Table 3.2. The rainfall difference between the contrasting crop-seasons ranged between 109 mm and 348 mm (irrigation inclusive) at both sites. Afterwards, the phenological stages of each crop-season were identified. Note that a crop season spanned from 2 weeks after sowing up until the bare soil phase, which is a seedbed preparatory practice for the next planting season.

Table 3.2: P in mm is the cumulative rainfall (+ irrigation for maize), and TA in °C is the mean air temperature over each crop season. The 'Timeline' column provides the duration of each crop season, while 'nos' represents the number of days for each timeline.

FR-Lam					**FR-Aur**				
	P	TA	Timeline	nos		P	TA	Timeline	nos
Maize dry	338	19.7	04/06/2008 - 30/11/2008	176	Rapeseed dry	425	13.4	18/11/2010 - 16/10/2011	328
Maize wet	447	18.6	11/05/2012 - 05/11/2012	176	Rapeseed wet	773	12.3	01/11/2012 - 30/09/2013	329
Wheat dry	564	12.6	09/11/2010 - 13/01/2012	426	Wheat dry	416	13.6	24/12/2005 - 05/09/2006	251
Wheat wet	693	11.7	31/10/2006 - 04/01/2008	426	Wheat wet	580	14.3	08/01/2014 - 19/09/2014	249

3.2.3 The sensible heat advection term

The estimation of the sensible heat advection (A_H) requires access to surface temperature maps at both sites. This is possible using satellite data and, in our study, the retrieved Landsat surface temperatures described in section 2.2.2.7 were used. These temperature values were used to estimate both the spatial, and the temporal temperature variability (ΔT in Equation 3.1) over FR-Lam and FR-Aur by adopting the methodology developed in Cuxart et al. (2016). Even though Landsat LST values were used instead of the ground LST (estimated from the Stefan-Boltzmann relationship), possible errors were minimized because only the temperature gradient was considered. Hence, in consideration to topography, and its horizontal thermal heterogeneity while minding uneven canopy strength and resistance, A_H, which is taken as a surface temperature heterogeneity proxy, was estimated using this expression:

$$A_H = \rho_a C_p z_{EC} WS \frac{\Delta T}{\Delta x} \tag{3.1}$$

where ρ_a is the air density, C_p is the specific heat capacity of air at constant pressure, z_{EC} is the measuring height of the EC, WS is the average wind speed of the prevailing wind during the estimation period, and $\frac{\Delta T}{\Delta x}$ is the temperature gradient (from the EC to the reference point whose position is a function of the direction of the prevailing wind) over a certain distance. This study explored the thermal advection at different spatial scales varying between 50 m and 400m because a larger scale would result in advection values that would be too small to be significant as highlighted in Cuxart et al. (2016), whereas, at a meter scale, the resulting values of A_H would be too large to be meaningful with respect to the missing energy. In addition, a scale too small would not be a representative of the site's footprint, and these processes might have been included in the turbulent sensible heat flux (García-Santos et al., 2018). Based on the simplification proposed in Cuxart et al. (2016), vertical advection was ignored in this study, and the latent heat advection term (A_{LE}) was unaddressed too since it would require a sophisticated network of moisture sensors which are currently unavailable at our study site.

3.3 Results

3.3.1 General considerations on SEB for both sites

Before investigating the SEB for the contrasting crop-seasons, we present some general results about the energy balance observed at both sites. In other words, this section and its related subsections are mainly descriptive, but they present a nice summary of the "SEB history" as well as a synthesis of the behavior of the flux partitioning according to the surface states at the sites.

3.3.1.1 Analysis of the ground heat flux

A subtle way to limit the "source area problem" mentioned in section 1.2 is via the installation of several heat flux plates for the measurement of G. A homogeneity test was carried out on the measurements from the HFPs to ensure a good representativeness of the G within the flux footprint for the SEB analysis. Figure 3.2(a and b) are the heat maps showing the time- and magnitude-variability of G in W m^{-2} between 2012 and 2015 at the FR-Lam and FR-Aur, respectively.

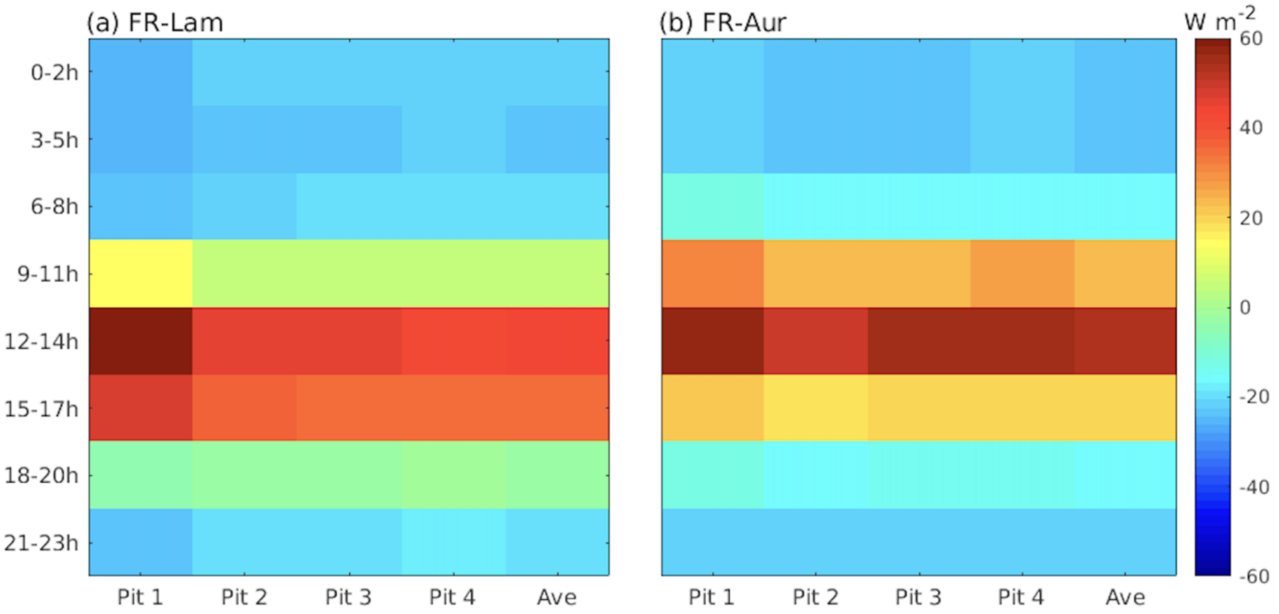

Figure 3.2: Mean variability of the ground heat flux (in W m^{-2}) over FR-Lam and FR-Aur between 2012 and 2015. Ave represents the average of measurement from Pits 2, 3, and 4.

Pit 1 corresponds to the permanent pit where the sensors are left untouched even when there is soil work (tillage, harvest, etc). As such, this pit is not a representative of the surface cover and the dynamism this plot experiences; also, it is located too close to the foot of the EC tower in an uncultivated area. Hence, its measurements are excluded from this study (i.e., from Ave), where Ave is the mean of pits 2, 3, and 4.

In FR-Lam, around mid-day, there exists an insignificant variation between pits 2, 3, and 4, while the value in pit 1 was about 27% larger than Ave. The larger magnitude in pit 1 is expected because there, the soil is more compact with decreased porosity- this in turn exerts a significant positive effect on the thermal conductivity. In the laboratory study of Abu-Hamdeh and Reeder, 2000, they found a noticeable increase in the thermal conductivity of many Jordanian soil types (including clay-loam) as the bulk density increased.

Unlike in FR-Lam, a slight variability is observed among the pits in FR-Aur. For example, between 12h and 14h, the percentage difference between the pits ranged between 2% to 14%. In contrast to the flatness in FR-Lam, FR-Aur is situated on a slopy field with a topography that results in a height difference of about 17.3 m. Consequently, this enhances the variability between soil depths, and according to Béziat et al., 2009, this difference could range from 5 m to about 12 m, thereby increasing the uncertainties of the ground heat flux. Nevertheless, Ave is considered spatially-representative enough to match the footprint of the other energy budget components.

3.3.1.2 How significant are the storage terms in the SEB?

Among the storage terms to be considered in this SEB study are G_{st}, S_{LE}, S_H and S_P (see section 2.2.2.4). Figure 3.3 presents the averaged diurnal storage terms over the study period. From this figure, it is apparent that G_{st} is the most significant term; its peak, which coincides with the midday is 180% and 185% larger than the average maximums of the other storage terms in FR-Lam and FR-Aur respectively. Furthermore, G_{st} in FR-Lam is about 20% larger (max = 36 W m^{-2}) than in FR-Aur (max = 29 W m^{-2}). These large values of G_{st} in FR-Lam could be due to (i) the soil properties: FR-Lam is mainly clayey; and according to some laboratory studies e.g., Abu-Hamdeh et al. (2003), specific and volumetric heat capacities are higher in clay soil than in other soil types even when the same moisture content and bulk density is maintained, (ii) fertilization: organic and mineral fertilization as generally applied in FR-Lam, this improves the soil's thermal properties (Sauer et al., 2005), (iii) topography: the slope in FR-Aur introduces large uncertainties in the measurements as previously mentioned, (iv) soil moisture: due to the proximity of the Touch river to FR-Lam, and its frequent irrigation, the soil water status of this plot improves the thermal conductivity of the soil as observed in the experimental study of Abu-Hamdeh and Reeder, (2000).

The trend in G_{st} and S_p is characterized by a gradual increase in the early morning, reaching its peak in the afternoon, and falling to its minimum in the late evenings as the soil cools. In contrast, the latent heat storage tends to decrease around midday. Overall, these storage terms constitute an insignificant fraction of Rn of about 0.1%, 0.6%, and 1.2% for S_{LE}, S_H, and S_p in FR-Lam respectively, and 0.04%, 0.4%, and 0.8% in FR-Aur respectively. Conversely, G_{st} accounts for 12% of Rn (in FR-Lam), and 11% in FR-Aur. These values are close to those observed over some agricultural systems. For instance, Oke 2002 found the sum of the canopy heat storage, and the energy related to biochemical processes to be less than 10 W m^{-2} over croplands. Similarly, in the experimental study of Masseroni et al. (2014) over a maize field, they found that G_{st} can reach a maximum value of 36 W m^{-2}. In the following section, the significance of these storage terms in the surface energy balance is investigated.

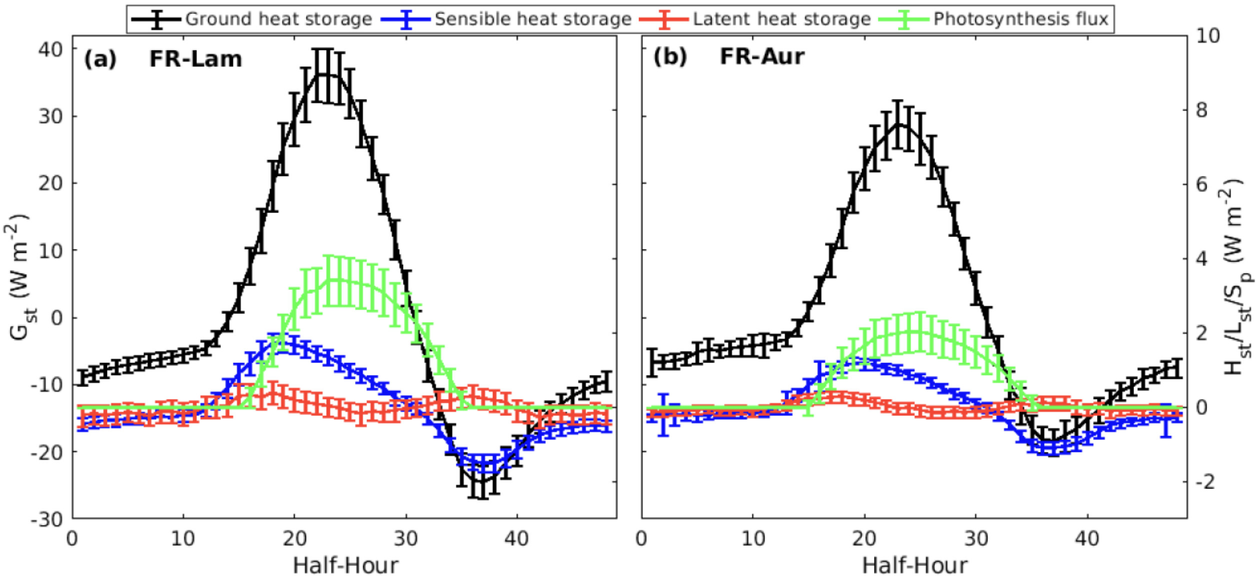

Figure 3.3: Average diurnal cycle of the storage terms estimated over the whole experimental period at (a) Lamasquère and (b) Auradé. Note that the photosynthetic storage term was estimated only over vegetation periods.

In this study, the energy balance closure (EBC) is the slope derived from the ordinary linear regression when the half-hourly values of the available energy $(Rn - G)$ is simultaneously plotted against the sum of the turbulent fluxes $(LE + H)$. A slope of 1 represents a 100% energy closure, while a lower value indicates either an underestimation of (one or both) turbulent fluxes, or an overestimation of the available energy. Figure 3.4 compares the EBC at both experimental sites with the addition of each storage term. The effect of these terms except for G_{st} is null at both sites. This is not surprising given that these components constitute an insignificant fraction of Rn. In comparison, with the inclusion of G_{st}, the slope of the linear regression increased by 1.5% in FR-Lam and by 8.4% in FR-Aur. This indicates that G_{st} plays a fundamental role in the improvement of the energy balance, as recommended by Foken et al. (2008). Consequently, only G_{st} was considered in this study, and hereafter, the sum of G (measured by the heat flux plates) and G_{st} is referred to as G in the following sections.

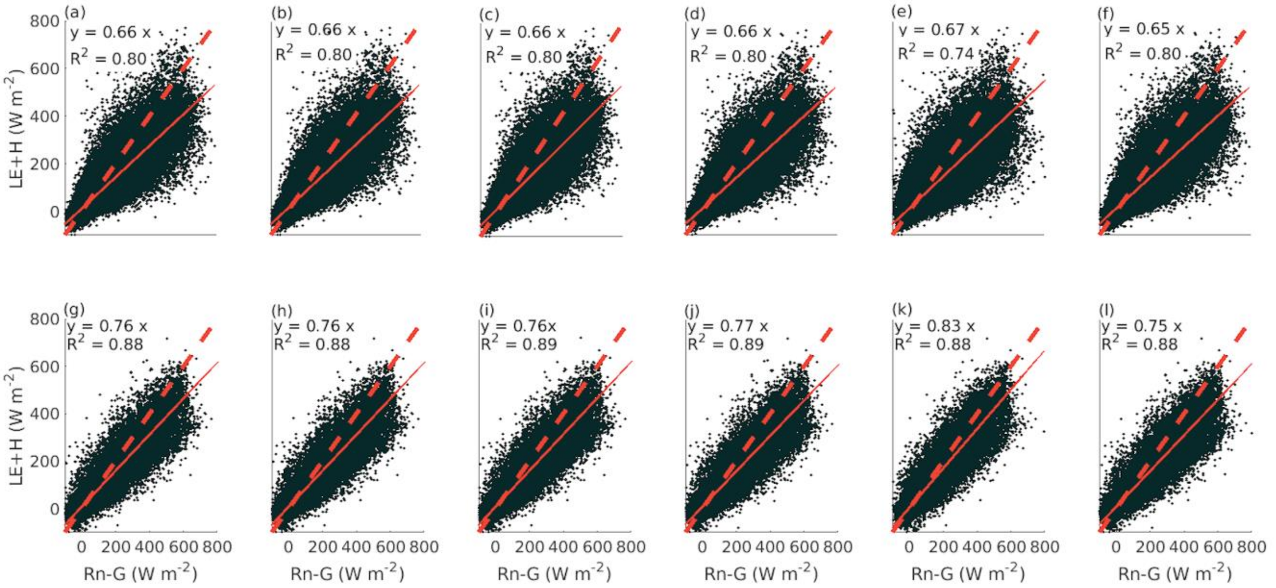

Figure 3.4: Energy balance closure based on half-hourly measurements taken during the experimental period (September 2005 to December 2015) at (a) Lamasquère (panels a-f), and (b) Auradé (panels g-i). The broken and solid red lines indicate x = y, and the regression line respectively. Columns 1, 2, 3, 4, 5, and 6 represent the EBC with (LE, H, G, Rn), (LE, H, G, S_{LE}, Rn), (LE, H, G, S_H, Rn), (LE, H, G, S_p, Rn), (LE, H, G, G_{st}, Rn), and $(LE, H, G, S_{LE},\ S_H, S_p, G_{st}, Rn)$, respectively.

3.3.1.3 Annual and monthly variability of the energy balance closure

Figures 3.5(a and b) present the annual, and the monthly mean EBC at FR-Lam and FR-Aur, respectively. This analysis, which covers 22 years of EC measurement reveals high variability in the annual closure at these sites. The mean annual EBC over FR-Lam is 0.66 ± 0.10, R^2 is 0.75, with residual energy of 56 W m^{-2}: whereas in FR-Aur, a more satisfying closure of 0.80 ± 0.13 is obtained with R^2 of 0.88, and a lower residual of 32 Wm^{-2}. Given that both sites are less than 20 km apart, it appears that the year with significantly higher closure in FR-Lam (2013) suffered poor closure in FR-Aur. In addition, EBC seasonality is marked in FR-Lam; monthly EBC ranged between 0.4 (in Jan) to 0.95 (in May) at FR-Lam, while in FR-Aur, the least closure of 0.4 was obtained in Dec, and in this plot, 61% of the months had closures that exceeded 0.75. This behavior (low EBC in winter and high EBC in summer) has been reported in several ecosystems (e.g., Wilson et al., 2002; Eshonkulov et al., 2019). Furthermore, as observed in Eshonkulov et al. (2019) over some sites in southwestern Germany, low EBC values associated with the winter months suffer larger variability (see Figures 3.5b and d). This seasonality could be a result of the solar radiation, which is expectedly low in winter, with subdued turbulence. On the other hand, in summer, the sun reaches its maximum altitude at zenith with stronger convective forces (Masseroni et al., 2014) (see section 3.3.2.1).

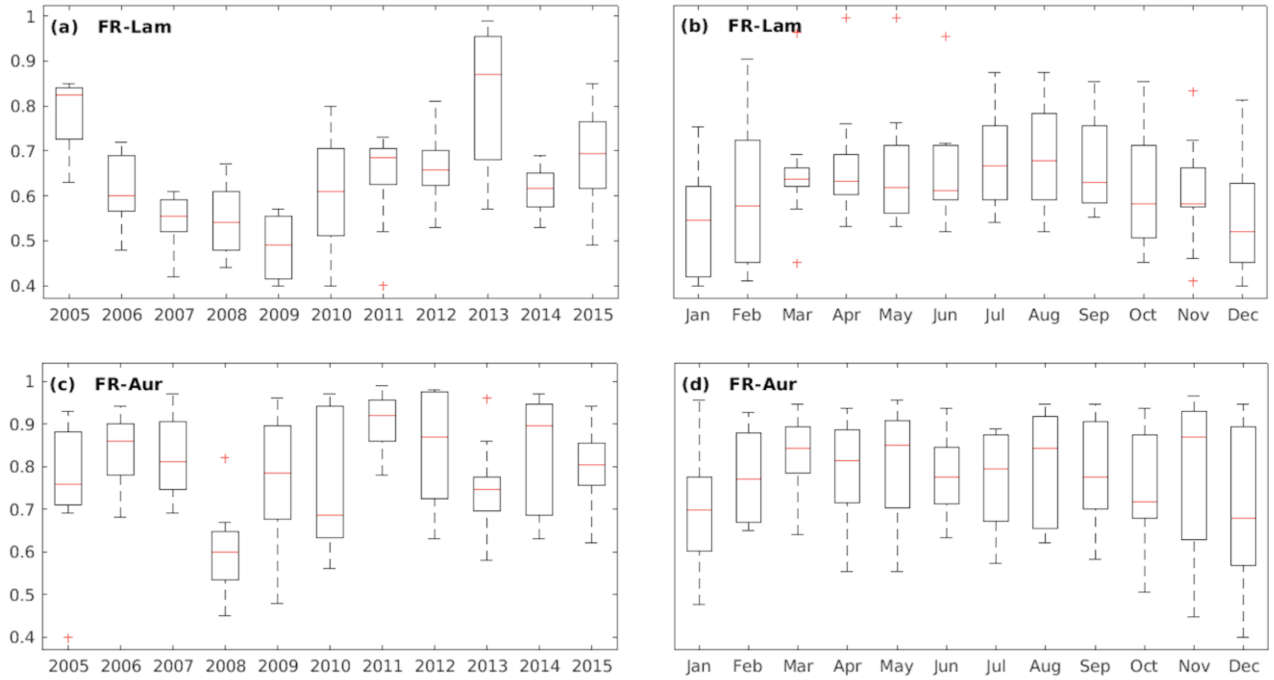

Figure 3.5: Inter-annual variability of the EBC between 2005 and 2016 for (a) FR-Lam and (c) FR-Aur. Mean monthly EBC (median, red lines) obtained between 2005 and 2015 for (b) FR-Lam, and (d) FR-Aur.

3.3.1.4 Dependence of the energy budget components on the time of the day

Figures 3.6(a and b) present the average diurnal evolution of the energy components, the energy balance closure, energy balance ratio ($EBR = (H + LE)/(Rn - G)$), and the residual ($Res = Rn - H - LE - G$) taken between 2005 and 2015 over FR-Lam and FR-Aur respectively. In the central hours of the day, as a response to the incoming solar radiation, Rn is positive, reaching 353 W m^{-2} in FR-Lam, and 312 W m^{-2} in FR-Aur. From the b-panels, during nighttime, there is continuous nocturnal transpiration/evaporation sometimes reaching 10 W m^{-2}. Similar values (3 to 15 W m^{-2}) had been reported in Cuxart et al. (2015) over a vineyard in Spain. Furthermore, LE in FR-Lam is about 20% larger than in FR-Aur, while H in FR-Aur is the predominant flux which is about 15% larger than the values in FR-Lam. This partitioning bias of Rn is due to the intense cultivation of FR-Lam while FR-Aur is often left fallow for longer periods. In addition, irrigation, and the shallow water table enhances evapotranspiration at FR-Lam whereas FR-Aur has drier soil due to its slopy terrain, and the absence of irrigation.

With focus on the Res (c-panels), it exhibits a dissimilar daily pattern at both sites. In FR-Lam, Res has a similar order of magnitude as H (90 W m^{-2}), while in FR-Aur, Res is about one-fourth of H, and one-third of G. Similarly, FR-Lam is characterized by positive values from 11h to 20h, while FR-Aur reports positive values much earlier (from 7h to 17h). Outside these time period, weak and negative Res values were observed with a minimum of -45 W m^{-2} found in FR-Lam in the early morning, while FR-Aur experienced its lowest value of -6 W m^{-2} in the late evening.

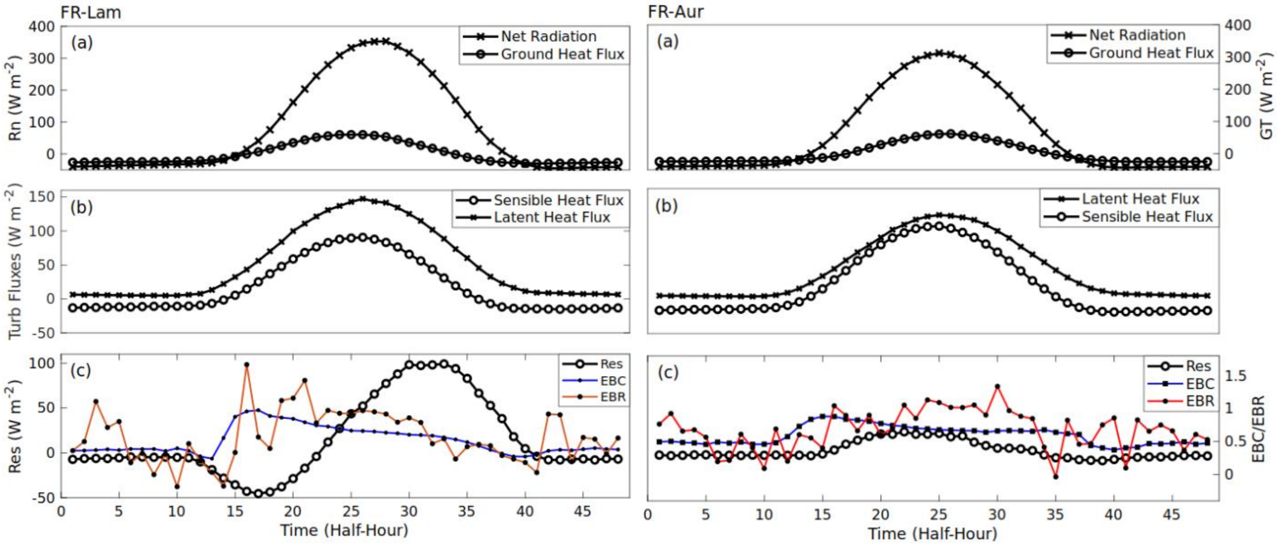

Figure 3.6: The mean diurnal cycle of (a) the net radiation and ground heat flux, (b) the latent and sensible heat flux, and (c) the energy balance closure, (in blue), energy balance ratio (in red), the residual energy at FR-Lam (column 1) and FR-Aur (column 2).

Panels-c display the daily the EBC. At these sites, between 0 and 6h, a low but stable EBC oscillating between 0.3 and 0.48 is observed. Afterwards, a gentle increase is observed, which peaked at 08h 30 (EBC = 0.94) in FR-Lam, and at 08h (EBC = 0.90) in FR-Aur. Thereafter, FR-Lam experienced a gradual drop with values below 0.5 for the rest of the day. This observation in FR-Lam (large closure in the morning) significantly contradicts the pattern reported in several experimental studies where the surface energy is best closed in the central hours of the day due to increased turbulence (Sánchez-Tomás et al., 2010; Gerken et al., 2017). This anomaly in FR-Lam could be due to lower advective processes in the early mornings (Mauder et al., 2021). Another possibility is perhaps the absence of stable atmospheric conditions in the early mornings. Using u^* as a proxy, a quick analysis revealed that during this time frame (07h 30 – 10h), the atmospheric stability of this plot swings between a neutral and an unstable state. In contrast, during the day in FR-Aur, EBC ranged between 0.6 and 0.9. Unlike the EBC, EBR is highly variable during the day- nonetheless, its shape slightly follows the EBC's pattern particularly in FR-Lam.

3.3.2 Overview of the energy balance closure for contrasted years

Figure 3.7 presents the mean EBC of the contrasting crop-seasons. Higher EBC values between 0.78 and 0.94 were observed at FR-Aur, while closure did not exceed 0.71 at FR-Lam. EBC was 18% and 20% higher for Wheat-Lam and Rapeseed-Aur, respectively, during the dry years than during the wet years. Similarly, the intercepts for these dry years were smaller, indicating smaller systematic errors. For the other crop-seasons, a contrasting behavior was observed-; EBC was much lower in the dry year. This implies an unclear impact of rainfall on the EBC; perhaps this is because there is rarely water shortage at both sites: FR-Lam is in the proximity of the river Le Touch, while at FR-Aur, crops are often grown between Autumn and the beginning of winter when water is not limiting.

The large difference between the EBC recorded for wheat in FR-Lam (0.65) and FR-Aur (0.89) implies that crop type has no obvious effect on EBC; rather, closure appears to be strongly dependent on site characteristics. Eshonkulov et al. (2019) reported similar findings over two contrasting regions in southwestern Germany. In their study, they observed that the sites had a statistically significant impact on EBC which is a function of the development of thermally- and mechanically-induced turbulence. On the other hand, a large disparity exist in the EBC of same crop type cultivated in the same year at the different EC sites.

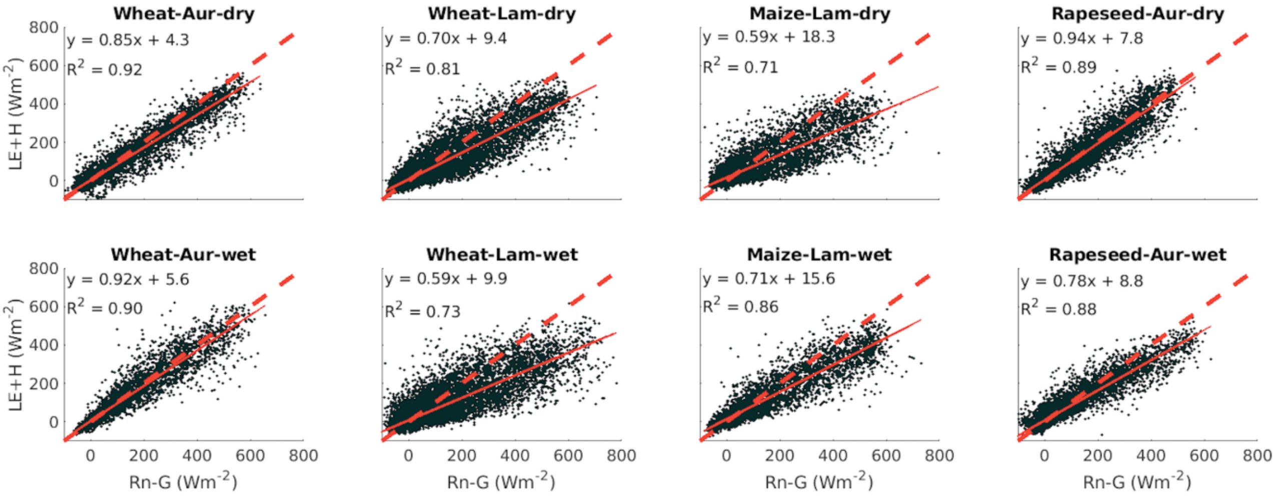

Figure 3.7: Linear regression between $(LE + H)$ and $(Rn - G)$ at half-hourly time step for the selected years (dry/wet, crop and site).

3.3.2.1 Dependency on atmospheric parameters

Wind direction

As shown in Figure 3.8, at both sites, the prevailing winds are majorly westerlies, which is typical of this region; with an averaged wind speed of 1.94 m s^{-1}, and 2.82 m s^{-1} in FR-Lam and FR-Aur respectively. In FR-Lam, high wind speeds were majorly measured within the E-SE-W-NW sectors with values 2.3 m s^{-1}, 2.4 m s^{-1}, 2.4 m s^{-1} and 2.2 m s^{-1} respectively. In contrast, winds blowing from the south- and southwest were rarely measured in FR-Lam (< 5%) with wind speed of 1.2 m s^{-1} and 1.3 m s^{-1} respectively. Likewise, in FR-Aur, the prevailing winds were observed in the E-SE-W-NW sectors with speeds 3.2 m s^{-1}, 3.8 m s^{-1}, 3 m s^{-1} and 2.6 m s^{-1} respectively. At FR-Aur, the share of these winds was insignificant in the NE (1.6%), S (3.5%), and SW (3.5%).

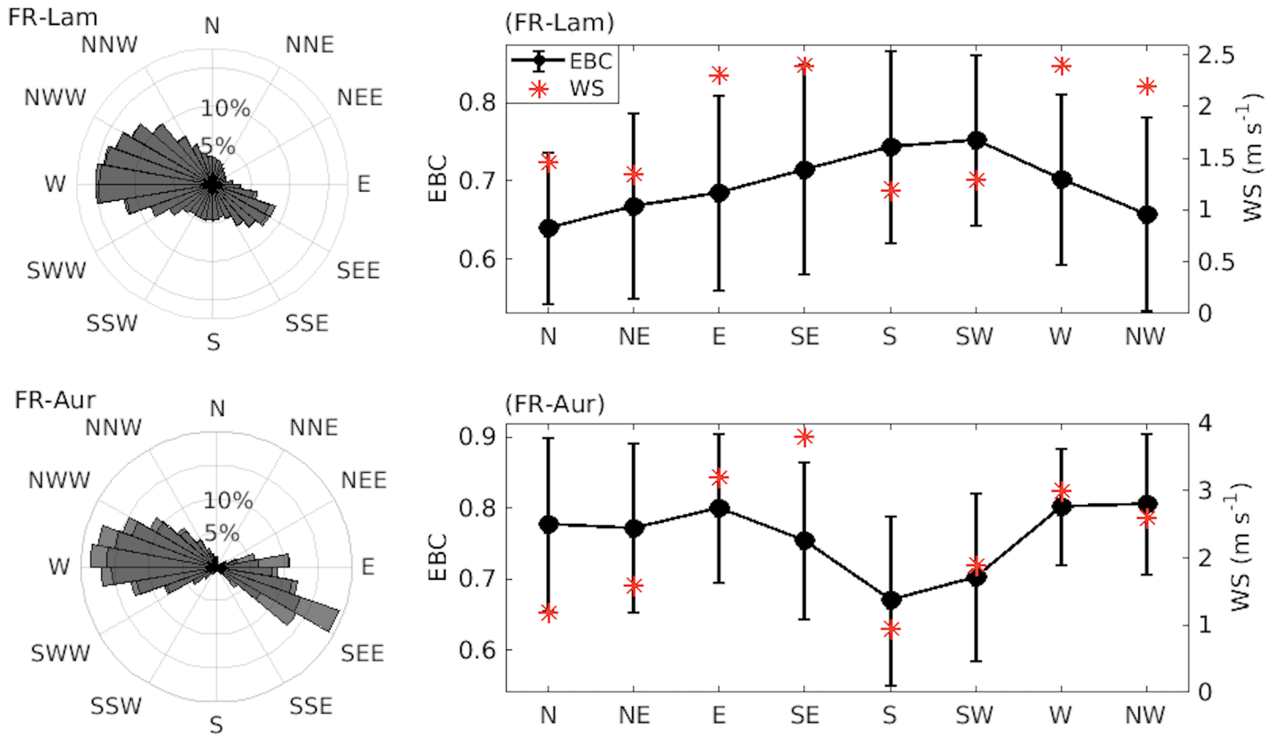

Figure 3.8: Average distribution of the EBC and the wind speeds as a function of the wind direction from 2005 to 2015 in FR-Lam and FR-Aur.

If we suppose that a surface is homogeneous, they should exchange the same fluxes whatever the direction, and the closure should be identical. To assess this spatial dependency, the EBC is analyzed as a function of the wind direction. EC measurements of the contrasting crop-seasons were categorized into 8 classes; each class corresponds to the following wind directions: N ($\theta < 22.5^{o}$ & $\theta \geq 337.5^{o}$), NE ($22.5^{o} \leq \theta < 67.5^{o}$), E ($67.5^{o} \leq \theta < 112.5^{o}$), S ($155.5^{o} \leq \theta < 202.5^{o}$), SE ($202.5^{o} \leq \theta < 225.5^{o}$), SW ($225.5^{o} \leq \theta < 247.5^{o}$), W ($247.5^{o} \leq \theta < 292.5^{o}$), and NW ($292.5^{o} \leq \theta < 337.5^{o}$). Afterwards, the EBC of each group was estimated as presented in Figure 3.9. The size of the dot represents the number of samples (which is smaller for maize because of its short life cycle), and the color corresponds to the EBC value.

At FR-Aur, the prevailing wind directions (E-SE-W-NW) are associated with better closure (> 0.8), while directions (S, SW) with fewer and weaker winds systematically have lower EBC (< 0.7). This strong wind dependence at FR-Aur is due to the high wind speeds experienced at this site, which are further strengthened by the gentle slope that encourages turbulence and instability. The statistical indicators obtained in this study are comparable to those reported for sites with similar climatic conditions (Eshonkulov et al., 2019; Xin et al. (2018). For example, Xin et al. (2018) classified the flux data of 10 study sites into 16 wind directions and observed higher closure (> 0.7) for the dominant wind direction, while closure (< 0.5) was lower for other directions.

However, at FR-Lam, all the 8 wind sectors for both crops had low EBC values between 0.52 and 0.75. This result is considered to be statistically significant since for each wind sector, the data set is largely representative (indicated by the dot size). A thick surrounding forest shields FR-Lam, and this significantly decreases the wind speeds, and dampens mechanical turbulence and flux transport (Giometto et al., 2017). On the contrary, the slope in FR-Aur which coincidentally corresponds to the main wind directions stimulates downslope flows creating larger turbulence.

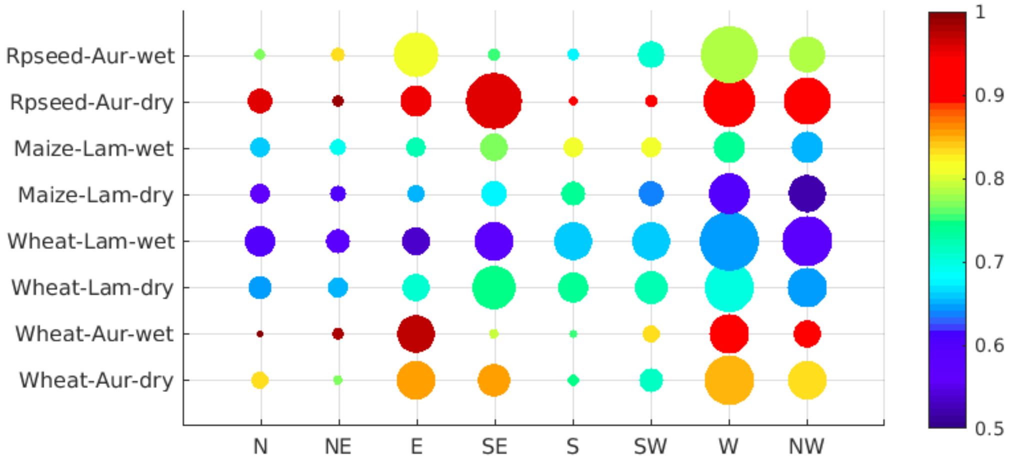

Figure 3.9: Distribution of the EBC in terms of the wind direction for the contrasting crop-seasons. High closure of 1 is presented in red, while blue indicates weak closure. The dot size represents the number of data points.

Friction velocity

The characteristic of atmospheric turbulence is fundamental for a reliable estimation of fluxes, so, to further compare the turbulent flows at both sites, Figure 3.10a shows the mean monthly plot of the turbulent parameter (u^*) obtained from the sonic anemometer between 2005 and 2016 at both sites. This figure reveals that the turbulent exchange of momentum within the atmosphere-vegetation-soil continuum was stronger at FR-Aur than at FR-Lam. The discrepancy between both sites is particularly obvious in summer (May-July) when FR-Aur and FR-Lam accommodated winter crops and summer crops, respectively.

Figure 3.10b shows the effect of u^* on the closure of the contrasting crop seasons. A threshold value that placed the u^* values in the low or high category (0.15 m s^{-1} at FR-Lam and 0.2 m s^{-1} at FR-Aur) was determined as the median value of the u^* distribution. At both sites, high u^* globally increased the EBC by 7% for both the dry and wet years as similarly reported in Franssen et al. (2010) and Xin et al. (2018). Franssen et al. (2010) obtained a linear relationship between the EBR and u^*, while Xin et al. (2018) reported a single peak relationship with the EBR peaking at 0.88 when the friction velocity is confined to 0.20-0.25 m s^{-1}. In the presence of weakly developed turbulence i.e., low u^* values, advection transport of scalar fluxes is subdued, and this results in an underestimation of the turbulent fluxes by the EC system. In the view of Masseroni et al. (2014), the consideration of turbulent mixing is an aspect against advective processes because a major theoretical assumption of the EC method is that advection can be neglected when the EC system is used over ideal surfaces. However, in spite of the flatness of FR-Lam, closure is lower than in FR-Aur. Nonetheless, this EBC-u^* relationship observed at our sites (particularly in FR-Aur) could be linked to the seasonal effect of increasing u^* with stronger Rn, as the phenological stages are not accounted for in Figure 3.10a (all surface states are included). However, this stability indicator played no significant role in the closure observed in maize whose growing season is shorter compared to that of the other crops.

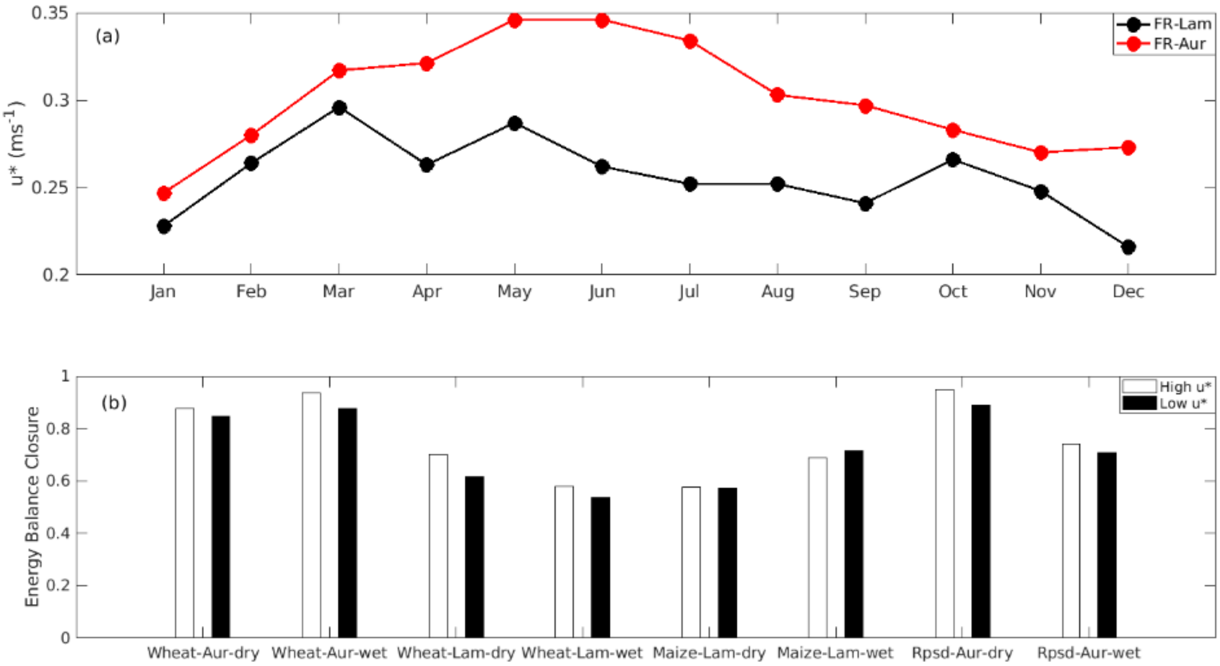

Figure 3.10: (a) Monthly mean values of the friction velocity (u^*) for FR-Lam (black) and FR-Aur (red); (b) Impact of friction velocity on the EBC of the contrasting crop seasons.

Atmospheric stability

The effect of buoyancy is to increase turbulence and intensify atmospheric mixing. The stability parameter $\zeta = z_{EC}/L$ was used to characterize the atmospheric state, where L is the Obukhov length. This stability parameter is the ratio of buoyancy suppression to shear production under equivalent neutral conditions- and L is the height where turbulence is generated more by buoyancy than by wind shear; below this height, shear dominates, and above it, buoyancy dominates (Stull, 1988; Bernhardt, 1995). With equal representation of each regime (i.e., similar dot size), flux measurements of the selected crops were classified under three stability regimes: $\zeta \leq -0.1$ (unstable condition), $-0.1 < \zeta < 0.1$ (neutral condition), and $\zeta \geq 0.1$ (stable condition). The closure of each class is shown in Figure 3.11. In the transition from stable to neutral condition in FR-Aur, an EBC increase ranging from 26% to 46% is observed (except in rapeseed-Aur-wet). A similar but weak pattern is observed over the crop-seasons in FR-Lam with percentage increase between 16-38%. In the transition from a neutral to an unstable atmospheric state, there is no EBC improvement except in wheat-Aur-dry (2%), wheat-Lam-wet (8%), and wheat-Lam-dry (2%).

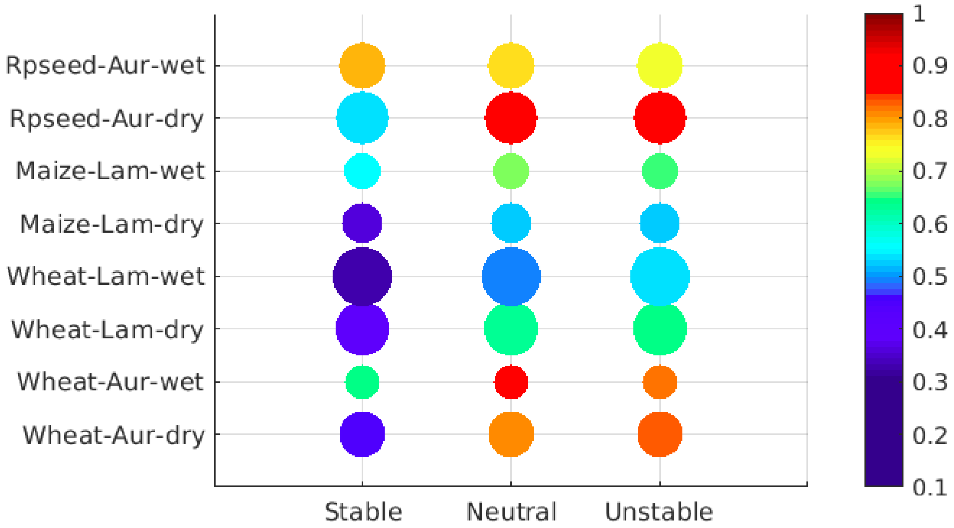

Figure 3.11: Variability of the EBC for the 3 regimes of atmospheric stability (stable: $\zeta \geq 0.1$; neutral: $-0.1 < \zeta < 0.1$; unstable: $\zeta \leq -0.1$)

Figures 3.10(a) and 3.11 distinctly reveal that FR-Aur benefits from stronger turbulence. This turbulence is generated by two effects: mechanical shear of the wind over rough surfaces, and convection due to higher surface temperature than in the air above. As u^* and ζ are related to momentum and turbulent scale, they are indicators of the mechanical turbulence for the three atmospheric stability conditions (Eshonkulov et al., 2019). As a result, both parameters favor the production of high frequency fluxes. The relevance of these parameters to energy closure has been noted in several studies (Franssen et al., 2010; Fratini and Mauder, 2014) which agree with our results. They usually invoke that the conditions of Taylor's hypothesis (the temporal average replaces spatial average) are better fulfilled with high u^* and unstable surface layer. Low EBC values in FR-Lam could also be attributed to turbulent structures with timescales larger than the averaging time (Foken et al., 2010).

3.3.3 Dependency of SEB on crop phenological stages and rainfall

3.3.3.1 Effect of the plant functioning on the SEB and its partitioning

Figure 3.12 presents the variability of the EBC for each surface type with values between 0.72 (LR) and 0.83 (DR) in FR-Aur, and between 0.59 (AMH) and 0.72 (DW) in FR-Lam (see Table 3.1 and Figure 3.12 for acronyms). To understand how soil works impact the EBC, comparison was restricted to LC and SBS at FR-Lam due to insufficient data in FR-Aur (LC). In FR-Lam, EBC was 0.61 for LC, and a slightly higher closure was found in SBS (see Figure A1 and A2 in Appendix A). Furthermore, at both sites except for wheat in FR-Aur, closure increases as low crops transition into developed crops. For example, at FR-Lam, EBC for DW was 6% higher than that of LW, and it was 8.8% higher in DM that in LM. Similarly, in FR-Aur, closure was 12% higher in DR than in LR. In brief, developed crops have higher EBC, and larger residual because of increased down-welling of solar radiation during this time of the year which increases the closure tendency. Also, the uncertainties surrounding the estimation of the storage terms during high vegetation explains the large residuals. Furthermore, after harvest, EBC experienced a 2-13% fall in FR-Lam, and a 12% fall in rapeseed (FR-Aur).

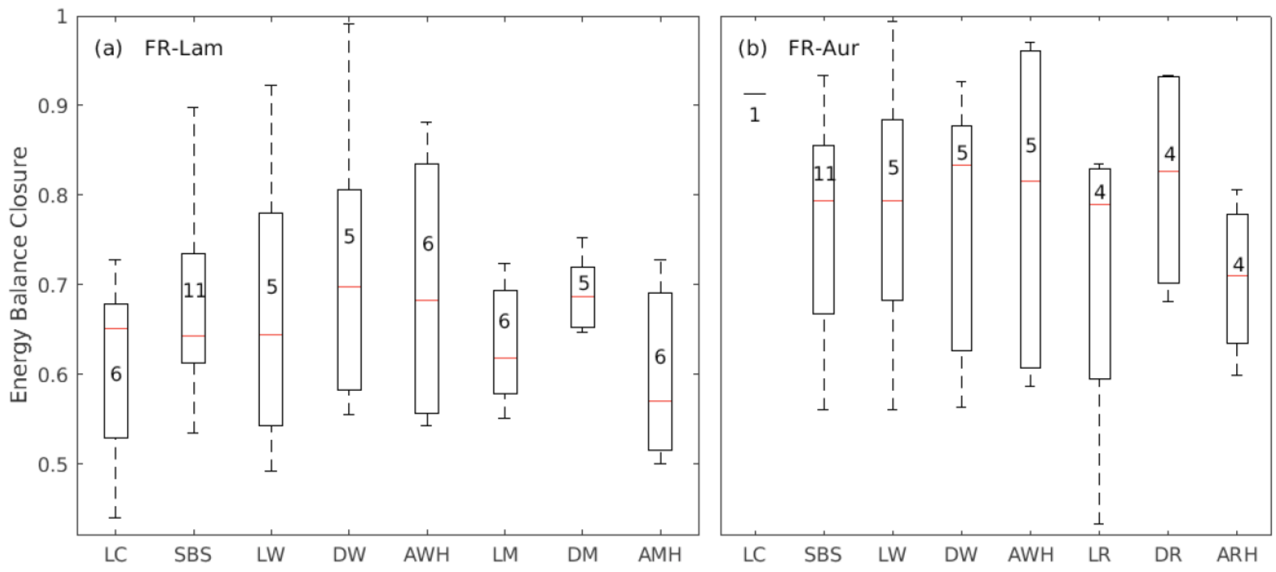

Figure 3.12: Comparison between the EBC of the different surface states at (a) FR-Lam and (b) FR-Aur. The number inserted within the boxes represent the frequency of each state within the study period. **LC** corresponds to large clods, **SBS** is smooth bare soil, **LW** is low wheat, **DW** is developed wheat, **AWH** is after wheat harvest, **LM** is low maize, **DM** is developed maize, **AMH** is after maize harvest, **LR** is low rapeseed, **DR** is developed rapeseed, and **ARH** is after rapeseed harvest.

For the contrasting crop-seasons, Figure 3.13 shows the EBC with its corresponding Res according to the crop stage and rainfall condition. Again, larger, and highly variable EBC (0.60 to 0.89) with smaller residuals was observed at FR-Aur, while FR-Lam exhibited more stability (0.50 to 0.62) across the crop stages. EBC and Res increased as low crops transitioned into developed crops for most winter crop seasons, except Rapeseed-Aur-wet and Wheat-Aur-wet. This could be the seasonal effect mentioned earlier whereby low vegetation period occurred during winter, a season associated with low incoming energy, while the periods of developed crops (April to June) corresponds to more energy and stronger convection. A similar observation was made in Wilson et al. (2002), who reported lower closure (0.72) for winter seasons and a higher closure for summer periods (0.81). This low closure (in low crops) and high closure (in developed crops) was also reported in Imukova et al. (2016) in the experimental analysis performed on winter wheat stands in Kraichgau, Germany, where towards the end of the growing season, an increase in EBC was observed.

For other crop seasons, no systematic pattern of the EBC in relation to crop stages was observed (Figure 3.13). At certain times, EBC was higher with higher vegetation, and residual decreased (Wheat-Aur-dry and Maize-Lam-dry), while at other times, EBC was lower for developed crops accompanied by larger residual (Maize-Lam-wet and Rapeseed-Aur-wet).

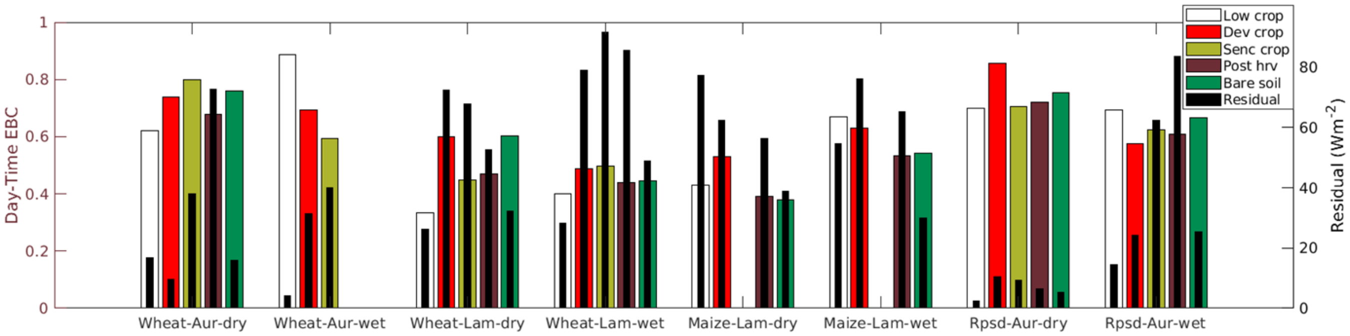

Figure 3.13: Daytime EBC (colored bars) and the corresponding residual (black bars) for the crop stages of the contrasting years. The colored bars also represent the different surface states: white corresponds to crops at the beginning of their development (Low crop), red to well-developed crops (Dev. crop), yellow corresponds to the senescent phase of the crop (Senc. crop), while brown and green stands for the post-harvest (post-hrv) and bare soil (Bare soil) periods respectively. Finally, the residual is to be read on the right-hand axis.

To complete the analysis, Figure 3.14 shows the distribution of the energy fluxes (normalized by Rn) for each crop at different stages of development for the contrasting crop-seasons. Each flux exhibits similar dynamics for the same crop type, with strong variability between the different phenological stages, while the behavior of each energy component remains unique. For all crop types, LE

constituted about 29% of Rn for low crops, 41% for developed crops, 25% during senescence, 19% for postharvest, and 22% over bare soils, while for H, 22%, 22%, 42%, 36, and 37% of Rn was partitioned during these crop stages respectively. The parabolic behavior of G was essentially regulated by the magnitude of Rn and canopy structure. Thus, over low crops, G accounted for 30% of Rn, dropping to 16% during growth peak and further during senescence (13%). Besides, closure was higher over the bare soil period that succeeded the residue-covered postharvest phase with an EBC increase of 11%, 24%, 1%, 4.7%, and 9% (with respective imbalance difference of 57 W m^{-2}, 20 W m^{-2}, 37 W m^{-2}, 1 W m^{-2}, and 59 W m^{-2}) in Wheat-Aur-dry, Wheat-Lam-dry, Wheat-Lam-wet, Rapeseed-Aur-dry, and Rapeseed-Aur-wet respectively. This suggests that the presence of harvest residues is important in the SEB. According to Figure 3.14, the ratio G/Rn is usually larger over the bare soil period (~17%) that followed post-harvest, except at FR-Lam where there's a longer presence of wheat residue (~3months). Such a situation indeed makes it difficult to distinguish the influence of seasonality and residue. In maize however, G/Rn over the bare-soil and post-harvest period are not very different because of the absence of residues after harvest.

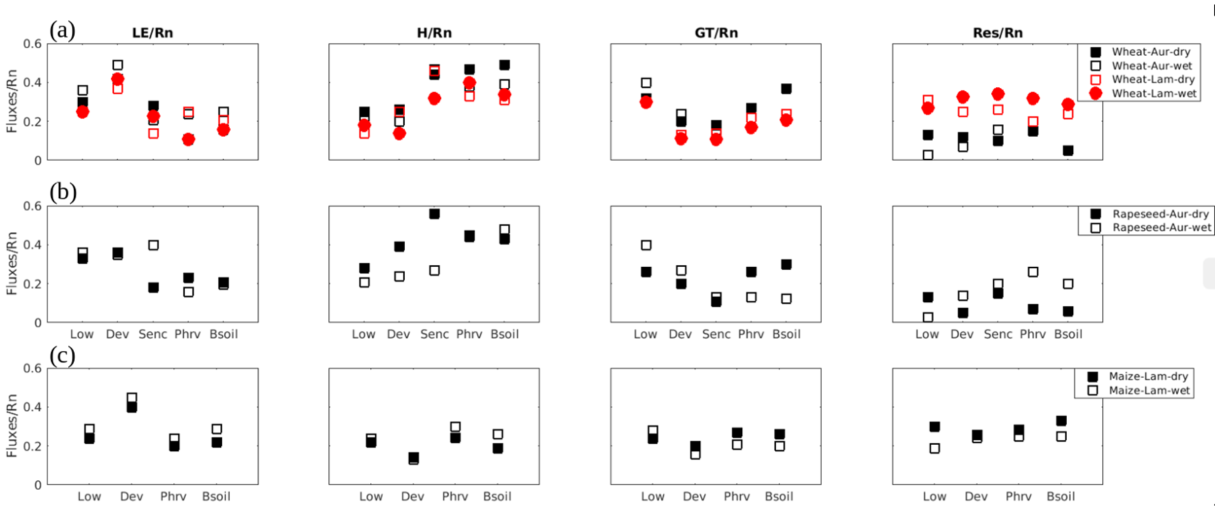

Figure 3.14: Variability of the energy fluxes normalized by net radiation according to each crop stage for (a) wheat at the FR-Lam and FR-Aur site; (b) rapeseed at FR-Aur; (c) maize at FR-Lam for the contrasting crop-seasons.

Further analysis of the impact of residues on G revealed that over the crop seasons in FR-Aur (except for Wheat-Aur-wet due to unavailable data), the maximum value for G varied from 80 W m^{-2} during post-harvest period to 104 W m^{-2} during the bare soil period (see Figure 3.15a). The least variability is observed in Rapeseed-Aur-dry due to the thin residue layer. This observation has been aptly described by Horton et al. (1996), and Chung and Horton (1987): residues act as a thermal insulator, and due to their high reflectivity, they permit low solar radiation absorption into the soil.

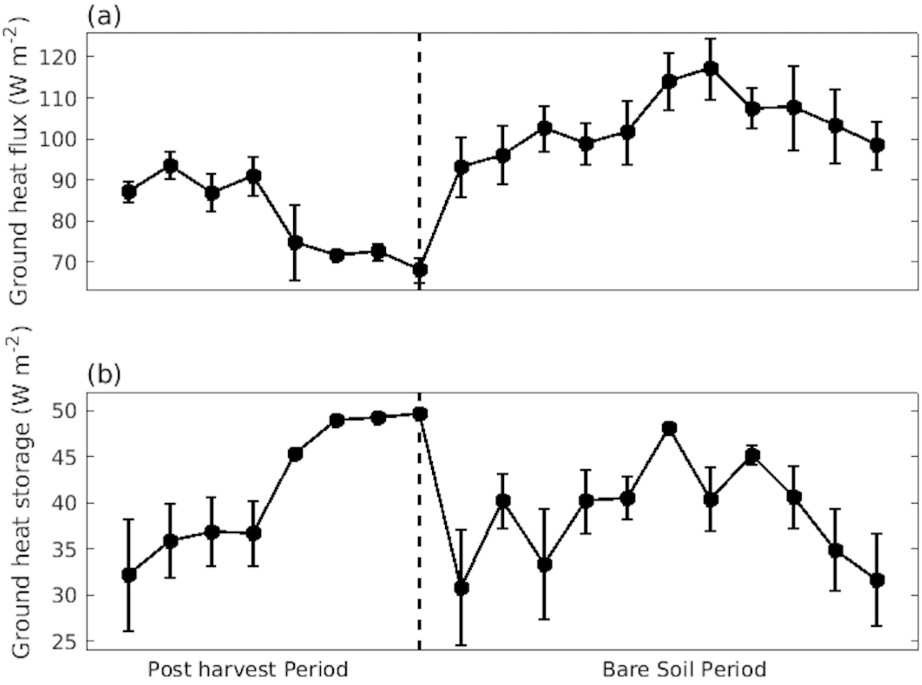

Figure 3.15: Comparison of the maximum values of (a) the ground heat flux (measured by the HFP only), and (b) the ground heat storage between the postharvest and bare soil periods of wheat-Aur-dry, rapeseed-Aur-dry, and rapeseed-Aur-wet.

Given that LAI modulates turbulent transfers and radiation absorption, developed crops (high LAI) intercept larger incoming radiation, which decreases the amount of energy absorbed by the soil substrate. Hammerle et al. (2008) demonstrated this experimentally over Stubai valley in Austria and reported that G accounted for 25% of Rn during periods with low foliage cover and much less under a dense canopy. Similarly, Santanello and Friedl (2003) found that G was usually less than 10% of Rn over thick canopies due to increased energy interception. In addition, the presence of vegetation resulted in higher LE/Rn due to increased transpiration (Heilman et al., 1994; Wohlfahrt et al., 2001; O'Brien, 2018), which dropped by 48% during senescence as discoloration started in transpiring leaves and stems except in Rapeseed-Aur-wet.

A role reversal was observed between the dry and wet years at FR-Aur (Figure 3.14). For low and developed crops of Wheat-Aur and Rapeseed-Aur, more energy was partitioned into G for wet years, while for subsequent crop stages, G was higher in the dry years than in the wet years. This observation is a combined effect of soil wetness and soil exposure. Periods with higher G values were characterized by higher rainfall amounts with differences of 200 mm (for low rapeseed), 45 mm (for developed rapeseed), 95 mm (for senescent rapeseed), 155 mm (for low wheat at FR-Aur), and 21 mm (for developed wheat at FR-Aur). Analysis revealed that G was regulated by high rainfall- this stimulated an increase in thermal conductivity, a reduction in soil albedo, and consequently an increase in energy absorption. This behavior was not observable in Wheat-Lam although the rainfall recorded for the developed crop in the wet year was 200 mm higher than that of the dry year. In summary, with an LAI peaking at 5.4 m^2 m^{-2}, the shading effect that the canopy of Wheat-Lam-wet provided could have masked the positive effect that a high soil thermal conductivity could contribute to G. Thus, the magnitude of G for Wheat-Lam-dry and Wheat-Lam-wet were comparable over developed vegetation.

Strong sensible heat fluxes ranging between 20-56% of the net radiation was observed across all the crop stages in rapeseed. In contrast, only 13-30% of Rn was partitioned into H in maize, and this was compensated for by LE. Of great interest is the scatter between the dry and the wet years especially for rapeseed during senescence. During this stage, LE and H clearly exhibited opposite behaviors. LE accounted for 40% of Rn (in the wet year) and 18% of Rn (in the dry year), while H had a weaker magnitude of 27% of Rn in the wet year and 56% of Rn in the dry year.

In conclusion, the site effect takes precedence over the crop type; both the turbulent and conduction fluxes are higher at FR-Aur compared to FR-Lam (Figure 3.14) even for the same crop type. Nevertheless, on a given site, we frequently find certain energy balance trends related to the surface state/vegetation stage, e.g., a better closure when comparing bare-soil periods to post-harvest periods, or when the vegetation is well developed rather than low.1

3.3.3.2 Effect of rainfall

Figure 3.16 shows the mean EBC according to each crop stage together with the corresponding cumulative rainfall (+ irrigation). As a result of its higher clay content (> 50%) and shallow water table depth, FR-Lam has a higher water holding capacity, whereby large puddles of water is a regular feature on this plot especially in winter and spring. In contrast, the openness, windiness, and steepness of FR-Aur make this site susceptible to quick drying, evaporation, and run-off, respectively.

For the crops at FR-Lam, total cumulative rainfall was 564 mm, 693 mm, 338 mm, 447 mm for Wheat-Lam-dry, Wheat-Lam-wet, Maize-Lam-dry, and Maize-Lam-wet, respectively. Higher rainfall was recorded for low and developed crops compared to other stages, especially maize, due to the irrigation events that favored evapotranspiration (see Figure 3.14).

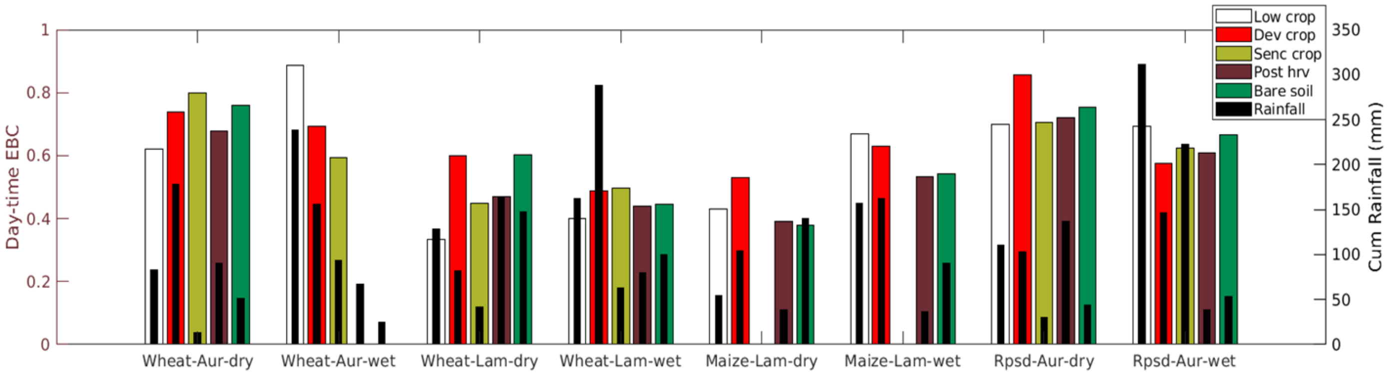

Figure 3.16: Daytime energy balance closure (colored bars) for the different crop stages with cumulative rainfall (black bars).

For Wheat-Aur-dry and Rapeseed-Aur-dry, the closure over the developed crop was 19% and 22%, respectively, higher than that of the low crops. Here, seasonality played a major role because even though rainfall was at least 100 mm during the mature phases, the atmospheric demand ($TA > 12$ °C and relative humidity < 80%) was higher than that of low crops ($TA < 5$°C and relative humidity > 86%). In contrast, over Wheat-Aur-wet and Rapeseed-Aur-wet, rainfall was 82 mm and 165 mm higher, respectively for low crops. The lower closure observed in the developed stages of the aforementioned crops can be related to the low wind velocities that prevailed during this period. For Wheat-Aur-wet and Rapeseed-Aur-wet, we observed wind velocities which were 29% and 8% lower respectively, during the developed crop than the low crop phases.

3.3.4 Impact of sensible heat advection on the surface energy balance

Figure 3.17a presents a temporal series of A_H and Res computed from 2006 to 2015 between 11h and 12h30 for both sites at spatial scales of 50, 100, 200 and 400 m. While low hectometric scales (50, 100, and 200 m) exaggerated the advection processes, A_H at 400 m very well mimicked the residual energy. Analyzing A_H at 400 m (see Figure 3.17b) in FR-Lam, A_H oscillated between 20 and 180 W m^{-2} and exhibited similar temporal dynamics as Res while capturing very closely the minimum and maximum values- this is similar to the observation of García-Santos et al. (2018). At FR-Aur, a similar trend but with a lower magnitude that ranged between 3 and 98 W m^{-2} was observed. Essentially, advection can be induced by topography, farm practices etc. Figure 3.17 shows that there is strong advective processes in FR-Lam, and this explains the low EBC. FR-Lam is topographically flat, but with a thick surrounding forest that could create secondary circulations with time scales that are too large to be captured by the EC within 30-mins. This theory agrees well with the findings of Xin et al.

(2018), who reported low EBR over 4 flat terrain areas on the Tibetan Plateau due to the presence of the buildings close to the sites.

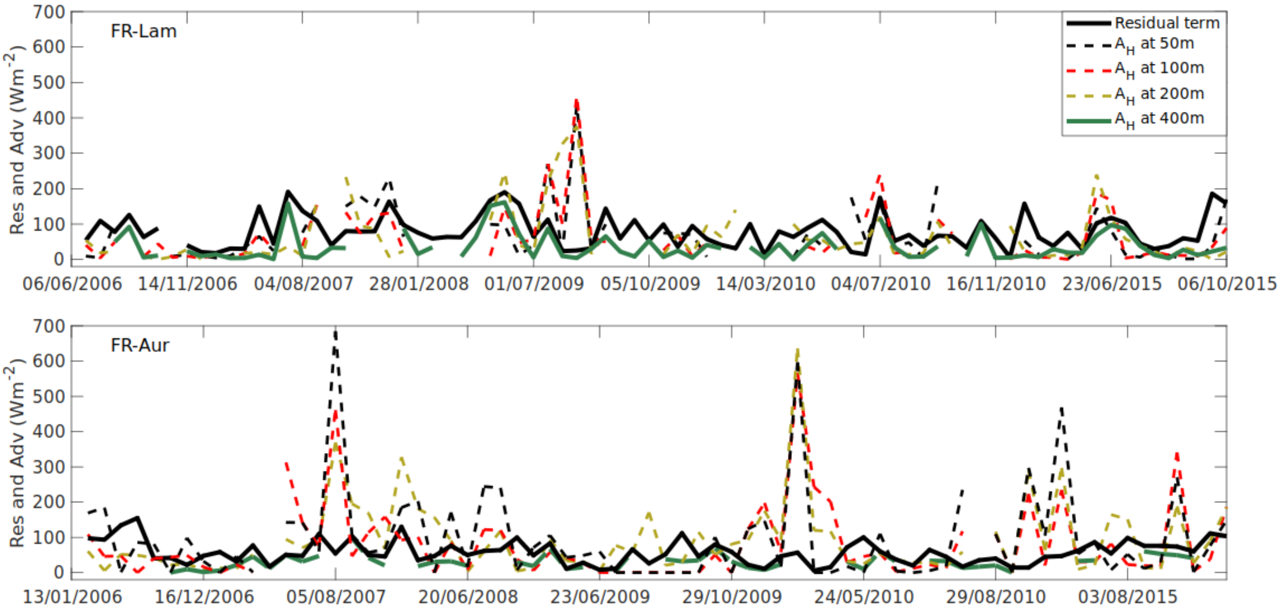

Figure 3.17a: Comparing along different spatial resolutions the order of magnitude of the sensible heat advection (A_H), and the residual (Res) estimated over FR-Lam and FR-Aur.

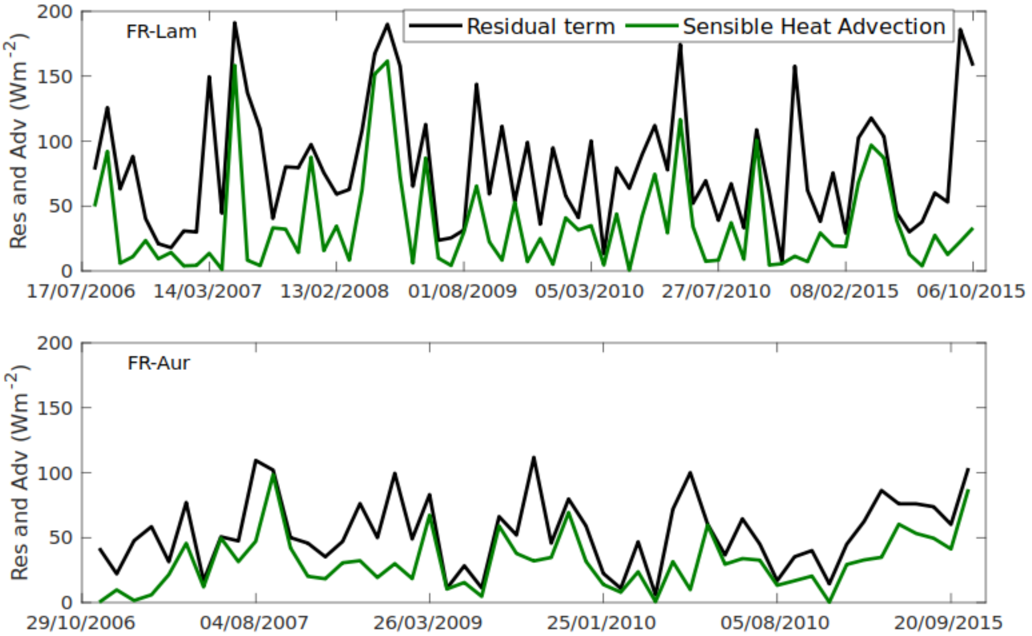

Figure 3.17b: Same as Figure 3.17a, but for $\Delta x = 400$ m.

Another heterogeneity-inducing factor is irrigation; FR-Lam is frequently irrigated to supplement rainfall during summer, while FR-Aur is never irrigated. The irrigation of the whole plot takes place in phases, and it lasts for about 4 to 5 days. This irrigation episode enhances the horizontal gradient in surface temperature between the already-irrigated, and the yet-to-be-irrigated areas. As observed in the experimental study of Xu et al. (2017), low EBR (0.6) was obtained during these periods of uneven wetness, and this increased (EBR > 0.8) after the plot has achieved a certain level of uniform wetness. At FR-Aur, heterogeneity introduced by topography played a minute role contrary to FR-Lam where EBC and A_H remained low and high, respectively. This reemphasizes the influence of agricultural practices and surrounding structures on the surface energy balance (Panin et al., 1998; Finnigan et al., 2003).

Overall, A_H accounted for 57% and 60% of the estimated imbalance at FR-Lam and FR-Aur, respectively, leaving the energy budget unclosed. At certain periods, A_H and Res were totally uncorrelated i.e., A_H could not explain the energy imbalance. Similar observation has been reported (e.g., Oncley et al., 2007), and this undoubtedly implies the presence of some unidentified energy sinks and exchange processes (Stoy et al., 2013; Mauder et al., 2020). One could be the advective transport of water vapor which although not estimated in this study could be significant if we refer to the experimental study of Simó et al. (2019) at UIB, Spain. However, for well-watered plots with adequate rainfall as FR-Aur and FR-Lam, weaker values of A_{LE} is expected due to an atmosphere that is not as dry as UIB. However, we hypothesize that this process would be more substantial in FR-Lam than in FR-Aur given the frequent presence of water puddles in FR-Lam especially in winter and spring. Also, the intermittent irrigation practice in FR-lam could encourage humidity transfers.

3.3.5 Effect of time averaging on the energy closure

Another possible factor responsible for the unclosed energy budget is the uncaptured secondary structures (Laubach and Teichmann, 1999). These structures are large-scale fluxes whose slow motion can make the typical 30-min averaging time insufficient to resolve the large eddies depending on the local landscape and the measurement height. To discuss the role of low-frequency processes (i.e., structures of at most a few kms) in the SEB, we used a rather simple approach which involves estimating the EBC with surface fluxes averaged over different periods ranging from half an hour to a few hours. Analysis conducted out over the contrasting wheat seasons in FR-Lam and FR-Aur (see Figure 3.18) reveals that an extension of the averaging time from 30 min to 6h only improved the EBC by about 4%. This implies that a significant portion of the low frequency fluxes have been adequately captured by the EC over wheat. This agrees with the findings of Charuchittipan et al. (2014) who suggests that 30 min is largely sufficient especially over low vegetation; while for taller species such as maize, an extension of this time is recommended to permit the contributions from low-frequency eddies. Some authors e.g., Lenschow et al. (1994) have similarly suggested an adaptation of the aggregation time to the atmospheric characteristics of each site; however, this would inevitably introduce several complexities that would downplay 'the spirit of common practices' which would make inter-site comparison difficult.

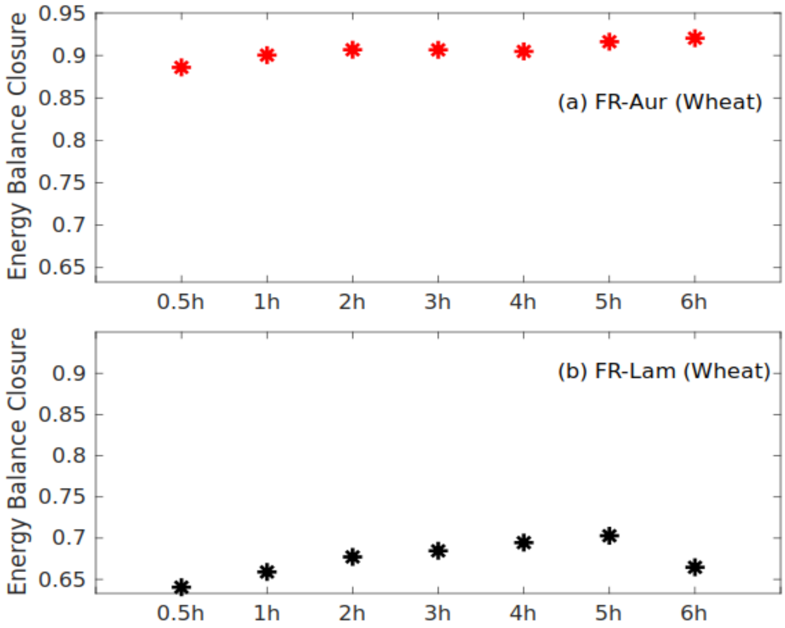

Figure 3.18: The EBC at different temporal scale for winter wheat at FR-Lam and FR-Aur.

Interestingly, for time scales larger than 6h (e.g., 24h) EBC further improved. Even so, as there are no boundary-layer processes with time scales longer than a few hours, compensation effects of the storage terms should appear, and may explain this improvement. Indeed, the energy stored in the morning is locally released in the afternoon and late evening (Foken, 2008). This also agrees with the study of Leuning et al. (2012) on the La Thuile dataset.

3.4 Conclusions

This chapter investigated the variability of the EBC over two croplands (FR-Lam and FR-Aur), and to understand factors that control flux partitioning. Emphasis was placed on comparing crop seasons with contrasting rainfall conditions, and the specific objective was to understand how crop types, phenologies, atmospheric conditions, and farm practices influence the surface energy balance. The outcome of this analysis revealed that the EBC is strongly dependent on site characteristics. Overall, closure was better in FR-Aur (82%), while only 67% of the available energy was detected in FR-Lam. Furthermore, the influence of crop type on the EBC is unclear; for instance, the common crop between both sites is wheat, and over this crop's cycle, closure in FR-Lam ranged between 0.53 and 0.87, whereas it was between 0.68 and 0.88 in FR-Aur. However, despite the proximity of both sites, this observation must be interpreted with care because the cultivation time for this crop (wheat) never coincides at both sites. Nonetheless, the closure difference suggests that each site's characteristic has a significant impact on the closure, which is stronger than that of the crop type.

Furthermore, in FR-Aur, larger EBCs (> 0.8) were associated with the west, southeast, and eastern wind regimes with high wind speeds. On the other hand, directions associated with weak, and few winds systematically had lower EBC. This observation is absent in FR-Lam- closure is low in all the wind sectors.

Finally, This chapter showed that the often-neglected sensible heat advection is a major component of the SEB, with larger magnitudes at FR-Lam in agreement with the plot's situation and activity. Although the advection of water vapor was not estimated owing to its expensive requirement; the frequent irrigation of FR-Lam suggests that this term might be significant.

Some main ideas of this chapter

- G_{st} is the most important storage term, and it significantly improved the EBC.

- EBC strongly depends on site's characteristics i.e., how well mechanical, and thermal turbulence are developed.

- Horizontal thermal advection is a major component of the surface energy budget.

- Land use, crop type, and crop stage strongly impact the partitioning of the net radiation.

Chapter 4: Estimation and partitioning of surface energy fluxes over a maize and wheat using a land surface model

The results presented in this chapter are published in the following paper:

Dare-Idowu, O.; Jarlan, L.; Le-Dantec, V.; Rivalland, V.; Ceschia, E.; Boone, A.; Brut, A: **Hydrological Functioning of Maize Crops in Southwest France Using Eddy Covariance Measurements and a Land Surface Model.** *Water* 2021, *13,* 1481. https://doi.org/10.3390/w13111481

4.1 Introduction

The hydrological functioning of crops which defines the dynamics of the different terms of the water budget including evapotranspiration and its constituents can be analyzed using LSMs of various complexities (Liang et al., 1994; Srivastava et al., 2018). This is particularly important in the monitoring of drought, soil-water status, and plant-water use (Maes and Steppe, 2012). Within this context, the objective of this chapter is two-folds:

(i) Assessing the ability of two LSMs to reproduce the different terms of the energy and water budget over 6 maize and 4 wheat crop seasons in FR-Lam. Here, the single-source ISBA is compared with the dual-source ISBA-MEB.

(ii) Afterwards, their ability to partition ET was investigated with a special emphasis on the water losses for the plant (drainage and soil evaporation).

4.2 Materials and methods

The measurements used in forcing and validating the models have been presented in Chapter 2, and Table 4.1 briefly presents the characteristics of the crop seasons under study. For ease, in the remaining part of this chapter, each crop year would be referred to by its year e.g., wheat in 2007 becomes wheat-2007.

Table 4.1: Selected crop seasons, total rainfall amount (P) and irrigation ($Irrig$) in mm, sowing and harvest dates, and the maximum leaf area index in m^2 m^{-2}.

Maize					**Wheat**				
Year	P/Irrig	Sowing	Harvest	Max LAI	Year	P (mm)	Sowing	Harvest	Max LAI
2008	362/27	20 May	12 Sep.	3.9	2007	615	18 Oct '06	15 Jul '07	4.5
2010	278/106	21 Apr.	20 Sep.	4.0	2009	633	19 Nov '08	13 Jul '09	1.74
2012	293/149	27 Apr.	27 Aug.	5.9	2011	526	03 Nov '10	12 Jul '11	5.5
2014	256/168	14 May	24 Sep.	5.2	2013	910	29 Oct '12	22 Jul '13	3.6
2015	262/150	05 May	08 Sep.	6.6					
2019	267/152	22 Apr.	12 Sep.	4.8					

NB: Each maize season is taken between the 1st of April to the 30th of September, and a wheat season is from the 1st of October to the 30th of September (of the following year), and the rainfall is the sum of the rain events over each crop season.

The ground heat flux

To guarantee the representativeness of the source area, the ground heat flux used in this chapter is the average measurement of the 3 HFPs (see Figure 2.1 and section 3.3.1) corrected with G_{st}. Due to instrumental failures and field operations, there were several missing data in maize-2014, maize-2015, and maize-2019 which required gap filling. This gap-filling exercise was carried out as follows: (i) When the LAI is less than 0.5 m^2 m^{-2}, G was set as a constant fraction of Rn as expressed in Equation 4.1a (Miralles et al., 2011). (ii) When LAI is greater or equal to 0.5 m^2 m^{-2}, the empirical method developed by Tasumi (2003) which accommodates the shielding effect of the canopies on the soil (Equation 4.1b) was used.

$$G = a_1 Rn \qquad \text{if } LAI < 0.5 \text{ m}^2 \text{ m}^{-2} \qquad (4.1a)$$

$$G = [a_2 + a_3 e^{-a_4 LAI}]\, Rn \qquad \text{if } LAI \geq 0.5 \text{ m}^2 \text{ m}^{-2} \qquad (4.1b)$$

The calibration of these two empirical expressions for the maize years with sufficient G measurements (maize-2008, maize-2010, and maize-2012) was done by splitting the data set into a 70% training set, and a 30% testing set using a Jacobian-based optimization method to minimize the root mean square error. For the low LAI category, the optimized coefficient value is $a_1 = 0.29$, which is close to the value used in the literature by different models (Choudhury et al., 1987). This value resulted in an R^2 of 0.80, 0.71, 0.78, and 0.76 for maize-2008, maize-2010, maize-2012 and the combined years, respectively. In addition, low RMSE values of 15 W m^{-2}, 18 W m^{-2}, 15 W m^{-2}, and 16 W m^{-2} were obtained. Likewise, in the second category of high LAI, the optimal coefficients ($a_2 = 0.049$; $a_3 = 0.135$; $a_4 = 0.249$) resulted in R^2 values of 0.89, 0.76, 0.88, and 0.83; RMSE of 9 W m^{-2}, 14 W m^{-2}, 9 W m^{-2}, and 11 W m^{-2} for maize-2008, maize-2010, maize-2012, and the combined years, respectively.

Water storage calculation

From the principal components of the hydrological budget highlighted in Equation 1.3, the soil water storage (S) was estimated from Equation 4.2 as an integral between the depths 1 cm and 50 cm (30 cm in maize-2008 and maize-2010 due to missing data) since most of the water uptake by maize is taken between these soil depths (Farré and Faci, 2006).

$$S = \sum_{1=1}^{5} swc_i z_i' \qquad (4.2)$$

where swc is the soil water content in m^3 m^{-3} at layer i, and z is the layer thickness between layer i and the preceding layer in meters. In maize-2019 and during the summer of maize-2014, S is computed using soil moisture estimates from ISBA-MEB because of large gaps in the field measurements. This study computed the fluctuation in the soil water storage (ΔS) as the difference between the storage at the beginning of the crop season, and the storage a few days before harvest. Finally, given the flatness of FR-Lam, the concise irrigation amount, and the brevity of irrigation events, this study considered total runoff negligible.

4.3 Results and Discussion

4.3.1 Experimental data analysis

4.3.1.1 Meteorological conditions and vegetation characteristics

Figure 4.1(a-c) provides a general overview of the climate, and the crop growth conditions over the maize seasons. There is a strong seasonal variability of air temperature and leaf area index. Although the inter-annual variability of rainfall (+ irrigation) is small (from 384 mm in maize-2010 to 441 mm in maize-2012), the seasonal variability of the irrigation events is significant. The highest irrigation occurs around the peak of the crops' growth between July and September concomitantly with the highest air temperature. The farmer applied no irrigation in June for maize-2008 and maize-2010, thanks to the abundant rainfall during the spring months by contrast with the other growing seasons. Maize-2019 was characterized by a drought period particularly in August and so, it obtained the highest irrigation inputs cumulated during July and August of all the growing seasons. Likewise, there is a strong seasonal variability of the *LAI* with a rapid growth in maize-2015 thanks to the favorable temperature conditions in April (13.2 °C) and in May (16.2 °C), while a late growth is evident in maize-2010 perhaps because of the below-normal air temperature (see Figure 4.1b). In maize-2008, the poor growth might have resulted from either a very late sowing, or the cultivation of a different species, or a combination of both. The maximum *LAI* values also differ strongly from one year to another, with an exceptional growth in maize-2015 as already underlined leading to a peak *LAI* of 6.6 m^2 m^{-2} thanks to the high irrigation inputs applied in July by contrast with maize-2008 and maze-2010 with *LAI* that is below 4.1 m^2 m^{-2}. Finally, significant variances up to one month is also observed for the harvest date.

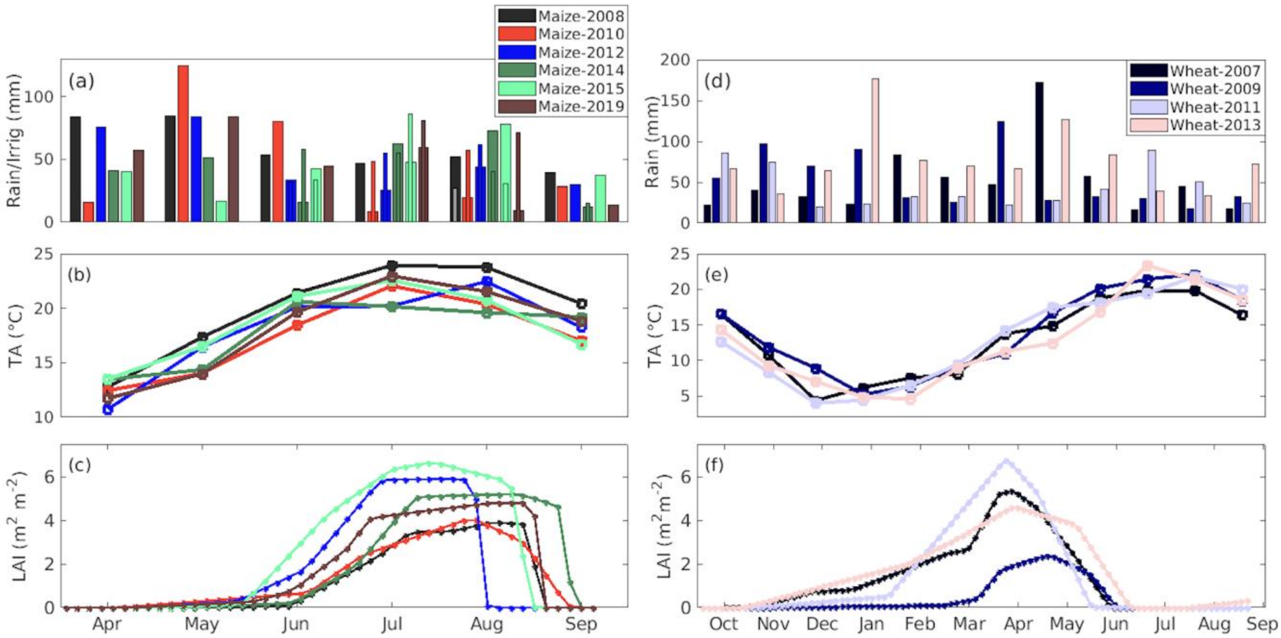

Figure 4.1: Seasonal variability of the climatic variables for maize (column 1) and wheat (column 2). (a): monthly cumulative sum of rainfall (in large bars) and irrigation amount (in thin bars for maize), (b): monthly averages of air temperature, and (c): 4-days mean of the leaf area index.

For wheat, (Figure 4.1(d-f)), wheat-2013 experienced a total rainfall of 910 mm which was 320 mm more than the average of the other wheat-years. Consequently, the average air temperature recorded over this particular year was 5% lower than the averages of the other wheat years. On the other hand, wheat-2011 was particularly warm in spring, due to low rains, and this year recorded air temperatures that were 7%, 16%, and 11% higher than the combined average of the other wheat-years in the months March, April, and May, respectively. Furthermore, the seasonal variability of the leaf area is significant Figure 4.1f. Wheat-2009 suffered the worst development with *LAI* that barely reached 2.3 m^2 m^{-2}, while in 2011, it peaked at 6.8 m^2 m^{-2}.

4.3.1.2 Energy balance closure

Maize

Figure 4.2(a) shows the monthly closure (box plot) and residual energy (black circles) of the maize years. The spring months had the lowest mean closure (median of 0.61 in April), while a better closure is observed in summer (0.73 in August) when vegetation is fully developed. Also, the average monthly residual energy varied between 37 and 51 W m^{-2} with the smallest and largest residual term found in maize-2015 (22 W m^{-2}) and 2008 (70 W m^{-2}) respectively.

Wheat

The EBC for the wheat years ranged between 0.4 (winter of wheat-2009, wheat-2010, and wheat-2011) and 0.9 (spring of wheat-2013). Also, *Res* was between 30 W m^{-2} and 83 W m^{-2}, the largest imbalance coincided with summer, while the lowest *Res* was found in the winter months. This seasonality has been described in chapter 3.

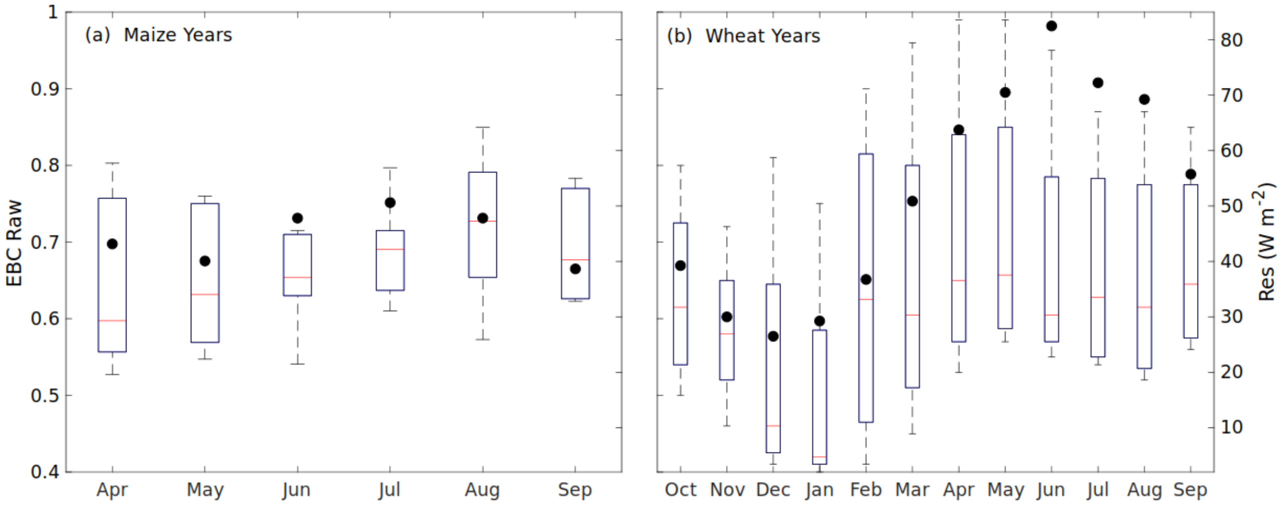

Figure 4.2: The monthly mean energy balance closure (in box plot) and the average residual energy (in black circles) using the raw turbulent fluxes over (a) maize, and (b) wheat.

These values are within those reported over croplands in this region (Imukova et al., 2016; Masseroni et al., 2014); Eshonkulov et al., 2019), which shows good data quality from the EC. Notwithstanding, owing to the non-closure (i.e., EBC < 1), a correction technique must be applied before a good model-data comparison can be made. Amidst the existing flux correction techniques (e.g., residual method (Simmons et al., 2007), regression method (Allen, 2008) etc), this study chose the Bowen ratio correction (Twine et al., 2000) because certain studies carried out over croplands have reported a successful forcing to closure of EC measurements using this approach (Teixeira and Bastiaanssen, 2012; Chebbi et al., 2018). More importantly, this approach assumes that the Bowen ratio (β) is correctly preserved by the EC system, and so, it distributes the deficit energy into both the latent and the sensible heat fluxes using Equation (4.3a) and (4.3b), respectively.

$$LE_{Corr} = \frac{(Rn - G)}{(1 + \beta)} \tag{4.3a}$$

$$H_{Corr} = \frac{(Rn - G)}{[1 + 1/\beta]} \tag{4.3b}$$

β is expressed as $\gamma(\Delta T/\Delta e)$ where γ is the psychometric constant in kPa °C^{-1}, ΔT is the vertical temperature gradient in °C, and Δe measured in kPa is the vertical water vapor pressure gradient. As expected, after correction, Figure 4.3 shows an improved closure (EBC > 0.8 and Res < 14 W m^{-2}). Hence, in subsequent sections, these corrected fluxes would be referred to as *in-situ* measurements and would be used in the evaluation of ISBA and ISBA-MEB. The monthly EBC values and the corresponding Res for each crop year can be found in Tables B1-B4 of Appendix B for both the raw and corrected fluxes.

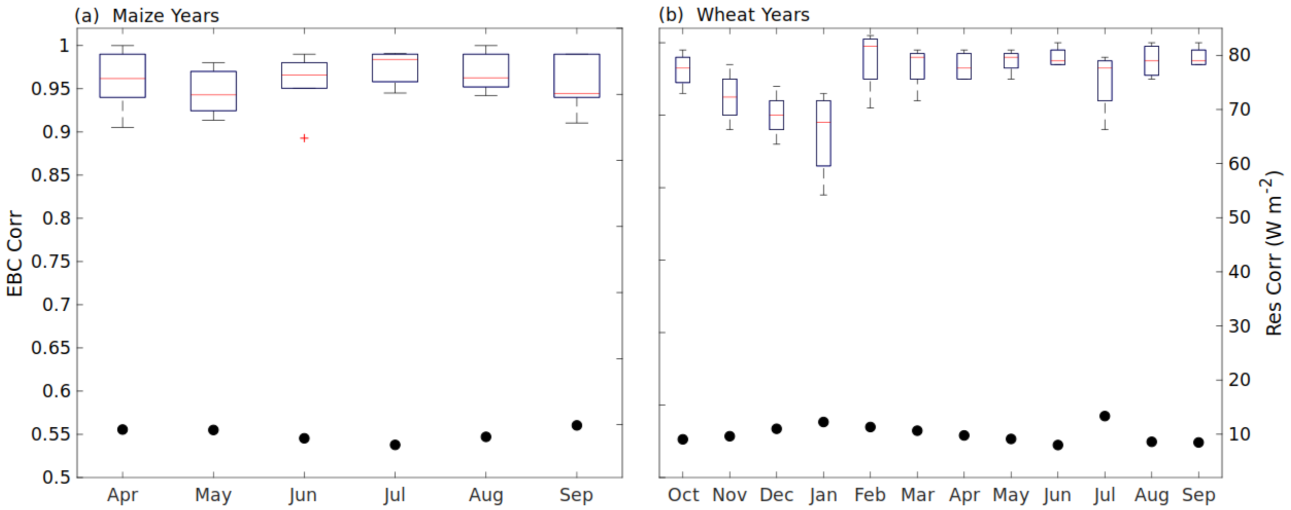

Figure 4.3: The monthly mean energy balance closure (in box plot) and the average residual energy (in black circles) of the corrected turbulent fluxes from the Bowen ratio method for (a) maize, and (b) wheat.

4.3.2 Assessment of the ISBA and ISBA-MEB models

4.3.2.1 The Energy Budget

This section evaluates the performance of ISBA and ISBA-MEB, it presents 2-days average time series of Rn, LE, H, and G between 12h and 15h 30 over maize (Figure 4.4) and wheat (Figure 4.5). Similarly, the statistical metrics comparing the performance of ISBA with ISBA-MEB in the prediction of Rn is summarized in Table 4.2, while the scores for the other energy components are shown in Figure (4.6) at half-hourly resolutions.

Maize

1. Net radiation

Both configurations have good agreement with the observations, and the seasonal dynamics were properly reproduced (Figure 4.4a) with R^2 between 0.96 and 0.98, while the mean absolute error (MAE) is lower than 32 W m^{-2} (Table 4.2)..This was expected as albedo is the main governing parameter, and it has been calibrated based on the on-site measurement of the incoming and outgoing shortwave radiation. Also, metrics of both models are close; although, on average, RMSE is lower in ISBA-MEB (Table 4.2). Considering that the shortwave component of Rn is computed similarly in both models, this observed difference might have arisen from the outgoing longwave component seen in the difference between the composite (surface) temperature predicted by ISBA and the explicit (soil and vegetation) temperatures predicted by ISBA-MEB (not shown).

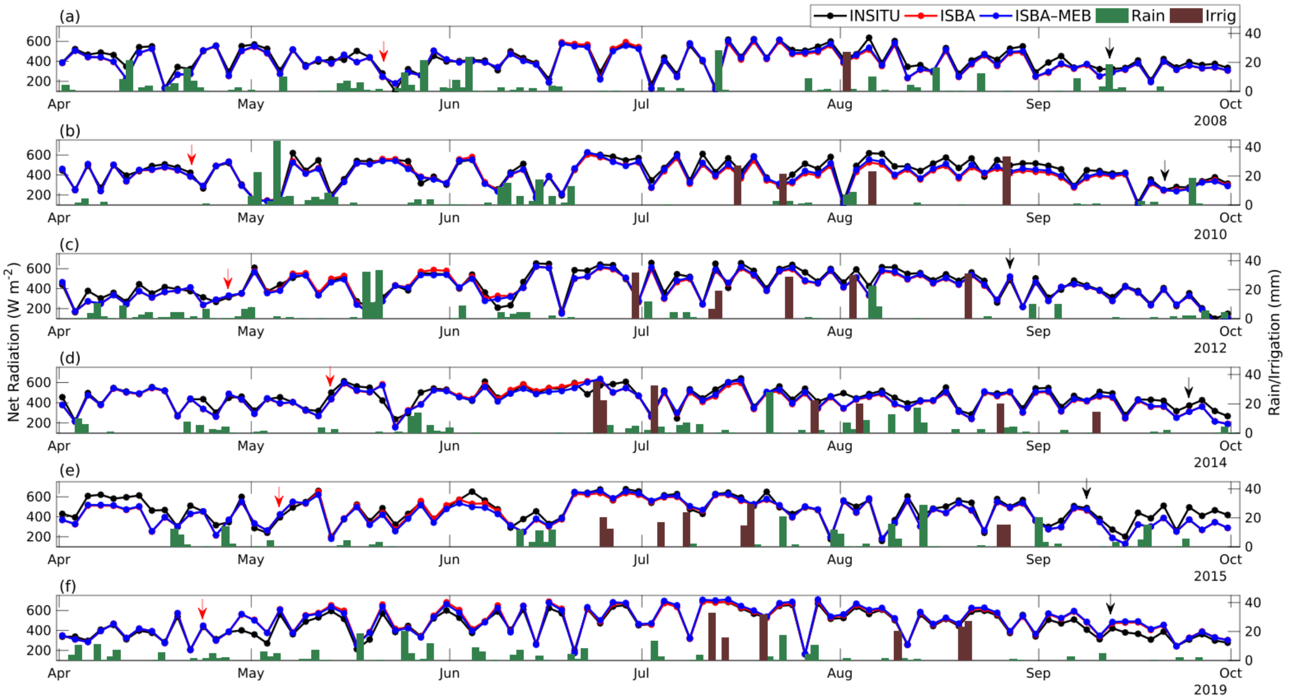

Figure 4.4a: 2days-average daytime series of the *in-situ* net radiation (*Rn*) measurements (in black) with those estimated by ISBA (in red), and ISBA-MEB (in blue). Panels (a-f) represent plots for maize-2008, maize-2010, maize-2012, maize-2014, maize-2015, and maize-2019, respectively. The red and black arrows signify the planting, and the harvest days, respectively.

2. The latent heat and sensible heat flux

During the early crop stages (Apr and May), *LE* showed weak values in response to *Rn*'s magnitude (Figure 4.4b). Afterwards, and up until harvest, a minimum of 70 W m^{-2} is maintained due to the transpiring plants, and high soil humidity. The seasonal dynamics including the magnitude of the *in-situ LE* were well captured, while the difference between both model configuration is small on average (Figure 4.4b). However, ISBA-MEB performed better with R^2 between 0.80 and 0.88 while for ISBA, R^2 over every maize year was consistently lower as observed in Figure (4.6).

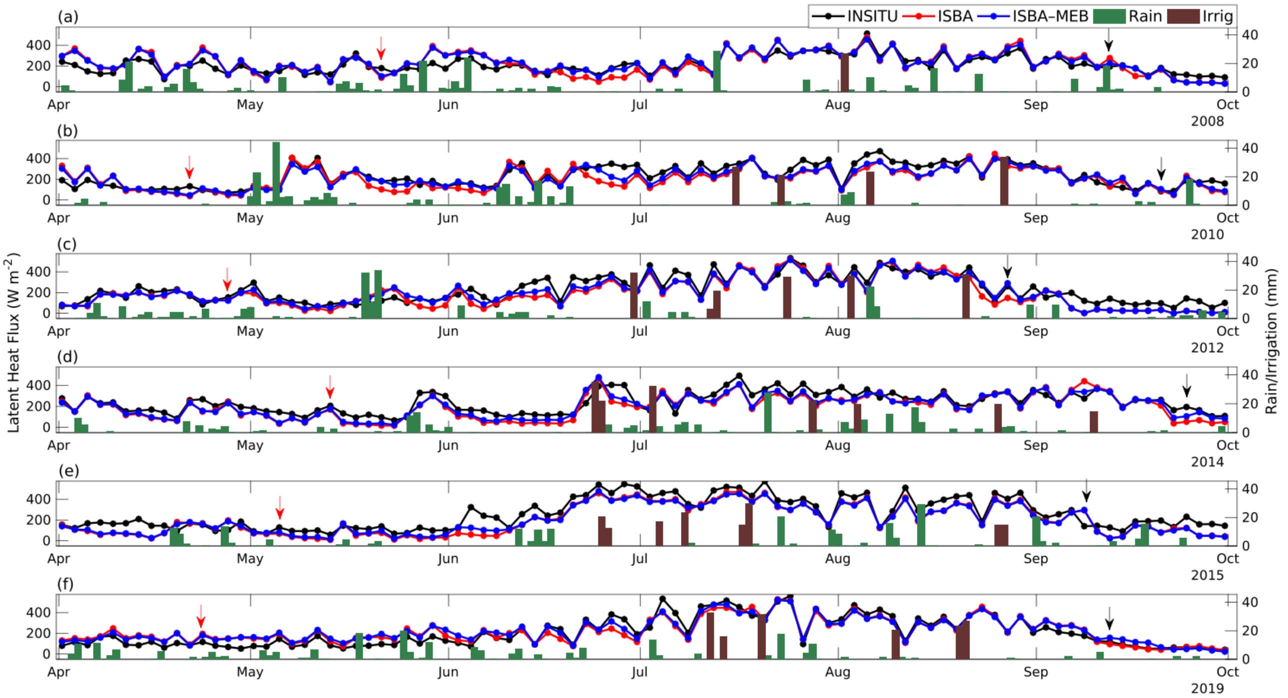

Figure 4.4b: The same as Figure 4.4a, but for the latent heat flux.

Interestingly, ISBA was unable to capture the transition period from low crop to developed crop when the heterogeneity of the field was high leading to a large underestimation with a mean MAE of 69 W m^{-2} during this period in comparison to ISBA-MEB (48 W m^{-2}). During these transition periods, RMSE in ISBA (49 W m^{-2}) was 28% higher than that of ISBA-MEB (38 W m^{-2}). Afterwards, after homogeneity had been restored, estimates of both models were again similar apart from some small discrepancies during senescence. This is consistent with the findings of Napoly et al. (2017) who observed that for 87% of their forested sites, the difference between the RMSE of ISBA and ISBA-MEB is more significant for sites with low leaf area.

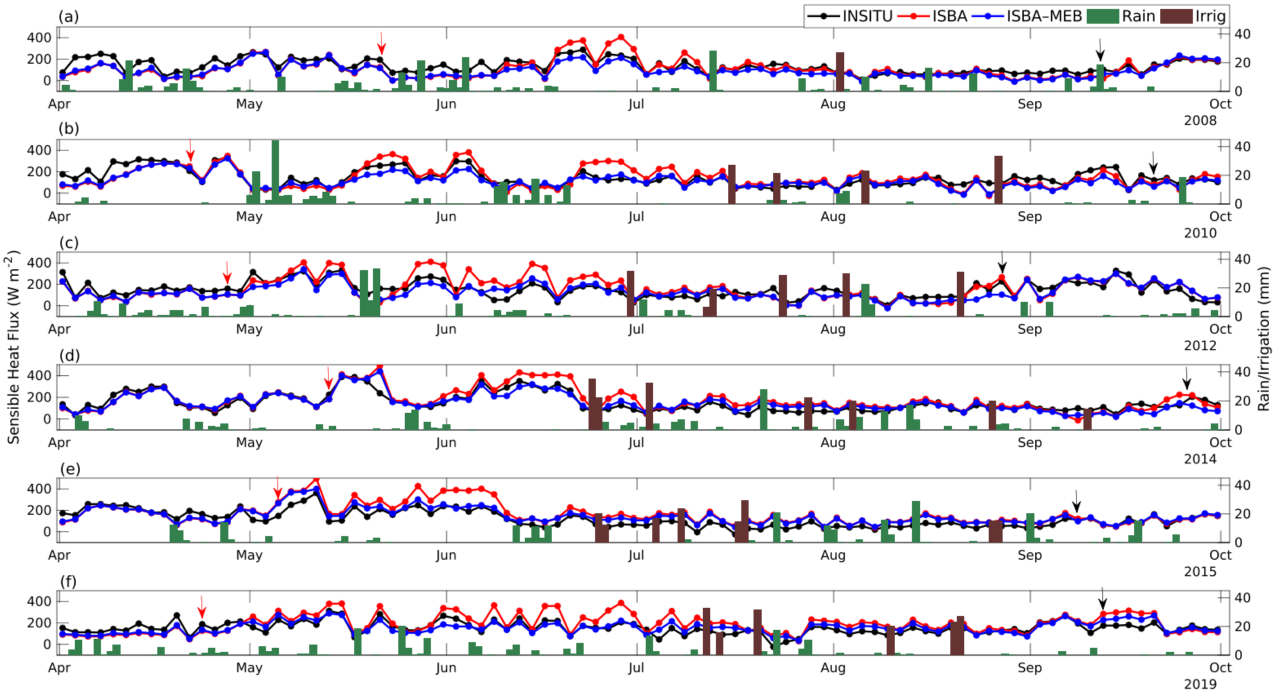

Figure 4.4c: The same as Figure 4.4a, but for the sensible heat flux.

Similar conclusions can be drawn from the time series of *H* (Figure 4.4c). Between April and May, when the site is almost bare, both models estimated similar values. During the aforementioned transition period, a notable discrepancy is observed, characterized by an over-estimation by ISBA- ~43 W m^{-2}, 38 W m^{-2}, 57 W m^{-2}, 56 W m^{-2}, 59 W m^{-2}, and 41 W m^{-2} for maize-2008, maize-2010, maize-2012, maize-2014, maize-2015, and maize-2019, respectively while the estimates of ISBA-MEB were in better agreement with *in-situ* measurements (bias was between 7 and 39 W m^{-2}). A similar observation was reported over an olive orchard in Aouade et al. (2019) who observed better prediction of convective fluxes by ISBA-MEB over open canopies characterized by a mix of vegetation and bare soils directly exposed to incoming radiation. ISBA-MEB, having a dual-source configuration couples both heat sources; thus, it is better suited during these phases of transition. Overall, R^2 of ISBA ranges from 0.66 to 0.78, whereas for ISBA-MEB, it is between 0.68 and 0.80.

3. The ground heat flux

Figure 4.4d shows that the models' prediction were in close in good agreement with *in-situ* data. The statistics (Figure 4.6) reveal that the accuracy of *G* by ISBA is lower than that of ISBA-MEB as R^2 on average increased from 0.76 to 0.83, while RMSE reduced from 35 W m^{-2} to 33 W m^{-2}.

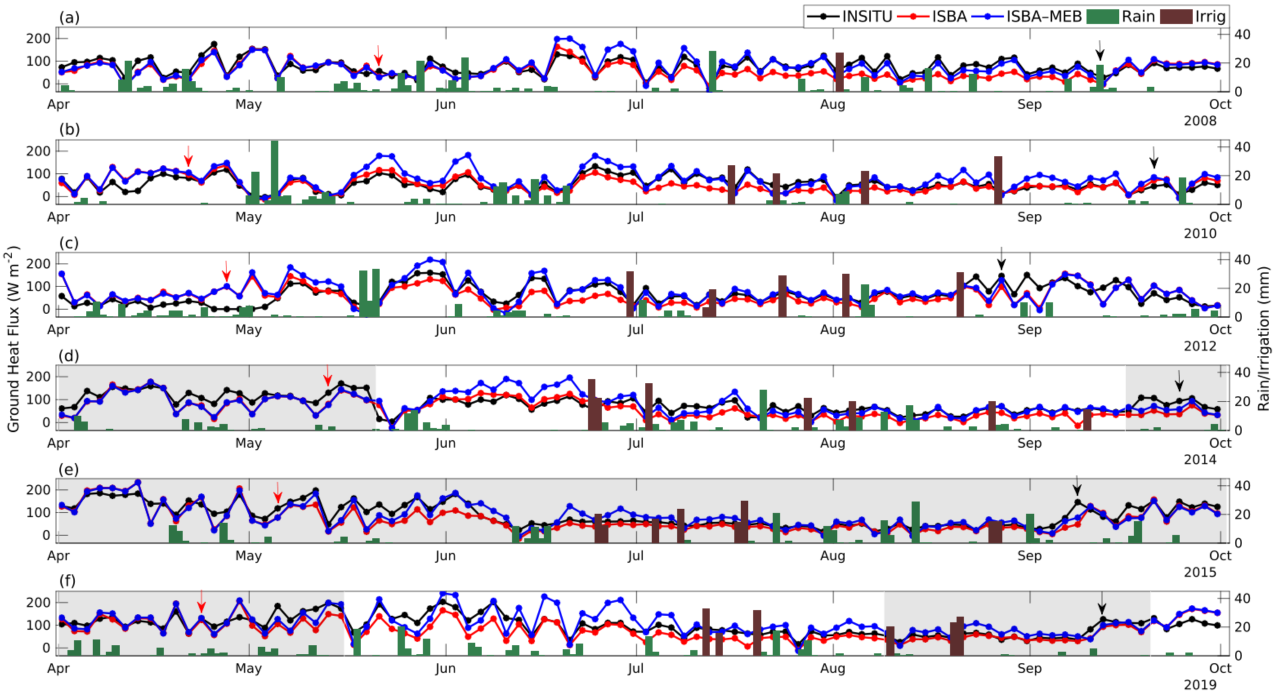

Figure 4.4d: The same as Figure 4.4a, but for the ground heat flux. The grey sectors represent periods when *in-situ* G was computed empirically (see section 4.2).

Wheat

1. The net radiation

Figure 4.5a shows the time series of the observed and simulated Rn over wheat. This component is well simulated for all the years as R^2 was close to 1. Similarly, the RMSEs and MAEs were within acceptable range; not higher than 33 W m^{-2} and 27 W m^{-2}, respectively. As observed in maize, the prediction difference between ISBA and ISBA-MEB is insignificant as the maximum difference between the RMSE and MAE is below 2 W m^{-2} respectively (see Table 4.2).

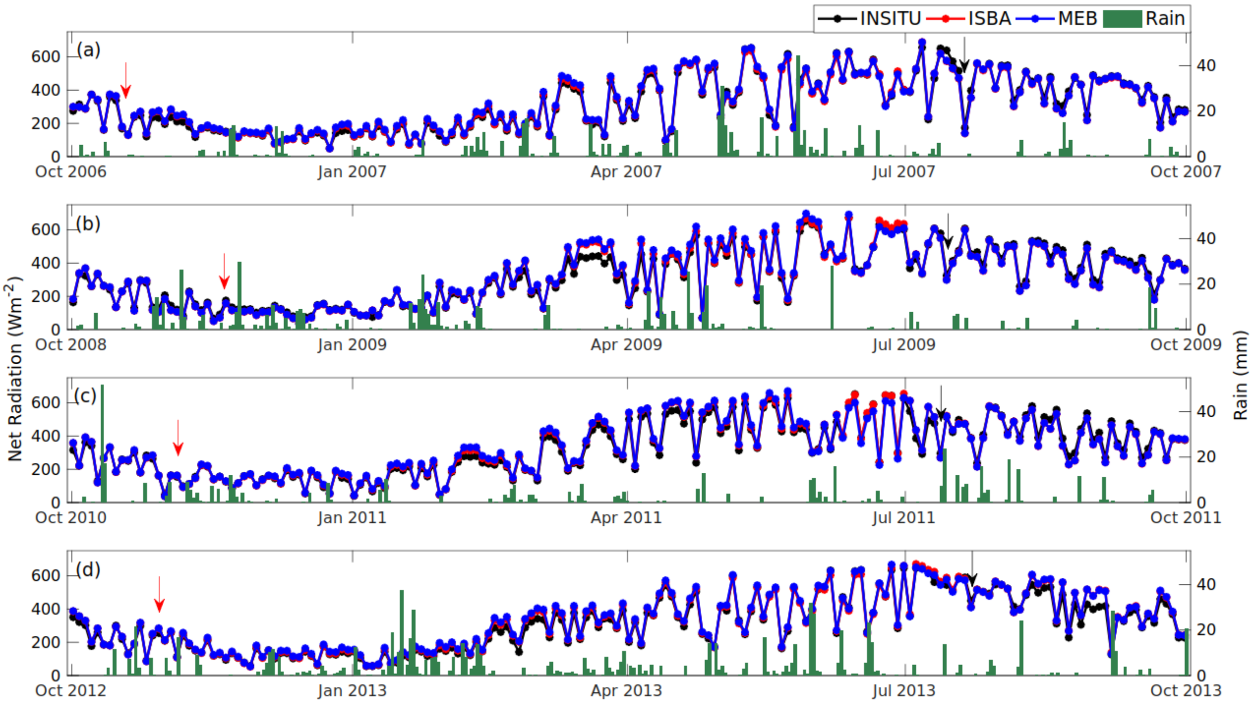

Figure 4.5a: 2days-average daytime series of the *in-situ* net radiation (*Rn*) measurements (in black) with ISBA's estimates (in red), and ISBA-MEB (in blue). Panels (a-d) represent plots for wheat-2007, wheat-2009, wheat-2011, and wheat-2013, respectively. The red and black arrows are the planting, and the harvest days, respectively.

Table 4.2: Statistics comparing the net radiation estimated by ISBA and ISBA-MEB against *in-situ* measurements at half-hourly time step over maize, and wheat. RMSE and MAE (in W m^{-2})

Crop		**Score/Year**	**2008**	**2010**	**2012**	**2014**	**2015**	**2019**
Maize	ISBA	R^2	0.97	0.98	0.96	0.96	0.97	0.96
		RMSE	34	33.4	42.7	46.6	40.6	44.2
		MAE	25	22.1	27.5	28.3	29.5	30.1
	ISBA-MEB	R^2	0.98	0.98	0.96	0.96	0.97	0.96
		RMSE	33.5	32.2	41.7	46.7	39.7	43.0
		MAE	27.5	22.6	28.2	29.4	29.9	31.7
Wheat	ISBA	**Score/Year**	**2007**	**2009**	**2011**	**2013**		
		R^2	0.97	0.97	0.97	0.97		
		RMSE	31.3	30.7	31	31.2		
		MAE	23	24.7	22.5	20.6		
	ISBA-MEB	R^2	0.97	0.98	0.97	0.97		

		RMSE	32.5	31.2	32.2	31.8		
		MAE	24	26.2	23.9	22		

2. The latent heat and sensible heat flux

Both models reproduced the magnitude and dynamics of *LE* fairly-well but with a strong underestimation in wheat-2011 and wheat-2013 between April and July (see Figure 4.5b). This poor performance in wheat-2013 could be linked to instrumental errors. Nonetheless, as indicated by the metrics (Figure 4.6), ISBA-MEB outperformed ISBA except for wheat-2011. For the these years, in terms of R^2, ISBA-MEB was at least 3% higher than ISBA. Similarly, the RMSE was lower in ISBA-MEB in comparison to ISBA by 9%, 8%, 3%, and 11% for wheat-2007, wheat-2009, wheat-2011, and wheat-2013, respectively.

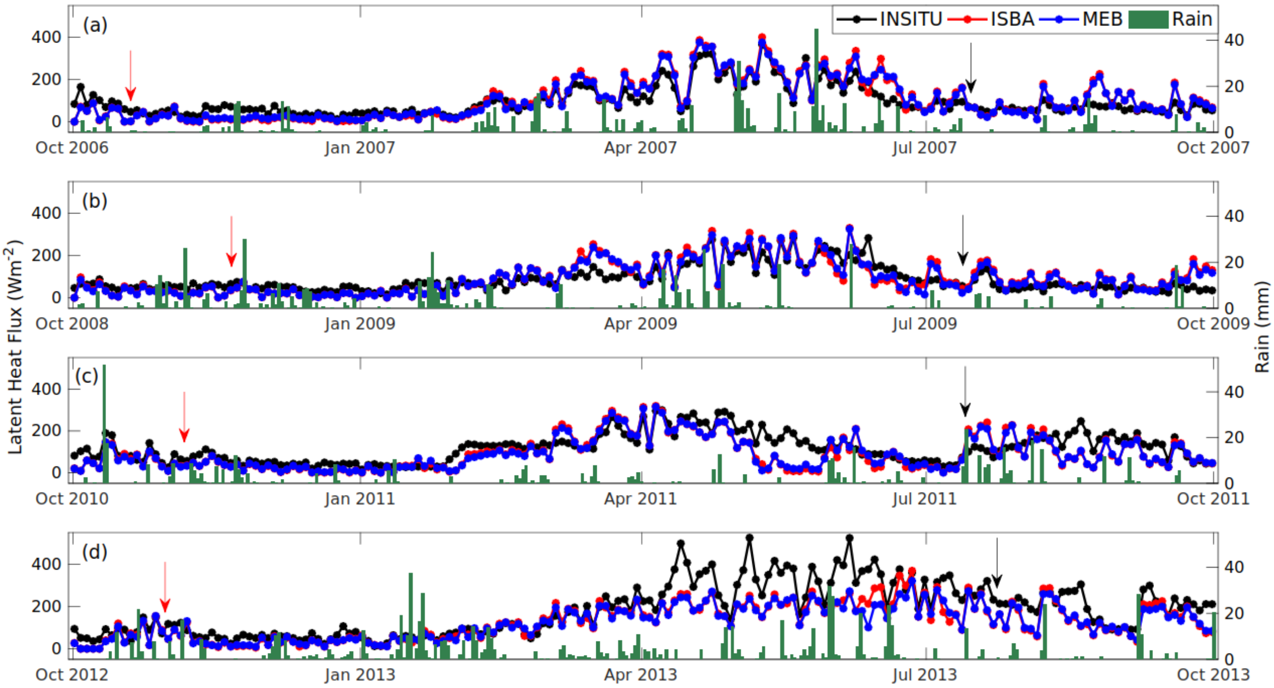

Figure 4.5b: The same as Figure 4.5a, but for the latent heat flux.

As in Figure 4.5c, between April and July, both models strongly overestimated *H*, with a larger disadvantage to ISBA particularly in June (for wheat-2009), and in May (for wheat-2011). These periods represent the senescence phase in the wheat plant. Monocarpic senescence is the advancement in the age of plant parts, and it is the final stage in wheat development. This process is often accompanied by color change, water loss, and subsequent shrinkage of plant (Buchanan-Wollaston, 2007; Wojciechowska et al., 2017). In the event of shrinkage, the fraction of the soil exposed to solar radiation is increased, subsequently increasing the plot's heterogeneity. Similarly, the radiative properties of the plants change at this time, although, in this study, a constant albedo is maintained for each crop year. During these senescing periods, H-ISBA exceeded the estimates of H-ISBA-MEB by at least 50 W m^{-2}. This behavior could not be observed in maize because they are harvested green. Overall, during the active vegetative period, both models had difficulty reproducing the magnitude of the observation. ISBA presents a larger dispersion with RMSE ranging between 33 and 46 W m^{-2}; whereas it was slightly reduced in ISBA-MEB by 2%, 20%, 5%, and 3%, for wheat-2007, wheat-2009, wheat-2011, and wheat-2013 respectively.

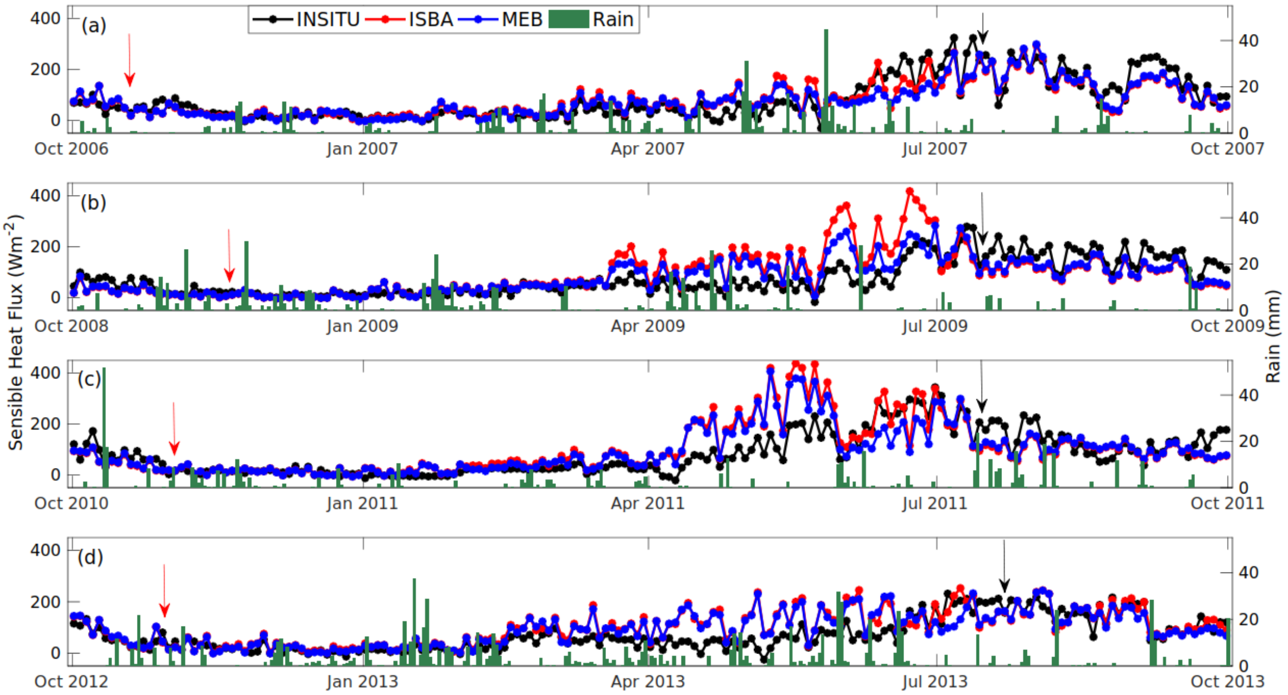

Figure 4.5c: The same as Figure 4.5a, but for the sensible heat flux.

3. The ground heat flux

In contrast to the expectation of a strong overestimation of G by ISBA given the fact that ISBA propagates more energy into the soil substrate via conduction (Napoly et al., 2017), estimates of ISBA were closer to the observation especially between spring and summer (Figure 4.5d). For the other periods, estimates of ISBA and ISBA-MEB were similar. This similarity could be related to the absence of litter at our study site. The litter option is a major parameterization within ISBA-MEB, and it strongly influences the ground heat flux. Due to the insignificant litter-layer in FR-Lam, this option was disabled for the ISBA-MEB experiment. Unfortunately, this hypothesis could not be tested in this study, and so, it is recommended for future work. Similarly, the partitioning of the surface temperature into the soil in ISBA-MEB was not analyzed; hence, the large conductive heat flux including the discrepancies between both models could not be investigated. Nevertheless, large uncertainties had always surrounded the prediction of G owing to the difficulty in obtaining it *in-situ*. On average, in terms of RMSE, ISBA outperformed ISBA-MEB by 4%, 9% , 2%, and 0.5% in wheat-2007, wheat-2009, wheat-2011, and wheat-2013, respectively (see Figure 4.6).

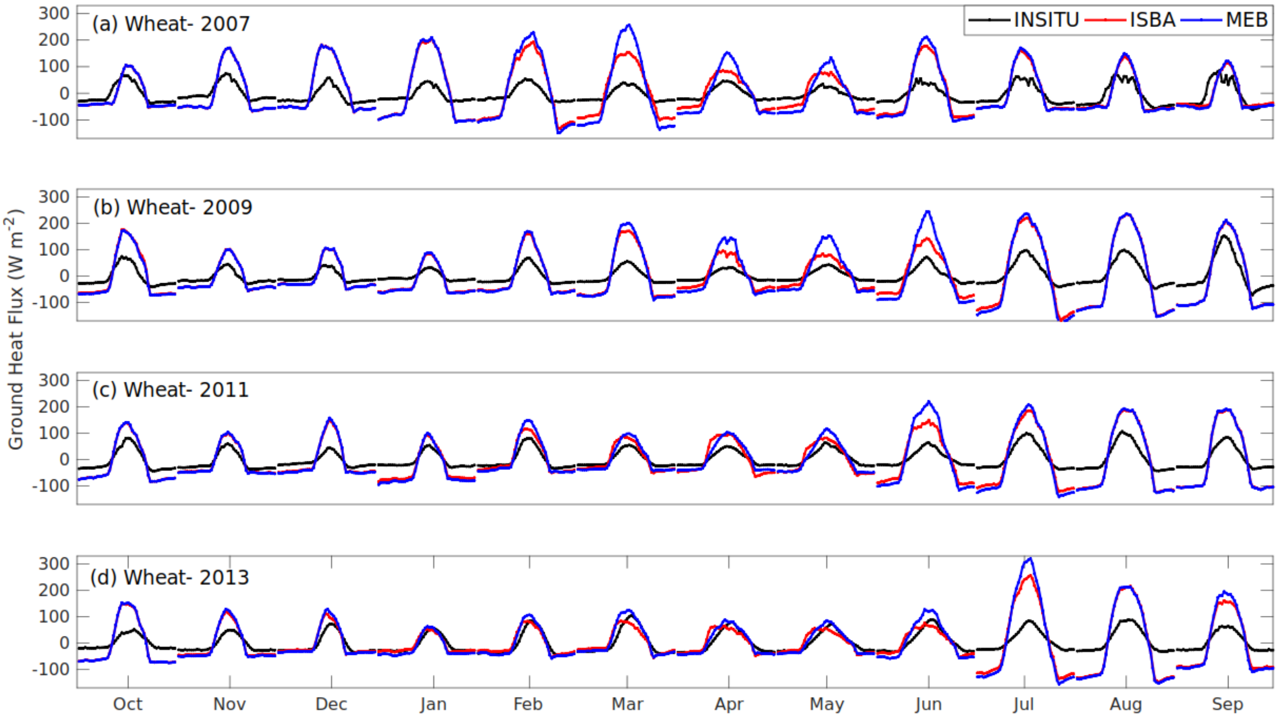

Figure 4.5d: Composite monthly diurnal cycles comparing the *in-situ* ground heat flux (in black) with those estimated by ISBA (in red), and ISBA-MEB (in blue) for wheat-2007, wheat-2009, wheat-2011, and wheat-2013.

The statistical metrics proves that: (1) ISBA-MEB is better suited for the surface energy fluxes at FR-Lam. (2) Both models performed excellently well over bare soils, and low-crop periods- while for active vegetation periods, both models performed much better in maize than in wheat.

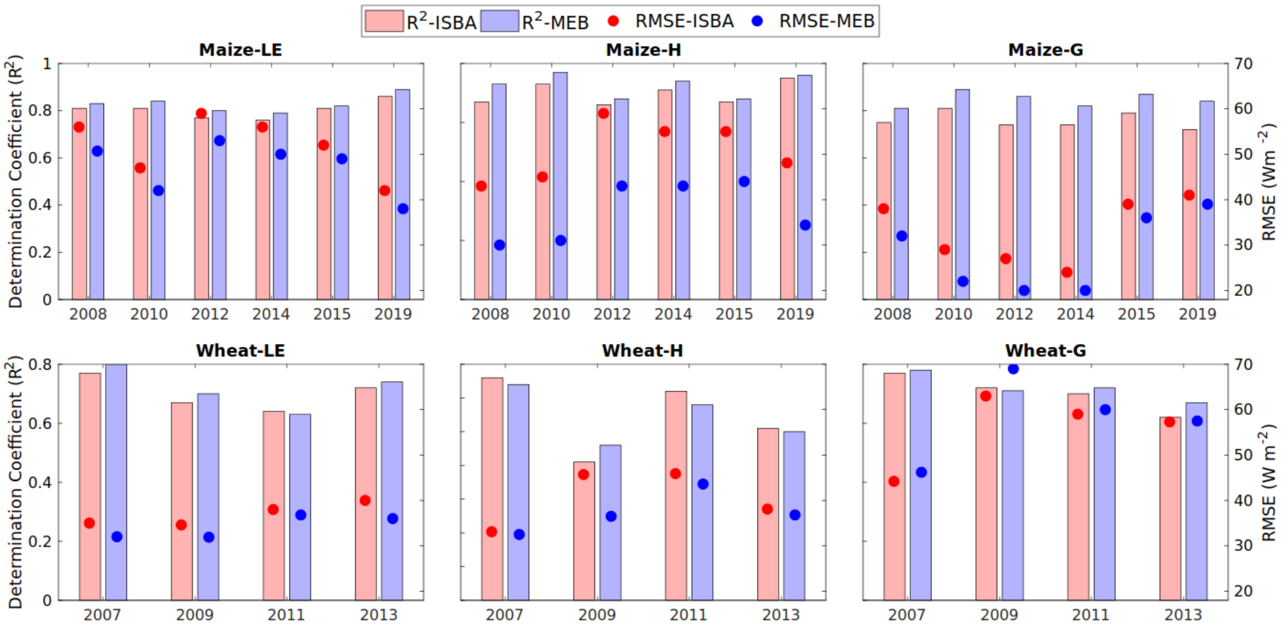

Figure 4.6: Statistical metrics (RMSE and R^2 are circles and bars respectively) obtained from the linear regression of half-hourly estimates of the model (ISBA in red and ISBA-MEB in blue) vs the EC measurements.

4.3.2.2 The soil moisture

Soil moisture is a variable that integrates all water balance components, and so, the ability of ISBA and ISBA-MEB to reproduce the soil water at both superficial and deep layers is evaluated in this section. For illustration purposes, Figure 4.7 shows the daily time series of the observed and the predicted soil water content during the sap flow campaign. It is observed that at all the layers, the model responded to all rain events. The model explains 81%, 77%, and 84% of the observed soil water at 0 cm, 5 cm, and 50 cm depth, respectively. At 10 and 30 cm, a poor agreement ($R^2 < 0.40$) was found- this could be due to the large clay content just above the 10 cm depth that limits water infiltration, although, the presence of cracks permitted water redistribution. For the other crop years, Table 4.3 and Table 4.4 present the metrics at all depths for maize and wheat, respectively.

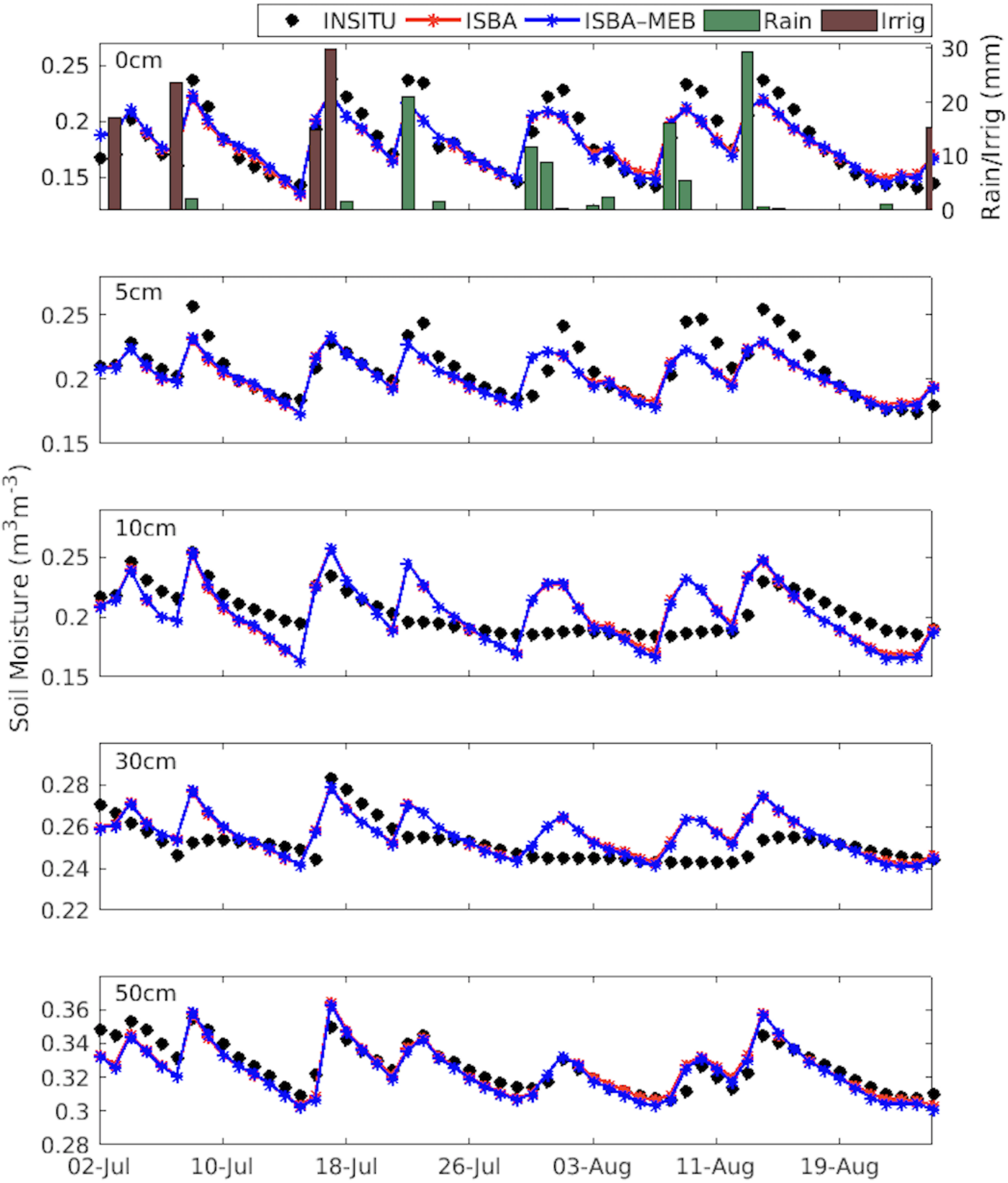

Figure 4.7: Daily series of the *in-situ* soil moisture and estimates of ISBA and ISBA-MEB at 0, 5, 10, 30, and 50 cm with total rainfall (+ irrigation) during the sap flow campaign (01/07 – 25/08 2015).

From Tables 4.3 and 4.4, it is observed that (i) the ability of both models to predict soil moisture is very variable from one year to another, (ii) better prediction is obtained from ISBA-MEB, with higher R^2 values in 60%, 80%, 75%, and 75% of the cases at 0 cm, 10 cm, 30 cm and 50 cm depth, respectively in maize. Also, metrics is better in ISBA-MEB over wheat.

Table 4.3: Statistical metrics comparing estimates of ISBA and ISBA-MEB with the field measurements for maize at a half-hourly time step. (RMSE and MAE are in m^3 m^{-3}).

Year	indicator	model	0cm	5cm	10cm	30cm	50cm	100cm
Maize-2008	R^2	ISBA	-	0.77	0.80	0.71	-	0.30
		ISBA-MEB	-	0.77	0.79	0.75	-	0.30
	RMSE	ISBA	-	0.024	0.021	0.019	-	0.029
		ISBA-MEB	-	0.026	0.023	0.019	-	0.032
	MAE	ISBA	-	0.026	0.032	0.053	-	0.060
		ISBA-MEB	-	0.029	0.037	0.056	-	0.062
Maize-2010	R^2	ISBA	-	0.60	0.71	0.46	-	0.40
		ISBA-MEB	-	0.59	0.76	0.51	-	0.39
	RMSE	ISBA	-	0.033	0.024	0.022	-	0.022
		ISBA-MEB	-	0.035	0.024	0.023	-	0.025
	MAE	ISBA	-	0.027	0.019	0.037	-	0.035
		ISBA-MEB	-	0.029	0.020	0.038	-	0.037
Maize-2012	R^2	ISBA	0.40	0.59	0.40	0.30	0.91	0.32
		ISBA-MEB	0.40	0.63	0.49	0.30	0.89	0.31
	RMSE	ISBA	0.060	0.032	0.032	0.025	0.019	0.027
		ISBA-MEB	0.062	0.034	0.034	0.025	0.023	0.033
	MAE	ISBA	0.059	0.031	0.039	0.025	0.065	0.045
		ISBA-MEB	0.064	0.033	0.04	0.025	0.079	0.052
Maize-2014	R^2	ISBA	0.42	0.42	0.68	0.33	0.73	0.38
		ISBA-MEB	0.46	0.40	0.76	0.36	0.77	0.47
	RMSE	ISBA	0.046	0.018	0.024	0.015	0.011	0.008
		ISBA-MEB	0.049	0.019	0.023	0.015	0.012	0.008
	MAE	ISBA	0.037	0.027	0.024	0.022	0.027	0.016
		ISBA-MEB	0.039	0.026	0.025	0.022	0.032	0.019
Maize-2015	R^2	ISBA	0.65	0.57	0.30	0.30	0.48	0.69
		ISBA-MEB	0.71	0.64	0.30	0.26	0.51	0.69
	RMSE	ISBA	0.031	0.021	0.031	0.017	0.013	0.007
		ISBA-MEB	0.023	0.022	0.032	0.029	0.016	0.010

	MAE	ISBA	0.027	0.017	0.045	0.033	0.011	0.013
		ISBA-MEB	0.036	0.018	0.043	0.030	0.015	0.017
Maize-2019	R^2	ISBA	0.31	0.46	0.53	0.41	0.62	0.58
		ISBA-MEB	0.30	0.45	0.54	0.41	0.67	0.57
	RMSE	ISBA	0.043	0.036	0.014	0.023	0.023	0.012
		ISBA-MEB	0.045	0.038	0.017	0.026	0.043	0.016
	MAE	ISBA	0.046	0.033	0.026	0.023	0.034	0.031
		ISBA-MEB	0.051	0.036	0.024	0.025	0.036	0.036

Table 4.4: Statistical metrics comparing estimates of ISBA and ISBA-MEB with the field measurements for wheat at a half-hourly time step. (RMSE and MAE are in m^3 m^{-3}).

Year	indicator	model	0cm	5cm	10cm	30cm	50cm	100cm
Wheat-2007	R^2	ISBA	-	0.46	0.47	0.34	-	0.22
		ISBA-MEB	-	0.47	0.46	0.34		0.24
	RMSE	ISBA	-	0.023	0.02	0.02	-	0.03
		ISBA-MEB	-	0.023	0.02	0.02	-	0.03
	MAE	ISBA	-	0.13	0.13	0.16	-	0.16
		ISBA-MEB	-	0.13	0.13	0.16	-	0.16
Wheat-2009	R^2	ISBA	-	0.74	0.70	0.57	-	0.42
		ISBA-MEB	-	0.70	0.68	0.59		0.41
	RMSE	ISBA	-	0.019	0.018	0.02	-	0.03
		ISBA-MEB	-	0.021	0.02	0.02	-	0.03
	MAE	ISBA	-	0.14	0.13	0.14	-	0.14
		ISBA-MEB	-	0.14	0.13	0.14	-	0.14
Wheat-2011	R^2	ISBA	-	0.25	0.23	0.53	-	0.26
		ISBA-MEB	-	0.26	0.24	0.54		0.26
	RMSE	ISBA	-	0.04	0.04	0.03	-	0.04
		ISBA-MEB	-	0.04	0.04	0.03	-	0.04
	MAE	ISBA	-	0.13	0.12	0.15	-	0.12
		ISBA-MEB	-	0.13	0.12	0.15	-	0.12

Wheat-2013	R^2	ISBA	0.58	0.78	0.55	0.58	0.66	0.58
		ISBA-MEB	0.63	0.83	0.58	0.59	0.66	0.59
	RMSE	ISBA	0.030	0.017	0.02	0.02	0.02	0.02
		ISBA-MEB	0.028	0.015	0.02	0.02	0.02	0.02
	MAE	ISBA	0.044	0.044	0.05	0.05	0.07	0.09
		ISBA-MEB	0.043	0.043	0.05	0.05	0.07	0.09

4.3.2.3 Transpiration

The LE from EC systems representing the ET is the composite of Tr, Es, and Ei. While ET highlights the amount of water vapor efflux from terrestrial surfaces, quantification of its constituents is required for a proper understanding of the land-surface feedback to available energy and water input. Studies have shown that these constituents respond differently to environmental drivers. For instance, Ei relies on both the canopy's structural density, and the precipitation characteristics (Miralles et al., 2010), Tr is a function of the plant functioning type, the leaf area, the evaporative demand, and the plant's access to underground reservoirs (Reynolds et al., 2000; Berg and Sheffield, 2019), while Es depends on the soil cover, the precipitation characteristics, and the evaporative demand as well (Cavanaugh et al., 2011). Several direct and indirect ET partitioning methods exists. The direct approaches involves separate measurement of Es (with soil chambers or microlysimeters), and Tr (with plant chambers, or sap flow sensors), while the indirect methods include the stable isotope technique, modeling etc (see Yepez et al., 2003; Wang et al., 2010; Fatichi and Pappas, 2017 for reviews). In this section, the plant transpiration measured by the sap flow method is compared with the partitioned estimates of ISBA and ISBA-MEB.

Figure 4.8 presents the daily transpiration over maize (Figure 4.8a), the mean diurnal cycles by 14-days period (Figure 4.8b), and the cumulative values over this period (Figure 4.8c). When compared with the total ET (not shown), daily ET lies between 1.6 and 9.5 mm while the sap flow ranged between 0.13 and 7.36 mm. Over this period, transpiration represents 88%, 84%, and 87% of total ET for the *in-situ* data, ISBA, and ISBA-MEB estimates, respectively. These are close to literature values reported over mature irrigated maize e.g., in Zhou et al. (2017), which showed that during the vegetation peak (LAI = 4 m^2 m^{-2}) for maize in northern China, transpiration reached 75% of the total ET; considering that LAI is above 6.3 m^2 m^{-2} in our study. As soil moisture impacts transpiration, cold fronts indicated by low incoming radiation and cool air temperature (both not shown) resulted in a drop in sap flow on the 30th of July, 9th of August, and 14th of August. Likewise, a gentle decline in transpiration is observed in early August due to commencement of senescence.

Figure 4.8b highlights the ability of both models to effectively reproduce the daily dynamics and magnitude of the sap flow with no strong time-shift apart from an earlier drop in transpiration from midday which is prominent during the first half of August. Both models overestimated transpiration during the first period, and under-estimated it afterwards as seen in Figure 4.9c. Over this campaign period, both models underestimated transpiration by about 24 mm with a slight advantage to ISBA-MEB. Table 4.5 presents the metrics, and it shows that the estimates of both models are similar. This similarity could be because the campaign was carried out over a mature and homogeneous maize field ($LAI > 4$ m^2 m^{-2}). Nevertheless, a slightly better estimation was provided by ISBA-MEB with R^2 of 0.91 and a lower RMSE of 0.071 mm h^{-1}; whereas, ISBA has R^2 of 0.90 and RMSE of 0.074 mm h^{-1}.

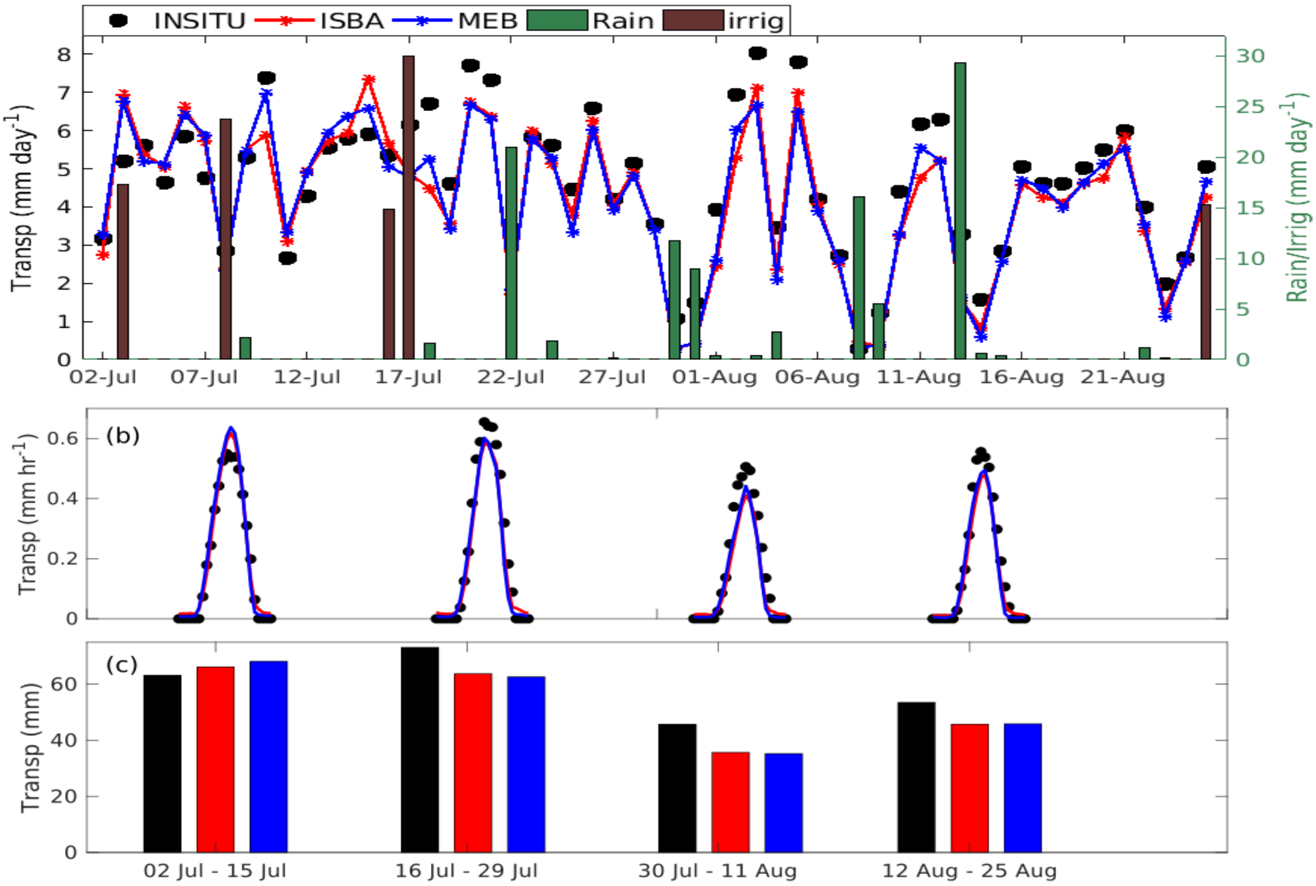

Figure 4.8: (a) Daily series comparing sap flow measurements (black) with estimates of ISBA (red) and ISBA-MEB (blue) and the cumulative rainfall and irrigation between 2 July and 25 August 2015. (b) Diurnal trend of transpiration averaged over a 13/14 days' periods. (c) Comparison of the cumulative transpiration over the period in panel (b).

Table 4.5: Statistical scores on an hourly scale between the sap flow measurements and estimates of ISBA and ISBA-MEB from 02/07/2015-25/08/2015.

Model	**R^2**	**RMSE (mm h^{-1})**	**MAE (mm h^{-1})**
ISBA	0.90	0.074	0.052
ISBA-MEB	0.91	0.071	0.048

4.3.3 Inter-annual variability of the water budget

Having established the good partitioning ability of the models, this section investigated the inter-annual variability of the ET components. Only the estimates of ISBA-MEB is presented here as it gave better metrics in the previous section.

Evapotranspiration partitioning over maize

Figure 4.9a shows a strong year-to-year variability of the ET components. For example, Es is the dominating component in maize-2008 accounting for over 52% of total ET, while Tr barely reached 40%. In maize-2010, a very close contribution of Tr and Es is observed. These two years are characterized by poor canopy development (maximum LAI below 4.1 m^2 m^{-2}), and a late growth attributed to the prevailing climate and the sown cultivar. Similarly, the air temperature which was about 10% higher than that of the other maize years enhanced soil evaporation in maize-2008 especially in May and June (see Figure 4.9b). In maize-2008, maize-2010, and maize-2012, Es was never lower than 10% of ET, even at the peak of vegetation. On the other hand, in September of maize-2014, July of maize-2015, and August of maize-2019, which represent the peak months, Es consumed less than 3.5% of ET. This behavior is related to the high vegetation cover, which reduced the available energy for soil evaporation. Overall, maize-2015 has the highest Tr of 344 mm and lowest Es of 136 mm due to the high LAI, favorable temperature, and well-distributed rainfall. An examination of the relationship between LAI and Tr showed a strong positive correlation coefficient ranging from 0.60 to 0.79 on a daily scale (see Figure B1 in Appendix B).

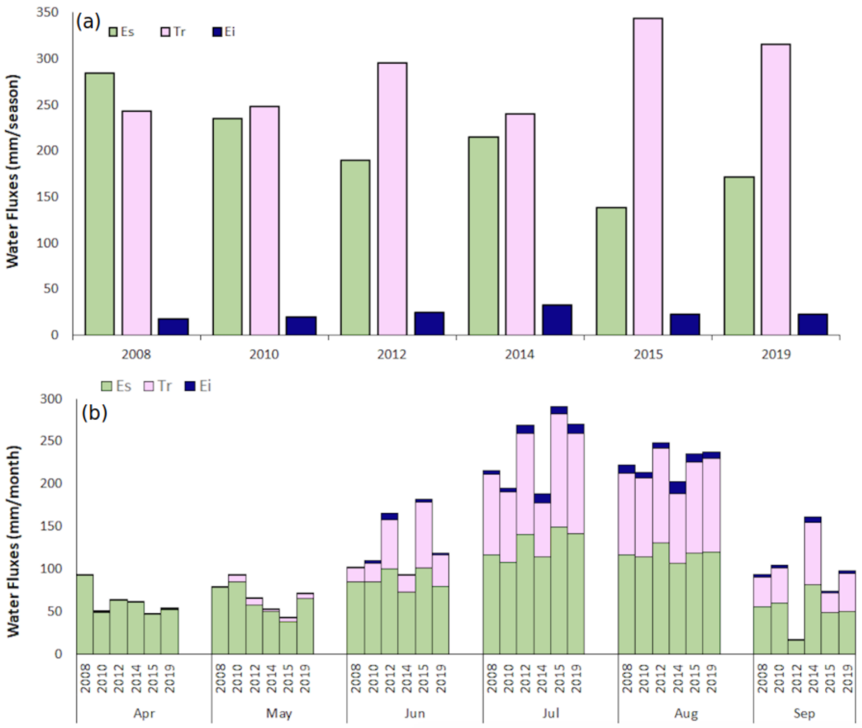

Figure 4.9: (a) Partitioning of the evapotranspiration (of ISBA-MEB) into soil evaporation (Es: green), plants transpiration (Tr: pink), and vegetation evaporation (Ei: blue) for maize; (b) the same as in (a) but monthly.

Evapotranspiration partitioning over wheat

Figure 4.10 shows the variability of ISBA-MEB's ET constituents over wheat. From Figure 4.10a, Es consumed at least 43% of total ET in wheat-2009, wheat-2011, and wheat-2013, while in wheat-2007, Tr accounts for 56% of the total ET. Figure 4.10b shows the monthly distribution of the ET components. For example, the highest transpiration was recorded in April (for wheat-2007 and wheat-2011), and in May (for wheat-2009 and wheat-2013), which coincided with the period of maximum LAI (except in wheat-2013). The disparity in wheat-2013 is due to the high rainfall (126 mm) recorded in May 2013. Furthermore, for the months that experienced intense soil evaporation, this is due to high air temperature; for example, in wheat-2007, Es in May increased by 85% in June due to the 21% increase in TA. Similarly, in wheat-2009, a 31% increase in TA resulted in a 40% increase in Es (in March), and a 7% increase in TA coupled with high rainfall (89 mm) caused a 32% increase in Es in July of wheat-2011. Similarly, the intense Es of 69 mm observed in July of wheat-2013 was due to a 6.5^{o}C increase in the air temperature. Lastly, the transpiration processes occurring at the end of wheat-2013 is due to the cover crop that was planted.

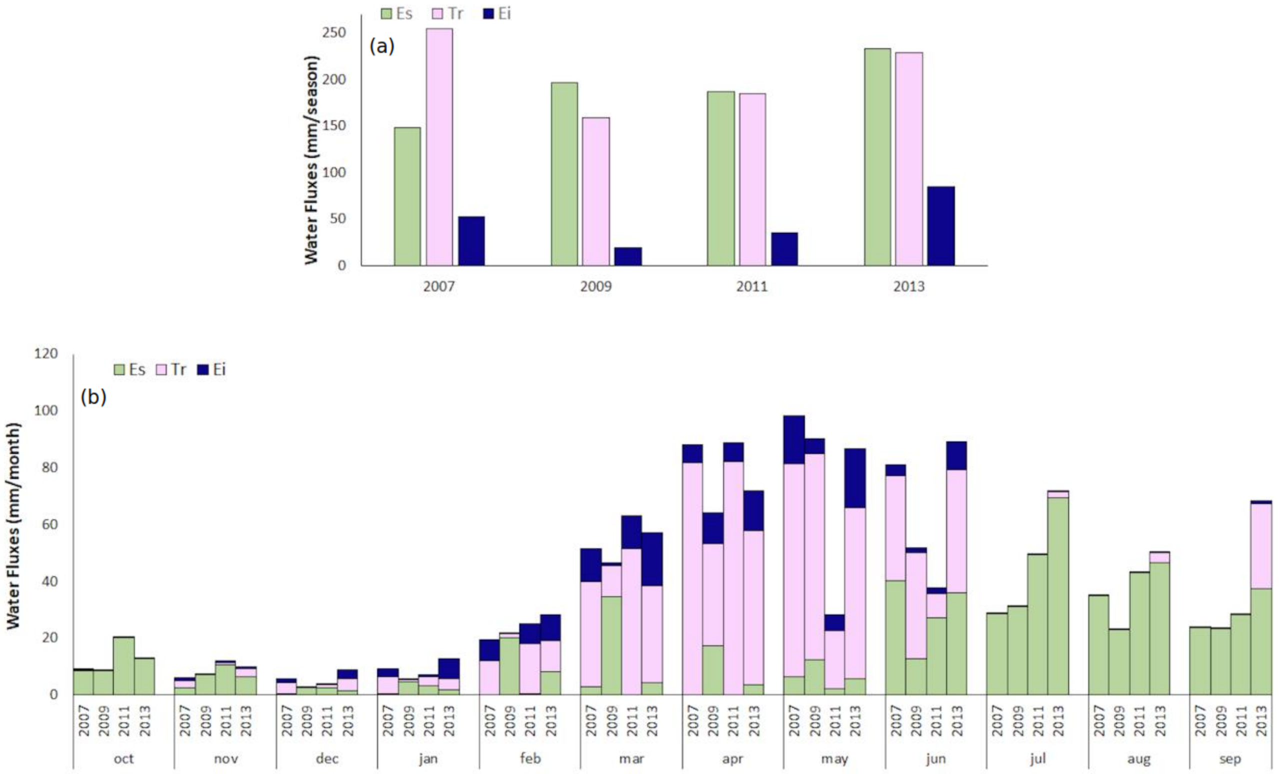

Figure 4.10: (a) Partitioning of the evapotranspiration (of ISBA-MEB) into soil evaporation (Es: green), plants transpiration (Tr: pink), and vegetation evaporation (Ei: blue) for wheat; (b) the same as in (a) but monthly.

Water budget

Maize

Figure 4.11 compares the cumulated $(P + Irrig)$, ET, Tr, and Es from ISBA-MEB and ΔS, while Table 4.6 presents the values of components. A negative or positive sign of D indicates soil water extraction, or drainage from depths below 50 cm, respectively. The striking feature of Figure 4.11 is that all years behave closely in terms of balance between water inputs and ET. Overall, $(P + Irrig)$ was lower than ET (see Table 4.6), and this has been observed over several agricultural sites (Lu et al., 2011; Chebbi et al., 2018). This at first indicates that there is no drainage at this site which has an impervious layer around 60 cm depth that limits drainage fluxes. Indeed, drainage values are low except in maize-2019 with a value of 95 mm. This is probably due to the two strong irrigation events in July (see Figures 4.4) scheduled by the farmer to refill the soil reservoir that was severely depleted by the drought period that occurred at this time. By contrast, the negative drainage value of −82 mm in maize-2015 could be related to available stagnant water above the impervious layer that contributed to the strong development of the plants during this season (characterized by the highest LAI (Figure

4.1c), and the highest transpiration (Figure 4.9). Low drainage values observed in maize-2010, maize-2012, and maize-2014 are characterized by average climatic conditions in terms of evaporative water demand and water inputs. Drainage in maize-2010, maize-2012, maize-2014 and maize-2019 accounted for 12%, 8%, 12%, and 63%, respectively of irrigation water. These values over the "average" years (maize-2010, maize-2012, and maize-2014) is lower than the 22% that is typically lost in this region (Serra-Wittling and Molle, 2020).

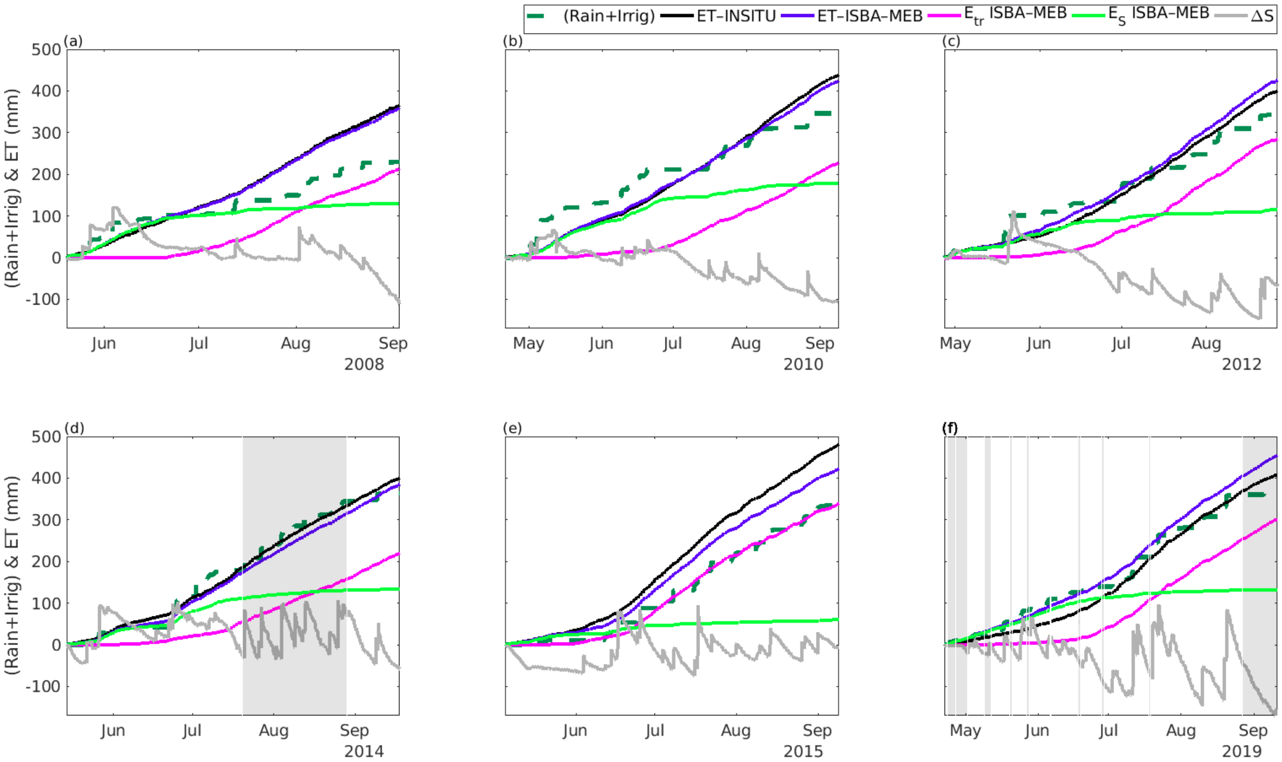

Figure 4.11: Comparing the cumulated rainfall (+ irrigation) with evapotranspiration (ET) from field measurements and ISBA-MEB estimates with plant transpiration (Tr), soil evaporation (Es), and change in soil water storage (ΔS) for maize at FR-Lam between the sowing and harvest dates. The grey areas are periods without *in-situ* soil-water data and periods substituted with ISBA-MEB estimates. Panels (a-f) represent maize-2008 to maize-2019, respectively.

Table 4.6: Cumulated water inputs ($P + Irrig$), measured evapotranspiration (ET *in-situ*), simulated transpiration (Tr ISBA-MEB), soil evaporation (Es ISBA-MEB), the computed change in the soil water storage (ΔS), and the seepage/extraction (D) beyond 50 cm depth. All measurements are in mm, and are for maize taken between the sowing and harvest dates.

Year	Maize-2008	Maize-2010	Maize-2012	Maize-2014	Maize-2015	Maize-2019
$P + Irrig$	229.1	347.9	343.9	362.7	333.8	368.1
ET *in-situ*	366.2	439.2	399.7	400.8	477.5	408.5
TrISBA-MEB	214.1	227.5	288.8	220.4	342.5	302.0
EsISBA-MEB	129.7	180.1	116.8	134.1	60.9	131.9
ΔS	109.2	103.8	68.2	58.3	61.5	136.2
D	-27.9	12.5	11.4	20.2	-82.2	95

ΔS ranging between 58 mm and 136 mm indicate that the plants extracted a substantial amount of water. This means that a full reservoir is needed at the start of the season to supplement irrigation and rainfall inputs. Even though no strict relationship is observed between the LAI and ΔS, in most of the maize years, the magnitude of ΔS is controlled by water availability rather than by canopy density. This observation is corroborated by Nielsen and Vigil, (2018), who observed that during the growing period of crops, rainfall amount influences strongly the amount of soil–water extracted. Another interesting feature is that the cumulative ET are of comparable magnitude across the years except in maize-2015 with a value exceeding 470 mm. This is a reconfirmation that the ground water reservoir at FR-Lam is key in the estimation of realistic soil water and energy fluxes. It also explains why after maize harvest, the site ends up with a very dry soil profile.

Wheat water budget

Figure 4.12 presents the water components for wheat. In contrast to Figure 4.11, and except for wheat-2011, water input (rainfall only in this case) strongly exceeded the total ET by at least 63 mm. This implies that there is a substantial drainage or run-off occurring. Conversely, to avoid water-stress because $P < ET$ in wheat-2011, strong capillary processes occurred between 0 and 50 cm depths (see Table 4.7, which presents the values of the components taken between the planting and harvest dates (see Table 4.1 for dates)). Tr is the most important component of ET_{MEB}; it accounts for 67%, 53%, 69%, and 52% in wheat-2007, wheat-2009, wheat-2011, and wheat-2013 respectively. Unfortunately, due to the strong underestimation of LE in wheat-2013, no relationship could be established between P and Tr; highest Tr (255 mm) is observed in wheat-2007 (P = 531 mm), whereas wheat-2013, the year with the heaviest rain (732 mm) only experienced Tr of 216 mm. Although, Ei is almost a function of rainfall-; it ranged from 20 mm (in wheat-2009) to 84 mm (in wheat-2013).

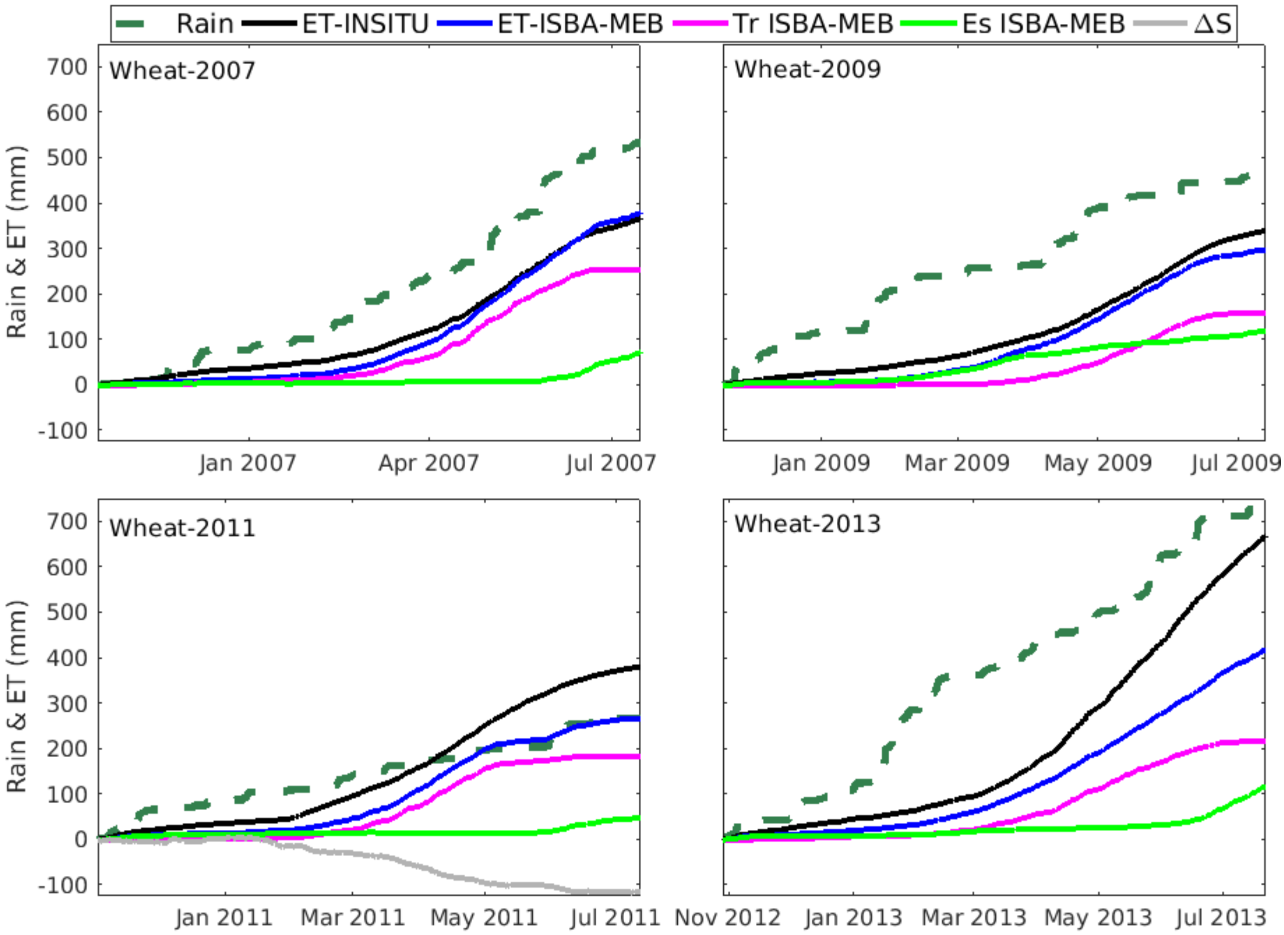

Figure 4.12: Comparing the cumulated rainfall with evapotranspiration (ET) from field measurements and ISBA-MEB estimates with plant transpiration (Tr), and soil evaporation (Es), for wheat at FR-Lam taken between the sowing and harvest dates.

Overall, the percentage of rainfall transpired by the crops ranged between 30% (in wheat-2013) and 69% (in wheat-2011); whereas about 14% (in wheat-2007) to 26% (in wheat-2009) was lost to soil evaporation. In addition, about 10% of total rainfall was evaporated after being intercepted by the canopy, and this quantity was not strongly regulated by the crop density, but perhaps a combination of the rainfall's intensity, the prevailing wind speed and direction etc (Toba and Ohta, 2008).

Table 4.7: Cumulated water inputs (P), measured evapotranspiration (ET *in-situ*), simulated transpiration (Tr ISBA-MEB), soil evaporation (Es ISBA-MEB), the change in soil water storage (ΔS), and the seepage/extraction (D) beyond 50 cm depth. All measurements are in mm, and for wheat. Values are taken between the sowing and harvest dates.

Year	**Wheat-2007**	**Wheat-2009**	**Wheat-2011**	**Wheat-2013**
P	531.4	459.2	266.9	732.1
ET ISBA-MEB	379	299	268	417
ET *in-situ*	367	340.8	380	669.5
Tr ISBA-MEB	255	159	185	216
Es ISBA-MEB	72	120	48	117
Ei ISBA-MEB	52	20	35	84
ΔS	–	–	114.3	–
D + Runoff	164.4	118.4	1.2	62.6

4.4 Conclusions

This chapter assessed and compared the performance of a single- and a double-energy budget LSM in simulating surface energy and water fluxes over six seasons of irrigated maize, and four seasons of non-irrigated wheat using *in-situ* EC measurements acquired in FR-Lam. ISBA (the single-source model) and its multi-energy balance version (ISBA-MEB) were chosen. Furthermore, a specific focus was given to ET-partitioning using sap flow measurements. Some major outcomes of this chapter are as follows:

1) The surface energy fluxes were satisfactorily estimated, but ISBA-MEB provided better estimates of H and LE when the fraction cover is low for both maize and wheat.
2) Both ISBA and ISBA-MEB had very good and similar agreement with the sap flow measurement. This similarity could be because the sap flow campaign took place when the canopy was fully developed, with homogeneous cover.

The second section investigated the inter-annual variability of the water budget components over maize and wheat.

1) The ET components exhibited a strong year to year variability that is closely related to the crops' development measured by the LAI in this study. For instance, over maize, transpiration accounted for 60% of the total ET in maize-2012, maize-2014, maize-2015, and maize-2019, and 46% in maize-2008 and maize-2010. In contrast, Es consumed the largest fraction of ET (at least 43%) in three of the four wheat years.
2) Another striking feature is that all maize years behave closely in terms of balance between water inputs and ET; $(P + Irrig)$ was consistently lower than ET.

As a conclusion, for the future projection of the hydrological functioning of irrigated maize and non-irrigated wheat at FR-Lam, dual-source models should be preferred to single-source models. Nevertheless, further local scale evaluations of ISBA-MEB over different crop types and climates are recommended to strengthen our conclusions, and to feed the global database of land surface parameters such as the ECOCLIMAP II.

Some main ideas of this chapter

- ISBA and ISBA-MEB satisfactorily estimated the energy and water components over maize and wheat.

- Single source models like ISBA could be replaced with multi-energy options like ISBA-MEB for the simulation of turbulent fluxes when the vegetation fraction cover is low.

- Both ISBA and ISBA-MEB had very good and similar agreement with the *in-situ* transpiration measurement. This similarity is perhaps because of the homogeneity of the field during the sap flow campaign.

Chapter 5: Estimating carbon components over maize and wheat using a land surface model

5.1 Introduction

In order to evaluate and exploit the sequestering potential of croplands, biospheric carbon fluxes amid various land-use changes must be measurable, and verifiable. Hence, this chapter has three focuses:

(i) A comparative study was first carried out between soil respiration measurements from an automated chamber, and an eddy covariance system.

(ii) Then, carbon fluxes from a canopy chamber was compared with EC measurements over wheat and maize.

(iii) Finally, given its performance in Chapter 4, ISBA-MEB (with A-gs option) was evaluated for the estimation of carbon fluxes over wheat and maize in FR-Lam.

5.2 Methodology

In this study, 11 crop years (in FR-Lam) were considered, and according to the cultural practice of this region (Ceschia et al., 2010), a crop year runs from the 1st of October to the 30th of September of the following year. Table 5.1 presents some biophysical characteristics of the selected years; the sowing and harvest dates can be found in Table 2.1. For ease, a cropping year would be referred to as the latter year e.g., year 2005-2006 becomes maize-2006. The parameterization of this model is similar to that discussed in section 4.2, and the following section describes the calibration procedure for GPP and $RECO$.

Table 5.1: Overview of the selected period. AGB is above ground biomass at harvest.

Crop	Year	Max Height (m)	Max LAI (m^2 m^{-2})	AGB (kg m^{-2})
Maize	2005-2006	2.42	3.33	1.75
	2007-2008	2.49	3.28	1.50
	2009-2010	2.50	3.87	1.57
	2011-2012	2.89	5.10	2.20
	2013-2014	3.00	4.82	1.92
	2014-2015	2.83	6.18	2.62
	2018-2019	3.35	6.40	--
Wheat	2006-2007	0.91	4.48	1.45
	2008-2009	0.70	1.74	1.04
	2010-2011	0.90	5.48	1.89
	2012-2013	1.03	3.59	2.30

5.2.1 Sensitivity analysis and calibration

Sensitivity analysis

Within the model, GPP is estimated as a function of the net assimilation, while in the representation of $RECO$, there exists several approaches that distinguish the components of the autotrophic and heterotrophic respiration. In this respect, two sets of calibrations were performed. For the first, to establish a good trade-off between the large input parameters required by ISBA-MEB, and the limited available computational resources, the following sequence was followed to obtain the optimal set of parameters for GPP and $RECO$:

(i) Based on past literatures and the knowledge of the model, 13 parameters were selected. To identify and isolate the sensitivity of each parameter, a quick one-at-a-time sensitivity test was performed for 3 maize (2008, 2014, 2015) and 2 wheat (2011, 2013) years. For each parameter, the range of values considered were often based on past literature values, and for each crop year, 50 simulations were performed per parameter (Table 5.2 presents these parameters, and their respective ranges).

(ii) Then, two objective functions (RMSE and R^2 in this study) were evaluated from the regression between each parameter's simulation and *in-situ* measurement.

(iii) Then, RMSE and R^2 scores were sorted (lowest and highest, respectively being the best) and ranked for the determination of the threshold needed to partition the ensemble into an acceptable and a non-acceptable region. The trade-off between the targeted objectives is obtained using a Pareto ranking system (Demarty et al., 2005).

(iv) Afterwards, the cumulative distribution of the acceptable region for each parameter values was compared with those of the non-acceptable region using the Kolmogorov-Smirnov (KS) test that relates the maximal distance to a probability value as described in Demarty et al. (2005).

(v) The probability value for each parameter is then plotted as in Figure 5.1 (for maize-2015 and wheat-2011 for illustration purposes). Three threshold levels represented by the red horizontal dotted lines were used to classify the significance level for each probability value into 'high sensitivity', 'medium sensitivity', and 'low sensitivity'. Hence, for bars below the 0.01 red line (it is high sensitivity), when it lies between 0.01 and 0.1 (it is medium sensitivity), and when it is above 0.1 (it is low sensitivity).

This exercise did not consider the multi-response interactions of the parameters due to the high computational resources required. From the model calibration, the optimal parameter values were chosen, and validation was carried out over the remaining crop years. Among the 13 parameters investigated, 3 (G_{MES}, G_C, F_{2I}) were particularly sensitive as seen from Figure 5.1. For the other parameters, literature values were chosen, and for the newly introduced parameters within ISBA-MEB ($\Gamma_{LW}, Z_{AM}, Z_{AW}$), the values recommended in Boone et al. (2017) were retained.

Table 5.2: List of parameters and their considered ranges

#	Definition	Range	Opt. Maize	Opt. Wheat	Reference
F_{2I}	Critical normalized swc for stress parameterization	0.2 – 0.5	0.334	0.275	Calvet, 2000
G_C	Cuticular conductance (m s^{-1})	0.00015 – 0.00030	0.0004	0.00021	Gibelin et al., 2006
G_{MES}	Mesophyll conductance (m s^{-1})	0.001 – 0.03	0.002	0.003	Calvet, 2000
a	Minimum soil CO_2 flux	6-10	7.5	8.25	Norman et al., 1992
b	Considers the response of LAI	3-5.7	4.75	3.7	Norman et al., 1992
$T_{s,ref}$	Reference soil temperature (°C)	25-58	26.5	25.75	Norman et al., 1992
Insensitive parameters		**Sensitivity ranges**	**Default Values used**		
D_{MAX}	Max leaf to air saturation deficit (kg kg^{-1})	0.05 – 0.5	0.065	0.10	Calvet, 2000
C_V	Vegetation thermal inertial (K m^2 J^{-1})	0.00002 – 0.0003	0.00005	0.00002	Noilhan and Planton, 1989
R_{GL}	Max solar radiation available for photosynthesis (W m^{-2})	80 - 120	100	100	Le Moigne, 2012
WR_{MAX}	Coeff for max inter water storage capacity	0.05 – 0.3	0.2	0.2	Le Moigne, 2012
RE_{25}	Ecosystem resp parameter	0.0000002 – 0.0000003	0.00000025	0.00000025	Le Moigne, 2012
LAI_{MIN}	Minimum LAI	0.1 – 0.4	0.3	0.3	Le Moigne, 2012
$Z_0\_Z_H$	Ratio of surface roughness lengths	7 – 10	9	9	Boone et al., 2017
		Uncalibrated	**Recommended Values**		
L_W	Leaf width (m)	Default kept	0.02	0.02	Boone et al., 2017
Z_{AM}	Attenuation coeff for momentum	Default kept	2	4	Boone et al., 2017
Z_{AW}	Attenuation coeff for wind	Default kept	3	3	Boone et al., 2017
Γ_{LW}	Longwave transmission factor	Default kept	0.5	0.5	Boone et al., 2017

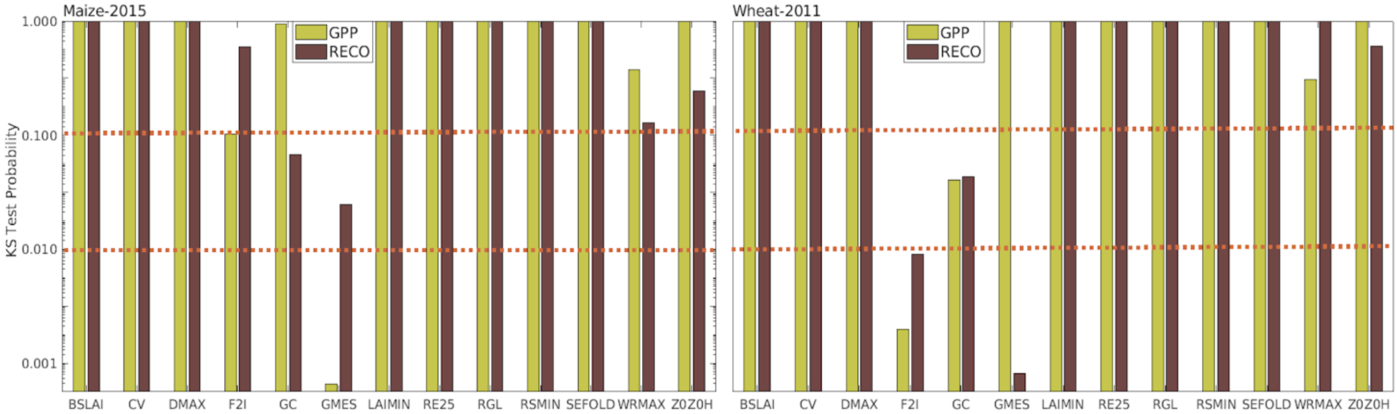

Figure 5.1: Result of the sensitivity analysis for maize-2015 and wheat-2011.

After the above calibration, runs of the model showed a strong overestimation of $RECO$. The second calibration involves the soil respiration (SR), a major constituent of $RECO$. This study adopts the parameterization developed in Norman et al. (1992) (see Equation 2.16g) which considers the emissions produced by the soil biota and the plant roots; hence, an optimization procedure was carried out over the previously-calibrated years for maize and wheat. Considering the few parameters involved, a simple brute force approach was adopted for optimization. First, each coefficient (a, b, and $T_{s,ref}$) is varied between 6-50% around their literature values (see Table 5.3). Q10 was kept at the default 2 because Delogu et al. (2017), who estimated this parameter over our study site obtained a close value. Afterwards, for each coefficient, six step sizes was selected, and 216 iterations was performed. The optimized values are those that presented the lowest RMSE in $RECO$ over the remaining crop years.

Table 5.3: The considered ranges and optimal values for soil respiration's optimization.

Parameters	Range	Opt value (Maize)	Opt value (Wheat)
A	0.06-0.10	0.075	0.0825
B	0.03-0.057	0.0475	0.037
$T_{s,ref}$ (ºC)	25-28	26.5	25.75

5.3 Results

5.3.1 Experimental data analysis

5.3.1.1 Comparison between three methods of soil respiration monitoring

Ecosystem respiration represents the second largest carbon flux within a terrestrial ecosystem, and soil respiration (SR) accounts for about 60-90% of this (Gao et al., 2017). Being a key component of the global carbon cycle, and given the vulnerability of croplands to climate change, soil respiration over crop lands have been receiving widespread attention. Of particular interest is the sensitivity of this component, and how it responds to environmental factors- e.g., soil temperature and soil water. These variables are critical in the evolution of carbon stocks and fluxes because they are the major drivers of organic matter decomposition (Jassal et al., 2008), root respiration (Bouma et al., 1997), and microbial activities (Skopp et al., 1990). To establish possible correlations, or dissimilarities between systems monitoring CO_2 fluxes, this section carried out two comparative studies: the first was between the EC system and the automatic chambers, then the second was between the canopy chamber and EC system. In the following section, measurements from the automated and canopy chambers are represented by subscripts ‘AC’ and ‘CC’ respectively.

Automated chamber vs eddy covariance measurements

Figure 5.2(a, c, and e) presents the temporal series of SR by AC and EC over some bare soil periods (see Table 2.5 for timeline). It is observed that both methodologies have similar measurement range; EC was between 0.03 and 9.4 gC m^{-2}, and AC was between 0.1 and 10.7 gC m^{-2}, and both methods exhibit similar dynamics. Similarly, the scatters in Figure 5.2(b, d, and f) reveal that both data sets are better correlated for low fluxes between 0 and 5 gC m^{-2}, while for fluxes outside this range, clustering reduces with larger respiration measurement by the chamber. In the first period (Figure 5.2a), the discrepancy between both systems is mostly due to tillage- as a preparatory practice for mustard sowing, this plot was tilled on the 16th of August 2013. This farm operation enhanced porosity which served as pathways for the transportation of the carbon fluxes- and the ACs were highly sensitive to this activity. On the other hand, the EC system was insensitive to this- perhaps due its extensive and non-localized field of view.

A similar response was observed in the second period (Figure 5.2c); the tillage that occurred in the last months of 2013 reduced the AC-EC agreement. Furthermore, between December and mid-January, SR crashed from 4.1 gC m^{-2} to about 0.7 gC m^{-2} (more so with the chamber system). During this period, a significant portion of the site was water-logged (see Figures C2-C4 in Appendix C); this reduced the available soil-oxygen to critical limits, and rendered the microbial-activities passive.

The decrease of soil respiration under soil-water saturation has similarly been observed in several studies (Carlyle and Bathan, 1988; Morales et al., 2015).

The discrepancy between both measurements is more significant during summer (Figure 5.2a), with a maximum difference of 5.9 gC m^{-2}, while for the other periods (in Figure 5.2c and Figure 5.2e), the maximum difference is 2.0 gC m^{-2} and 3.6 gC m^{-2} respectively. Overall, from the linear regression of all the measurements (Figure C1 in Appendix C), the explanatory value of the trendline is 51%, with a slope of 0.97, and a small intercept of 0.20 gC m^{-2} d^{-1}.

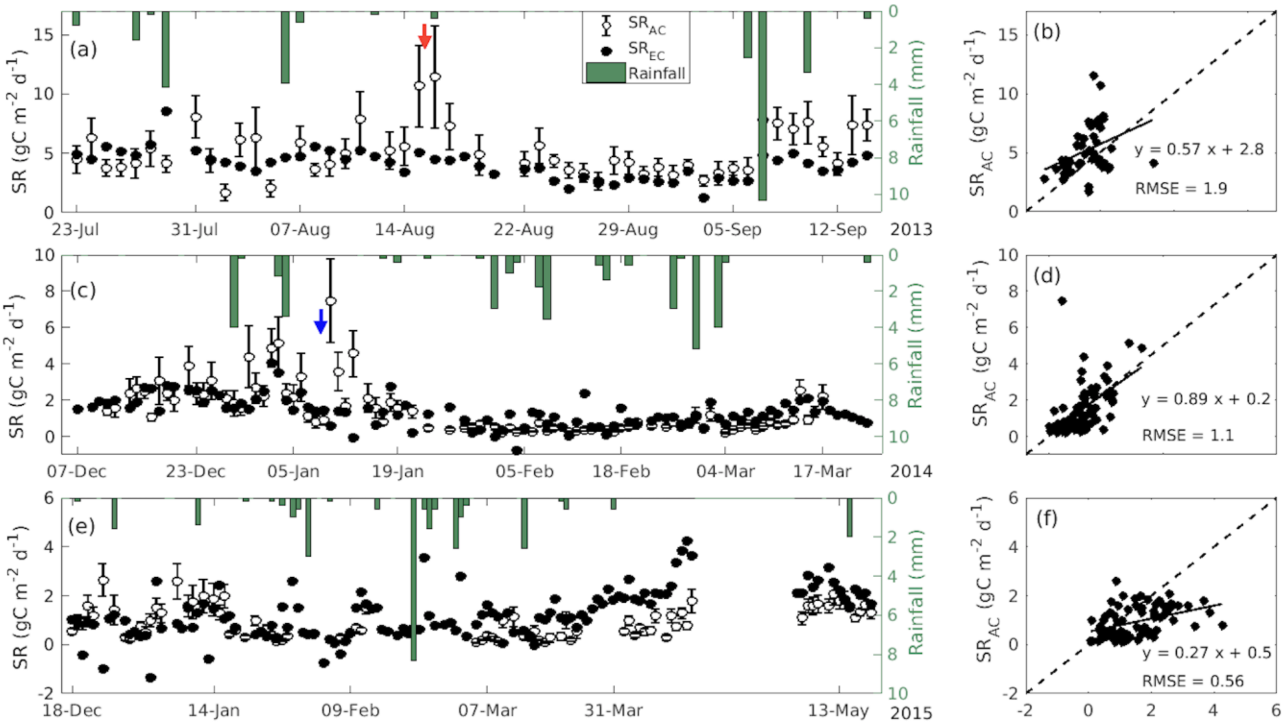

Figure 5.2: Panels (a, c, and e) show the time series comparing soil respiration from the automated chamber (AC) with the eddy covariance system (EC); panels (b, d, and f) present the scatter and metrics for the corresponding series on the left hand side. The red, and blue arrows represent the tilled, and large clods period respectively. The error bars on SR_{AC} are the flux uncertainties (AC_{uncer}).

This analysis concludes that in the absence of external disturbances, better agreement is obtained between both systems. It must however be recalled that SR_{AC} which in fact should be the reference is sometimes fueled with errors owing to the leaks that sometimes result from soil cracks- these cracks are frequent phenomenon particularly in summer given the high clay content of the soil. In addition, chambers are generally invasive, and can be over-sensitive to small disturbances (Davidson et al., 2002).

Canopy chamber vs eddy covariance measurements

(i) Wheat

In this section, carbon fluxes from the canopy chamber were compared with EC measurements. The mean LAI presented in Figure 5.3a indicates great similarity in the vegetation characteristics over the main plot (evolving from 1.8 to 2.5 m^2 m^{-2}) and under the sample points (ranges from 1.9 to 2.7 m^2 m^{-2})-; although, the latter has higher values. This could explain the higher respiration recorded for the chamber (Figure 5.3b) which ranged between 0.2 and 2.1 gCO_2 m^{-2} in contrast to the 0.2 and 1.0 gCO_2 m^{-2} of the EC. Based on the chamber's measurements, the plot had a cumulative gross primary production of 110 gCO_2 m^{-2}, 32% of which released as CO_2 efflux back into the atmosphere via respiration. Meanwhile, according to the EC measurements, total respiration and NEE comprised 21% and 79%, respectively of GPP_{EC}. Over this campaign period, cumulative $RECO_{CC}$ and GPP_{CC} were estimated at 35 gCO_2 m^{-2} and 110 gCO_2 m^{-2}, respectively, which were 48% and 23% respectively higher than the EC measurements. Although, both systems indicated the C-sink status of the site, nevertheless, according to the EC, the plot sequestered 8% less carbon than the chamber's indication. This observation slightly contradicts the report of the experimental study of Wang et al. (2009) which compared EC and a chamber-based measurements over a temperate mixed forest. This study reported NEE_{EC} to be higher than the chamber's NEE. This contradicting report could be because their analysis was carried out over mature trees (~250 years old), while ours was over baby wheat. Zamolodchikov et al. (2003) however found $RECO_{EC}$ to be 30% lower than the chamber's estimates.

To further buttress our result (i.e., why EC < CC), we invoke the concept of footprint mismatch. EC systems obtain sample fluxes from large patches in multiple directions whereas the CC is completely focalized on a single sample per measurement. Hence, CC measurements do not suffer from weak turbulence and horizontal advection like an EC. Similarly, the scaling of the canopy chamber's measurements could introduce certain errors (Wang et al., 2009). Hence, this EC-CC comparison should be interpreted with caution; plus, the fact that these data points were never a full-day's measurement (at most, 10 data points per day).

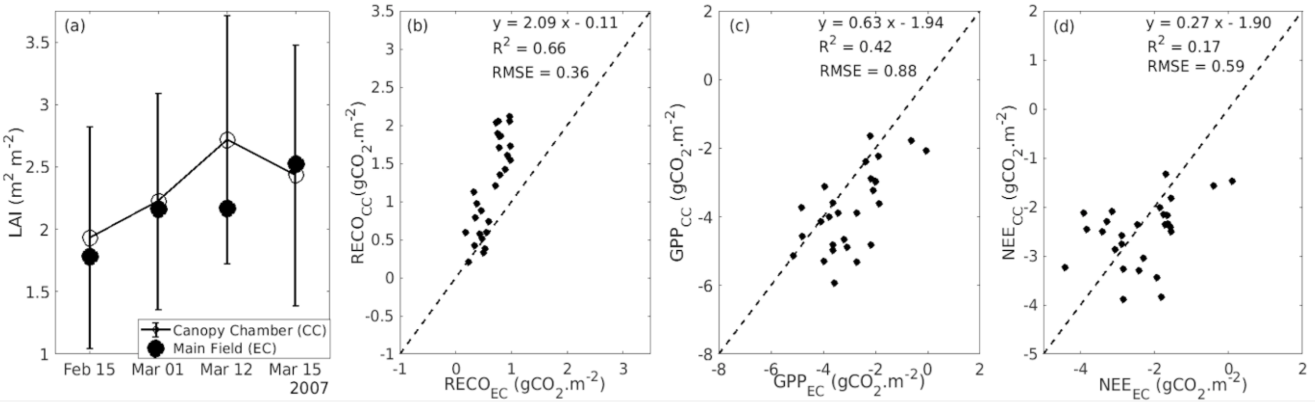

Figure 5.3: Comparison of measurements taken over the main field by the eddy-covariance system (EC) with that taken under the canopy chamber (CC) between the 15th of February, and 15th of March 2007. Where: (a) is the leaf area index over wheat, (b), (c), and (d) is the scatter of the ecosystem respiration, gross primary production, and the net ecosystem exchange, respectively. The broken black line is the 1:1 linear fit line, and the error bars represent the standard deviation showing the variability between the LAI of the sample points.

(ii) Maize

The comparison for maize is presented in Figure 5.4, and measurements were taken between the 5th and the 26th of June 2008. Unlike in wheat, the LAI and the C fluxes do not correspond at all. At each point, the LAI_{CC} is at least 54% larger than LAI_{EC}, and $RECO_{CC}$ and GPP_{CC} are about 50% larger than the EC estimates. Unlike in wheat with R^2 value of 0.42 for GPP, a poor correlation is obtained over maize. This could be due to surface homogeneity which is often higher in wheat during the early stages of development (see Figure 5.6). In contrast, over maize, there is a larger exposure of the background soil under the chamber (see Figure 5.6); hence, carbon assimilation is lower. Moreover, comparison and interpretation would be difficult over maize because the measurement campaign started just 2 weeks after sowing. As such, over this campaign period, the cumulative net CO_2 exchange is close to equilibrium i.e., almost all the assimilated carbon was respired (NEE_{EC} = 0.2 gCO_2 m^{-2} & NEE_{CC} = 3.8 gCO_2 m^{-2}.

In summary, the EC-CC comparison is difficult because of the source area mismatch mentioned earlier, and also because the potential of C losses is higher in the EC system. Another reason is the fact that inside the canopy chamber, atmospheric turbulence is difficult to produce even with operating ventilators (Kimball and Lemon, 1971; Kimball and Lemon, 1972). Notwithstanding, we propose a campaign over a longer period, and also, we recommend sample points that are representatives of the plot for a good comparison.

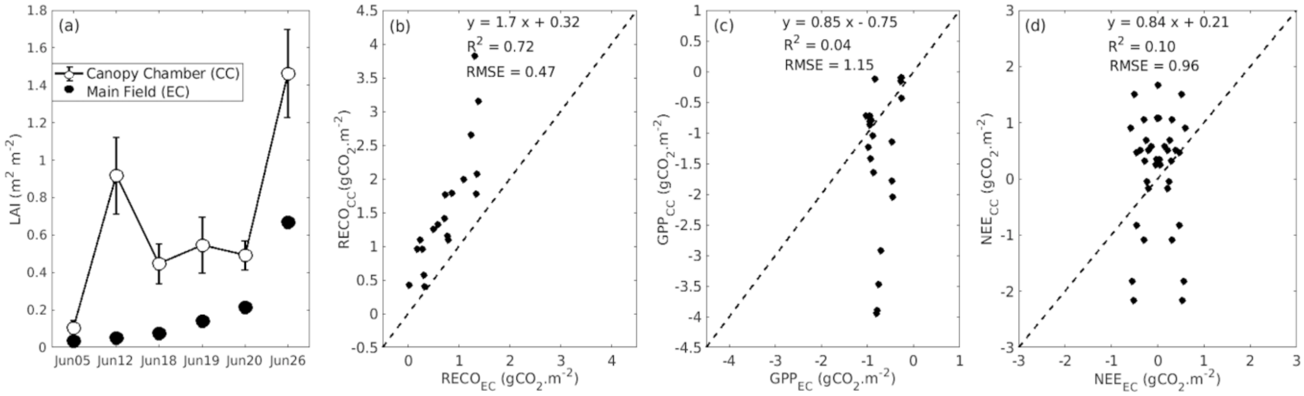

Figure 5.4: Same as Figure 5.3, but over maize between 5th to 26th of June 2008.

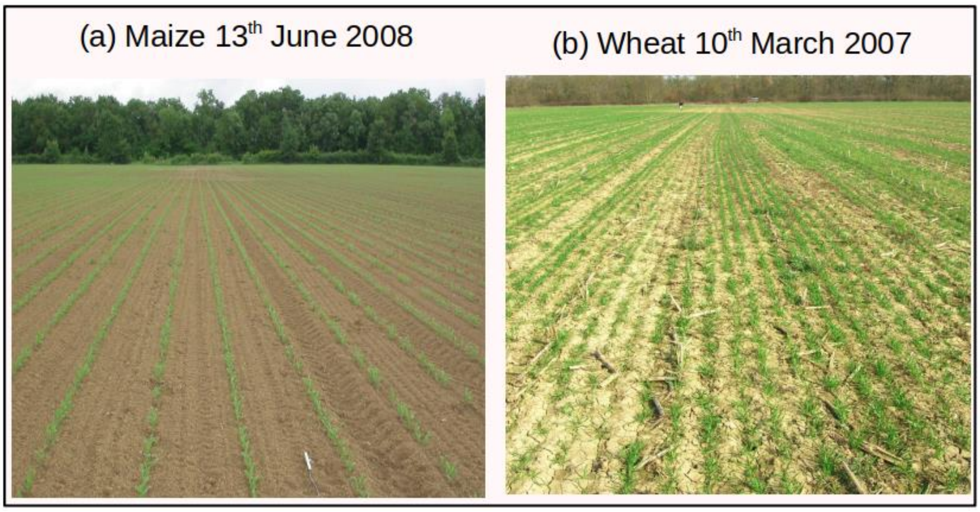
(a) Maize 13th June 2008

(b) Wheat 10th March 2007

Figure 5.5: State of plot during the canopy chamber measurement campaign.

5.4.1.2 Response of soil respiration to soil moisture and temperature

One of the hot topics of the scientific community includes understanding mechanisms that trigger soil respiration given the ongoing changes in the climate. Some studies have shown that SR is highly correlated with temperature (Kirschbaum, 1995; Jassal et al., 2005), while other studies identified soil moisture and the availability of easily-decomposable organic matter as major drivers (Davidson and Janssens, 2006) especially in water-limiting conditions that encourage a decoupling of SR and Ts (Tang et al., 2005). For dynamic croplands as FR-Lam, the sensitivity of SR to these variables is still poorly understood. This section assessed the sensitivity of SR_{EC} and SR_{AC} to Ts and swc, and the timelines defined in Table 2.5 would be referenced as P1, P2, and P3.

The coefficient of determination between soil respiration and soil moisture, and soil temperature are presented in Table 5.4 and 5.5 respectively. For the first period (23/07/2013-14/09/2013: for both EC and AC), soil moisture between 0 and 10 cm depth explained at least 65% of the variation in the CO_2 fluxes, while at deeper depths, correlation was poorer. In contrast to the positive linear relationship obtained at the first 4 depths, a negative correlation was obtained between SR and swc at the deeper depths (for both EC and AC). This could be the influence of the Touch river which saturated these depths as the absolute soil water values at these layers was close to field capacity. On the other hand, SR decreased with increasing temperature (Table 5.4) implying that SR are majorly being impacted by the soil water at the superficial layers. This can be attributed to the heterogeneity of the soil profile at different depths, and also the presence of fertilizers which is more available at the surface.

In contrast to the first period, and in response to the season (winter/spring), fluxes increased with decreasing soil water in P2 (07/12/2013 – 23/03/2014). However, a large percentage of the variation in the flux is unexplained by neither the soil water nor the soil temperature. For P3, (18/12/2014 – 19/05/2015), SR_{EC} was completely insensitive to the changes in the soil water, while SR_{AC} showed weak responses.

Table 5.4: Coefficient of determination of SR vs swc at depths of 0 cm to 100 cm.

SWC	**P1 (106)**		**P2 (174)**		**P3 (154)**	
	EC	AC	EC	AC	EC	AC
0 cm	0.66	0.72	-0.12	-0.10	0.02	-0.13
5 cm	0.67	0.75	-0.34	-0.30	-0.01	-0.31
10 cm	0.68	0.76	-0.31	-0.31	-0.01	-0.35
30 cm	0.04	0.10	-0.32	-0.25	-0.01	-0.36
50 cm	-0.37	-0.34	-0.41	-0.40	0.01	-0.19
100 cm	-0.47	-045	-0.29	-0.29	0.04	-0.18

+ *and - values indicate positive and negative relationship respectively.* In parentheses are the number of data points available for each timeline (6h step)

Table 5.5: Coefficient of determination of SR vs T_S at depths of 0 cm to 100 cm.

TS	**P1 (106)**		**P2 (174)**		**P3 (154)**	
	EC	AC	EC	AC	EC	AC
0 cm	-0.46	-0.51	0.01	-0.10	0.21	0.10
5 cm	-0.37	-0.39	0.10	-0.10	0.21	0.12
10 cm	-0.33	-0.34	0.10	-0.10	0.19	0.10
30 cm	-0.24	-0.23	0.10	0.10	0.14	0.11
50 cm	-0.24	-0.22	0.10	0.13	0.24	0.20
100 cm	-0.24	-0.12	0.20	0.44	0.11	0.27

5.3.2 Assessment of ISBA-MEB for carbon exchanges

The performance of the model was evaluated using EC measurements at FR-Lam. To represent regrowths and weeds, vegetation indices estimated from MODIS (see Chapter 2) were included for maize-2006, wheat-2007, wheat-2009, wheat-2011, and wheat-2013. Figure 5.7 summarizes the statistical scores between the model estimates and the in-situ measurements (see monthly time series of maize-2014 in Figure C1 for illustration in Appendix C)

Maize-2006 and Maize-2008

Figure 5.6a presents the daily temporal evolution of the fluxes for maize-2006 and maize-2008. The estimates of both runs (insitu veg and insitu + MODIS veg) agree well with the observation. Although, between Oct and Dec of maize-2006, the latter run captured very well the assimilatory and respiratory processes- and it strongly improved the estimation with an R^2 of 0.91 (for GPP), 0.85 (for $RECO$), and 0.79 (for NEE) which was about 5% higher than the GPP and NEE estimated when these regrowths were not considered. Similarly, the observed RMSE are within the values reported by other models over this cropland (e.g., Meroni et al., 2019; Pique et al., 2020). Furthermore, with the inclusion of regrowths and weeds, RMSE dropped by 24% in GPP and by 13% in NEE. However, in maize-2006, GPP was poorly estimated at the beginning (in June) and at the end of the crop growth in late August. During these periods, the model overestimated GPP by about 3.1 gC m^{-2} and 1.1 gC m^{-2} respectively. This overestimation is because the minimum number of days for the prescription of the vegetation characteristics is 10-, this is too large for fast growing crops like maize; as such, very low, and very high characteristics are masked within these 10-days averages.

On the other hand, with the absence of weeds, maize-2008 showed better agreement with R^2 of 0.95, 0.90, and 0.81 for GPP, $RECO$, and NEE respectively. Similarly, in comparison to maize-2006, the errors were about 20% lower: 1.2 gC m^{-2} d^{-1}, 0.9 gC m^{-2} d^{-1}, and 1.1 gC m^{-2} d^{-1} for GPP, $RECO$, and NEE respectively.

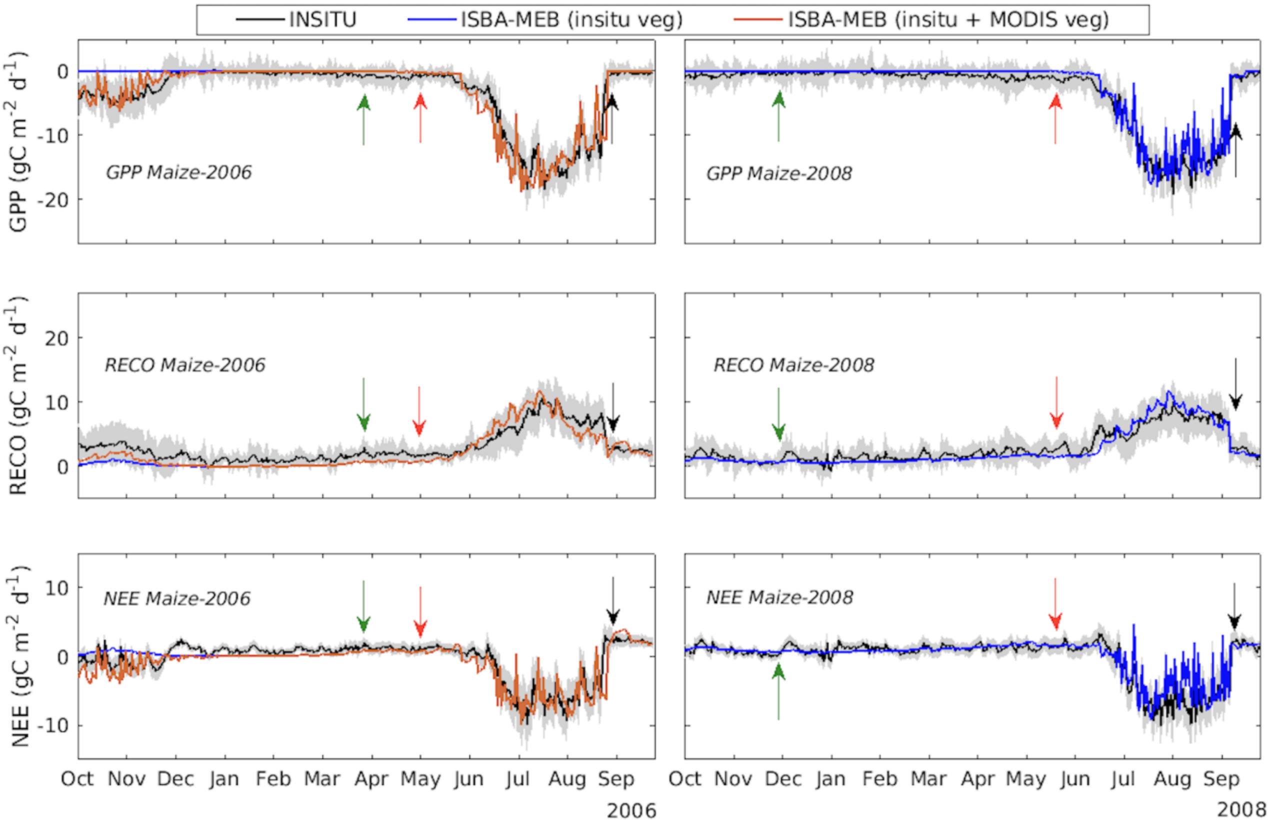

Figure 5.6a: Temporal evolution of the daily carbon fluxes measured on FR-Lam and estimated by ISBA-MEB for maize-2006, and maize-2008. The shaded regions represent the maximum daily standard deviations (in GPP and $RECO$), and the uncertainties (in NEE). The green, red, and black arrows represent tillage, sowing, and harvest dates, respectively.

Maize-2010 and Maize-2012

Figure 5.6b compares the modeled fluxes against the observations for maize 2010 and 2012. In 2010, the minima and maxima of GPP were very well captured by the model, but the end of the crop season was poorly simulated due to the limitation of the previously mentioned averaging period. In October 2009, $RECO$ as high as 3.1 gC m^{-2} d^{-1} was sometimes recorded owing to the presence of harvest residues that was not considered within the model, but that were continuously exchanging with the atmosphere. This process can be described in two ways (see Figure 5.6bi): (i) Wheat stems/stalks that are still deeply rooted inside the soil provide pathways for carbon outflow, (ii) harvest residues lying horizontally on the plot are subject to decomposition and increases heterotrophic respiration. Between October and December, respiration increased, reaching 3.9 gC m^{-2} d^{-1} in December due to the presence of weeds. Few weeks afterwards up until the 21st of April 2010, the plot was left fallow following a deep incorporation of these residues into the soil. During this period, a better model-data agreement was observed. Furthermore, some days after seeding, high respiration pulses reaching 4.5 gC m^{-2} was recorded due to a 28 mm rain event; unfortunately, the model was not very sensitive to this. Nevertheless, over the remaining part of the year, the model reproduced $RECO$ quite well with an R^2 of 0.88, and RMSE of 0.8 gC m^{-2} d^{-1}.

In contrast to maize-2010, a worse model-data agreement is observed in maize-2012 especially with $RECO$ which suffered a slight delay at the start of the season leading to an overestimation throughout the crop's growth. The daily and seasonal variability of GPP was reasonably captured by the model, but with a large discrepancy in July and August. This discrepancies could have resulted from data processing errors because no soil-water stress was experienced. Nevertheless, the model explained between 77% and 92% of the variation in the daily carbon fluxes.

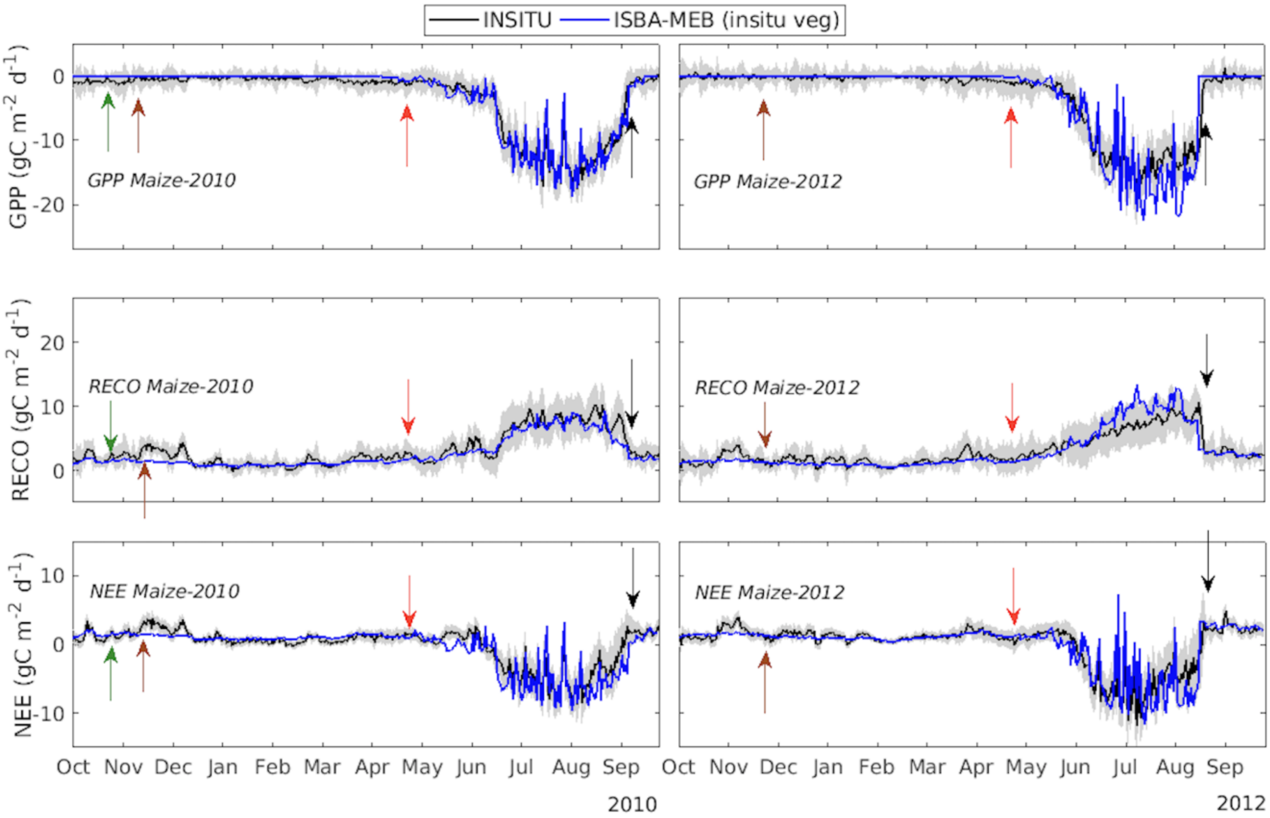

Figure 5.6b: Same as in Figure 5.6a, but for maize-2010, and maize-2012.

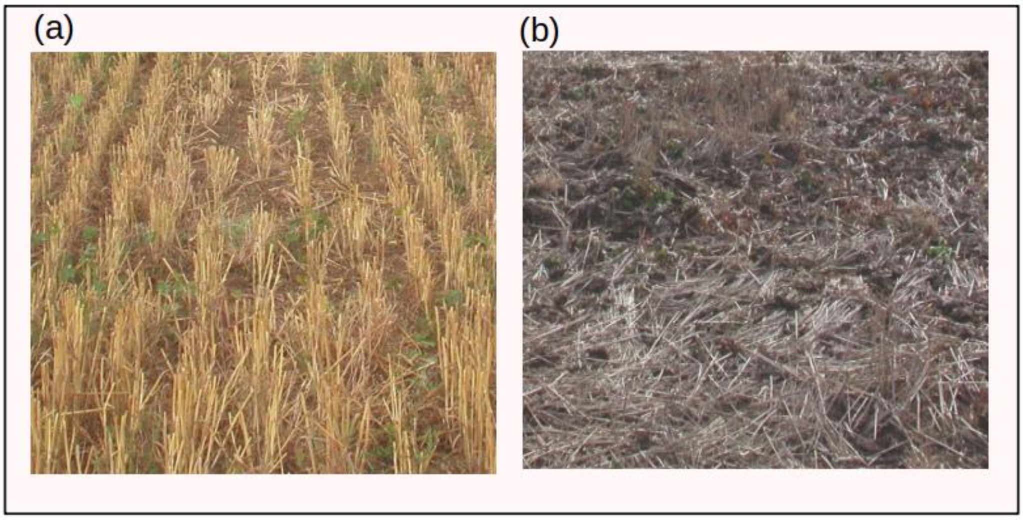

Figure 5.6bi: Two typical state of the site after wheat harvest in FR-Lam. (a) Wheat stubble still firmly rooted in the ground (b) Residues lying horizontally on plot before incorporation into the soil.

Maize-2014 and Maize-2015

Figure 5.6c showcases the ability of ISBA-MEB to give good predictions of carbon fluxes during intercropping periods. As a bio-fumigant cover crop, white mustard was sown and harvested between August and December 2013, and maize-2014 is the first year with cover crop preceding a maize cropping year. The homogeneous nature of this crop over the field eased the estimation of the fluxes by the model. This contrasts periods with re-growths and weeds which are often highly heterogeneous. The day-to-day variability of GPP was well captured by the model up until mid-August. From the 12th of August, *in-situ* measurements exhibited a *false* early-senescence (see Figure 4.2 for the evolution of the LAI). Nonetheless, the prediction of the model was in fair agreement with the observation especially towards the season end, with an R^2 and RMSE of 0.83 and 1.54 gC m^{-2} d^{-1}, respectively.

In maize-2015, between the 30th of March and the end of May, some photosynthetic activities that could not be modeled were recorded by the EC system due to the sprouting of some weeds. Also, large discrepancies were observed in August following cloudy days with limiting light conditions. Overall, the performance of the model was satisfactory with R^2 ranging between 0.61 and 0.90, and an RMSE below 2.1 gC m^{-2} d^{-1}.

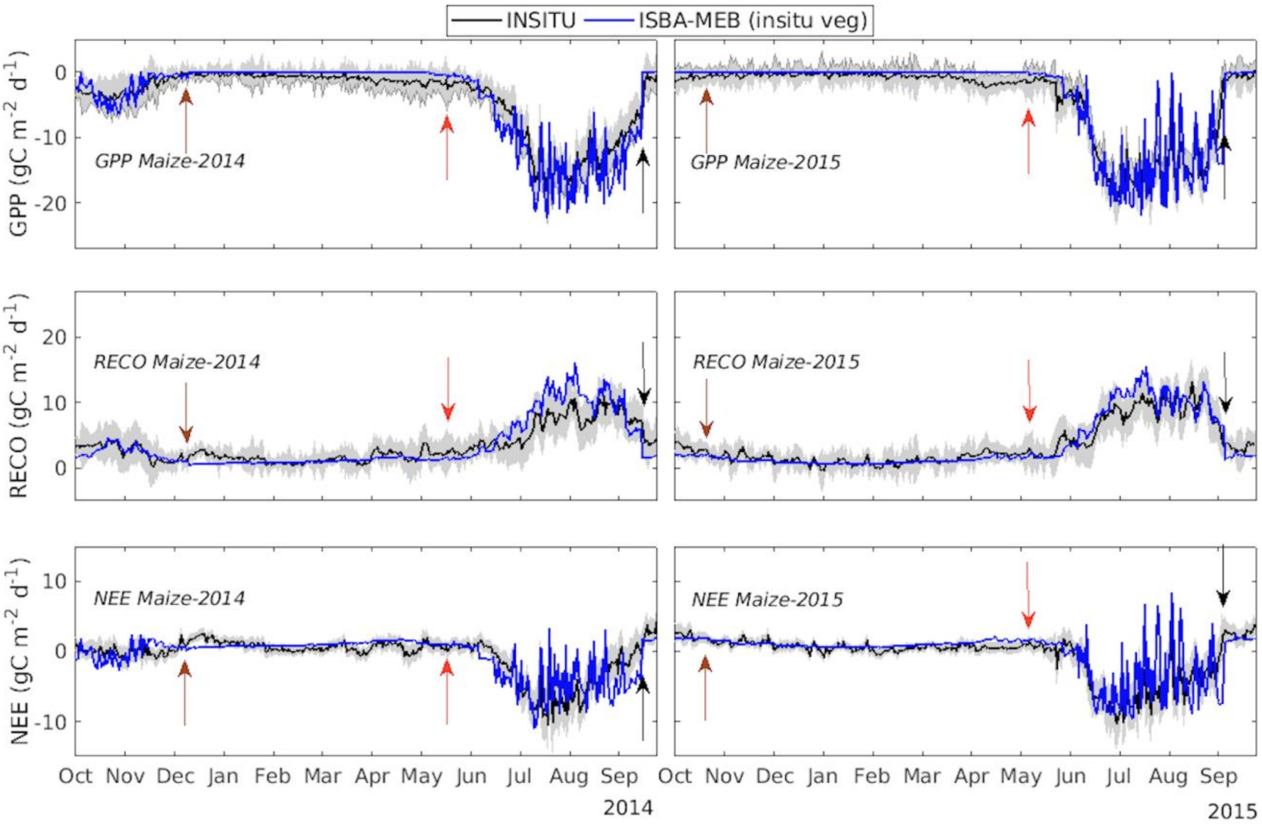

Figure 5.6c: Same as in Figure 5.4a, but for maize-2014, and maize-2015.

Maize-2019

Using the corrected leaf area indices, the day-to-day, and seasonal variability of the observed fluxes wese well predicted by ISBA-MEB. Likewise, the highest assimilated carbon estimated by the model coincided well with that of the observation, with an overall good agreement ($R^2 = 0.83$, and RMSE = 1.6 gC m^{-2} d^{-1}). 2019 is of interest because of the heat wave that struck in this region. Although, as shown in Figure 4.2, the expected high TA was unobservable; this could be due to the high transpiratory nature of maize, plus the large irrigation amount applied by the farmer. However, the maximum GPP ($RECO$) observed in maize-2019 was at least 27% (3%) larger than the maximum recorded in the preceding maize-years. This observation is supported by the experimental study of Xu et al. (2020) conducted over nine FLUXNET sites. Their results revealed that during heatwaves, GPP was depressed over most ecosystems except over C4 ecosystems where GPP was enhanced.

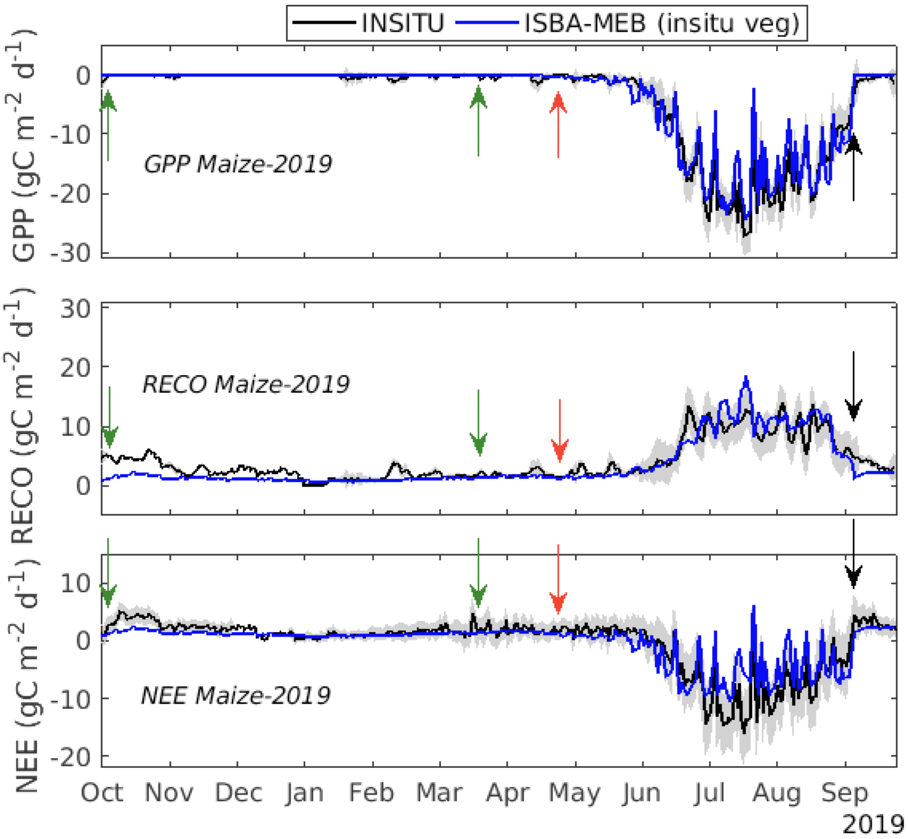

Figure 5.6d: Same as in Figure 5.4a, but for maize-2019.

Wheat-2007 and Wheat-2009

Figure 5.7a presents the fluxes for wheat-2007 and wheat-2009. The model explained more than 87% of the variation in daily GPP of wheat-2007, and 78% of wheat-2009. However, at the beginning of the season, there is a slight tendency of ISBA-MEB to underestimate low GPP fluxes. This could be due to errors linked with the acquisition of the LAI of young plants. Still, the RMSE for wheat-2007 (1.5 gC m^{-2} d^{-1}) and wheat-2009 (1.0 gC m^{-2} d^{-1}) lie within the range of values generally reported over wheat. Unlike the maize years, $RECO$ was underestimated almost throughout the growing period, with a larger bias after harvest. In this region (southwestern France), a common practice of farmers is to leave the harvest stalks (of wheat) over the field before the next farm operation (see Figure 5.6bi). Unfortunately, the effect of harvest stalks is not represented within the model; even though these residues impact the carbon exchanges. Furthermore, after harvest in wheat-2007, the (insitu + MODIS veg)'s run led to an overall improvement of $RECO$; R^2 and RMSE increased and decreased by 9% and 22%, respectively. Also, its prediction improved in wheat-2009 as R^2 increased from 0.42 to 0.54 (in $RECO$), and from 0.70 to 0.75 (in NEE), with an RMSE that is at least 15% lower for both fluxes.

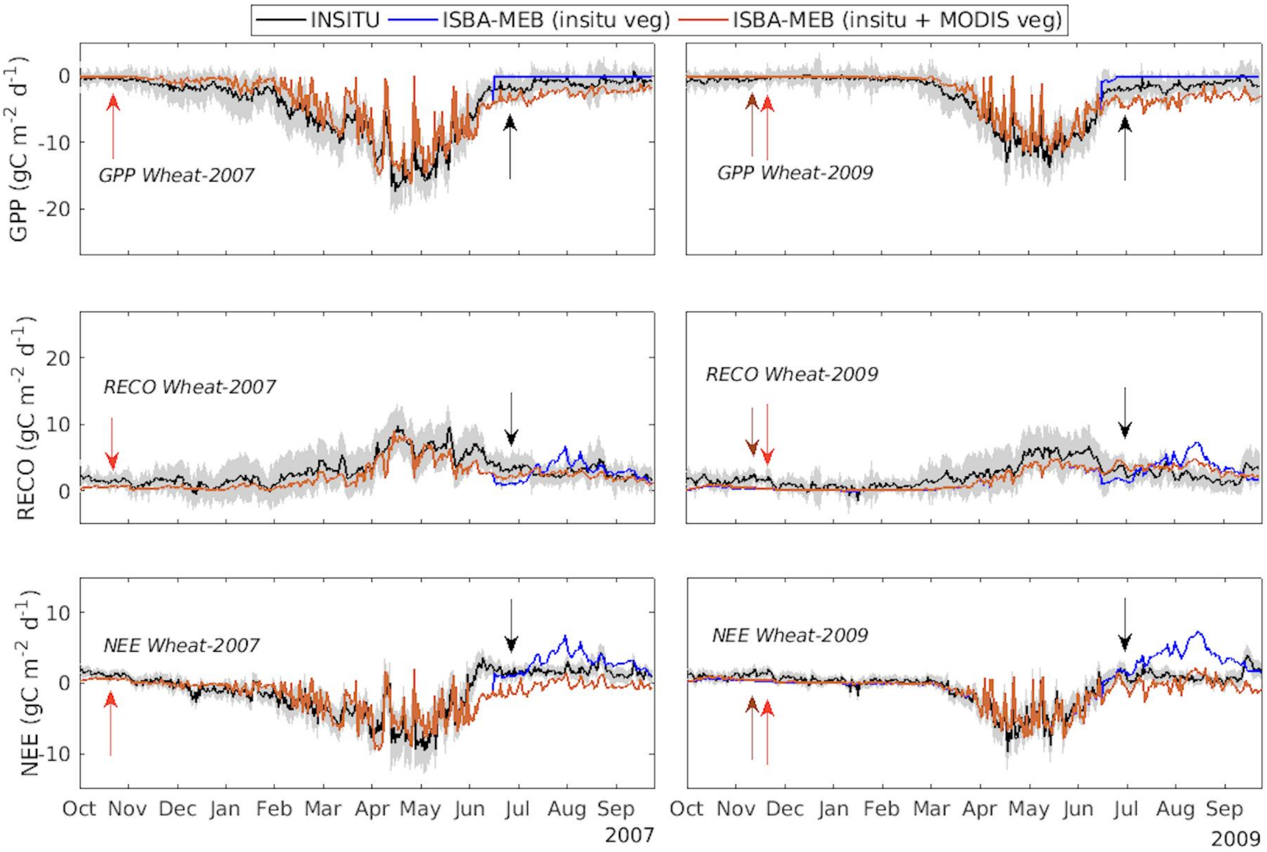

Figure 5.7a: Temporal evolution of the daily carbon fluxes measured on site and estimated by the model for wheat-2007, and wheat-2009. The shaded regions represent the maximum daily standard deviations (in GPP and $RECO$), and the uncertainties (in NEE).

Wheat-2011 and Wheat-2013

In wheat-2011, all the carbons components were poorly simulated. At the start of 2011 (civil year), a strong underestimation of GPP (Figure 5.7b) is observed. From the LAI in Figure 4.2, between December and the second week of January, wheat-2011 presented a steady and slow growth, which took a rapid turn afterwards. Unfortunately, from the 1st of January till the 11th of March, flux measurements were unavailable due to instrumental failure; consequently, this period had to be gap-filled which could have introduced some errors. Nevertheless, between the 12th of March up until the 12th of July (harvest), the model reproduced GPP quite well. After harvest, this plot experienced a buoyant regrowth which was fairly reproduced by the (insitu + MODIS veg)'s run. Despite all the constraints surrounding this year, the model-data agreement is fairly acceptable- GPP (R^2 = 0.72, RMSE = 2.1 gC m^{-2} d^{-1}), $RECO$ (R^2 = 0.53, RMSE = 1.3 gC m^{-2} d^{-1}), and NEE (R^2 = 0.78, RMSE = 1.4 gC m^{-2} d^{-1}), although in comparison with the other years, its GPP and $RECO$ has the lowest R^2 and highest RMSE values.

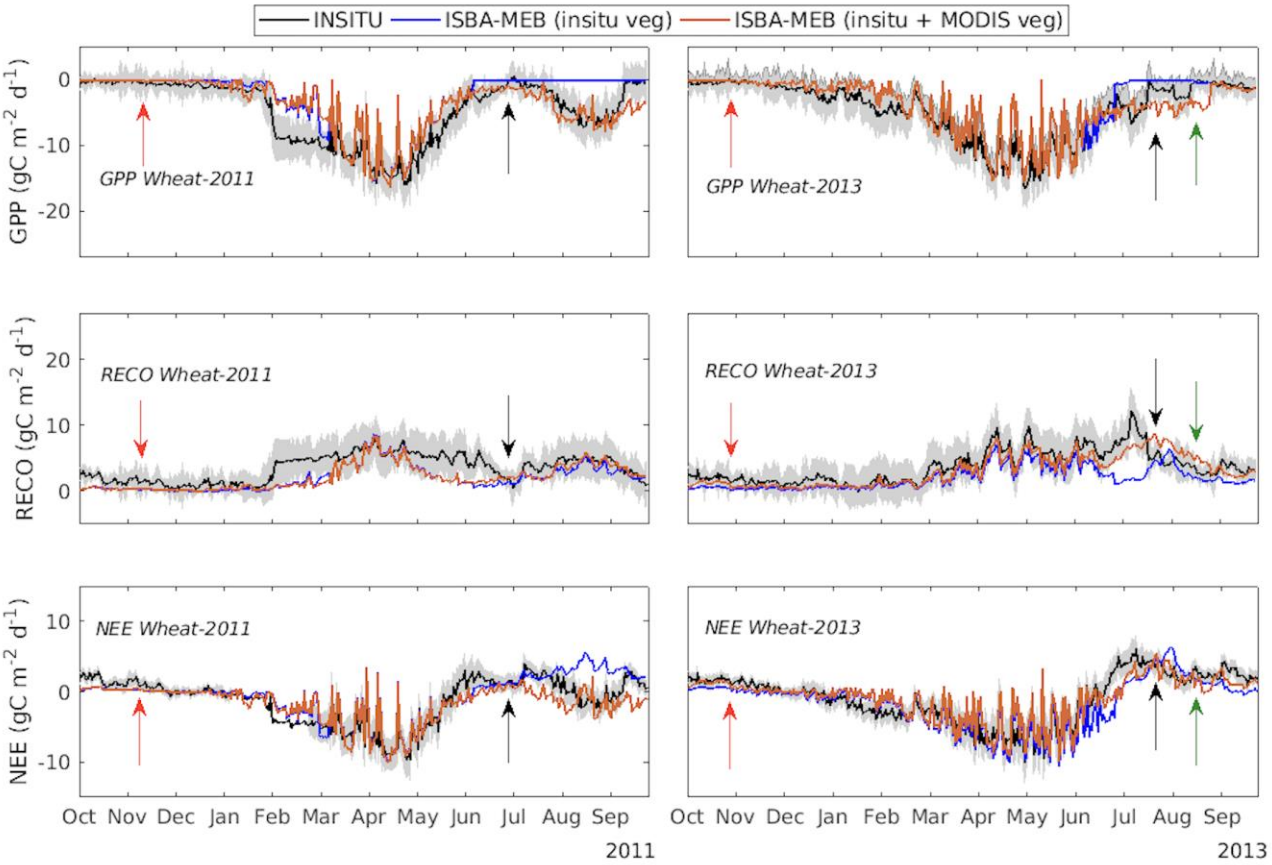

Figure 5.7b: Same as in Figure 5.6a, but for wheat-2011 and wheat-2013.

As observed in the other years, ISBA-MEB gave better estimates during the vegetative period but had difficulty simulating the start and the end period of wheat-2013. In the first week of July, just as senescence sets in, there was a rapid sprouting of weeds which was not aptly captured by remote sensing. Nevertheless, with the inclusion of weeds and regrowths, statistical metrics became more significant; R^2 experienced a 26% and 7% increase in $RECO$ and NEE, respectively, while there was a 20% decrease in the RMSE for the net flux (Figure 5.8).

The above results revealed that the model can capture both the day-to-day, and seasonal variability of the observation. Unfortunately, the representation of agricultural activities such as residue management, tillage practices etc are yet to be available within ISBA-MEB- this is required for improved accuracy.

The statistical metrics in Figure 5.8 shows that on average, ISBA-MEB performs better over maize. Over maize, R^2 values ranged between 0.9 and 0.96 for GPP, 0.83 and 0.90 for $RECO$, and 0.6 and 0.81 for NEE, whereas for wheat, maximum R^2 values for GPP, $RECO$, and NEE are 0.87, 0.81, and 0.75 respectively. This could be attributed to strong homogeneity in maize, particularly during the peak growth, while wheat can be sparser, permitting the strong presence of weeds. Furthermore, it is generally difficult to obtain a good model-data agreement for NEE because it is easier to model larger fluxes (GPP and $RECO$), than smaller fluxes (NEE). Although, model-data agreement is worse for $RECO$ in wheat.

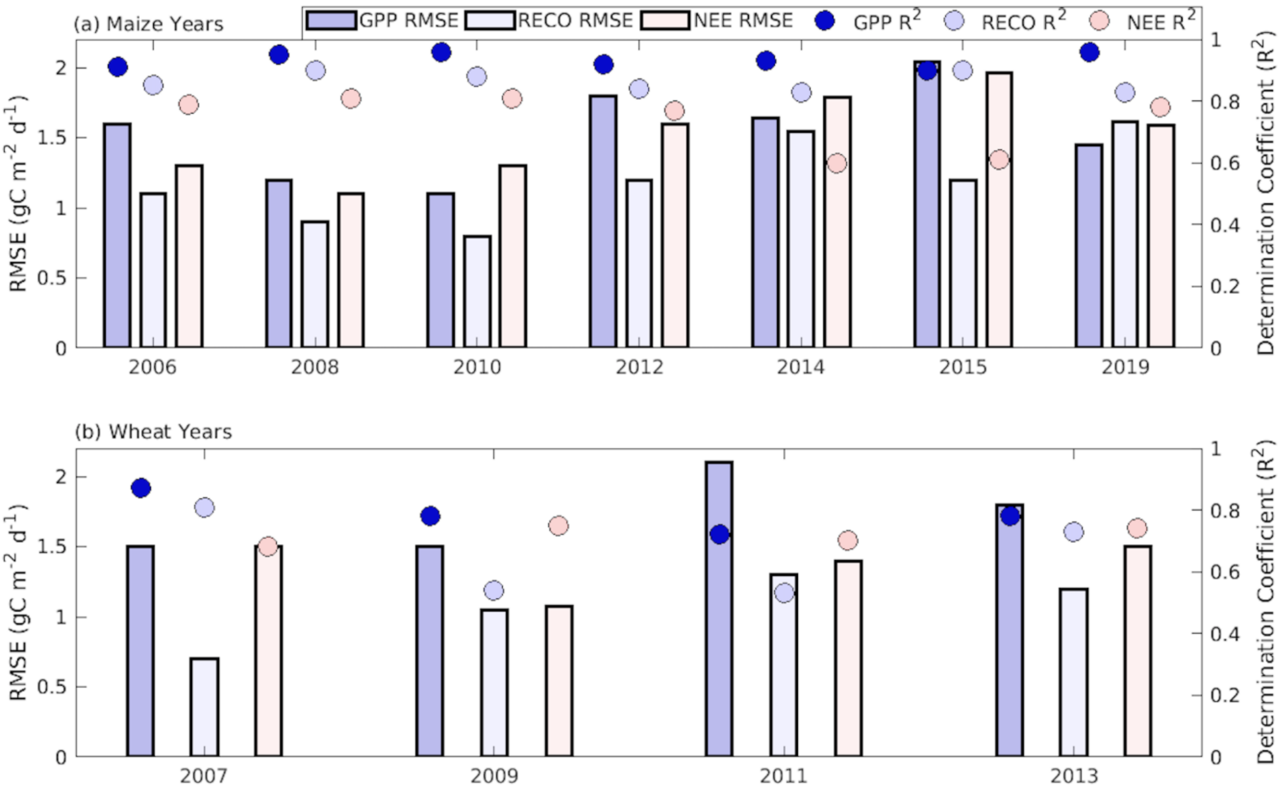

Figure 5.8: Statistical metrics (RMSE and R^2 in bars and circles respectively) obtained from the linear regression of the daily estimates of the model vs the EC measurements for GPP, $RECO$, and NEE for maize and wheat. NB: For maize-2006 and all the wheat years, these statistics represent the (insitu + MODIS veg)'s run.

5.3.3 Net annual ecosystem production

This section estimates the Net Ecosystem Production (NEP); that is, the integral NEE over a cultural year. From the convention adopted in this study plus *if* lateral fluxes had been considered, a negative NEP value would indicate a carbon sink, while a positive NEP implies a carbon source.

Figure 5.9 compares the cumulative sum of the measured and observed net ecosystem exchange, and Table 5.6 presents these values. For maize, ISBA-MEB-NEP varied between 38 gC m^{-2} yr^{-1} and -363.2 gC m^{-2} yr^{-1} which is within the range of the EC values that ranged between 15 gC m^{-2} yr^{-1} and -218gC m^{-2} yr^{-1}. In absolute terms, maize-2014 has the lowest model-data difference of 3.3 gC m^{-2}.

This is the cover-crop year, and the reason for this level of goodness is the availability of *in-situ* vegetation indices during the intercrop period. On the other hand, in relative terms, the largest discrepancy is found in maize-2012 (diff % = 325%), while in absolute values, the largest model-data difference is in maize-2015 (166 gC m^{-2} yr^{-1}). In spite of the representation of regrowths and weeds by MODIS indices, NEP is largely overestimated in maize-2006 because MODIS pixel typically contains mixed LAI signatures from different crops and phenologies (Etchanchu et al., 2017)

For NEP over wheat, ISBA-MEB(insitu veg) was between +25 gC m^{-2} yr^{-1} and -505 gC m^{-2} yr^{-1}, whereas ISBA-MEB(insitu + MODIS veg) ranged between -322 gC m^{-2} yr^{-1} and -605 gC m^{-2} yr^{-1} with greater disadvantage in wheat-2007 and wheat-2011 when compared to *in-situ* data that varied between -168 gC m^{-2} yr^{-1} and -428 gC m^{-2} yr^{-1}. The largest model-data disparity is found in wheat-2011; in absolute terms (178 gC m^{-2} yr^{-1}), with a relative difference of about forty percent. The constraining factors in wheat-2011 include a 3-months data gap, regrowths, tillage, etc-; and so, for an improved model performance, processes that are crucial to surface-atmosphere exchanges must be represented (a few include residue management, carbon exportation, organic amendments, human respiration within the footprint etc).

Furthermore, owing to the longer growing period of wheat, NEP is about 40% larger compared to maize. For example, considering *in-situ* measurements, maximum NEP of -428 gC m^{-2} yr^{-1} was recorded in wheat-2011, while in maize, it was -218 gC m^{-2} yr^{-1} in maize-2014. Also, maize-2014 sequestered the largest carbon due to the presence of mustard plant- this is consistent with the studies (Poeplau and Don, (2015); Pellerin et al. (2019)) that have identified cover-crop planting as a carbon-sequestration strategy. Overall, this study can safely conclude that the management practices at FR-Lam is sustainable, but can be improved e.g., by planting more cover crops. In addition, the current residue management for wheat could be improved because the CO_2 released is significant.

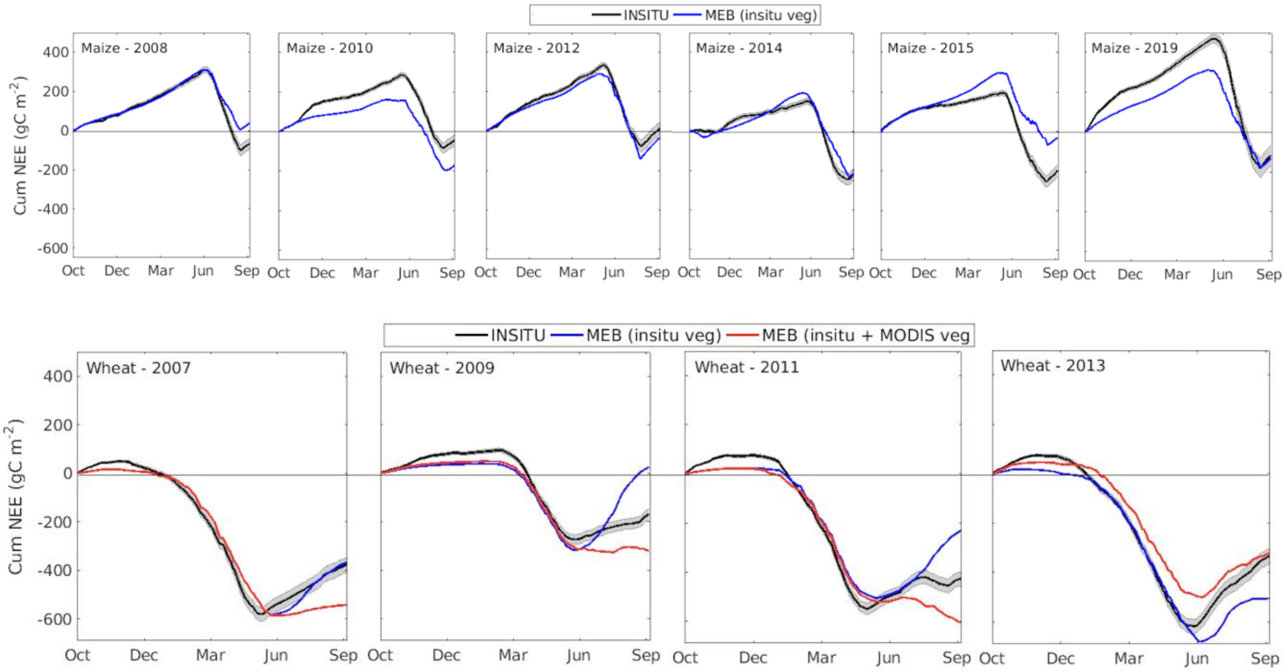

Figure 5.9: Cumulative temporal evolution of the modeled and measured NEE for maize (first row), and wheat (second row).

Table 5.6: Cumulative NEP values for EC and ISBA-MEB for the studied crop years.

Crop	Year	IN-SITU	ISBA-MEB (insitu veg)	ISBA-MEB (insitu + MODIS veg)	Diff	Diff%
			[gC m^{-2} yr^{-1}]			%
Maize	2006	-141.9	-227.5	-363.2	-221.3	156
	2008	-68.1	+37.8	--	105.9	155
	2010	-43.1	-166.4	--	-123.3	286.1
	2012	14.5	-32.7	--	-47.2	325.6
	2014	-217.8	-214.5	--	3.3	1.5
	2015	-196.6	-31.1	--	165.5	84
	2019	-117.6	-131.1	--	-13.5	12
Wheat	2007	-378.5	-375.5	-540.1	-161.6	43
	2009	-168.4	+25.8	-319.9	-151.5	89
	2011	-427.9	-232.5	-605.4	-177.5	41
	2013	-333.1	-505.3	-322.4	+10.7	3.2

NB: Each crop year runs from the 1st of Oct. to the 30th of Sept.

5.4 Conclusions

First, a soil respiration comparative study between AC and EC systems was conducted to examine the limits of each system, and if and how well they complement. The study period was between the 23rd of July 2013, and the 19th of May 2015. The analysis revealed that both measurements have good agreement- they gave a comparable measurement range; SR_{EC} was between 0.03 gC m^{-2} and 9.4 gC m^{-2}, and 0.1gC m^{-2} and 10.7 gC m^{-2} for SR_{AC}. Overall, measurements from the AC exhibit higher variability and sensitivity to rainfall and tillage. Hence, at FR-Lam, the management of the ACs requires further improvement particularly on the reduction of the frequent removal and re-installation of the chambers prior to soil works.

Secondly, carbon fluxes from an eddy covariance system and a canopy chamber were compared over wheat and maize. For wheat, based on the CC, 32% of the assimilated carbon was released into the atmosphere via respiration, and 73 gCO_2 m^{-2} was sequestered. On the other hand, from the EC, $RECO$ accounts for 21% of GPP, while 67 gCO_2 m^{-2} was sequestered. On average, the NEE of both systems were in close agreement. In contrast, there is a large discrepancy between the measurements over maize especially GPP. This could have resulted due to the strong heterogeneity over the plot in the early stages of maize.

Finally, ISBA-MEB was evaluated against EC measurements for $GPP, RECO$ and NEE. This was in two parts: (i) For the first part, only *in-situ* vegetation variables were used to run the model. This gave acceptable metrics particularly during the primary vegetative periods. However, because the vegetation characteristics of the plot are not surveyed after harvest, the fluxes of the intercrop period could not be represented within the model. (ii) As a result, the second part of the experiment introduced vegetation indices drawn from MODIS to represent these intercrop periods. The new estimates presented a slight improvement in some years, statistical metrics were within acceptable ranges; R^2 was between 0.72 and 0.96 for GPP, 0.53 and 0.90 for $RECO$, and 0.60 and 0.81 for NEE. (ii) Also, RMSE values ranged from 1.1 gC m^{-2} d^{-1} to 2.1 gCm^{-2} d^{-1} for GPP, 0.7 gC m^{-2} d^{-1} to 2.0gC m^{-2} d^{-1} for $RECO$, and 1.1 gC m^{-2} d^{-1} to 2.0 gC m^{-2} d^{-1} for NEE. To improve the model's estimates, access to leaf area products of higher resolution is required.

Some main ideas of this chapter

- Comparison of AC with EC demonstrated that the EC system looks promising in the provision of long-term soil respiration measurements.

- Even with minimal calibration, the estimates of ISBA-MEB agreed well with the EC measurements with significant correlations.

- Model predictions can be improved through the representation of critical farm activities within the model- after then, ISBA-MEB can become a carbon-status monitoring tool.

- Within the model, the 10-days averaging of the vegetation variables needs to be reduced to better capture rapid and subtle growths.

- Planting of cover crops is a good strategy to increase soil carbon.

Chapter 6: General conclusions

6.1 General conclusion

Croplands have an ambivalent relationship with the climate. As a major contributor to France's greenhouse gas emissions, the mere existence or expansion of croplands is not only vital for the sustenance of the growing populace, but they play a major role in the future-state of our planet through their ability to sequester and release carbon. This thesis work is aimed to improve our understanding of the functioning of two croplands in the southwest of France through the assessment of its interaction with the atmosphere via energy, water, and carbon fluxes. During this thesis, I analyzed some *in-situ* measurements, some remotely-sensed data, and I implemented the ISBA-Ags model developed by Noilhan and Planton (1989) and Calvet et al. (1998), as well as its MEB version that was revised by Boone et al. (2016) over FR-Lam and FR-Aur- the model is able to jointly simulate water, energy, and carbon fluxes. The major findings of this study are as follows:

6.1.1 The surface energy balance

The surface energy balance is the cornerstone that guides the theoretical description of the Earth's climate system. Besides this, its knowledge is required because they represent boundary conditions for a wide range of studies e.g., water management in agricultural plots, validation of land-atmosphere simulations etc. The quality of these surface fluxes must be checked via the energy balance closure (EBC), and factors that control the degree of closure and non-closure must be investigated. In addition, in view of the close biophysical coupling between energy, water, and carbon fluxes, the EBC could also provide a hint on the quality of the CO_2 fluxes measured by the EC system. Therefore, the first part of this PhD work was a surface energy balance study with EC measurements. One of its specific objectives was to identify how crop types and stages, climatic variables, farm practices, and surrounding topography impact the energy balance closure and energy partitioning.

Overall, the degree of the EBC depended on how well mechanically and thermally induced turbulence was developed; as such, for all the considered scenarios, EBC was constantly higher in FR-Aur compared to FR-Lam. With this in mind, the impact of crop type on the EBC is inevident; for instance, the common crop between both sites is wheat, and over this crop's cycle, EBC in FR-Lam ranged between 0.53 and 0.87, whereas it was between 0.68 and 0.88. Nevertheless, in spite of the proximity of both sites, this observation must be interpreted with care because the cultivation time for this crop (wheat) never coincided at both sites;- the wheat years are intercalated at both sites. Hence, for future studies, this between-site comparison should be performed over the same crop type that share the same, or similar planting dates to limit the interference of climatic variability. On the other hand, a crop's phenology exerts a crucial control on the surface fluxes, even though its influence on the EBC remains unclear because it was impossible to isolate the control of seasonality in this study. Also, our results imply an unclear effect of rainfall on the EBC, and this could be because there is rarely water shortage at both sites. Hence, for future investigation, it would be interesting to compare a tropical climate with an arid climate for the same crop type.

To understand the source of the missing energy, the commonly neglected component (sensible heat advection term (A_H)) was estimated using surface temperature values drawn from Landsat7/8 within the framework developed in Cuxart et al. (2016). The outcome of this exercise (Dare-Idowu et al., 2021a) revealed that this term is responsible for over half of the residual energy at our study sites with larger magnitudes at FR-Lam in agreement with the situation surrounding the plot, and the on-site activities. Due to the required sophisticated set-up, this study found its limitation in its inability to estimate the latent heat advection term (A_{LE}). Nonetheless, the irrigation pattern and frequent waterloggedness at FR-Lam suggests a tendency of a non-negligible A_{LE}. In future studies, it would be interesting to account for the horizontal exchanges of surface humidity at these sites- this might be a pathway to further narrow the energy gap.

Another limitation of this study is the unavailability of many Landsat scenes; hence, the seasonal variability of A_H could not be assessed- this could have provided more insights into why larger residual energy is found during summer. Nonetheless, this study provided us with key elements for the validation of ISBA and ISBA-MEB, alongside with a caution during the model-data comparison because the energy balance closure study remains an outstanding problem that requires a continuous effort of the scientific community.

6.1.2 The energy and water budget

In the second part of this study, a composite soil-vegetation scheme (ISBA) and its dual-source version (ISBA-MEB) (both with the A-gs module) were implemented over 4 wheat and 6 maize seasons in FR-Lam. This makes it possible to estimate the surface energy fluxes, soil components, and also to determine the most suitable configuration for both crop types. Even though, these models can be run with remotely-sensed data, in this study, they were strictly driven by *in-situ* measurements, and the models' estimates were evaluated against EC measurements. The results (Dare-Idowu et al., 2021b) revealed that although the estimates of both versions of the ISBA model laid within acceptable ranges, ISBA-MEB outperformed ISBA in the prediction of the turbulent fluxes when the vegetation fraction cover is low (i.e., when the field is composed of a mix of bare soil and vegetation). Even though ISBA-MEB was initially developed for forested sites with snow covers, it was successfully applied over FR-Lam cropland for the first time, and from the results presented in Chapter 4, it provided better estimation of the ET for both wheat and maize due to its configuration that explicitly separates the vegetation from the soil surface.

In addition, the ET-partitioning capability of each energy budget configuration was evaluated using some sap flow measurements obtained over maize in FR-Lam. In spite of the similarities in the estimates of both models owing to the strong homogeneity and high structural density of the maize canopy during the period of data availability, ISBA-MEB proved slightly more suitable. Notwithstanding, the choice between a single and a dual-source model remains strongly constrained by the scale of the study site and the degree of sparseness. So, in spite of ISBA-MEB's performance, more local-scale evaluation of this model is recommended over different crops and sites with different levels of heterogeneity and climate condition in order to strengthen our conclusions, and to feed the global database of land surface parameters such as the ECOCLIMAP II. Similarly, further evaluation of the partitioning capability of ISBA and ISBA-MEB is recommended over crops with high heterogeneity using sap flow sensors and soil evaporation chambers.

One minor limitation that this sap flow method holds is that the term that accounts for the changes in the storage of heat at the heated section of the plant's stem was neglected and omitted in the heat balance equation. Unfortunately, certain studies such as Senock and Ham (1993) have found this term to account for about 3% of the total daily heat flux. Hence, for future campaigns, the inclusion of this term is recommended.

Finally, results from the analysis of the inter-annual variability of the crop water budget can be summarized as follows: (1) The partitioning of the ET revealed a strong year-to-year variability with Tr ranging between 40% and 67% of total ET in maize, and between 42%-56% in wheat. On the other hand, Es dominated in maize-2008 and maize-2010 due to the late and poor canopy development, whereas for all the wheat years, soil evaporation was the largest component except in wheat-2007. (2) Over the maize years, drainage losses were close to null because of an impervious layer at 60 cm depth, while in the wheat years, surface run off was substantial with the exception of wheat-2011 being particularly dry. In conclusion, this study provided insights into the good irrigation practice of the farmer which precludes this study from offering recommendations on irrigation amount and scheduling.

One challenge encountered in the simulation of the surface fluxes was the difficulty in obtaining the soil hydraulic parameters. Although they were generated by providing in situ fractions of clay and sand to compute parameters for Clapp and Hornberger 1978, there are certain uncertainties surrounding these measured soil fractions. According to Van den Hurk et al. (2016) and Garrigues et al. (2019), a small error in the computation of these hydraulic properties could result in a large bias between measured and estimated ET. Similarly, due to unavailable in situ measurements, literature values were adopted for the root profiles of the crops. The downside of this includes: (i) the uniqueness of the crops and the site's characteristics are lost, (ii) given that a single parameterization was maintained for all the years for the same crop type; the uniqueness of each year is masked- this can impact the interpretation of the model's output especially when making a year-to-year comparison. In the wheat years for instance, the minimum and maximum leaf area index was obtained in 2009 (LAI = 2.4 m^2 m^{-2}) and in 2011 (LAI = 6.8 m^2 m^{-2}) respectively. These two years would as matter of course have different root systems.

6.1.3 The carbon balance

In the concluding part of this study, three aspects were focused on:

(a) First, a comparison study was carried out between some soil respiration measurements obtained from an eddy covariance system, and measurements from an automated chambers over bare soils in FR-Lam between the 23rd of July 2013 and the 18th of November 2015. Measurements from both systems showed fair agreement with similar magnitude that is between 0.03 gC m^{-2} and 9.4 gC m^{-2} for the EC system, and between 0.1 gC m^{-2} and 10.7 gC m^{-2} for the AC system. However, there were certain disagreements between both measurements during soil works and rain events to which the automated chamber is particularly sensitive- thus raising questions about the reliability of the automated chamber under such disturbances. Overall, the discrepancies found between both measurements could be associated to (i) Differences in the operating principles: the EC method is based on a principle of vertical turbulence whereas the automated chamber uses a simple diffusion principle. (ii) Dissimilar source area: the footprint of the EC system is large, complex, and dynamic, while the automated chamber has a static and smaller footprint; hence, the reconciliation of the source areas can be a challenge. In addition, the chamber measurements which should serve as a reference is fueled with uncertainties because of cracks in the soil which is a frequent phenomenon in FR-Lam during summer because of the high clay content. Nonetheless, more comparative studies are required to provide better understanding of the not-well-understood errors.

(b) The second focus is the comparison of the CO_2 fluxes measured by a canopy chamber and the EC system over wheat (15th February to 19th April 2007) and maize (5th June to 26th June 2008). For wheat, the correlation coefficient was 0.81, 0.65, and 0.41 for $RECO$, GPP, and NEE, respectively. However, a poorer correlation was found over maize; this could be due to the high heterogeneity of the plot during this period, plus the non-representativeness of the selected sample points- in order words, there is a strong spatial variability in the vegetation characteristics at each sample point, and this presented a major bottleneck in this comparative study. For future work, a longer campaign period is proposed, and sample points whose vegetation matches those within the field of view of the EC system is advised.

(c) This study was concluded with an evaluation of ISBA-MEB, to demonstrate this model's ability to predict good estimations of the major carbon components. This evaluation was carried out over 7 maize, and 4 wheat years. While the presented results are preliminary findings and must be interpreted with caution, the performance of the model is promising. To account for the assimilatory and respiratory processes of the intercrop-period, vegetation indices drawn from MODIS was used because regrowths and weeds are never monitored in-situ. All in all, the model-data comparison presented acceptable statistics: R^2 values laid between 0.72 and 0.96 for GPP, 0.53 and 0.90 for $RECO$, and 0.60 and 0.81 for NEE. Also, the RMSEs are within acceptable ranges of 1.1 gC m^{-2} d^{-1} to 2.1 gC m^{-2} d^{-1} for GPP, 0.7 gC m^{-2} d^{-1} to 2.0 gC m^{-2} d^{-1} for $RECO$, and 1.1 gC m^{-2} d^{-1} to 2.0 gC m^{-2} d^{-1} for NEE. On crop type basis, ISBA-MEB performed poorly over wheat compared to maize. This could be linked to the deficiency of MODIS scenes whose spatial resolution is low, and so, the pixels often contain mixed LAI signatures. Along with its low visitation frequency (16 days), this product was unable to aptly capture the magnitude and the rapidity that is often associated with weeds and regrowths. Indeed, LAI values drawn from MODIS tend to be an overestimate during inter-cropping periods, and an underestimate during major crop seasons. A potential means of improvement lies in using remote sensing products with decametric resolutions and higher revisit time (e.g., Sentinel-2). As an improvement within the model, imported and exported carbon should be considered; as such, ISBA-MEB can be used to identify the carbon status of a cropland. In addition, our result highlighted that cover crops (mustard in this study) enhanced the carbon-sequestration of the plot, and the farmer could be advised to keep them for longer periods. This proposal must be handled with care because it could impact the upcoming cropping seasons significantly in terms of the soil's fertility and water status.

Furthermore, specific attention was given to the drought of 2019 in order to offer a rough prediction on the response of the FR-Lam plot should it experience frequent, and more intense heat waves. From our result, carbon uptake was extremely enhanced due to the direct and positive effect of high air temperatures on canopy conductance, while the amount of carbon released back into the atmosphere increased by a lower proportion.

The first limitation of this study is the large averaging time period for the prescription of the biophysical variables in the model. The minimum time step currently available is 10 days, and this is too large for fast-growing crops like maize and wheat. The error this introduces cannot be neglected, as it is evident at the beginning and at the end of each growing season. Furthermore, a major constraint of this assessment lies in the non-uniformity in the acquisition of the leaf area index. In the early years, the destructive method was used; this sampling method considers only the leaves, whereas the whole plant system in fact participate in carbon exchange with the atmosphere. The omission of the other parts of the plant could lead to an underestimation by the model. Conversely, LAI measurements of recent years were carried out with non-destructive methods. This dissimilarity becomes important when making a year-to-year comparison and could mislead interpretation.

Another main limitation is that for a complete computation of a carbon balance, the effect of input (e.g., organic amendments) and output carbon (e.g., exported straws and farm produce) is required. Unfortunately, this data is unavailable *in-situ*, and could not be retrieved by remote sensing. These omitted elements prohibit the determination of the sink-source status of the plot. In addition, due to the expensive instrumental set up required in the estimation of the horizontal $\mathrm{CO_2}$ advection, this term was not measured at FR-Lam. However, studies have attested to its importance particularly under calm and stable conditions- which is a typical situation of FR-Lam.

While ISBA-MEB looks promising and could be a gap-filling resource, an improvement to the model will be to have smaller averaging days for the vegetation parameters of fast-growing crops. This would improve the timing of the sowing, peaking, and senescing. Another improvement should be the inclusion of the effect of management events- while specifying sowing and harvest dates. Furthermore, as already discussed in many studies, soil organic carbon should be considered when computing soil hydraulic properties. As a conclusion, more evaluation studies is recommended for different climatic conditions and crop types of different geometry.

6.1 Conclusion générale

Les terres cultivées entretiennent une relation ambivalente avec le climat. En tant que contributeur majeur aux émissions de gaz à effet de serre en France, la simple existence ou l'expansion des terres cultivées n'est pas seulement vitale pour la subsistance de la population croissante, mais elles jouent un rôle majeur dans l'état futur de notre planète par leur capacité à séquestrer et libérer le carbone. Ce travail de thèse vise à améliorer notre compréhension du fonctionnement de deux terres cultivées dans le sud-ouest de la France par l'évaluation de son interaction avec l'atmosphère via les flux d'énergie, d'eau et de carbone. Au cours de cette thèse, j'ai analysé des mesures in-situ, des données télédétectées, et j'ai implémenté le modèle ISBA-Ags développé par Noilhan et Planton (1989) et Calvet et al. (1998), ainsi que sa version MEB révisée par Boone et al. (2016) sur FR-Lam et FR-Aur- le modèle est capable de simuler conjointement les flux d'eau, d'énergie et de carbone. Les principaux résultats de cette étude sont les suivants:

6.1.1 Le bilan énergétique de surface

Le bilan énergétique de surface est la pierre angulaire qui guide la description théorique du système climatique de la Terre. En outre, sa connaissance est nécessaire car il représente les conditions limites pour un large éventail d'études, par exemple, la gestion de l'eau dans les parcelles agricoles, la validation des simulations terre-atmosphère, etc. La qualité de ces flux de surface doit être vérifiée par la fermeture du bilan énergétique (EBC), et les facteurs qui contrôlent le degré de fermeture et de non-fermeture doivent être étudiés. En outre, compte tenu du couplage biophysique étroit entre les flux d'énergie, d'eau et de carbone, l'EBC pourrait également fournir un indice sur la qualité des flux CO_2 mesurés par le système EC. Par conséquent, la première partie de ce travail était une étude du bilan énergétique de surface avec des mesures EC. L'un de ses objectifs spécifiques était d'identifier comment les types et les stades de culture, les variables climatiques, les pratiques agricoles et la topographie environnante ont un impact sur la fermeture du bilan énergétique et le partage de l'énergie.

Dans l'ensemble, le degré de l'EBC dépendait du développement de la turbulence induite mécaniquement et thermiquement; ainsi, pour tous les scénarios considérés, l'EBC était constamment plus élevé dans la zone FR-Aur par rapport à la zone FR-Lam. En gardant cela à l'esprit, l'impact du type de culture sur l'EBC est inévitable; par exemple, la culture commune aux deux sites est le blé, et sur le cycle de cette culture, l'EBC en FR-Lam a varié entre 0,53 et 0,87, alors qu'il était entre 0,68 et 0,88. Néanmoins, malgré la proximité des deux sites, cette observation doit être interprétée avec précaution car la période de culture de cette culture (blé) n'a jamais coïncidé sur les deux sites; les années de blé sont intercalées sur les deux sites. Par conséquent, pour les études futures, cette comparaison entre sites devrait être effectuée sur le même type de culture qui partage les mêmes dates de plantation, ou des dates similaires, afin de limiter l'interférence de la variabilité climatique. D'autre part, la phénologie d'une culture exerce un contrôle crucial sur les flux de surface, même si son influence sur l'EBC reste peu claire car il a été impossible d'isoler le contrôle de la saisonnalité dans cette étude. De plus, nos résultats impliquent un effet peu clair des précipitations sur l'EBC, ce qui pourrait être dû au fait qu'il y a rarement un manque d'eau sur les deux sites. Ainsi, pour de futures recherches, il serait intéressant de comparer un climat tropical avec un climat aride pour le même type de culture.

Pour comprendre la source de l'énergie manquante, la composante communément négligée (terme d'advection de la chaleur sensible (A_H)) a été estimée à l'aide des valeurs de température de surface tirées de Landsat7/8 dans le cadre développé par Cuxart et al. (2016). Le résultat de cet exercice (Dare-Idowu et al., 2021a) a révélé que ce terme est responsable de plus de la moitié de l'énergie résiduelle sur nos sites d'étude avec des magnitudes plus importantes à FR-Lam en accord avec la situation entourant la parcelle, et les activités sur place. En raison de l'installation sophistiquée requise, cette étude a trouvé sa limite dans son incapacité à estimer le terme d'advection de la chaleur latente (A_{LE}). Néanmoins, le schéma d'irrigation et la fréquente saturation en eau à FR-Lam suggèrent une tendance à un A_{LE} non négligeable. Dans les études futures, il serait intéressant de prendre en compte les échanges horizontaux d'humidité de surface sur ces sites- cela pourrait être une voie pour réduire davantage l'écart énergétique.

Une autre limite de cette étude est la non-disponibilité de nombreuses scènes Landsat; par conséquent, la variabilité saisonnière de A_H n'a pas pu être évaluée- ce qui aurait pu permettre de mieux comprendre pourquoi une plus grande énergie résiduelle est trouvée en été. Néanmoins, cette étude nous a fourni des éléments clés pour la validation d'ISBA et d'ISBA-MEB, avec une mise en garde lors de la comparaison modèle-données car l'étude de la fermeture du bilan énergétique reste un problème en suspens qui nécessite un effort continu de la communauté scientifique.

6.1.2 Le bilan énergétique et hydrique

Dans la deuxième partie de cette étude, un schéma composite sol-végétation (ISBA) et sa version à double source (ISBA-MEB) (tous deux avec le module A-gs) ont été mis en œuvre sur 4 saisons de blé et 6 saisons de maïs en FR-Lam. Ceci permet d'estimer les flux d'énergie de surface, les composantes du sol, et aussi de déterminer la configuration la plus appropriée pour les deux types de cultures. Bien que ces modèles puissent être exécutés avec des données télédétectées, dans cette étude, ils ont été strictement pilotés par des mesures *in-situ*, et les estimations des modèles ont été évaluées par rapport aux mesures EC. Les résultats (Dare-Idowu et al., 2021b) ont révélé que bien que les estimations des deux versions du modèle ISBA se situent dans des fourchettes acceptables, ISBA-MEB a surpassé ISBA dans la prédiction des flux turbulents lorsque la fraction de couverture végétale est faible (c'est-à-dire lorsque le champ est composé d'un mélange de sol nu et de végétation). Même si ISBA-MEB a été initialement développé pour des sites forestiers avec des couvertures neigeuses, il a été appliqué avec succès sur des terres cultivées de FR-Lam pour la première fois, et d'après les résultats présentés au chapitre 4, il a fourni une meilleure estimation de l'ET pour le blé et le maïs grâce à sa configuration qui sépare explicitement la végétation de la surface du sol.

En outre, la capacité de partitionnement de l'ET de chaque configuration de bilan énergétique a été évaluée à l'aide de certaines mesures de flux de sève obtenues sur le maïs en FR-Lam. Malgré la similitude des estimations des deux modèles, due à la forte homogénéité et à la haute densité structurelle de la canopée du maïs pendant la période de disponibilité des données, ISBA-MEB s'est avéré légèrement plus adapté. Néanmoins, le choix entre un modèle à source unique et un modèle à double source reste fortement contraint par l'échelle du site d'étude et le degré de dispersion des données. Ainsi, malgré les performances d'ISBA-MEB, une évaluation à une échelle plus locale de ce modèle est recommandée sur différentes cultures et différents sites avec différents niveaux d'hétérogénéité et de conditions climatiques afin de renforcer nos conclusions, et d'alimenter la base de données globale des paramètres de surface terrestre telle qu'ECOCLIMAP II. De même, il est recommandé de poursuivre l'évaluation de la capacité de partitionnement d'ISBA et d'ISBA-MEB sur des cultures très hétérogènes en utilisant des capteurs de flux de sève et des chambres d'évaporation du sol.

Une limitation mineure de cette méthode de flux de sève est que le terme qui tient compte des changements dans le stockage de la chaleur à la section chauffée de la tige de la plante a été négligé et omis dans l'équation du bilan thermique. Malheureusement, certaines études comme celle de Senock et Ham (1993) ont trouvé que ce terme représentait environ 3% du flux thermique quotidien total. Par conséquent, pour les campagnes futures, l'inclusion de ce terme est recommandée.

Enfin, les résultats de l'analyse de la variabilité inter-annuelle du bilan hydrique des cultures peuvent être résumés comme suit: (1) Le partitionnement de l'ET a révélé une forte variabilité d'une année sur l'autre avec Tr variant entre 40 % et 67% de l'ET total pour le maïs, et entre 42% et 56% pour le blé.

D'autre part, Es a dominé dans le maïs-2008 et le maïs-2010 en raison du développement tardif et faible de la canopée, tandis que pour toutes les années de blé, l'évaporation du sol était la composante la plus importante, sauf dans le blé-2007. (2) Au cours des années de maïs, les pertes par drainage étaient proches de zéro en raison d'une couche imperméable à 60 cm de profondeur, tandis que pour les années de blé, le ruissellement de surface était important, à l'exception du blé-2011 qui était particulièrement sec. En conclusion, cette étude a fourni un aperçu de la bonne pratique d'irrigation de l'agriculteur, ce qui empêche cette étude de proposer des recommandations sur la quantité et le calendrier d'irrigation.

Un défi rencontré dans la simulation des flux de surface était la difficulté d'obtenir les paramètres hydrauliques du sol. Bien qu'ils aient été générés en fournissant des fractions in situ d'argile et de sable pour calculer les paramètres de Clapp et Hornberger 1978, il existe certaines incertitudes autour de ces fractions de sol mesurées. Selon Van den Hurk et al. (2016) et Garrigues et al. (2019), une petite erreur dans le calcul de ces propriétés hydrauliques pourrait entraîner un biais important entre l'ET mesurée et estimée. De même, en raison de l'indisponibilité des mesures in situ, des valeurs de la littérature ont été adoptées pour les profils racinaires des cultures. Les inconvénients de cette méthode sont les suivants (i) le caractère unique des cultures et des caractéristiques du site est perdu, (ii) étant donné qu'une seule paramétrisation a été maintenue pour toutes les années pour le même type de culture, le caractère unique de chaque année est masqué- ce qui peut avoir un impact sur l'interprétation des résultats du modèle, en particulier lors d'une comparaison d'une année sur l'autre. Dans les années de blé par exemple, l'indice de surface foliaire minimum et maximum a été obtenu en 2009 (LAI = 2,4 m^2 m^{-2}) et en 2011 (LAI = 6,8 m^2 m^{-2}) respectivement. Ces deux années auraient bien entendu des systèmes racinaires différents.

6.1.3 Le bilan carbone

Dans la partie finale de cette étude, trois aspects ont été examinés :

(a) Tout d'abord, une étude comparative a été réalisée entre certaines mesures de respiration du sol obtenues à partir d'un système de covariance de Foucault, et les mesures d'une chambre automatisée sur des sols nus dans FR-Lam entre le 23 juillet 2013 et le 18 novembre 2015. Les mesures des deux systèmes ont montré un bon accord avec une magnitude similaire, c'est-à-dire entre 0,03 gC m^{-2} et 9,4 gC m^{-2} pour le système EC, et entre 0,1 gC m^{-2} et 10,7 gC m^{-2} pour le système AC. Cependant, certains désaccords entre les deux mesures ont été constatés lors de travaux du sol et d'événements pluvieux auxquels la chambre automatisée est particulièrement sensible- ce qui soulève des questions quant à la fiabilité de la chambre automatisée face à de telles perturbations. Globalement, les divergences constatées entre les deux mesures pourraient être associées à (i) Des différences dans les principes de fonctionnement: la méthode EC est basée sur un principe de turbulence verticale alors que la chambre automatisée utilise un principe de diffusion simple. (ii) Des zones sources différentes: l'empreinte du système EC est grande, complexe et dynamique, alors que la chambre automatisée a une empreinte statique et plus petite; par conséquent, la réconciliation des zones sources peut être un défi. En outre, les mesures de la chambre, qui devraient servir de référence, sont entachées d'incertitudes en raison des fissures dans le sol, un phénomène fréquent à FR-Lam en été en raison de la forte teneur en argile. Néanmoins, d'autres études comparatives sont nécessaires pour mieux comprendre ces erreurs qui ne sont pas bien comprises.

(b) Le deuxième point est la comparaison des flux de CO_2 mesurés par une chambre de canopée et le système EC sur le blé (15 février au 19 avril 2007) et le maïs (5 juin au 26 juin 2008). Pour le blé, le coefficient de corrélation était de 0,81, 0,65 et 0,41 pour le $RECO$, le GPP et le NEE, respectivement. Cependant, une corrélation plus faible a été trouvée pour le maïs; cela pourrait être dû à la forte hétérogénéité de la parcelle pendant cette période, ainsi qu'à la non-représentativité des points d'échantillonnage sélectionnés- en d'autres termes, il y a une forte variabilité spatiale dans les caractéristiques de la végétation à chaque point d'échantillonnage, et cela a présenté un goulot d'étranglement majeur dans cette étude comparative. Pour les travaux futurs, une période de campagne plus longue est proposée, et il est conseillé de choisir des points d'échantillonnage dont la végétation correspond à celle du champ de vision du système EC.

(c) Cette étude a été conclue par une évaluation d'ISBA-MEB, afin de démontrer la capacité de ce modèle à prédire de bonnes estimations des principaux composants du carbone. Cette évaluation a été réalisée sur 7 années de maïs et 4 années de blé. Bien que les résultats présentés soient préliminaires et doivent être interprétés avec prudence, les performances du modèle sont prometteuses. Pour tenir compte des processus assimilatoires et respiratoires de la période d'interculture, des indices de végétation tirés de MODIS ont été utilisés car les repousses et les mauvaises herbes ne sont jamais suivies *in-situ*. Dans l'ensemble, la comparaison modèle-données a présenté des statistiques acceptables: Les valeurs R^2 se situent entre 0,72 et 0,96 pour le GPP, 0,53 et 0,90 pour le $RECO$, et 0,60 et 0,81 pour le NEE. De même, les RMSE se situent dans des fourchettes acceptables de 1,1 gC m^{-2} d^{-1} à 2,1 gC m^{-2} d^{-1} pour le GPP, de 0,7 gC m^{-2} d^{-1} à 2,0 gC m^{-2} d^{-1} pour le $RECO$ et de 1,1 gC m^{-2} d^{-1} à 2,0 gC m^{-2} d^{-1} pour le NEE. Sur la base du type de culture, ISBA-MEB a donné de mauvais résultats sur le blé par rapport au maïs. Cela pourrait être lié à la déficience des scènes MODIS dont la résolution spatiale est faible, et donc, les pixels contiennent souvent des signatures LAI mixtes. En plus de sa faible fréquence de visite (16 jours), ce produit n'a pas pu capturer correctement l'ampleur et la rapidité qui sont souvent associées aux mauvaises herbes et aux repousses. En effet, les valeurs de *LAI* tirées de MODIS ont tendance à être surestimées pendant les périodes d'inter-cultures, et sous-estimées pendant les saisons de grandes cultures. Un moyen potentiel d'amélioration réside dans l'utilisation de produits de télédétection ayant des résolutions décamétriques et un temps de revisite plus élevé (par exemple, Sentinel-2). Pour améliorer le modèle, il faudrait prendre en compte le carbone importé et exporté; ainsi, ISBA-MEB peut être utilisé pour identifier le statut carbone d'une terre cultivée. En outre, notre résultat a mis en évidence que les cultures de couverture (moutarde dans cette étude) améliorent la séquestration du carbone de la parcelle, et il pourrait être conseillé à l'agriculteur de les conserver plus longtemps. Cette proposition est à prendre avec précaution car elle pourrait avoir un impact important sur les prochaines saisons culturales en termes de fertilité du sol et d'état hydrique.

En outre, une attention particulière a été accordée à la sécheresse de 2019 afin d'offrir une prédiction approximative sur la réponse de la parcelle FR-Lam si elle devait subir des vagues de chaleur fréquentes et plus intenses. D'après nos résultats, l'absorption de carbone a été extrêmement améliorée en raison de l'effet direct et positif des températures élevées de l'air sur la conductance de la canopée, tandis que la quantité de carbone libérée dans l'atmosphère a augmenté dans une proportion moindre.

La première limite de cette étude est la grande période de calcul de la moyenne pour la prescription des variables biophysiques dans le modèle. Le pas de temps minimum actuellement disponible est de 10 jours, ce qui est trop important pour des cultures à croissance rapide comme le maïs et le blé. L'erreur que cela introduit ne peut être négligée, car elle se manifeste au début et à la fin de chaque saison de croissance. En outre, une contrainte majeure de cette évaluation réside dans la non-uniformité de l'acquisition de l'indice de surface foliaire. Les premières années, la méthode destructive a été utilisée; cette méthode d'échantillonnage ne considère que les feuilles, alors que l'ensemble du système végétal participe en fait à l'échange de carbone avec l'atmosphère. L'omission des autres parties de la plante pouvait conduire à une sous-estimation par le modèle. A l'inverse, les mesures du *LAI* de ces dernières années ont été réalisées avec des méthodes non-destructives. Cette dissemblance devient importante lors d'une comparaison d'une année sur l'autre et pourrait induire en erreur l'interprétation.

Une autre limitation principale est que pour un calcul complet d'un bilan carbone, l'effet du carbone d'entrée (par exemple, les amendements organiques) et de sortie (par exemple, les pailles exportées et les produits agricoles) est nécessaire. Malheureusement, ces données ne sont pas disponibles *in-situ*, et ne peuvent être récupérées par télédétection. Ces éléments omis interdisent la détermination du statut puits-source de la parcelle. De plus, en raison de l'installation instrumentale coûteuse requise pour l'estimation de l'advection horizontale de CO_2, ce terme n'a pas été mesuré à FR-Lam. Cependant, des études ont attesté de son importance, en particulier dans des conditions calmes et stables, ce qui est une situation typique de FR-Lam.

Bien que ISBA-MEB semble prometteur et pourrait être une ressource pour combler les lacunes, une amélioration du modèle serait d'avoir des jours de moyenne plus petits pour les paramètres de végétation des cultures à croissance rapide. Cela permettrait d'améliorer la synchronisation du semis, du pic et du sénescence. Une autre amélioration devrait être l'inclusion de l'effet des événements de gestion- tout en spécifiant les dates de semis et de récolte. En outre, comme cela a déjà été discuté dans de nombreuses études, le carbone organique du sol devrait être pris en compte lors du calcul des propriétés hydrauliques du sol. En conclusion, des études d'évaluation plus approfondies sont recommandées pour différentes conditions climatiques et types de cultures de géométrie différente.

References

Abdurrahman, M., Chaki, S., Saini, G., 2020. Stubble burning: Effects on health & environment, regulations, and management practices. Environmental Advances. 2. 100011. https://doi.org/10.1016/j.envadv.2020.100011.

Abu-Hamdeh, N., Reeder, R., 2000. Soil Thermal Conductivity Effects of Density, Moisture, Salt Concentra tion, and Organic Matter. Soil Science Society of America Journal 64, 1285-1290. https://doi.org/10.2136/sssaj2000.6441285x.

AIRUSE, 2016. Abatement of Emissions from Domestic and Agricultural Biomass Burning. Report 20. 12/2006.

Aouade, G., Jarlan, L., Ezzahar, J., Er-Raki, S., Napoly, A., Benkaddour, A., Khabba, S., Boulet, G., Garrigues, S., Chehbouni, A., Boone, A., 2019. Evapotranspiration partition using the multiple energy balance version of the ISBA-A-g$_s$ land surface model over two irrigated crops in a semi-arid Mediterranean region (Marrakech, Morocco). https://doi.org/10.5194/hess-24-3789-2020.

Allen, R.G., Tasumi, M., Trezza, R., 2007. Satellite-based energy balance for mapping evapotranspiration with internalized calibration (METRIC) - Model. J. Irrig. Drain. Eng., 133, 380–394.

Allen, R., 2008. Quality assessment of weather data and micro-meteorological flux—impacts on evapotranspiration calculation. J Agric. Meteorol., 64(4), 191–204.

Anyah, R. O., C.-P. Weaver, G. Miguez-Macho, Y. Fan, Robock, A., 2008. Incorporating water table dynamics in climate modeling: 3. Simulated groundwater influence on coupled land-atmosphere variability, J. Geophys. Res., 113, D07103, https://doi.org/10.1029/2007JD009087.

Arora, N., 2019. Impact of climate change on agriculture production and its sustainable solutions. Environmental Sustainability. 2. https://doi.org/10.1007/s42398-019-00078-w.

Aubinet, M., Feigenwinter, C., Heinesch, B., Laffineur, Q., Papale, D., Reichstein, M., Rinne, J., & Van Gorsel, E. (2012). Nighttime Flux Correction. In *Eddy Covariance: A Practical Guide to Measurement and Data Analysis.*133-157. Springer Atm. Sciences. https://doi.org/10.1007/978-94-007-2351-1_5.

Aubinet, M., Grelle, A., Ibrom, A., Rannik, Ü., Moncrieff, J., Foken, T., Kowalski, A.S., Martin, P., Berbigier, P., Bernhofer, C., Clement, R., Elbers, J., Granier, A., Grünwald, T., Morgenstern, K., Pilegaard, K., Rebmann, C., Snijders, W., Valentini, R., Vesala, T., 2000. Estimates of the Annual Net Carbon and Water Exchange of Forests: The EUROFLUX Methodology. https://doi.org/10.1016/S0065-2504(08)60018-5.

Aubinet, M., Chermanne, B., Vandenhaute, M., Longdoz, B., Yernaux, M., & Laitat, E., 2001. Long term car bon dioxide exchange above a mixed forest in the Belgian Ardennes. Agricultural and Forest Meteorology, 108, 293-315.

Baker, J.M., Van Bavel, C.H.M., 1987. Measurement of mass flow of water in the stems of herbaceous plants. Plant Cell Environ., 10, 777–782.

Baldocchi, D., Falge, E., Gu, L., Olson, R., Hollinger, D., Running, S., Anthoni, P., Bernhofer, Ch., Davis, K., Evans, R., Fuentes, J., Goldstein, A., Katul, G., Law, B., Lee, X., Malhi, Y., Meyers, T., Munger, W., Oechel, W., Paw U, K. T., Pilegaard, K., Schmid, H. P., Valentini, R., Verma, S., Vesala, T., Wilson, K., & Wofsy, S., 2001. FLUXNET: A New Tool to Study the Temporal and Spatial Variability of Ecosystem-Scale Carbon Dioxide, Water Vapor, and Energy Flux Densities, *Bulletin of the American Meteorological Society*, *82*(11), 2415-2434.

Baldocchi, D., Falge, E., Gu, L., Olson, R., Hollinger, D., Running, S., Wofsy, S., 2001. FLUXNET: A new tool to study the temporal and spatial variability of ecosystem-scale carbon dioxide, water vapor, and energy flux densities. Bulletin of the Amer. Meteor. Soc., 82(11), 2415-2434.

Bastiaanssen, W.G.M., Menenti, M.; Feddes, R.A., Holtslag, A.A.M., 1998. A remote sensing Surface Energy Balance algorithm for land (SEBAL): 1. Formulation. J. Hydrol., 198–213.

Bastiaanssen, W.G.M., 1995. Regionalization of surface flux densities and moisture indicators in composite terrain, Ph.D. thesis, Agricultural University, Wageningen, The Netherlands, 288.

Battude, M., Al Bitar, A., Brut, A., Tallec, T., Huc, M., Cros, J., Weber, J., Lhuissier, L., Simonneaux, V., Demarez, V., 2017. Modeling water needs and total irrigation depths of maize crop in the southwest of France using high spatial and temporal resolution satellite imagery. Agric. Water Manag., 189, 123–136. https://doi.org/10.1016/j.agwat.2017.04.018.

Berg, A., Sheffield, J., 2019. Evapotranspiration Partitioning in CMIP5 Models: Uncertainties and Future Pro jections. Journal of Climate. 32. https://doi.org/10.1175/JCLI-D-18-0583.1.

Bernhofer, C., 1992. Applying a simple three-dimensional eddy correlation system for latent and sensible heat flux to contrasting forest canopies. Theor Appl Climatol., 46:163–172. https://doi.org/10.1007/BF00866096.

Best, M.J., Pryor, M., Clark, D.B., Rooney, G. G., Essery, R.L.H., Ménard, C.B., Edwards, J. M., Hendry, M. A., Porson, 5 A., Gedney, N., Mercado, L. M., Sitch, S., Blyth, E., Boucher, O., Cox, P. M., Grimmond, C. S. B. and Harding, R. J., 2011. The Joint UK Land Environment Simulator (JULES), model description – Part 1: Energy and water fluxes, Geosci. Model Dev., 4(3), 677–699. https://doi.org/10.5194/gmd-4-677-2011.

Béziat, P., Rivalland, V., Jarosz, N., Ceschia, Eric., Boulet, G., Gentine, P., 2009. Crop evapotranspiration partitioning and comparison of different water use efficiency approaches

Bhumralkar, C.M., 1975. Numerical Experiments on the Computation of Ground Surface Temperature in an Atmospheric General Circulation Model, Journal of Applied Meteorology*, 14*, 1246-1258.

Bigeard, G., Coudert, B., Chirouze, J., Er-Raki, S., Boulet, G., Ceschia, E., and Jarlan, L., 2019. Ability of a soil–vegetation–atmosphere transfer model and a two-source energy balance model to predict evapotranspiration for several crops and climate conditions, Hydrol. Earth Syst. Sci., 23, 5033–5058. https://doi.org/10.5194/hess-23-5033-2019.

Bonan, G. B., 1996. A Land Surface Model (LSM Version 1.0) for Ecological, Hydrological, and Atmospheric Studies: Technical Description and User's Guide (No. NCAR/TN-417+STR), University Corporation for Atmospheric Research. https://doi.org/10.5065/D6DF6P5X.

Bonan, G.B., 2008. Forests and climate change: Forcings, feedbacks, and the climate benefits of forests. Science (80). 320, 1444–1449. https://doi.org/10.1126/science.1155121.

Boone, A., 2000. Modelisation des processus hydrologiques dans le schema de surface ISBA : Inclusion d'un reservoir hydrologique, du gel et modelisation de la neige, Ph.D. dissertation, University Paul Sabatier, Toulouse, France (in French).

Boone, A., Samuelsson, P., Gollvik, S., Napoly, A., Jarlan, L., Brun, E., and Decharme, B., 2017. The interact tions between soil–biosphere–atmosphere land surface model with a multi-energy balance (ISBA-MEB) option in SURFEXv8 – Part 1: Model description, Geosci. Model Dev., 10, 843–872. https://doi.org/10.5194/gmd-10-843-2017.

Boulet, G., Chehbouni, A., Braud, I., and Vauclin, M., 1999. Mosaic versus dual source approaches for mod elling the surface energy balance of a semi-arid land, Hydrol. Earth Syst. Sci., 3, 247–258, https://doi.org/10.5194/hess-3-247-1999.

Boulet, G., Mougenot, B., Lhomme, J.-P., Fanise, P., Lili-Chabaane, Z., Olioso, A., Bahir, M., Rivalland, V., Jarlan, L., Merlin, O., Coudert, B., Er-Raki, S., and Lagouarde, J.-P., 2015. The SPARSE model for the prediction of water stress and evapotranspiration components from thermal infra-red data and its evaluation over irrigated and rainfed wheat, Hydrol. Earth Syst. Sci., 19, 4653–4672. https://doi.org/10.5194/hess-19-4653-2015.

Braud, I., Varado N., and Olioso A., 2005. Comparison of root water uptake modules using either the surface energy balance or potential transpiration, J. Hydrol., 301, 267 –286. https://doi.org/10.1016/j.jhydrol.2004.06.033.

Briggs, L. J., and Shantz H. L., 1913. The water requirement of plants. II. A review of the literature. Pages 1-96 in US Dep. Agric. Bur. Plant Ind. Bull. No. 285. 1917. The water requirement of plants as influenced by environment. Pages 95- 107 in Proc. Second Pan-American Science Congress. Washington, D

Brooks, R. H. and Corey, A. T., 1966. Properties of porous media affecting fluid flow, J. Irrig. Drain. Am. Soc. Civil Eng., 17, 187–208.

Buchanan-Wollaston, V., Page, T., Harrison, E., Breeze, E., Lim, P. O., Nam, H. G., et al., 2005. Comparative transcriptome analysis reveals significant differences in gene expression and signaling pathways between developmental and dark/starvation-induced senescence in Arabidopsis. Plant J. 42, 567–585. https://doi.org/10.1111/j.1365-313X.2005.02399.x.

Burba, G., Anderson, D., 2007. Introduction to the Eddy Covariance Method: General Guidelines and Conventional Workflow. https://doi.org/10.13140/RG.2.1.3723.5683.

Burba, G., Anderson, D.J., 2010. A Brief Practical Guide to Eddy Covariance Flux Measurements: Principles and Workflow Examples for Scientific and Industrial Applications. https://doi.org/10.13140/RG.2.1.1626.4161.

Burns, S., *Metzger, S., Blanken, P.,* Burba, G., Swiatek, E., Li, J., Conrad, B., Luo, H., Taylor, J., 2014. A comparison of infrared gas analyzers above a subalpine forest in complex terrain American Meteorological Society Committee on Atmospheric Measurements. 21st Conference on Applied Climatology/17th Symposium on Meteorological Observation and Instrumentation, Westminster, Colorado, 9–13 June 2014.

Caldwell, B., O'Hara, K., 2017. Correlation of Leaf Area Index to Root Biomass in Populus tremuloides Michx supports the Pipe Model Theory, Journal of Biodiversity Management & Forestry. 06. https://doi.org/10.4172/2327-4417.1000186.

Calvet, J., 2000. Investigating soil and atmospheric plant water stress using physiological and micrometeorological data. Agricultural and Forest Meteorology. 103. 229-247. https://doi.org/10.1016/S0168-1923(00)00130-1.

Calvet, J.C., Noilhan, J., Roujean, J.L., Bessemoulin, P., Cabelguenne, M., Olioso, A., Wigneron, J.P., 1998. An interactive vegetation SVAT model tested against data from six contrasting sites. Agric. For. Meteorol., 92, 73-95.

Campbell, G.S., Norman, J.M., 1998. An Introduction to Environmental Biophysics, 2nd ed. Springer-Verlag, New York, 286.

Carlson, T., Wooster, M., Islam, S., 2009. A review of Ts/VI remote sensing based methods for the retrieval of land surface energy fluxes and soil surface moisture. Progress in Physical Geography. 33. 224-250. https://doi.org/10.1177/0309133309338997.

Casa, R., Upreti, D., Pelosi, F., 2019. Measurement and estimation of leaf area index (*LAI*) using commercial instruments and smartphone-based systems. IOP Conference Series: Earth and Environmental Science. 275. 012006. https://doi.org/10.1088/1755-1315/275/1/012006.

Cavanaugh, M., Papuga, S., Scott, R., 2011. Evapotranspiration partitioning in semiarid shrubland ecosystems: A two-site evaluation of soil moisture control on transpiration. Ecohydrology. 4. 671 - 681. https://doi.org/10.1002/eco.157.

Ceschia, E., Béziat, P., Dejoux, J.F., Aubinet, M., Bernhofer, Ch., Bodson, B., Buchmann, N., Carrara, A., Cellier, P., Di Tommasi, P., Elbers, J.A., Eugster, W., Grünwald, T., Jacobs, C.M.J., Jans, W.W.P., Jones, M., Kutsch, W., Lanigan, G., Magliulo, E., Marloie, O., Moors, E.J., Moureaux, C., Olioso, A., Osborne, B., Sanz, M.J., Saunders, M., Smith, P., Soegaard, H., Wattenbach, M., 2010a. Management effects on net ecosystem carbon and GHG budgets at European crop sites. Agriculture, Ecosystems & Environment 139, 363–383.

Charuchittipan, D., Babel, W., Mauder, M. et al., 2014. Extension of the Averaging Time in Eddy-Covariance Measurements and Its Effect on the Energy Balance Closure. Boundary-Layer Meteorol 152, 303–327. https://doi.org/10.1007/s10546-014-9922-6.

Chebbi, W., Boulet, G., Le Dantec, V., Chabaane, Z., Fanise, P., Mougenot, B., Ayari, H., 2018. Analysis of evapotranspiration components of a rainfed olive orchard during three contrasting years in a semi-arid climate. Agricultural and Forest Meteorology. 256. 159-178. https://doi.org/10.1016/j.agrformet.2018.02.020.

Choudhury, B.J. and Monteith, J.L. (1988), A four-layer model for the heat budget of homogeneous land sur faces. Q.J.R. Meteorol. Soc., 114: 373-398. https://doi.org/10.1002/qj.49711448006.

Choudhury, B.J., Idso, S.B., Reginato, R.J., 1987. Analysis of an empirical model for soil heat flux under a growing wheat crop for estimating evaporation by an infrared-temperature based energy balance equation. Agric. For. Meteorol., 39, 283–297

Clement, R., 1999. EdiRe Data Software, University of Edinburgh: Edinburgh, UK.

Chung, S.O., Horton, R., 1987. Soil heat and water flow with a partial surface mulch. Water Resour. 23 (12), 2175–2186. https://doi.org/10.1029/WR023i012p02175.

Clapp, R. B. and Hornberger, G. M., 1978 Empirical equations for some soil hydraulic properties, Water Re sour. Res., 14, 601–604.

Collatz, G.J., Ball, J.T., Grivet, C., Berry, A.J., 1991. Physiological and environmental regulation of stomatal conductance, photosynthesis, and transpiration: A model that includes a laminar boundary layer. Agricultural and Forest Meteorology. 54. 107-136. https://doi.org/10.1016/0168-1923(91)90002-8.

Cronin, J., Anandarajah, G. and Dessens, O., 2018. Climate change impacts on the energy system: a review of trends and gaps, Climatic Change 151, 79–93. https://doi.org/10.1007/s10584-018-2265-4.

Culf, A., Foken, T., Gash, J. 2004. The Energy Balance Closure Problem. https://doi.org/10.1007/978-3-642-18948-7_13.

Culf, A.D., Foken, T., Gash, J.H.C., 2002. The energy balance closure problem. In: Vegetation, Water, Hu mans and the Climate., (in press).

Cuxart, J., Wrenger, B., Martínez-Villagrasa, D., Reuder, J., Jonassen, M., Jiménez, M., Lothon, M., Lohou, F., Hartogensis, O.K., Dünnermann, J., Conangla, L., Garai, A., 2016. Estimation of the advection effects induced by surface heterogeneities in the surface energy budget. Atmospheric Chemistry and Physics Discussions. 2016. 1-16. https://doi.org/10.5194/acp-2015-1051.

Cuxart J., Conangla L., Jiménez M.A., 2015. Evaluation of the surface energy budget equation with experi mental data and the ECMWF model in the Ebro Valley. J. Geophys. Res. 120, 1008–1022. https://doi.org/10.1002/2014JD022296.

Dafermos, Y., Nikolaidi, M., Galanis, G., 2018. Climate Change, Financial Stability and Monetary Policy. Ecological Economics. 152. https://doi.org/10.1016/j.ecolecon.2018.05.011.

Dai, Y., Zeng, X., Dickinson, R. E., Baker, I., Bonan, G. B., Bosilovich, M. G., Denning, A. S., Dirmeyer, P. A., Houser, P. R., Niu, G., Oleson, K. W., Schlosser, C. A., & Yang, Z., 2003. The Common Land Model, *Bulletin of the American Meteorological Society*, *84*(8), 1013-1024.

Deardorff, J. W., 1978. Efficient prediction of ground surface temperature and moisture, with inclusion of a layer of vegetation, J. Geophys. Res., 83(C4), 1889–1903, https://doi.org/10.1029/JC083iC04p01889.

Deardorff, J. W., 1977. A Parameterization of Ground-Surface Moisture Content for Use in Atmospheric Pre diction Models, J. Appl. Meteor., 16, 1182–1185.

Decharme, B., Delire, C., Minvielle, M., Colin, J., Vergnes, J.P., Alias, A., Saint-Martin, D., Séférian, R., Sé nési, S., Voldoire, A., 2019. Recent changes in the ISBA-CTRIP land surface system for use in the CNRM CM6 climate model and in global offline hydrological applications. J. Adv. Model Earth Syst., 11, 1207–1252

Decharme, B., Boone, A., Delire, C., and Noilhan, J., 2011. Local evaluation of the Interaction between Soil Biosphere Atmosphere soil multilayer diffusion scheme using four pedotransfer functions, J. Geophys. Res., 116, D20126, https://doi.org/10.1029/2011JD016002.

Desjardins RL, MacPherson JI, Schuepp PH, Karanja F., 1989. An evaluation of aircraft flux measurements of CO2, water vapor and sensible heat. Boundary-Layer Meteorol. 47, 55–69. https://doi.org/10.1007/BF00122322.

Dickinson, J. W., 1977. A parameterization of ground surface moisture content for use in atmospheric predict tion models. J. Appl. Meteor., 16, 1182-1185.

Delogu, E., Boulet, G., Olioso, A., Garrigues, S., Brut, A., Tallec, T., Demarty, J., Soudani, K., Lagouarde, J., 2018. Evaluation of the SPARSE Dual-Source Model for Predicting Water Stress and Evapotranspiration from Thermal Infrared Data over Multiple Crops and Climates. Remote Sensing. 10. 1806. https://doi.org/10.3390/rs10111806.

De Roo, F., Zhang, S., Huq, S., Mauder, M., 2018. A semi-empirical model of the energy balance closure in the surface layer. PLOS ONE 13(12): e0209022. https://doi.org/10.1371/journal.pone.0209022.

Desjardins, T., Barros, E., Sarrazin, M., Cyril, Girardin, M.A., 2004. Effects of forest conversion to pasture on soil carbon content and dynamics in Brazilian Amazonia. Agriculture, Ecosystems & Environment. 103, 365-373. https://doi.org/10.1016/j.agee.2003.12.008.

Dickinson, R. E., Shaikh, M., Bryant, R., Graumlich, L., 1998. Interactive Canopies for a Climate Model, Jour nal of Climate, 11(11), 2823-2836. Retrieved Sep 29, 2021, from https://journals.ametsoc.org/view/journals/clim/11/11/15200442_1998_011_2823_icfacm_2.0.co_2.xml

Ding, R.S., Kang, S.Z., Zhang, Y.Q., Hao, X.M., Tong, L., Du, T.S., 2013. Partitioning evapotranspiration into soil evaporation and transpiration using a modified dual crop coefficient model in irrigated maize field with ground-mulching, Agric. Water Manag., 127, 85–96. https://doi.org/10.1016/j.agwat.2013.05.018.

Elagina, L. G., Zubkovskii, S. L., Kaprov, B. M., and Sokolov, D. Y., 1973. Experimental investigations of the energy balance near the surface, Trudy Glavny Geofiziceskij Observatorii, 296, 38–45, (in Russian).

Elagina, L. G., Kaprov, B. M., and Timanovskii, D. F., 1978. A characteristic of the surface air layer above snow, Izvestia AN SSSR Fizika Atmosfery I Oceana, 14, 926–931 (in Russian).

Eshonkulov, R., Poyda, A., Ingwersen, J., Pulatov, A., Streck, T., 2018. Improving the energy balance closure over a winter wheat field by accounting for minor storage terms, Agricultural and Forest Meteorology. 264, 283-296. https://doi.org/10.1016/j.agrformet.2018.10.012.

Etchanchu, J., Rivalland, V., Gascoin, S., Cros, J., Tallec, T., Brut, A., Boulet, G., 2017. Effects of high spatial and temporal resolution Earth observations on simulated hydrometeorological variables in a cropland (southwestern France), Hydrology and Earth System Sciences. 21. https://doi.org/10.5194/hess-21-5693-2017.

Falge, E., Baldocchi, D., Olson, R.J., Anthoni, P., Aubinet, M., Bernhofer, C., Burba, G., Ceulemans, R., Clem ent, R., Dolman, H., Granier, A., Gross, P., Gru¨nwald, T., Hollinger, D., Jensen, N.O., Katul, G., Keronen, P., Kowalski, A., Ta Lai, C., Law, B.E., Meyers, T., Moncrieff, J., Moors, E., Munger, J.W., Pilegaard, K., Rannik, U., Rebmann, C., Suyker, A., Tenhunen, J., Tu, K., Verma, S., Vesala, T., Wilson, K., Wofsy, S., 2001. Gap filling strategies for defensible annual sums of net ecosystem exchange, J. Agric. For. Meteorol. 107, 43–69.

Foken, T., Gerstmann, W., Richter, S.H. et al., 1993. Study of the energy exchange processes over different types of surfaces during TARTEX-90, Dt Wetterd Forsch Entwicklung Arbeitsergebnisse 4, 34.

Foken, T., Göckede, M., Mauder, M., Mahrt, L., Amiro, B.D., & Munger, J.W., 2004. Post-field data quality control, In Handbook of Micrometeorology (eds X. Lee, W. Massman & B.E. Law), 181-203. Kluwer Academic Publishers

Foken, T., Wichura, B., 1996. Tools for quality assessment of surface-based flux measurements. Agricultural and Forest Meteorology, 78, 83-105.

Fratini, G., Mauder, M., 2014. Towards a consistent eddy-covariance processing: an intercomparison of Eddy Pro and TK3, Atmospheric Measurement Techniques Discussions. 7, 2107–2126. https://doi.org/10.5194/amt-7-2273-2014.

Farré, I., Faci, J.M., 2006. Comparative response of maize (Zea mays L.) and sorghum (Sorghum bicolor L. Moench) to deficit irrigation in a Mediterranean environment, Agric. Water Mgmt., 83, 135–143.

Ferrara, G., Flore, J., 2003. Comparison Between Different Methods for Measuring Transpiration in Potted Apple Trees. Biologia Plantarum 46, 41–47. https://doi.org/10.1023/A:1022301931508.

Finnigan, J.-J., Clement, R., Malhi, Y., 2003. A re-evaluation of long-term flux measurement techniques, part I: averaging and coordinate rotation, Boundary-Layer Meteorol 107, 1–48.

Fisher, J.B., Tu, K.P., Baldocchi, D.D., 2008. Global estimates of the land–atmosphere water flux based on monthly AVHRR and ISLSCP-II data, validated at 16 FLUXNET sites. Remote Sens. Environ., 112, 901–919.

Fisher, R. A., Koven, C. D., 2020. Perspectives on the future of land surface models and the challenges of representing complex terrestrial systems. Journal of Advances in Modeling Earth Systems, 12, e2018MS001453. https://doi.org/10.1029/2018MS001453.

Fleming, J.R., 1998. Historical Perspectives on Climate Change. Oxford: Oxford University Press. ISBN 978-0195078701

Foken, T., Leuning, R., Oncley, S., Mauder, M., Aubinet, M., 2012. Corrections and Data Quality Control. https://doi.org/10.1007/978-94-007-2351-1_4.

Foken, T., 2008. The Energy Balance Closure Problem: An Overview. Ecological applications, a publica tion of the Ecological Society of America, 18, 1351-67. https://doi.org/10.1890/06-0922.1.

Foken, T., Mauder, M., Liebethal, C., Wimmer, F., Beyrich, F., Leps, J.P., Raasch, S., DeBruin, H., Meijninger, W., Bange, J., 2010. Energy balance closure for the LITFASS-2003 experiment, Theor. Appl. Climatol., 101, 149–160. https://doi.org/10.1007/s00704-009-0216-8.

Franssen, H., Stockli, ¨ R., Lehner, I., Rotenberg, E., Seneviratne, S., 2010. Energy balance closure of eddy-covariance data: a multi-site analysis for European FLUXNET stations, Agric. For. Meteorol. 150, 1553–1567. https://doi.org/10.1016/j.Agrformet.2010.08.005.

Gaillardet, J.I., Braud, F., Hankard, S., Anquetin, Olivier B., et al., 2018. OZCAR: The French Network of Critical Zone Observatories, Vadose Zone Journal, Soil science society of America - Geological society of America 17 (1), 1–24. https://doi.org/10.2136/vzj2018.04.0067.

Gao, X., Mei, X., Gu, F. et al. Ecosystem respiration and its components in a rainfed spring maize cropland in the Loess Plateau, China. Sci Rep 7, 17614 (2017). https://doi.org/10.1038/s41598-017-17866-1.

Gao, Z., Liu, H., Katul, G., Foken, T., 2017. Non-closure of the surface energy balance explained by phase difference between vertical velocity and scalars of large atmospheric eddies. Environmental Research Letters. 12. https://doi.org/10.1088/1748-9326/aa625b.

García-Santos, V., Cuxart, J., Jim´enez, M., Villagrasa, D., Jim´enez, M., Simo, G., Picos, R., Caselles, V., 2018. Study of Temperature Heterogeneities at Sub-Kilometric Scales and Influence on Surface–Atmosphere Energy Interactions. IEEE T. Geosci. Remote. 57, 640–654. https://doi.org/10.1109/TGRS.2018.2859182.

Garrigues, S., Boone, A., Decharme, B., Olioso, A., Albergel, C., Calvet, J. -C., Moulin, S., Buis, S., Martin, E., 2017. Impacts of the Soil Water Transfer Parametrization on the Simulation of Evapotranspiration over a 14-Year Mediterranean Crop Succession. Journal of Hydrometeorology, 19, https://doi.org/10.1175/JHM-D-17-0058.1.

Garrigues, S., Olioso, A., Calvet, J. C., Martin, E., Lafont, S., Moulin, S., Chanzy, A., Marloie, O., Buis, S., Desfonds, V., Bertrand, N., and Renard, D., 2015. Evaluation of land surface model simulations of evapotranspiration over a 12-year crop succession: impact of soil hydraulic and vegetation properties, Hydrol. Earth Syst. Sci., 19, 3109–3131. https://doi.org/10.5194/hess-19-3109-2015.

Gerken, T., Ruddell B.L., Fuentes, J.D., Araujo, A., Brunsell, N.A., Maia, J., Manzi, A., Mercer, J., dos Santos, R.N., Von Randow, C., Stoy, P., 2017. Investigating the mechanisms responsible for the lack of surface energy balance closure in a central Amazonian tropical rainforest, Agricultural & Forest Meteorology. https://doi.org/10.1016/j.agrformet.2017.03.023.

Gibelin, A. L., Calvet, J. C., Roujean, J. L., Jarlan, L., and Los, S. O., 2006. Ability of the land surface model ISBA-A-gs to simulate leaf area index at the global scale: Comparison with satellites products, J. Geophys. Res., 111, D18102. https://doi.org/10.1029/2005JD006691.

Gibelin, A.-L., Calvet, J.-C., and Viovy, N., 2008. Modelling energy and CO2 fluxes with an interactive vege tation land surface model- Evaluation at high and middle latitudes, Agr. Forest Meteorol., 148, 1611–1628.

Giometto, M., Christen, A., Egli, P., Schmid, M.F., Tooke, R.T., Coops, N.C., Parlange, M., 2017. Effects of trees on mean wind, turbulence, and momentum exchange within and above a real urban environment, Adv. Water Res. https://doi.org/10.1016/j. Advwatres.2017.06.018.

Göckede, M., Rebmann, C., Foken, T., 2004. A combination of quality assessment tools for eddy covariance measurements with footprint modelling for the characterisation of complex sites, Agricultural and Forest Meteorology, 127, 175-188.

Goeckede, M., 2005. Adoption of footprint methods for the quality control of eddy-covariance measurements.

Goudriaan, J., van Laar, H. H., van Keulen, H., and Louwerse, W., 1985. Photosynthesis, CO2 and plant pro duction, in: Wheat growth and modelling, edited by: Day, W. and Atkin, R. K., Plenum Press, New York, Series A, 86, 107–122.

Grossiord, C., Buckley, T.N., Cernusak, L.A., Novick, K.A., Poulter, B., Siegwolf, R.T.W., Sperry, J.S. and McDowell, N.G., 2020. Plant responses to rising vapor pressure deficit, New Phytol. 226, 1550-1566. https://doi.org/10.1111/nph.16485

Gu, L., et al., 2007, Influences of biomass heat and biochemical energy storages on the land surface fluxes and radiative temperature, J. Geophys. Res., 112, D02107, https://doi.org/10.1029/2006JD007425.

Guerrieri, R., Belmecheri, S., Ollinger, S., Asbjornsen, H., Jennings, K., Xiao, J., Stocker, B., Martin, M., Hollinger, D., Bracho, Rosvel, Clark, Kenneth & Dore, Sabina & Kolb, Thomas & Munger, J., Novick, K., Richardson, A., 2019. Disentangling the role of photosynthesis and stomatal conductance on rising forest water-use efficiency, Proceedings of the National Academy of Sciences. 116. https://doi.org/10.1073/pnas.1905912116.

Hadria, R., Duchemin, B., Lahrouni, A., Khabba, S., Er-raki, S., Dedieu, G., Chehbouni, A.G., Olioso, A., 2006. Monitoring of irrigated wheat in a semi-arid climate using crop modelling and remote sensing data: Impact of satellite revisit time frequency, International Journal of Remote Sensing 27, 1093–1117. https://doi.org/10.1080/01431160500382980.

Hammerle, A., Haslwanter, A., Tappeiner, U., Cernusca, A., Wohlfahrt, G., 2008. Leaf area controls on energy partitioning of a temperate mountain grassland, Biogeosciences 5, 421–431. https://doi.org/10.5194/bg-5-421-2008.

Haslwanter A, Hammerle A, Wohlfahrt G., 2009. Open- vs. closed-path eddy covariance measurements of the net ecosystem carbon dioxide and water vapour exchange: a long-term perspective, Agric. For Meteorol., 149(2), 291-302. https://doi.org/10.1016/j.agrformet.2008.08.011.

Heilman, J.L., McInnes, K.J., Savage, M.J., Gesch, R.W., Lascano, R.J., 1994. Soil and canopy balances in a west Texas vineyard. Agric. For. Meteorol. 71, 99–114. https://doi.org/10.1016/0168-1923(94)90102-3.

Hollinger, D, Kelliher F, Byers J et al., 1994. Carbon dioxide exchange between an undisturbed old-growth temperate forest and the atmosphere, Ecology, 75, 134–150.

Horton, R., Bristow, K.L., Kluitenberg, G.J., et al., 1996. Crop residue effects on surface radiation and energy balance - review. Theor. Appl. Climatol. 54, 27–37. https://doi.org/10.1007/BF00863556.

Imukova, K., Ingwersen, J., Hevart, M., and Streck, T. Energy balance closure on a winter wheat stand: com paring the eddy covariance technique with the soil water balance method, Biogeosciences, 13, 63–75, https://doi.org/10.5194/bg-13-63-2016, 2016.

Jackson, R.B., Canadell, J., Ehleringer, J.R., Mooney, H.S.O., Schulze, E.A., 1996. Global Analysis of Root Distributions for Terrestrial Biome. Oecologia 1996, 108, 389–411.

Jacobs, C.M.J., van den Hurk, B.J.J.M., de Bruin, H.A.R., 1996. Stomatal behaviour and photosynthetic rate of unstressed grapevines in semi-arid conditions, Agric. For. Meteorol. 80, 111–134

Jacobs, C., 1994. Direct impact of CO2 enrichment on regional transpiration, Ph.D. thesis, Agricultural University, Wageningen, The Netherlands.

Jacquemin, B., Noilhan, J., 1990. Sensitivity study and validation of a land surface parameterization using the

HAPEX-MOBILHY data set, Boundary Layer Meteorol. 52, 93–134. https://doi.org/10.1007/BF00123180.

Jarvis, P. G., 1976. The interpretation in the variations of leaf water potential and stomatal conductance found in canopies in the field, Philos. T. R. Soc. Lon. B., 273, 593–610.

Jin, M., Liang, S., 2006. An Improved Land Surface Emissivity Parameter for Land Surface Models Using Global Remote Sensing Observations. Journal of Climate. 19. https://doi.org/10.1175/JCLI3720.1.

Kalma, J.D., McVicar, T.R. & McCabe, M.F., 2008. Estimating Land Surface Evaporation: A Review of Meth ods Using Remotely Sensed Surface Temperature Data, Surv. Geophys. 29, 421–469. https://doi.org/10.1007/s10712-008-9037-z.

Kanemasu, E.T., Verma, S.B., Smith E.A., 1992. Surface flux measurements in FIFE: an overview. J Geophys Res 97:18547–18555

Keenan, T., Hollinger, D., Bohrer, G. et al., 2013. Increase in forest water-use efficiency as atmospheric carbon dioxide concentrations rise. Nature 499, 324–327. https://doi.org/10.1038/nature12291.

Kljun, N., Calanca, P., Rotach, M.P., & Schmid, H.P., 2004. A simple parameterisation for flux footprint predictions. Boundary-Layer Meteorology, 112, 503-523.

Koitzsch, R, Dzingel, M, Foken, T, Mücket, G., 1988. Probleme der experimentellen Erfassung des Energieaustausches über Winterweizen, Z Meteorol 38, 120–155.

Kong, L., Chu, L.M., 2015. Carbon Dioxide Fluxes of Turfgrass Species in Urban Turfs in Hong Kong.

Kowalczyk, E.A., Wang, Y.P., Law, R.M., Davies, H.L., McGregor, J.L., Abramowitz, G.S., 2006. The CSIRO Atmosphere Biosphere Land Exchange (CABLE) model for use in climate models and as an offline model, Aspendale, Vic., CSIRO Marine and Atmospheric Research. https://doi.org/10.4225/08/58615c6a9a51d.

Kustas, W. P., Norman, J. M., 1996. Use of remote sensing for evapotranspiration monitoring over land sur faces. Hydrological sciences journal, 41, 495-516. https://doi.org/10.1080/02626669609491522.

Kustas, W.P., Norman, J.M., 1999. Evaluation of soil and vegetation heat flux predictions using a simple two-source model with radiometric temperatures for partial canopy cover, Agric. For. Meteorol., 94, 13–29.

Lafont, S., Zhao, Y., Calvet, J.-C., Peylin, P., Ciais, P., Maignan, F., Weiss, M., 2011. Modelling *LAI*, surface water and carbon fluxes at high-resolution over France: comparison of ISBA-A-gs and ORCHIDEE, Biogeosciences. 9. 439-456, https://doi.org/10.5194/bg-9-439-2012.

Lasslop, G., Reichstein, M., Papale, D., Richardson, A., Arneth, A., Barr, A., Stoy, P., Wohlfahrt, Georg., 2010. Separation of net ecosystem exchange into assimilation and respiration using a light response curve approach: critical issues and global evaluation: Separation of NEE into GPP and RECO. Global change biology - glob change biol. 16, 187-208. https://doi.org/10.1111/j.1365-2486.2009.02041.x.

Laubach, J., Teichmann, U., 1999. Surface Energy Budget Variability: a Case Study over Grass with Special Regard to Minor Inhomogeneities in the Source Area. Theor. Appl. Climatol. 62, 9–24. https://doi.org/10.1007/s007040050070.

Lee X., Massman W., Law B., 2005. Handbook of Micrometeorology - A Guide for Surface Flux Measurement and Analysis. Kluwer Academic Publishers

Le Moigne, P., 2012. SURFEX Scientific Documentation. Note de Centre (CNRM/GMME), Météo-France, Toulouse, France, Volume 87, 211p

Lee, X., Massman, W., Law, B., 2004. Handbook of Micrometeorology: A Guide for Surface Flux Measure ment and Analysis. Springer: Dordrecht, The Netherlands, Volume 29, ISBN 978-1-4020-2264-7.

Leuning, R., Van Gorsela, E., Massman, W.J., Isaac, P.R., 2012. Reflections on the surface energy imbalance problem, Agric. For. Meteorol. 156, 65–74. https://doi.org/10.1016/j.agrformet.2011.12.002.

Leuning, R., Denmead, O.T., Lang, A.R.G., Ohtaki, E., 1982. Effects of heat and water vapor transport on eddy covariance measurement of CO2 fluxes, Boundary-Layer Meteorol. 23, 209–222. https://doi.org/10.1007/BF00123298

Lhomme, J. P., Chehbouni, A., 1999. Comments on dual-source vegetation–atmosphere transfer models, Agric. Meteorol. (in press). https://doi.org/10.1016/S0168-1923(98)00109-9.

Lhomme, J.P., Montes, C., Jacob, F., Prévot, L., 2012. Evaporation from Heterogeneous and Sparse Canopies: On the Formulations Related to Multi-Source Representations. Boundary-Layer Meteorology 144, 243-262. https://doi.org/10.1007/s10546-012-9713-x.

Li, L., Vuichard, N., Viovy, N., Ciais, P., Wang, T., Ceschia, E., Jans, W., Wattenbach, M., Beziat, P., Grünwald, T., Lehuger, S., Bernhofer, C., 2011. Importance of crop varieties and management practices: Evaluation of a process-based model for simulating CO2 and H2O fluxes at five European maize (Zea mays L.) sites, Biogeosciences 8, 1721-1736. https://doi.org/10.5194/bg-8-1721-2011.

Li, Z., Yu, G.-R., Wen, X., Zhang, L.M., Ren, C.Y. Fu, Y.L., 2005. Energy balance closure ChinaFLUX sites. Science in China series D-Earth Sciences. 48, 51-62. https://doi.org/10.1360/05zd0005.

Liang, S., 2003. Estimation of Land Surface Biophysical Variables, pp. 246-309.

Liu, Y., Weaver, C. P., and Avissar, R., 1999. Toward a parameterization of mesoscale fluxes and moist convection induced by landscape heterogeneity, J. Geophys. Res., 104(D16), 19515–19533, https://doi.org/10.1029/1999JD900361.

Lloyd, J., Taylor, J.A., 1994. On the temperature dependence of soil respiration, Functional Ecology, 8, 315-323

Long, Di., Singh, V., 2012. A Two-source Trapezoid Model for Evapotranspiration (TTME) from satellite imagery, Remote Sensing of Environment 121, 370–388. https://doi.org/10.1016/j.rse.2012.02.015.

Lu, N., Chen, S., Wilske, B., Sun, G., Chen, J., 2011. Evapotranspiration and soil water relationships in a range of disturbed and undisturbed ecosystems in the semi-arid Inner Mongolia, China, J. Plant Ecol. 4, 49–60. https://doi.org/10.1093/jpe/rtq035.

Maes, W., Steppe, K., 2012. Estimating evapotranspiration and drought stress with ground-based thermal remote sensing in agriculture: A review, Journal of experimental botany 63, 4671-712. https://doi.org/10.1093/jxb/ers165.

Mahfouf, J.-F., Noilhan, J., 1996. Inclusion of gravitational drainage in a land surface scheme based on the force-975restore method, J. Appl. Meteor. 35, 987–992.

Mahrt, L., 2010. Computing turbulent fluxes near the surface: Needed improvements. Agricultural and Forest Meteorology. 150. 501-509. https://doi.org/10.1016/j.agrformet.2010.01.015.

Majozi, N. P., Mannaerts, C. M., Ramoelo, A., Mathieu, R., Nickless, A., and Verhoef, W., 2017. Analysing surface energy balance closure and partitioning over a semi-arid savanna FLUXNET site in Skukuza, Kruger National Park, South Africa, Hydrol. Earth Syst. Sci. 21, 3401–3415, https://doi.org/10.5194/hess-21-3401-2017.

Manabe, S., 1969. Climate and the ocean circulation, *Monthly Weather Review*, *97*(11), 739-774. https://journals.ametsoc.org/view/journals/mwre/97/11/1520-0493_1969_097_0739_catoc_2_3_co_2.xml.

Mangalassery, S., Sjögersten, S., Sparkes, D., Sturrock, C., Craigon, J., Mooney, S., 2014. To what extent can zero tillage lead to a reduction in greenhouse gas emissions from temperate soils, Scientific reports 4, 4586. https://doi.org/10.1038/srep04586.

Masseroni, D., Ravazzani, D., Corbari, C., Mancini, M., 2012. Turbulence integral length and footprint dimension with reference to experimental data measured over maize cultivation in Po Valley, Italy, Atmosfera. 25.

Masseroni, D., Corbari, C., Mancini, M., 2014. Limitations and improvements of the energy balance closure with reference to experimental data measured over a maize field, Atmósfera. 141. https://doi.org/10.1016/S0187-6236(14)70033-5.

Masson, V., Le Moigne, P., Martin, E., Faroux, S., Alias, A., Alkama, R., Belamari, S., Barbu, A., Boone, A., Bouyssel, F., Brousseau, P., Brun, E., Calvet, J.-C., Carrer, D., Decharme, B., Delire, C., Donier, S., Essaouini, K., Gibelin, A.-L., Giordani, H., Habets, F., Jidane, M., Kerdraon, G., Kourzeneva, E., Lafaysse, M., Lafont, S., Lebeaupin Brossier, C., Lemonsu, A., Mahfouf, J.-F., Marguinaud, P., Mokhtari, M., Morin, S., Pigeon, G., Salgado, R., Seity, Y., Taillefer, F., Tanguy, G., Tulet, P., Vincendon, B., Vionnet, V., and Voldoire, A., 2013. The SURFEXv7.2 land and ocean surface platform for coupled or offline simulation of earth surface variables and fluxes, Geosci. Model Dev. 6, 929–960. https://doi.org/10.5194/gmd-6-929-2013.

Mauder, M., Desjardins, R., and MacPherson, I., 2007. Scale analysis of airborne flux measurements over heterogeneous terrain in a boreal ecosystem, J. Geophys. Res. 112, D13, 112.

Mauder, M., Foken, T. & Cuxart, J., 2020. Surface-Energy-Balance Closure over Land: A Review, Boundary-Layer Meteorol. 177, 395–426. https://doi.org/10.1007/s10546-020-00529-6.

Menenti, M., Choudhury, B., 1993. Parameterization of Land Surface Evapotranspiration Using a Location Dependent Potential Evapotranspiration and Surface Temperature Range. Exchange Processes at the Land Surface for a Range of Space and Time Scales, IAHS Publication 212, 561-568.

Meng, C., 2020. Surface Albedo Assimilation and Its Impact on Surface Radiation Budget in Beijing. Advances in Meteorology, 1-14. https://doi.org/10.1155/2020/8312451.

Meroni, M., Fasbender, D., Lopez-Lozano, R., Migliavacca, M., 2019. Assimilation of Earth Observation Data Over Cropland and Grassland Sites into a Simple GPP Model, Remote Sensing 11. https://doi.org/10.3390/rs11070749.

Meyers, T., Hollinger, S., 2004. An assessment of storage terms in the surface energy balance of maize and Soybean, Agricultural and Forest Meteorology 125, 105-115. https://doi.org/10.1016/j.agrformet.2004.03.001.

Miyajima, S., Uoi, N., Murata, T., Takeda, M., Morishima, W., Watanabe, M., 2015. Effect of structural mod ification on heat transfer through man-made soils in urban green areas, Soil Science and Plant Nutrition 61, 70-87. https://doi.org/10.1080/00380768.2015.1051929.

Miralles, D. G., Holmes, T. R. H., De Jeu, R. A. M., Gash, J. H., Meesters, A. G. C. A., and Dolman, A. J., 2011. Global land-surface evaporation estimated from satellite-based observations, Hydrol. Earth Syst. Sci., 15, 453–469. https://doi.org/10.5194/hess-15-453-2011.

Moderow, U., Aubinet, M., Feigenwinter, C. et al., 2009. Available energy and energy balance closure at four coniferous forest sites across Europe, Theor. Appl. Climatol. 98, 397–412. https://doi.org/10.1007/s00704-009-0175-0

Molle, B., Tomas, S., Hendawi, M. and Granier, J., 2012. Evaporation and wind drift losses during sprinkler irrigation influenced by droplet size distribution, Irrig. and Drain. 61, 240-250. https://doi.org/10.1002/ird.648.

Montagnani, L., Grünwald, T., Kowalski, A., Mammarella, I., Merbold, L., Metzger, S., Sedlak, P., Siebicke, L., 2018. Estimating the storage term in eddy covariance measurements: The ICOS methodology, International Agrophysics 32, 32. https://doi.org/10.1515/intag-2017-0037.

Montgomery, R.B., 1948. Vertical eddy flux of heat in the atmosphere, J. Meteorol. 5, 265–274.

Monteith, J. L., Szeicz, G. and Yabuki, K., 1964. Crop photosynthesis and the flux of carbon dioxide below the canopy, J. Appl. Ecol. 1, 32r-337.

Moore, C.J., 1986. Frequency response corrections for eddy correlation systems, Boundary-Layer Meteorology. 37, 17–35. https://doi.org/10.1007/BF00122754.

Morales, M., Ortiz, M., Sellés, G., 2015. Effects of transient soil waterlogging and its importance for rootstock Selection, Chilean Journal of Agricultural Research 75, 1. https://doi.org/10.4067/S0718-58392015000300006.

Morison, J.I.L., 1987. Intercellular CO2 concentration and stomatal response to CO2. In: E Zeiger, IR Cowan, GD Farquhar, eds. Stomatal Function, Stanford, CA, USA, Stanford University Press, 229– 251.

Moureaux, C., Debacq, A., Hoyaux, J., Suleau, M., Tourneur, D., Vancutsem, F., Bodson, B. and Aubinet, M., 2008. Carbon balance assessment of a Belgian winter wheat crop (Triticum aestivum L.), Global Change Biology 14, 1353-1366. https://doi.org/10.1111/j.1365-2486.2008.01560.x

Mu, Q., Zhao, M., Running, S.W. Improvements to a modis global terrestrial evapotranspiration algorithm. Remote Sens. Environ. 2011, 115, 1781–1800.

Napoly, A., Boone, A., Samuelsson, P., Gollvik, S., Martin, E., Seferian, R., Carrer, D., Decharme, B., and Jarlan, L., 2016. The Interactions between Soil-Biosphere-Atmosphere (ISBA) land surface model Multi-Energy Balance (MEB) option in SURFEX – Part 2: Model evaluation for local scale forest sites, Geosci. Model Dev. Discuss., https://doi.org/10.5194/gmd-2016-270, in review.

Napoly, A., Boone, A., Samuelsson, P., Gollvik, S., Martin, E., Séférian, R., Carrer, D., Decharme, B., Jarlan, L., 2017. The interactions between soil–biosphere–atmosphere (ISBA) land surface model multi-energy balance (MEB) option in SURFEXv8 – Part 2: Introduction of a litter formulation and model evaluation for local-scale forest sites, Geoscientific Model Development 10, 1621-1644. https://doi.org/10.5194/gmd-10-1621-2017.

Navarro, E., Lam, S., and Trębicki, P., 2020. Elevated Carbon Dioxide and Nitrogen Impact Wheat and Its Aphid Pest, Frontiers in Plant Science 11. https://doi.org/10.3389/fpls.2020.605337.

Nielsen, D.C., Vigil, M.F., 2018. Soil Water Extraction for Several Dryland Crops, Agronomy Journal 110, 2447-2455. https://doi.org/10.2134/agronj2018.05.0335.

Noilhan, J., Planton, S., 1989. A Simple Parameterization of Land Surface Processes for Meteorological Mod els, Mon. Weather Rev. 117, 536–549.

Noilhan, J., Donier, S., Lacarrere, P., Sarrat, C., and Le Moigne, P., 2011. Regional-scale evaluation of a land surface scheme from atmospheric boundary layer observations, J. Geophys. Res. Atmos. 116, D01104, https://doi.org/10.1029/2010JD014671.

Norman, J. M., Garcia, R., and Verma, S. B., 1992. Soil surface CO2 fluxes and the carbon budget of a grassland, J. Geophys. Res. 97(D17), 18845–18853, https://doi.org/10.1029/92JD01348.

Norman, J.M., Kustas, W.P., and Humes, K.S., 1995. Source approach for estimating soil and vegetation energy fluxes in observations of directional radiometric surface temperature, *Agricultural and Forest Meteorology 77*, 263-293.

Novick, K., Biederman, J., Desai, A., Litvak, M., Moore, D., Scott, R., Torn, M., 2017. The AmeriFlux network: A coalition of the willing, Agric. For Meteorol., 249.

Obukhov, A.M., 1951. Charakteristiki mikrostruktury vetra v prizemnom sloje atmosfery (Charac-teristics of the micro-structure of the wind in the surface layer of the atmosphere), Izv ANSSSR ser Geofiz 3, 49–68 (6).

Oncley, S. Foken, T., Vogt, R., Kohsiek, W., de Bruin, H., Bernhofer, C., Christen, A., van Gorsel, E., Grantz, D., Feigenwinter, C., Lehner, I., Liebethal, C., Liu, H., Mauder, M., Pitacco, A., Frölén R.L., 2007. The Energy Balance Experiment EBEX-2000. Part I: Overview and energy balance, Boundary-Layer Meteorology 123, 1-28. https://doi.org/10.1007/s10546-007-9161-1.

O'Brien, P.L., DeSutter, T.M., Casey, F.X.M., Daigh, A.L., Heitman, J.L., Derby, N.E., Khan, E., 2018. Day time Surface Energy Fluxes over Soil Material Remediated Using Thermal Desorption, Agrosystems, Geosciences & Environment 1 (1–9), 180027. https://doi.org/10.2134/age2018.08.0027.

Papale, D., Valentini, R., 2003. A new assessment of European forests carbon exchanges by eddy fluxes and artificial neural network spatialization, Global Change Biol. 9, 525–535.

Pique, G., Rémy, F., Debaeke, P., Al Bitar, A., Tiphaine, T., Ceschia, E., 2020. Combining High-Resolution Remote Sensing Products with a Crop Model to Estimate Carbon and Water Budget Components: Application to Sunflower, Remote Sensing 12, https://doi.org/10.3390/rs12182967.

Poeplau, C., Don, A., 2015. Carbon sequestration in agricultural soils via cultivation of cover crops – A meta-Analysis, Agriculture Ecosystems & Environment. 200, 33-41. https://doi.org/10.1016/j.agee.2014.10.024.

Pokovai, K., Fodor, N., 2019. Adjusting Ceptometer Data to Improve Leaf Area Index Measurements. Agron omy 9, 866. https://doi.org/10.3390/agronomy9120866.

Panin, G.N., Tetzlaff, G., Raabe, A., 1998. Inhomogeneity of the land surface and problems in the parameterization of surface fluxes in natural conditions, Theor. Appl. Climatol. 60, 163–178. https://doi.org/10.1007/s007040050041.

Reichstein, M., Falge, E., Baldocchi, D., Papale, D., Aubinet, M., Berbigier, P., Bernhofer, C., Buchmann, N., Gilmanov, T., Granier, A., Grunwald, T., Havrankova, K., Ilvesniemi, H., Janous, D., Knohl, A., Laurila, T., Lohila, A., Loustau, D., Matteucci, G., Meyers, T., Miglietta, F., Ourcival, J.-M., Pumpanen, J., Rambal, S., Rotenberg, E., Sanz, M., Tenhunen, J., Seufert, G., Vaccari, F., Vesala, T., Yakir, D., and Valentini, R., 2005. On the separation of net ecosystem exchange into assimilation and ecosystem respiration: review and improved algorithm, Global Change Biology 11, 1424-1439.

Reynolds, J.F., Kemp, P.R., Tenhunen. J.D., 2000. Effects of long-term rainfall variability on evapotranspiration and soil water distribution in the Chihuahuan Desert: a modeling analysis, Plant Ecology 150, 145–159.

Roerink, G.J., Su, Z., Menenti, M., 2000. S-SEBI: A Simple Remote Sensing Algorithm to Estimate the Surface Energy Balance. Physics and Chemistry of the Earth, Part B, Hydrology, Oceans and Atmosphere 25, 147-157. https://doi.org/10.1016/S1464-1909(99)00128-8.

Saito, M., Miyata, A., Nagai, H., Yamada, T., 2005. Seasonal variation of carbon dioxide exchange in rice paddy field in Japan, Agricultural and Forest Meteorology 135, 93-109. https://doi.org/10.1016/j.agrformet.2005.10.007.

Sakuratani, J., Abe, T., 1985. A heat balance method for measuring water flow rate in stems of intact plants and its application to sugarcane plants. JARQ Jpn. Agric. Res. Q., 37, 9–17.

Samson, R., Lemeur, R., 2001. Energy balance storage terms and big-leaf evapotranspiration in a mixed deciduous forest, Ann. For. Sci. 58, 529–541.

Sánchez-Tomás, J., Caselles, V., Rubio, E., 2010. Analysis of the energy balance closure over a FLUXNET boreal forest in Finland. Hydrology and Earth System Sciences 14. https://doi.org/10.5194/hessd-7-2683-2010.

Sauer, T.J. and Horton, R., 2005. Soil Heat Flux. In Micrometeorology in Agricultural Systems (eds J. Hatfield and J. Baker). https://doi.org/10.2134/agronmonogr47.c7.

Schmid, H. P., 1997. Experimental design for flux measurements: matching scales of observations and fluxes, Agricultural and Forest Meteorology 87, 179-2.

Schotanus, P., Nieuwstadt, F.T.M., de Bruin, H., 1983. Temperature-Measurement with a Sonic Anemometer and its Application to Heat and Moisture Fluxes. Boundary-Layer Meteorology 26, 81-93. https://doi.org/10.1007/BF00164332.

Scott, R.L., Huxman, T.E., Cable, W.L. and Emmerich, W.E., 2006. Partitioning of evapotranspiration and its relation to carbon dioxide exchange in a Chihuahuan Desert shrubland, Hydrol. Process. 20, 3227-3243. https://doi.org/10.1002/hyp.6329.

Sellers, P. J., Mintz, Y., Sud, Y. C., and Dalcher, A., 1986. A Simple Biosphere Model (SIB) for Use within General
Circulation Models, *Journal of Atmospheric Sciences*, *43*(6), 505-531. https://journals.ametsoc.org/view/journals/atsc/43/6/15200469_1986_043_0505_asbmfu_2_0_co_2.xml.

Sellers, P., Randall, D., Collatz, G., Berry, J., Field, C., Dazlich, D., Zhang, C., and Collelo, G., Bounoua, L., 1996.
A Revised Land Surface Parameterization (SiB2) for Atmospheric GCMS. Part I: Model Formulation, *Journal of Climate* *9*(4), 676-705. https://journals.ametsoc.org/view/journals/clim/9/4/1520-0442_1996_009_0676_arlspf_2_0_co_2.xml.

Sellers, P.J, Berry, J.A., Collatz, G.J., Field, C.B., and Hall, F.G., 1992. Canopy reflectance, photosynthesis, and transpiration. III. A reanalysis using improved leaf models and a new canopy integration scheme, Remote Sensing of environment 42(3), 187-216. https://doi.org/10.1016/0034-4257(92)90102-p.

Sellers, P.J, Dickinson, R.E., Randall, D.A., Betts, A.K., Hall, F.G., Berry, J.A., Collatz, G.J., Denning, A.S., Mooney, H.A., Nobre, C.A., Sato, N., Field, C.B., and Henderson-Sellers, A., 1997. Modeling the Exchanges of Energy, Water, and Carbon Between Continents and the Atmosphere, Science 275(5299), 502-9. PMID: 8999789. https://doi.org/10.1126/science.275.5299.502.

Semenza, J.C., 2014. Climate Change and Human Health. *Int., J. Environ. Res. Public Health 11*, 7347-7353. https://doi.org/10.3390/ijerph110707347.

Serra-Wittling, C., Molle, B., Cheviron, B., 2019, Plot level assessment of irrigation water savings due to the shift from sprinkler to localized irrigation systems or to the use of soil hydric status probes. Application in the French context, Agricultural Water Management 223, 105682, https://hal.inrae.fr/hal-02609656/document.

Shahzad, U., 2015. Global Warming: Causes, Effects and Solutions.

Shanshan, Z., Wenzhao, L., Wen, L., 2017. The ratio of transpiration to evapotranspiration in a rainfed maize field on the Loess Plateau of China, *Water Supply* 17 (1), 221–228. https://doi.org/10.2166/ws.2016.108.

Simmons, L.J., Wand, J., Sammis, T.W., Miller, D.R., 2007. An evaluation of two inexpensive energy-balance techniques for measuring water use in flood-irrigated pecans (Carya illinoinensis), Agricultural Water Management 88, 181-191.

Simó, G., Martínez-Villagrasa, D., Jimenez, M.A., Caselles, V., Cuxart, J., 2019. Impact of the Surface–Atmosphere Variables on the Relation Between Air and Land Surface Temperatures. In: Vilibic, I., Horvath, K., Palau, J. (Eds.), Meteorology and Climatology of the Mediterranean and Black Seas, Pageoph Topical Volumes. Birkhauser. Cham. https://doi.org/10.1007/978-3-030-11958-4_13.

Singh, J.S., and Gupta, S.R., 1977. Plant decomposition and soil respiration in terrestrial ecosystem, Bot. Rev. 43, 449–528.

Smith, D.M., and Allen, S., 1996. Measurement of sap flow in plant stems, Journal of Experimental Botany 47, 1833-1844. https://doi.org/10.1093/jxb/47.12.1833.

Stannard, D.I., Blanford, J.H., Kustas, W.P., Nichols, W.D., Amer, S.A., Schmugge, T.J., Weltz, M.A., 1994. Interpretation of surface flux measurements in heterogeneous terrain during the Monsoon'90 experiment. Wat. Resour. Res. 30 (5), 1227–1239.

Stoy, P., Mauder, M., Foken, T., Marcolla, B., Boegh, E., Ibrom, A., Arain, M., Arneth, A., Aurela, M., Bernhofer, C., Cescatti, A., Dellwik, E., Duce, P., Gianelle, D., van Gorsel, E., Kiely, G., Knohl, A., Margolis, H., McCaughey, H., Varlagin, A., 2013. A data-driven analysis of energy balance closure across FLUXNET research sites: The role of landscape-scale heterogeneity, Agricultural and Forest Meteorology 171-172, 137-152. https://doi.org/10.1016/j.agrformet.2012.11.004.

Su, Z., 2002. The Surface Energy Balance System (SEBS) for estimation of turbulent heat fluxes, Hydrol. Earth Syst. Sci. 6, 85–100. https://doi.org/10.5194/hess-6-85-2002.

Sanderman, J., Hengl, T., Fiske, G., Solvik, K., Adame, F., Benson, L., Bukoski, J., Carnell, P., Cifuentes, M., Donato, D., Duncan, C., Eid, E., Zu Ermgassen, P., Ewers Lewis, C., Glass, L., Gress, S., Jardine, S., Jones, T., Macreadie, P., Landis, E., 2018. A global map of mangrove forest soil carbon at 30 m spatial resolution, Environmental Research Letters 13, 055002. https://doi.org/10.1088/1748-9326/aabe1c.

Swinbank, W.C., 1951. The measurement of vertical transfer of heat and water vapor by eddies in the lower atmosphere. J. Meteorol. 8, 135–145.

Sylvain, P., Laure, B., Julie, C., Camille, L., Raphaël, Martin., 2019. A model based assessment of the soil C storage potential at the national scale: A case study from France. Food security and climate change: 4 per 1000 initiative new tangible global challenges for the soil, Poitiers, France

Tardy, B., Rivalland, V., Huc, M., Hagolle, O., Marcq, S., Boulet, G., 2016. A Software Tool for Atmospheric Correction and Surface Temperature Estimation of Landsat Infrared Thermal Data, Remote Sens. 8, 696. https://doi.org/10.3390/rs8090696.

Tasumi, M., 2003. Progress in Operational Estimation of Regional Evapotranspiration Using Satellite Imagery, Ph.D. Thesis, University of Idaho, Moscow, ID, USA.

Taylor G.I., 1938. The spectrum of turbulence, Proc. R. Soc. Lon. Ser-A, 164(919), 476-490.

Teixeira, A.H. Bastiaanssen, W.G.M., 2010. Five methods to interpret field measurements of energy fluxes over a micro-sprinkler-irrigated mango orchard, Irrigation Science 30, 13-28. https://doi.org/10.1007/s00271-010-0256-y.

Thompson, N., Barrie, I.A., Ayles, M., 1981. The Meteorological Office rainfall and evaporation calculation system: (MORECS), Hydrol. Memo. 45, Meteorological Office, Bracknell.

Tsvang, L.R, Fedorov, M.M, Kader, B.A., 1991. Turbulent exchange over a surface with chessboard-type in Homogeneities, Boundary-Layer Meteorol. 55, 141–160.

Twine, T.E., Kustas, W.P., Norman, J.M., 2000. Correcting eddy-covariance flux underestimates over a Grassland, Agric. For. Meteorol. 103, 279–300. https://doi.org/10.1016/S0168-1923(00)00123-4.

Twine, T., Kustas, W.P., Norman, J., Cook, D., Houser, P., Teyers, T.P., Prueger, J.H., Starks, P., Wesely, M., 2000. Correcting Eddy-Covariance Flux Underestimates over a Grassland, Agricultural and Forest Meteorology 103. https://doi.org/10.1016/S0168-1923(00)00123-4.

Van den Hurk, B., et al., 2016. LS3MIP (v1.0) contribution to CMIP6: The Land Surface, Snow and Soil moisture Model Intercomparison Project—Aims, setup and expected outcome, Geosci. Model Dev. 9, 2809–2832, https://doi.org/10.5194/gmd-9-2809-2016.

Van Hurk, B.J.J.M.D., Verhoef, A., Van Berg, A.R.D., De Bruin, H.A.R., 1995. An intercomparison of three vegetation/soil models for a sparse vineyard canopy, Q. J. R. Meteorol. Soc. 121, 1867–1889.

Verma, S., Dobermann, A., Cassman, K., Walters, D., Knops, J. Arkebauer, T., Suyker, A., Burba, G., Amos, B., Yang, H., Ginting, D., Hubbard, K., Gitelson, A., Walter-Shea, E., 2005. Annual carbon dioxide exchange in irrigated and rainfed maize-based agroecosystems, Agricultural and Forest Meteorology 131, 77-96. https://doi.org/10.1016/j.agrformet.2005.05.003.

Vickers, D., Mahrt, L., 2000. Quality Control and Flux Sampling Problems for Tower and Aircraft Data, Journal of Atmospheric and Oceanic Technology 14. https://doi.org/10.1175/1520-0426(1997)014<0512:QCAFSP>2.0.CO;2.

Wallace, J. M., Hobbs, P. V., 2006. Atmospheric Science, Second Edition: An Introductory Survey, (second ed.). New York: Academic press.

Wang, L., Caylor, K. K., Villegas, J. C., Barron-Gafford, G. A., Breshears, D. D., and Huxman, T. E., 2010. Partitioning evapotranspiration across gradients of woody plant cover: Assessment of a stable isotope technique, Geophys. Res. Lett. 37, L09401. https://doi.org/10.1029/2010GL043228

Wang, M., Guan, D.-X., Han, S.-J., Wu, J-L., 2009. Comparison of eddy covariance and chamber-based methods for measuring CO2 flux in a temperate mixed forest, Tree physiology 30, 149-63. https://doi.org/10.1093/treephys/tpp098.

Webb, E.K., Pearman, G.I., Leuning, R., 1980. Correction of flux measurements for density effects due to heat and water vapour transfer. Q.J.R. Meteorol. Soc. 106, 85-100. https://doi.org/10.1002/qj.49710644707.

West, T. O., Marland, G., King, A. W., Post, W. M., Jain, A. K., & Andrasko, K., 2004. Carbon Management Response curves: estimates of temporal soil carbon dynamics, Environmental management 33(4), 507–518. https://doi.org/10.1007/s00267-003-9108-3.

Wohlfahrt, G., Sapinsky, S., Tappeiner, U., Cernusca, A., 2001. Estimation of plant area index of grasslands from measurements of canopy radiation profiles, Agric. For. Meteorol. 109, 1–12. https://doi.org/10.1016/S0168-1923(01)00259-3.

Wang, K., Liu, C., Zheng, X., Pihlatie, M., Li, B., Haapanala, S., Vesala, T., Liu, H., Wang, Y., Liu, G., and

Hu, F., 2013. Comparison between eddy covariance and automatic chamber techniques for measuring net ecosystem exchange of carbon dioxide in cotton and wheat fields, Biogeosciences 10, 6865–6877. https://doi.org/10.5194/bg-10-6865-2013.

Wilhelm, W.W., Ruhe K., 2000. Schlemmer, M.R. Comparison of three Leaf Area Index Meters in a corn Canopy, CropSci. 40, 1179-1183.

Wilson, K., Goldstein, A., Falge, E., Aubinet, M., Baldocchi, D., Berbigier, P., Bernhofer, C., Ceulemans, R., Dolman, H., Field, C., Grelle, A., Ibrom, A., Law, B., Kowalski, A., Meyers, T., Moncrieff, J., Monson, R., Oechel, W., Tenhunen, J., Valentini, R., Verma, S., 2002. Energy balance closure at FLUXNET sites, *Agric. For. Meteor.* **113**, 223–243. https://doi.org/10.1016/S0168-1923(02)00109-0.

Wolf, J., Van Diepen, C.A., 1995. Effects of climate change on grain maize yield potential in the european community, Climatic Change 29, 299–331. https://doi.org/10.1007/BF01091866

Wojciechowska, N., Sobieszczuk-Nowicka, E., Bagniewska-Zadworna, A., 2017. Plant organ senescence – regulation by manifold pathways, Plant Biology 20. https://doi.org/10.1111/plb.12672.

Wu, X., Vuichard, N., Ciais, P., Moors, E., Jans, W., Elbers, J., 2016. ORCHIDEE-CROP (v0), a new process-based agro-land surface model: Model description and evaluation over Europe. https://doi.org/10.5194/gmd-9-857-2016.

Xu, H., Xiao, J., Zhang, Z.Q., 2020. Heatwave Effects on Gross Primary Production of Northern Mid-latitude Ecosystems, Environmental Research Letters. https://doi.org/10.1088/1748-9326/ab8760.

Xu, K., Pingintha-Durden, N., Luo, H., Durden, D., Sturtevant, C., Desai, A., Florian, C., Metzger, S., 2019. The eddy-covariance storage term in air: Consistent community resources improve flux measurement reliability, Agricultural and Forest Meteorology 279, 107734. https://doi.org/10.1016/j.agrformet.2019.107734.

Xin, Y.F., Chen, F., Zhao, P., Barlage, M., Blanken, P., Chen, Y.L., Chen, B., Wang, Y.J., 2018. Surface energy balance closure at ten sites over the Tibetan plateau, Agric. For. Meteorol. 259, 317–328. https://doi.org/10.1016/j.agrformet.2018.05.007.

Xu, Z., Ma, Y., Liu, S., Shi, W., Wang, J., 2017. Assessment of the Energy Balance Closure under Advective Conditions and Its Impact Using Remote Sensing Data, J. Appl. Meteor. Climatol. 56, 127–140. https://doi.org/10.1175/JAMC-D-16-0096.1.

Yang, Z., Dickinson, R.E., 1996. Description of the Biosphere-Atmosphere Transfer Scheme (BATS) for the Soil Moisture Workshop and evaluation of its performance.

Yepez, E.A., Williams, D.G., Scott, R.L., Lin, G., 2003. Partitioning overstory and understory evapotranspiration in a semiarid savanna woodland from the isotopic composition of water vapor, Agricultural and Forest Meteorology 119, 53–68. https://doi.org/10.1016/S0168-1923(03)00116-3.

Zamolodchikov, D. G., Karelin, D. V., Ivaschenko, A. I., Oechel, W. C., and Hastings, S. J., 2003. CO_2 flux measurements in Russian Far East tundra using eddy covariance and closed chamber techniques, Tellus B 55(4), 879–892, 2003.

Zhang, K., Kimball, J. S. and Running, S. W. (2016), A review of remote sensing based actual evapotranspiration estimation. WIREs Water 3, 834–853. https://doi.org/10.1002/wat2.1168.

APPENDIX A: Surface energy balance and flux partitioning of annual crops in southwestern France

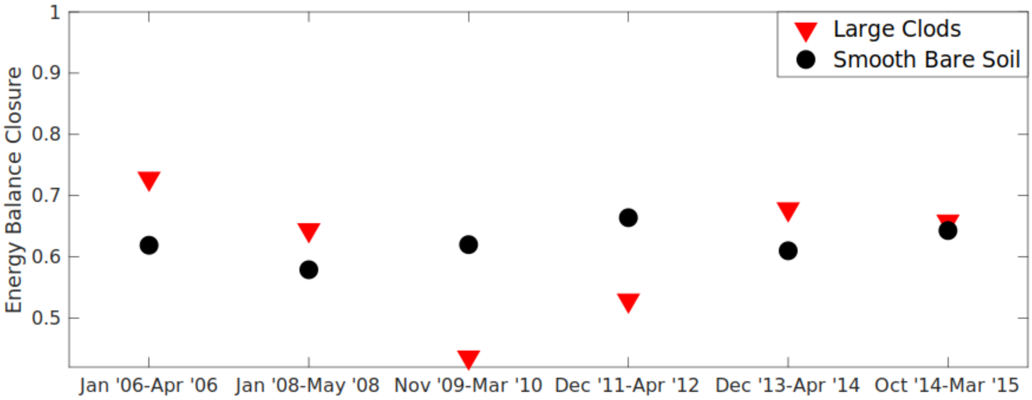

Figure A1: Comparing the EBC of large clod soils and the succeeding smooth bare soil period.

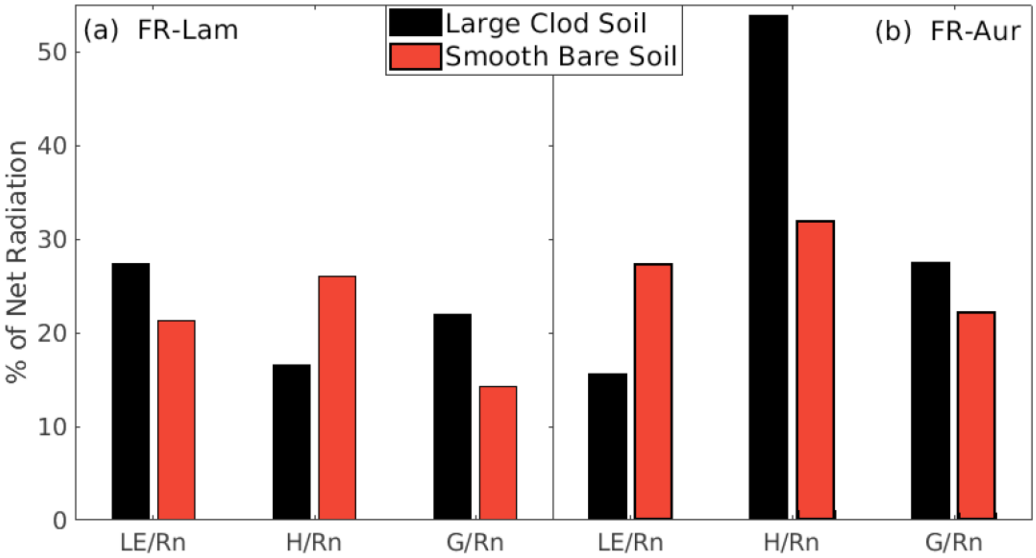

Figure A2: Impact of tillage on energy partitioning in FR-Lam and FR-Aur for large clods (LC) and smooth bare soils (SBS). Note that FR-Aur was only deep tilled once (i.e., large clod).

In FR-Lam, *LE* is the dominant flux in LC because LC periods are often observed during winter, and this period is associated with high soil water content. Also, LC had 29% more evaporative fluxes than SBS. However, more energy is partitioned into *H* in FR-Aur because LC was observed during summer, and so, most of the energy was used for atmospheric heating. At both sites, large clods stored more energy in the soil substrate compared to SBS because the LC surfaces have higher bulk density, lower albedo, and they experience diffuse reflection- this influences the volumetric heat capacity and encourages re-reflection of energy into the soil in contrast to smooth soils that experience specular reflection.

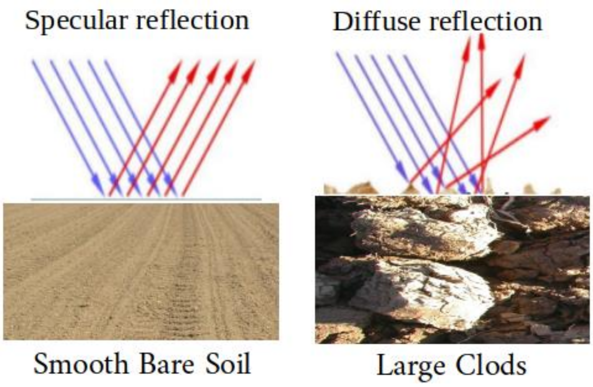

Figure A3: Structure difference between a smooth bare soil and large clods.

APPENDIX B: Estimation and partitioning of energy fluxes over a maize and wheat field using a land surface model.

Table B1: EBC for the raw and corrected fluxes (in parenthesis) for maize.

Months	Maize-2008	Maize-2010	Maize-2012	Maize-2014	Maize-2015	Maize-2019
Apr	0.56 (0.99)	0.53 (0.99)	0.62 (0.97)	0.58 (0.94)	0.76 (0.96)	0.80 (0.91)
May	0.55 (0.91)	0.57 (0.98)	0.68 (0.97)	0.58 (0.93)	0.76 (0.96)	0.75 (0.93)
Jun	0.66 (0.98)	0.54 (0.98)	0.72 (0.99)	0.65 (0.89)	0.71 (0.95)	0.63 (0.95)
Jul	0.72 (0.99)	0.69 (0.99)	0.69 (0.99)	0.61 (0.98)	0.80 (0.95)	0.64 (0.96)
Aug	0.79 (0.99)	0.73 (0.99)	0.65 (0.94)	0.57 (0.95)	0.85 (0.97)	0.72 (0.96)
Sep	0.73 (0.99)	0.62 (0.99)	0.63 (0.94)	0.63 (0.94)	0.77 (0.91)	0.78 (0.95)

Table B2: Residual energy in W m^{-2} for the raw and corrected fluxes (in parenthesis) for maize.

Months	Maize-2008	Maize-2010	Maize-2012	Maize-2014	Maize-2015	Maize-2019
Apr	77 (6)	70 (4)	50 (8)	25 (12)	20 (12)	43 (15)
May	73 (5)	63 (5)	52 (7)	19 (12)	19 (12)	40 (16)
Jun	83 (5)	60 (4)	58 (4)	32 (5)	22 (17)	48 (13)
Jul	63 (3)	62 (4)	65 (4)	34 (5)	27 (16)	51 (10)
Aug	62 (3)	63 (5)	70 (12)	38 (6)	23 (12)	48 (11)
Sep	60 (4)	54 (4)	49 (12)	21 (9)	19 (18)	39 (12)

Table B3: EBC for the raw and corrected fluxes (in parenthesis) for wheat.

Months	Wheat-2007	Wheat-2009	Wheat-2011	Wheat-2013
Oct	0.58 (0.97)	0.50 (0.96)	0.80 (0.99)	0.65 (0.93)
Nov	0.58 (0.88)	0.46 (0.92)	0.58 (0.97)	0.72 (0.93)
Dec	0.48 (0.94)	0.44 (0.90)	0.41 (0.86)	0.81 (0.90)
Jan	0.42 (0.91)	0.42 (0.87)	0.40 (0.79)	0.75 (0.93)
Feb	0.52 (0.99)	0.41 (0.91)	0.73 (0.99)	0.90 (0.99)
Mar	0.57 (0.98)	0.45 (0.92)	0.64 (0.98)	0.96 (0.99)
Apr	0.61 (0.99)	0.53 (0.95)	0.69 (0.95)	0.99 (0.98)
May	0.60 (0.99)	0.57 (0.95)	0.71 (0.98)	0.99 (0.98)
Jun	0.59 (0.99)	0.55 (0.97)	0.62 (0.97)	0.95 (0.98)
Jul	0.54 (0.88)	0.56 (0.97)	0.70 (0.98)	0.87 (0.96)
Aug	0.52 (0.99)	0.55 (0.96)	0.68 (0.99)	0.87 (0.95)
Sep	0.59 (0.99)	0.56 (0.97)	0.70 (0.98)	0.85 (0.97)

Table B4: Residual energy in W m^{-2} for the raw and corrected fluxes (in parenthesis) for wheat.

Months	Wheat-2007	Wheat-2009	Wheat-2011	Wheat-2013
Oct	40 (10)	44 (7)	35 (7)	38 (12)
Nov	35 (13)	34 (9)	28 (8)	23 (10)
Dec	26 (10)	27 (8)	30 (12)	23 (13)
Jan	30 (11)	32 (11)	34 (16)	21 (11)
Feb	34 (9)	49 (14)	36 (11)	28 (11)
Mar	53 (8)	66 (16)	44 (10)	41 (9)
Apr	73 (6)	71 (11)	57 (13)	54 (8)
May	76 (8)	77 (12)	60 (8)	69 (8)
Jun	94 (5)	90 (9)	73 (9)	73 (9)
Jul	78 (25)	78 (9)	58 (8)	75 (11)
Aug	76 (6)	78 (10)	61 (7)	62 (11)
Sep	69 (7)	58 (9)	44 (7)	52 (10)

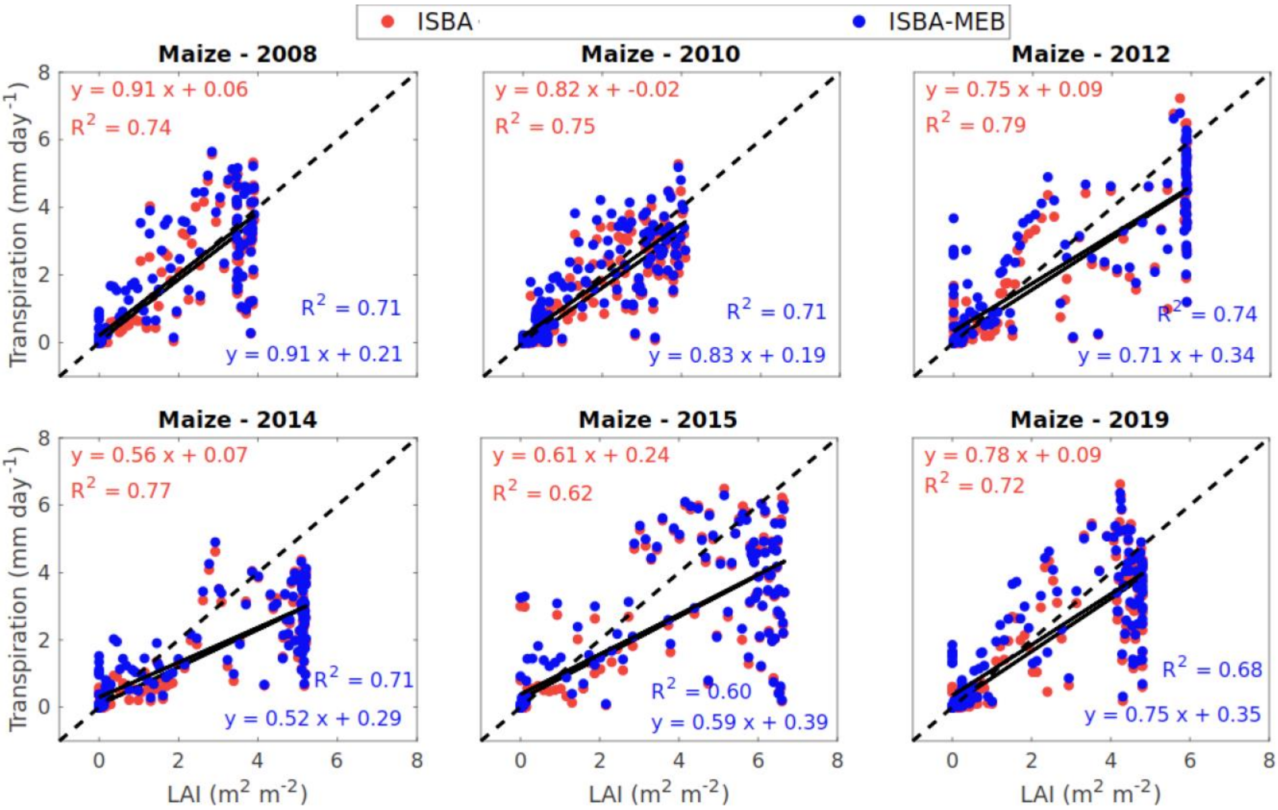

Figure B1: Relationship between estimated transpiration and leaf area index.

APPENDIX C: Estimating carbon components over maize and wheat using a land surface model

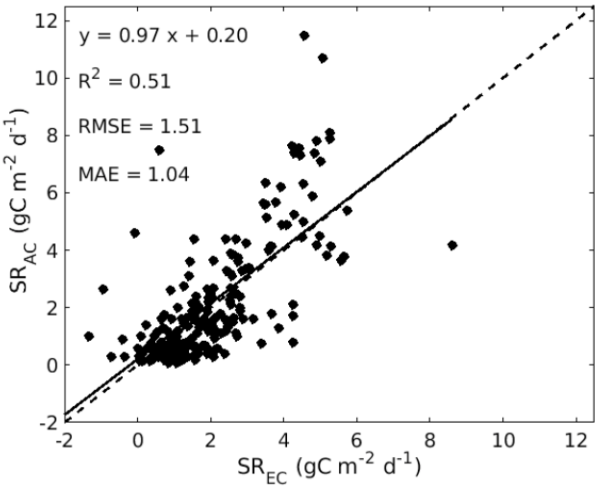

Figure C1: Soil respiration measured with automated chamber (AC) and eddy covariance (EC) system during the bare soil period of 23rd July 2013 to 19th May 2015 in FR-Lam site.

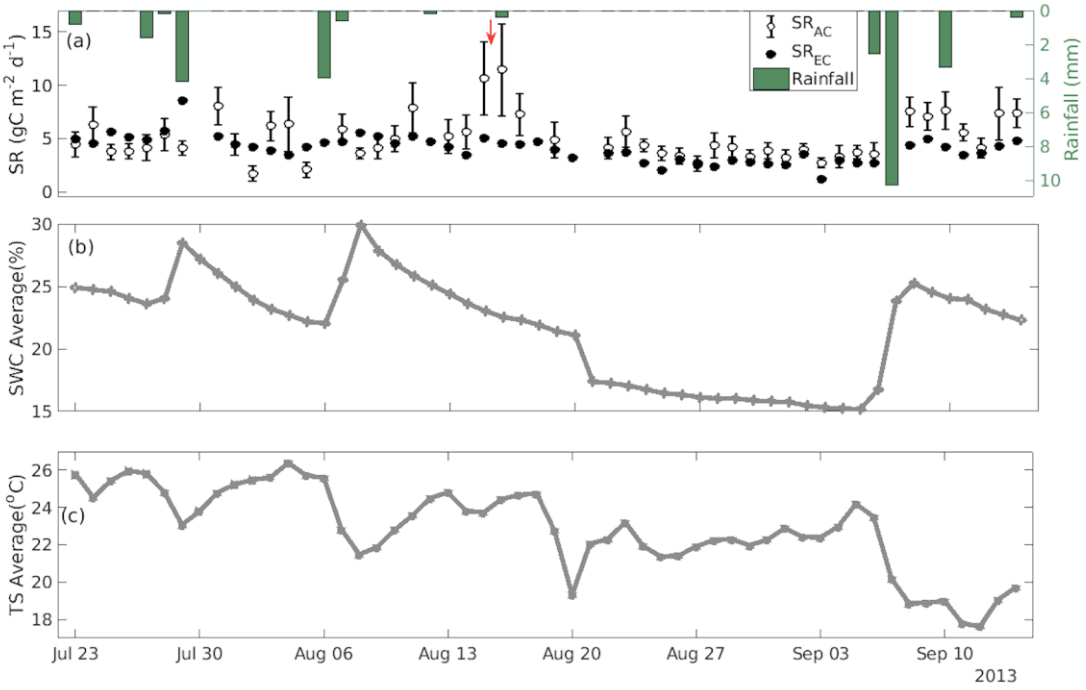

Figure C2: Time series of (a) soil respiration obtained from the automated chamber and eddy covariance system, (b) the soil water content averaged between 0 and 10 cm depth, (c) same as (b) but for soil temperature between 23rd July to 14th September 2013. The red arrow signifies tillage.

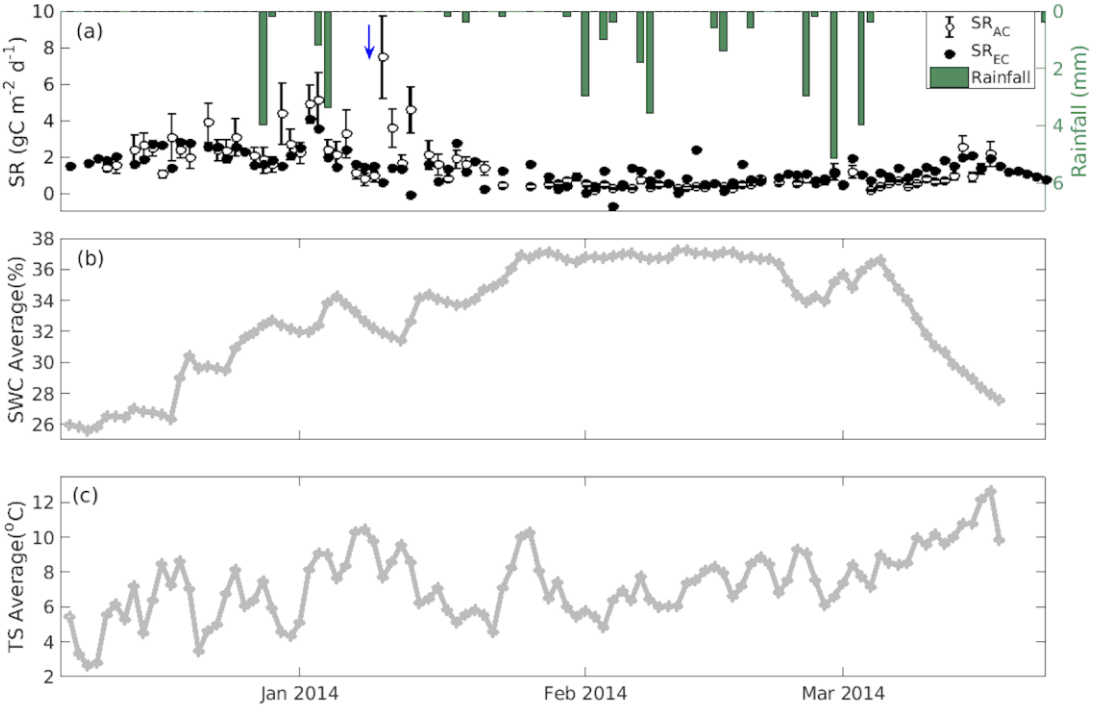

Figure C3: The same as Figure C2, but for the period 7th December 2013 to 23rd March 2014. The blue arrow signifies large clods.

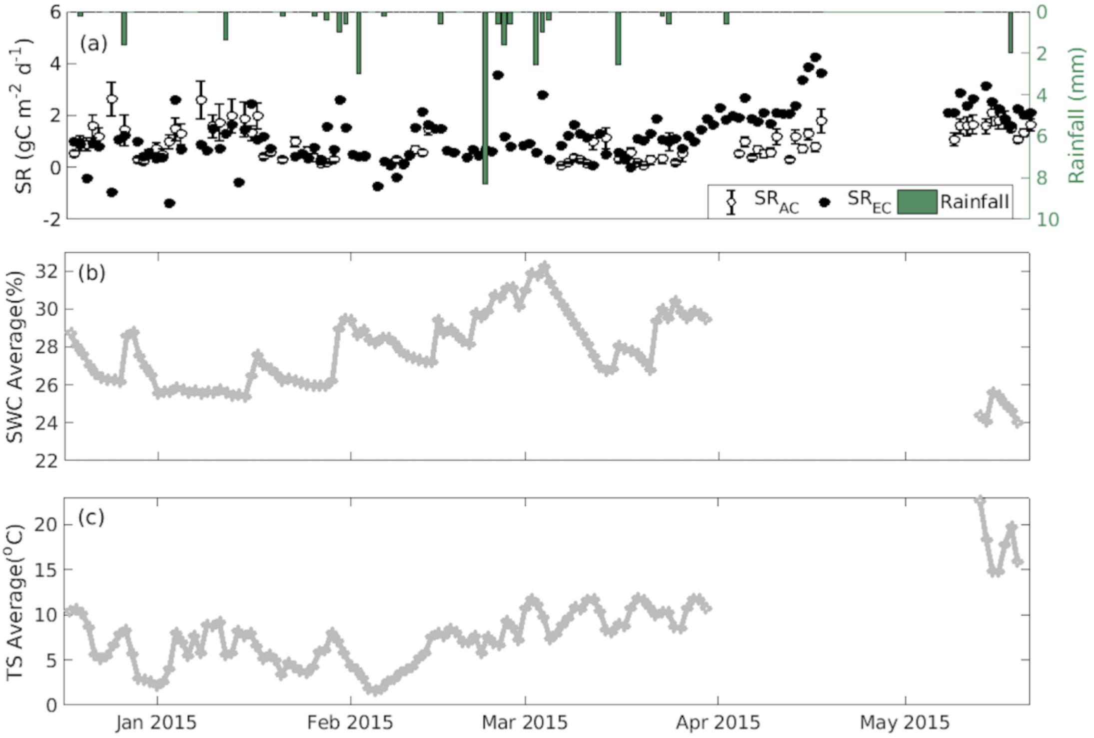

Figure C4: The same as Figure C2, but for the period 18th December 2014 to 19th May 2015.

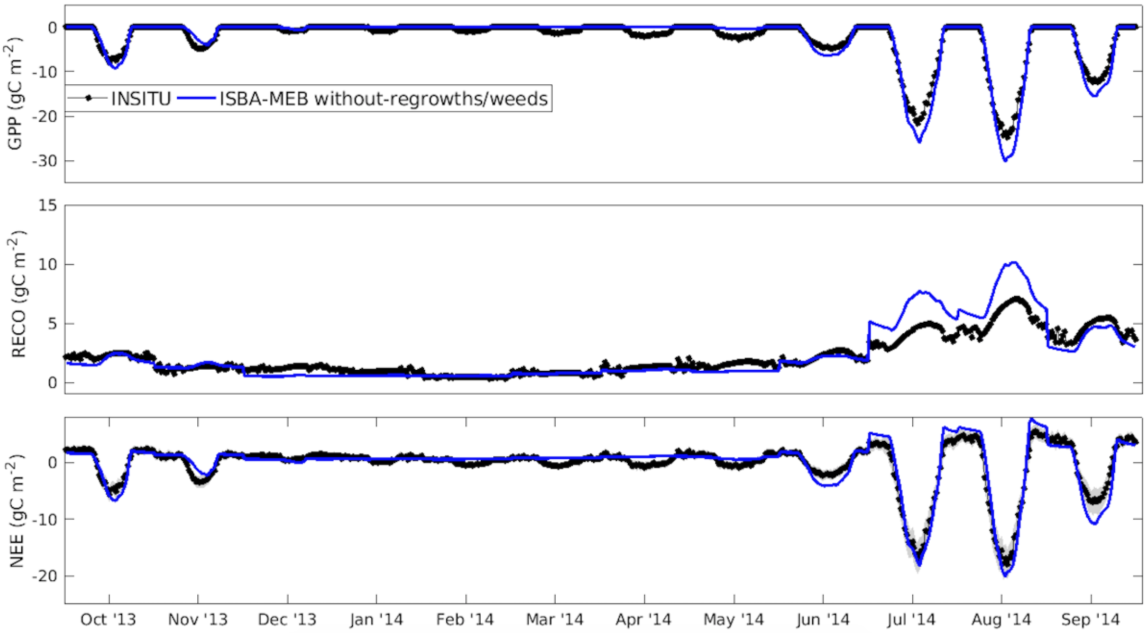

Figure C5: Monthly time series of observed (black) and simulated (blue) GPP, $RECO$, and NEE for maize-2014. The shaded regions represent the standard deviations (in GPP and $RECO$) and the uncertainties (in NEE).